AD_____

Award Number: DAMD17-00-1-0071

TITLE: Genetics of Bone Mineralization and Morphology in Inbred
        Mice: Analysis of the HcB/Dem Recombinant Congenic
        Strains

PRINCIPAL INVESTIGATOR: Robert D. Blank, M.D., Ph.D.

CONTRACTING ORGANIZATION: University of Wisconsin
                           Madison, WI 53706-1490

REPORT DATE: April 2005

TYPE OF REPORT: Final

20060215 109

PREPARED FOR: U.S. Army Medical Research and Materiel Command
               Fort Detrick, Maryland 21702-5012

DISTRIBUTION STATEMENT: Approved for Public Release;
                         Distribution Unlimited

The views, opinions and/or findings contained in this report are
those of the author(s) and should not be construed as an official
Department of the Army position, policy or decision unless so
designated by other documentation.

REPORT DOCUMENTATION PAGE

1. AGENCY USE ONLY (Leave blank)	2. REPORT DATE April 2005	3. REPORT TYPE AND DATES COVERED Final (1 Apr 00 – 31 Mar 05)

4. TITLE AND SUBTITLE
Genetics of Bone Mineralization and Morphology in Inbred Mice: Analysis of the HcB/Dem Recombinant Congenic Strains

5. FUNDING NUMBERS
DAMD17-00-1-0071

6. AUTHOR(S)
Robert D. Blank, M.D., Ph.D.

7. PERFORMING ORGANIZATION NAME(S) AND ADDRESS(ES)
University of Wisconsin
Madison, WI 53706-1490

E-Mail: rdb@medicine.wisc.edu

8. PERFORMING ORGANIZATION REPORT NUMBER

9. SPONSORING / MONITORING AGENCY NAME(S) AND ADDRESS(ES)
U.S. Army Medical Research and Materiel Command
Fort Detrick, Maryland 21702-5012

10. SPONSORING / MONITORING AGENCY REPORT NUMBER

11. SUPPLEMENTARY NOTES

12a. DISTRIBUTION / AVAILABILITY STATEMENT
Approved for Public Release; Distribution Unlimited

12b. DISTRIBUTION CODE

13. ABSTRACT (Maximum 200 Words)

This work will analyze the genetics of the first of these components through the use of recombinant congenic mice. We performed an intercross between HcB/13 and HcB/14. Broad-sense heritability of failure load is approximately 0.5, matching the expectation based on epidemiology. Linkage mapping in this cross will allow more accurate mapping of a subset of these bone strength genes and investigation into pairwise epistatic interactions among loci. Further breeding will be performed to develop true congenic lines and refine the mapping of the candidate genes for their positional cloning. A cross examining $Col1a2^{oim}/+$ heterozygotes has identified several bone strength modifying loci. Interestingly, these largely overlap quantitative trait loci found to affect bone mineral density and bone size in wild-type mice. Additional work in this system has identified a dental phenotype in both homozygotes and heterozygotes harboring the $Col1a2^{oim}$ mutation. Nanoindentation testing, including compliance analysis has allowed determination of Young's modulus and Meyer hardness independent of sample geometry. Identifying mouse chromosome regions that control peak bone mineralization and morphology will allow prediction of the corresponding human regions by synteny and facilitate human genetic studies of this problem.

14. SUBJECT TERMS
Osteoporosis, quantitative traits, epistasis, fracture risk, biomechanics, biomineralization

15. NUMBER OF PAGES
121

16. PRICE CODE

17. SECURITY CLASSIFICATION OF REPORT Unclassified	18. SECURITY CLASSIFICATION OF THIS PAGE Unclassified	19. SECURITY CLASSIFICATION OF ABSTRACT Unclassified	20. LIMITATION OF ABSTRACT Unlimited

Table of Contents

INTRODUCTION

The broad purpose of this work is to understand the genetic basis of fracture risk. In order to accomplish this goal, we are working to detect and identify genes whose segregation alters bone biomechanical performance in young adult mice. Two crosses are being analyzed; the first is an intercross of recombinant congenic strains HcB/13 X HcB/14. These strains each carry 1/8 of their genomes from C57BL/10ScSnA and the remainder from C3H/DiSnA. HcB/13 and HcB/14 are highly divergent in their bone properties, but only ~1/4 of the genome segregates in this cross, allowing analysis of epistatic interactions in a moderately sized cross. The second cross is between outbred B6C3/Fe-a/a-$Cola2^{oim/+}$ heterozygotes and B6C3/Fe-a/a F1 animals. The B6C3 background is closely related to the HcB/Dem system. In both cases, bones from 4 month animals will be phenotyped by 3-point bend testing, radiographic analysis, ash percentage, Fourier-transformed infrared spectroscopy, and histomorphometry. Histograms of the trait values will be used to select animals for use in linkage mapping, which will then be carried out using the QTL Cartographer software suite. Linkage mapping of distributed microsatellite markers will be supplemented by markers isolated through representational difference analysis of phenotypically extreme animals from each cross. QTLs identified in both crosses will be isolated through the generation of congenic lines by marker-assisted selection. The approach taken in this work expands on earlier investigations of bone genetics in that biomechanical performance is a primary endpoint and that pleiotropy testing of biomechanical outcomes and sub-phenotypes relates QTLs to specific components of bone strength.

BODY

Statement of Work Item 1: Intercross between HcB/13 and HcB/14

Progress on this item was delayed approximately 6 months due to issues arising from my relocation to the University of Wisconsin. Some, but not all of the delay has been made up since that time.

We have generated and phenotyped the 13 X 14 and 14 X 13 F1 populations. Approximately 360 animals were generated in the cross and sacrificed at 17 ± 1 weeks. Phenotyping has included each of the following:
1. body mass at sacrifice
2. ash percentage of femora, humeri, and radii from each of the animals (1 side only)
3. femoral, humeral, and radial volumes by Archimedes' principle from each of the animals (1 side only)
4. volumetric BMDs of the femora, humeri, and radii using data from items 2 and 3 above (1 side only)
5. areal BMDs of the femora, humeri, and radii using the PIXIMus DXA system (GE Lunar) (both sides)
6. micro-CT scans of femora, humeri, and radii using the micro-CAT (ImTek, Knoxville, TN) (1 side only)
7. 3 point bend testing of femora, humeri, and radii (1 side only).

Analyses of these data is in progress. This aspect of the work is proving to be quite time-consuming due to the sheer quantity of information accumulated, and unfortunately is still not complete. A subset of the phenotypic data have been analyzed sufficiently to make their presentation informative. These are briefly summarized below.

Significant sex, cross direction, and interaction effects on body mass and BMD in the F2 generation: In earlier experiments, we noted that differences in biomechanical performance between HcB/13 and HcB/14 can be accounted for largely by differences in bone dimensions and is accompanied by similarly large differences of body mass. F2 animals sacrificed at 17± 1 weeks have been weighed and had long bones examined *ex vivo* by DXA. These data are briefly summarized below in table 1.

Table 1. Body Masses and BMDs of HcB/13 X HcB/14 F2 Animals

	13 X 14 Females N = 96	13 X 14 Males N = 102	14 X 13 Females N = 99	14 X 13 Males N = 102
Body Mass (g)	21.4 ± 2.7	22.9 ± 2.6	20.0 + 2.8	22.7 ± 2.4
Femoral BMD (g/cm^2)	0.0642 ± 0.0038	0.0611 ± 0.0037	0.0616 ± 0.0049	0.0601 ± 0.0033
Humeral BMD (g/cm^2)	0.0486 ± 0.0030	0.0473 ± 0.0027	0.0464 ± 0.0037	0.0465 ± 0.0033
Radial BMD (g/cm^2)	0.0245 ± 0.0014	0.0246 ± 0.0014	0.0242 ± 0.0018	0.0246 ± 0.0015

Values in cells are means ± standard deviation. BMDs are averages of right and left bones at each site.

The body masses and BMDs of the F2 are normally distributed within arm and sex grouping by the Kolmogorov-Smirnov test. Comparison among the 4 groups of F2 by 2 way ANOVA reveals that there are significant differences between males and females ($P < 0.001$), between 13 X 14 and 14 X 13 arms of the cross ($P = 0.004$), and a significant interaction between these 2 factors ($P = 0.028$). Femoral BMD shows significant effects of cross arm ($P = 4 \times 10^{-5}$) and sex ($P = 10^{-5}$), but no interaction between these factors. At the humerus, there is a significant cross arm effect ($P = 4 \times 10^{-5}$), but no sex or interaction effect. No strain or sex effects are noted at the radius. Taken together, the data indicate that areal BMD is greater among 13 X 14 F2 mice than 14 X 13 F2 mice. These observations illustrate that performing a reciprocal cross not only provides additional linkage mapping information, but also can reveal additional biology.

Intersite correlation and left-right disparities of DXA measurements: These observations are summarized in 2 appended manuscripts. The first manuscript, now in press at the *Journal of Clinical Densitometry*, describes performance characteristics of *ex vivo* densitometry. The second manuscript has been submitted to *Calcified Tissue International* and is now undergoing review.

Multiplexed Micro-CT scanning of long bones: In order to incorporate micro-CT measurements of bone dimensions into biomechanical testing on the scale of a several hundred animal intercross, it is necessary to devise a scanning protocol that allows many specimens to be scanned simultaneously. We have accomplished this by positioning bones inside the corrugations of corrugated cardboard, with empty spaces in the lattice left to allow indexing of the positions of the individual bones and so identify each specimen unequivocally. This allows us to scan ~100 bones at once. **Figure 1** below is a scout view of such an array and **figure 2** is an arbitrary cross section.

Figure 1. Scout View of Micro-CT

Slice 90

Row 3

Row 2

Slice 890
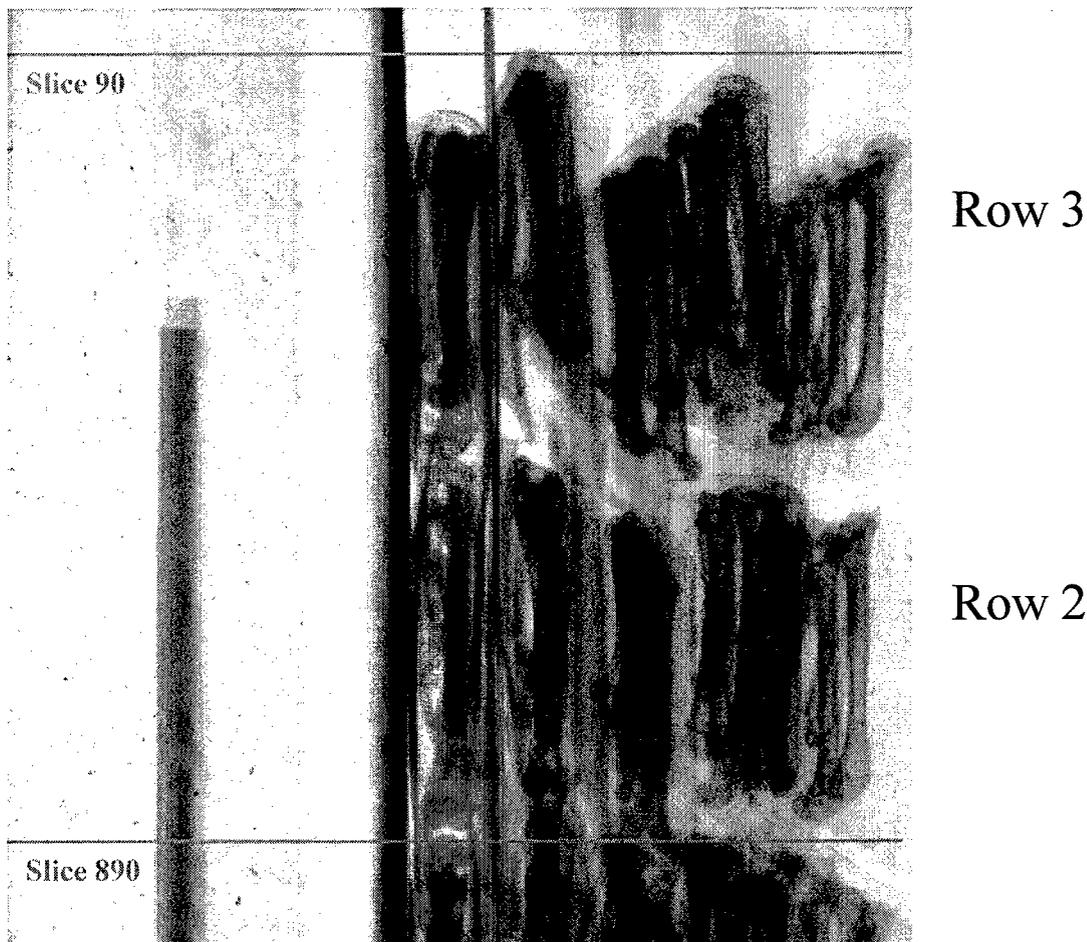
Reconstruction of the correct cross-sections for calculation of cross-sectional area (CSA) and cross sectional moment of inertia (I) still requires additional analysis once the micro-CT images have been acquired. Slice number corresponding to the point of force application must be approximated and the neutral axis assigned. As is apparent from the single slice illustrated in **figure 2**, the mid-diaphyses of the individual specimens are not aligned, so slice selection must be done for each bone, as illustrated in **figure 3**.

7

Figure 2. Arbitrary Micro-CT Cross-Section, Low Resolution Image
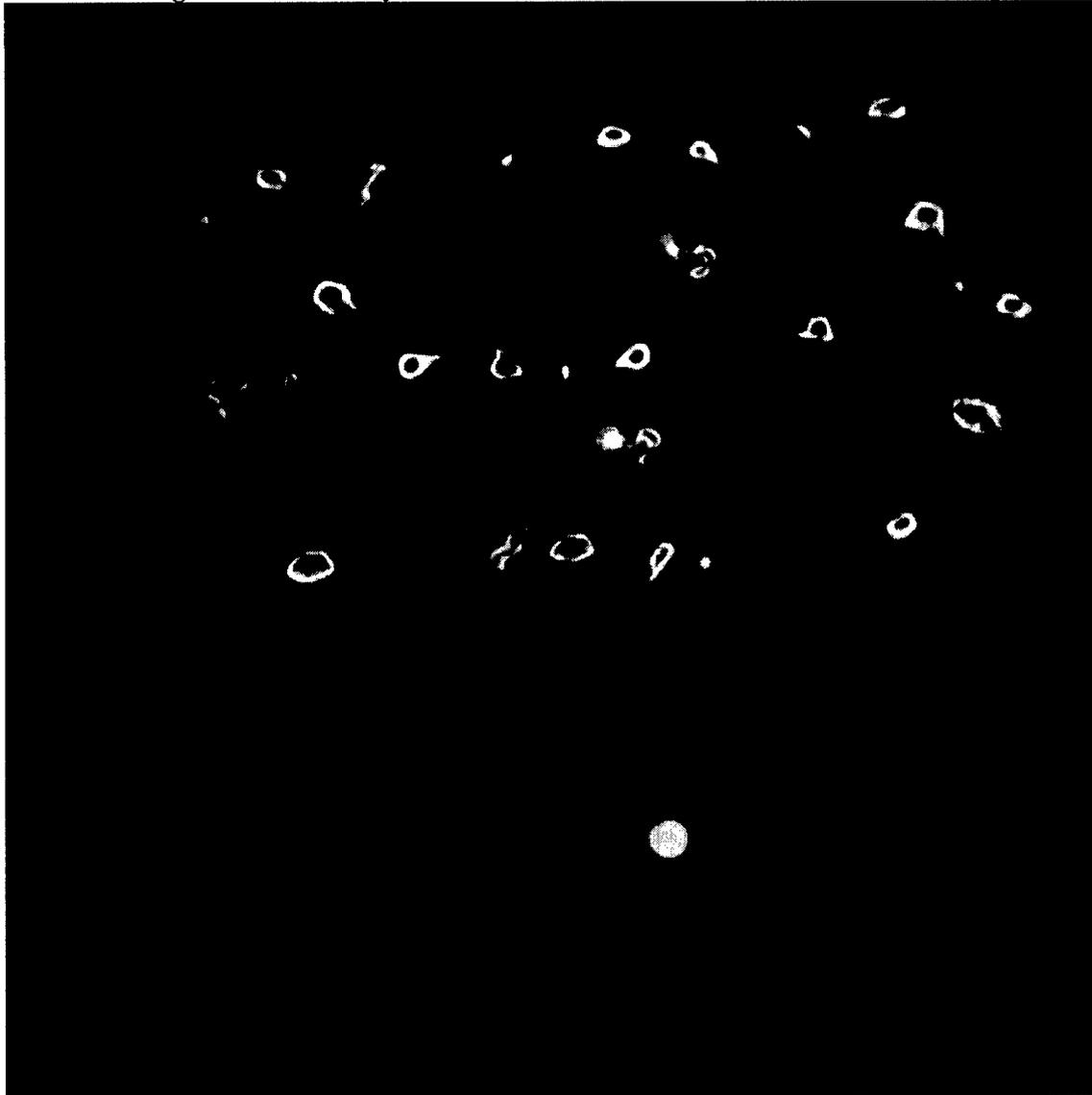
Femora,humeri, and radii are included in this cross-section.

Figure 3. Determination of centroid, and I in an Individual Femoral Diaphysis
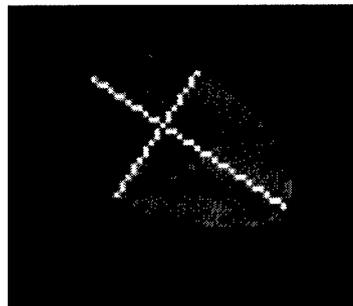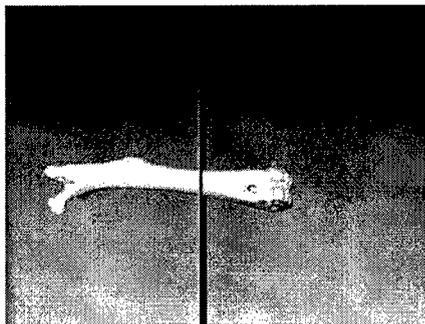
Analysis of the biomechanical testing data to determine material properties depends on images such as that at the right of figure 3. For each bone tested, a similar reconstruction is undertaken. Our image analysis software allows for automated threshold assignment of each pixel as bone or non-bone and determination of the centroid. We must assign the neutral axis manually. The software then calculates $I = \Sigma(\text{pixel area}) \times (\text{distance of pixel from neutral axis})^2$ over all bone pixels. This represents a major improvement over the calculation of I using the elliptical approximation in our earlier work.

The manually performed portions of the image analysis, while not inherently difficult, are tedious and time consuming. We have not completed enough of this work to be able to include meaningful summary data regarding bone dimensions. Similarly, we analyze biomechanical data in tandem with the image analysis, so these data are also largely unanalyzed.

Biomechanical testing of long bones: **Table 2** summarizes whole bone properties of femora, including heritabilities of the whole bone mechanical properties. These data are notable in confirming the pilot data regarding differences in failure load between HcB/13 and HcB/14 and in showing that the mechanical properties have a substantial genetic component. Also, as for body mass, the 2 arms of the cross differ biomechanically. Findings are similar, but less robust, at the humerus and radius (not shown).

Table 2. Femoral Whole Bone Biomechanical Performance

	Failure Load (N)	H^2	Stiffness (N/mm)	H^2	Energy to Failure (Joules^{-3})	H^2
HcB/13	12.51 ± 1.24		81 ± 14		4.48 ± 0.76	
HcB/14	19.28 ± 3.89		104 ± 17		7.96 ± 0.51	
F1 all	15.53 ± 1.78		103 ± 17		6.01 ± 1.17	
F1 males	15.30 ± 1.64		100 ± 14		5.56 ± 0.81	
F1 females	15.75 ± 1.99		107 ± 20		6.53 ± 1.35	
13 X 14 F1	14.07 ± 1.76		95 ± 13		5.41 ± 1.50	
14 X 13 F1	16.01 ± 1.56		107 ± 18		6.23 ± 1.02	
F2 all	15.6 ± 2.51	0.50	98 ± 27	0.60	6.20 ± 1.57	0.44
F2 males	15.46 ± 2.37	0.52	95 ± 26	0.71	6.31 ± 1.61	0.75
F2 females	15.86 ± 2.65	0.44	101 ± 28	0.49	6.06 ± 1.51	0.20
13 X 14 F2	16.09 ± 2.37	0.45	100 ± 29	0.80	6.29 ± 1.60	0.12
14 X 13 F2	15.18 ± 2.59	0.64	96 ± 25	0.48	6.16 ± 1.55	0.57

Data are mean ± sd.
Heritability calculated as [variance(F2)-variance (F1)]/variance(F2)

A striking feature of the data is that in the intercross females exhibit superior biomechanical performance to males. This appears to be due to an allele or combination present in HcB/14, as the same pattern was observed in the HcB/14 parental mice.

Determination of tissue-level mechanical properties is still in progress, as this requires prior completion of the micro-CT determination of I for each bone. As noted above, this task has taken far longer than anticipated.

Linkage analysis of the data has not yet been performed because the phenotypes are still being analyzed. This will be accomplished following calculation of the tissue-level mechanical properties.

Statement of Work Item 2: Genetic Characterization of Col1a2$^{oim/+}$ heterozygotes

We have completed the initial genetic analysis of this cross. We used composite interval mapping in QTL cartographer to interpret the data as an F3 intercross. We chose to interpret the cross as an F3 because the *oim* breeding scheme results in the inheritance of 1 F2 chromosome and 1 chromosome that has a chromosome that has been derived from an advanced intercross of at least F3, providing more opportunities for crossing over than would exist in an F2 intercross.

Major findings from the initial linkage analysis are the presence of statistically significant coincident linkage peaks for failure load and structural striffness on chromosomes 4 and 6, for cross-sectional moment of inertia on chromosomes 1, 6, and 16, and for body mass on chromosome 1. Data for the chromosome 4 QTL are illustrated below in **Figure 4**. Regression of failure load on genotype shows that there is a significant regression of $P = 7.84 \times 10^{-4}$, with no evidence of dominance, with C3 alleles favoring higher failure load, accounting for approximately 6.7% of the observed variance. This locus coincides with that found by Robling *et al.* mediating mechanoresponsiveness in wild type mice [1].

Figure 4. Linkage Map and Genotype-Phenotype Regression for Chromosome 4
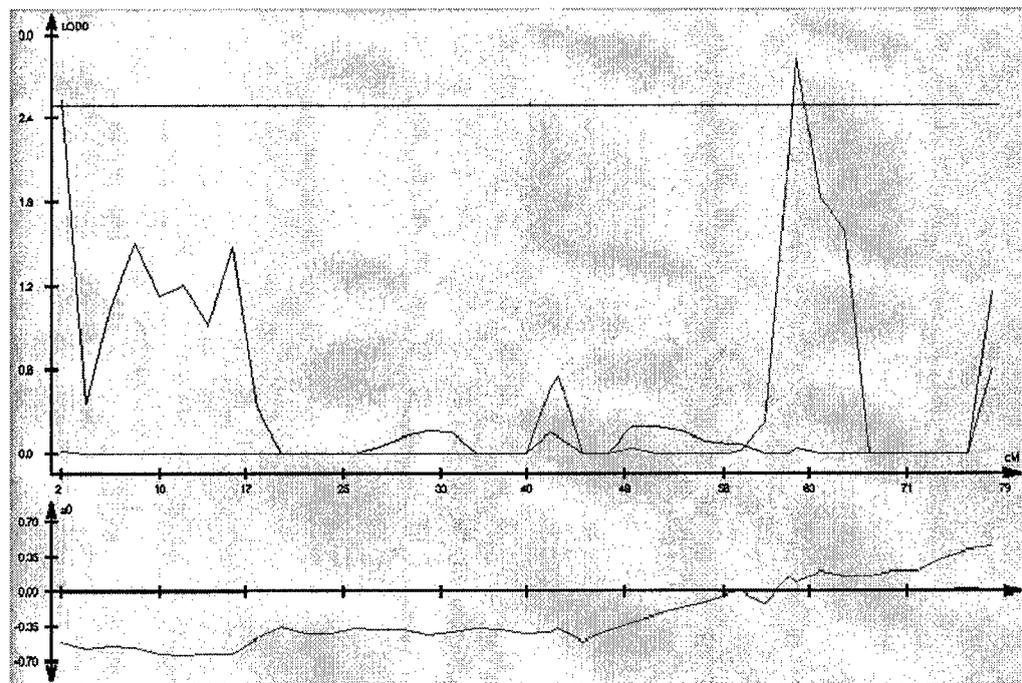
A. Multipoint linkage showing failure load (red) and cross-sectional moment of inertia (black) as a function of map position on mouse chromosome 4.

10

Regression, Conf. & Pred.
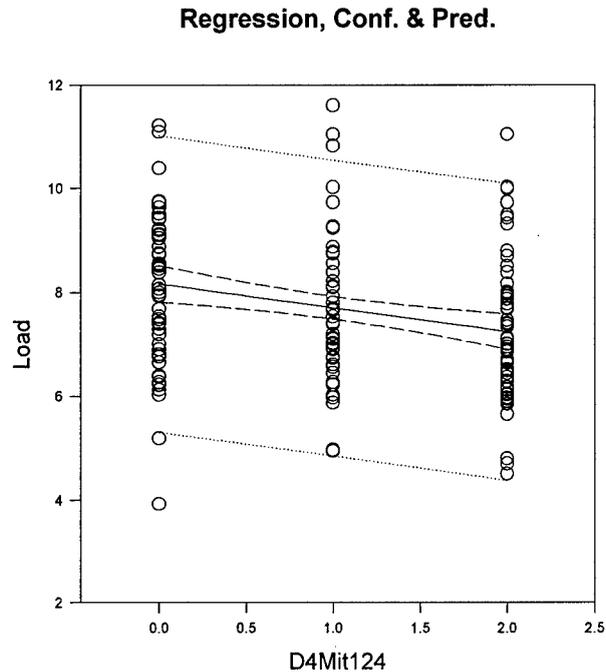
B. Regression of failure load on genotype. Genotypes are coded as C3/C3 = 0, C3/B6 = 1, and B6/B6 = 2. The regression has P = 7.84 x 10^{-4} and R^2 = 0.067.

In addition to the linkage data showing a distal chromosome 4 modifier of $Col1a2^{oim}$, we also isolated a marker in this chromosomal region by RDA. The finding of a locus in this region by multiple groups working independently, in quite different experimental systems provides evidence that an important skeletal gene is present in this chromosomal region. However, it is important to note that it is not possible to determine whether the region harbors a single gene or multiple linked genes affecting bone strength.

Our chromosome 6 linkage peak overlaps linkage peaks identified by Rosen et al. for BMD and IGF-1 levels [2, 3] and by Klein et al. for femoral cross-sectional area [4]. As for chromosome 4, the fact that multiple groups of investigators have found coincident QTLs provides evidence that these are biologically important chromosome regions.

We have chosen to undertake a 2nd linkage analysis of the oim/+ population using the SOLAR linkage package. We have done this because, as that population is not a clean intercross. In order to better account for the outbreeding of the B6C3 a/a background, we are reanalyzing the cross using the available pedigree information. Because of my inexperience using the SOLAR package, this too has taken longer than expected. However, we expect to submit a final manuscript on this work sometime this summer. We will forward the final, accepted manuscript to you when available.

Statement of Work Item 3: Initiation of Breeding to Generate Congenic Lines

This aspect has not yet begun, as it is contingent on mapping data from statement of work item 1.

KEY RESEARCH ACCOMPLISHMENTS

- Completion of the HcB/13 X HcB/14 reciprocal intercross.
- Comprehensive phenotyping of the F2 generation
- Completion of genotyping and preliminary analysis of the $Col1a2^{oim/+}$ animals
- Finding that modifiers of $Col1a2^{oim}$ largely overlap bone QTLs found in wild-type mice
- Observation of cross direction effects on body mass and biomechanical performance
- Observation of greater BMD and BMC in left bones at 3 long bone sites
- Determination of the performance characteristics of *ex vivo* mouse bone DXA
- Observation of a tooth phenotype in $Col1a2^{oim/oim}$ and $Col1a2^{oim/+}$ mice
- Development of capabilities in nanoindentation, including use of this testing method in unembedded cortical bone
- Demonstration that Young's modulus is greater in 11-week old $Col1a2^{oim/oim}$ mice than either their heterozyogous or wild type littermates.
- Demonstration that Young's modulus of cortical bone is dependent on orientation
- Demonstration that Young's modulus of cortical bone is greater in $LRP5^{HBM}$ mice than in their nontransgenic littermates

REPORTABLE OUTCOMES

Manuscripts
The preliminary data included in the original application for this award are reported in a paper published in *The Journal of Bone and Mineral Research* [5]. It is included as an appendix.

An invited perspective [6] was published in *The Journal of Bone and Mineral Research* and is included as an appendix.

An original manuscript describing the inhibitory effects of sulfate on *in vitro* mineralization was published in 2001 [7] and is included as an appendix. While not a component of the approved Statement of Work, the investigation was greatly facilitated by this award.

The manuscript describing the use of GC-clamps as an aid to the design of denaturing high performance liquid chromatography originally submitted to *Clinical Chemistry* was published in *Clinical Medicine and Research* [8]. The original reviewers requested significant shortening the report to approximately ¼ of its present length and limitation to a single figure. The co-authors and I therefore decided to submit it elsewhere because we felt that the requested revisions would have compromised our message. This paper is included as an appendix. While not a component of the approved Statement of Work, this work nevertheless could not have been accomplished without this award.

An original manuscript describing Fourier Transform Infrared spectroscopic data from the HcB/8 and HcB/23 recombinant congenic strains was published in *Connective Tissue Research* in 2003 [9]. While study of this pair of strains was not included in the approved Statement of Work, the large differences in the calculated tissue strength of bones from these strains prompted our choice of these strains for initial investigation of collagen cross-link maturity and crystallinity in these strains. Support provided by this award was invaluable in performing these studies. This paper is included as an appendix.

An original manuscript reporting the accuracy and precision of *ex vivo* DXA scanning of mouse long bones was published in the *Journal of Clinical Densitometry* [10]. The major findings include the presence of a position artifact in our instrument, resulting in the need to adjust data according to specimens' placement. Performance is poorer than for intact mice. As expected, performance varies inversely with bone size, with radii too small for valid data to be obtainable. There is no advantage to scanning bones submerged in water over scanning them in air. The paper is included as an appendix.

An invited perspective on skeletal genetics was published in IBMS BoneKEy [11] and is included as an appendix.

An original manuscript reporting BMD correlations between DXA measurements of *ex vivo* femora, humeri, and radii was published in *Calcified Tissue International* [12]. The main findings are that mice from our intercross have higher BMDs on the left than on the right side at both the femur and humerus. This paper is included as an appendix.

An original manuscript reporting the obstacles to application of the International Society for Clinical Densitometry's lumbar spine DXA interpretation guidelines was published in the *Journal of Bone and Mineral Research* [13]. This clinical work developed in part because of our earlier work with DXA scanning in mice.

An original manuscript describing the dental phenotype of homozygous and heterozygous mice harboring the $Col1a2^{oim}$ mutation is in press at *Bone* [14]. The main findings are that the mutation causes reduction of pulp chamber size, reduction of the number and organization of dental tubules, and reduction of dentin mineralization. Proofs of this paper are included as an appendix.

An original manuscript describing the tissue-level biomechanical properties of cortical bone in B6C3 *a/a* mice harboring various *Col1a2* genotypes is in the final stages of preparation. The main findings include demonstration of age and genotype-dependent effects on Young's modulus. An additional study demonstrated anisotropic behavior in spite of nanoindentation's insensitivity to specimen orientation. Finally, the manuscript reports use of nanoindentation using a novel technique in which specimens are not embedded, allowing compliance analysis to be performed. A draft is included as an appendix.

Abstracts

"Bone Strength Variability in Mice Heterozygous for the $Cola2^{oim/+}$ Mutation" was presented as a poster at the American Society for Bone and Mineral Research 2000 annual meeting.

"Emergence of Fracture-Resistant $Cola2^{oim/oim}$ Mice" was presented as a poster at the American Society for Bone and Mineral Research 2000 annual meeting.

Representational difference analysis comparison of fully outbred $Cola2^{oim/oim}$ homozygotes and partially inbred $Cola2^{oim/oim}$ homozygotes was presented as a poster at The American Society for Bone and Mineral Research 2001 annual meeting.

Geometry as a Heritable Determinant of Bone Strength was presented as a poster at The American Society for Bone and Mineral Research 2001 annual meeting.

"Phenotypic Variability of OI Due to the $Col1a2^{oim}$ Mutation" was presented orally at the 2001 Osteogenesis Imperfecta Workshop.

Genotypic and Phenotypic Characterization of Mouse Bone was presented orally at the Care and Characterization of Genetically Engineered Mice and Comparative Pathology in Functional Genomics Co-Conferences sponsored by the NIH-OLAW and the C.L. Davis, DVM Foundation.

"Collagen Cross-Link Maturity and Crystallinity Indices Differ Markedly in Recombinant Congenic Mice Having Divergent Calculated Tissue Strength" was presented as a poster at The American Bone and Mineral Research 2002 annual meeting.

"Modifiers of Biomechanical Performance in Osteogenesis Imperfecta Mice: Use of Genomic Representational Difference Analysis to Identify Linked RFLP Markers" was presented orally at the 2002 Central Society for Clinical Research meeting.

"Dual Energy X Ray Absorptiometry of Ex Vivo Mouse Long Bones: Site and Side Comparisons" was presented as a poster at the American Bone and Mineral Research 2003 annual meeting.

"Supermice: Mapping Putative Modifiers of Mechanical Performance In $Col1a2^{oim}$ Homozygotes and Heterozygotes" was presented orally at the 2003 Osteogenesis Imperfecta Workshop.

"$Col1a2^{oim/oim}$ and $Col1a^{2oim/+}$ Mice Express Dentinogenesis Imperfecta" was submitted to the 8th International Conference on the Chemistry and Biology of Mineralized Tissues. A second version of this abstract was submitted to the American Society for Bone and Mineral Research for presentation at the 2004 annual meeting. Dr. Lopez received a young investigator award for this work from ICCBMT.

"Young's Modulus of C57BL/6J Cortical Bone Is Less Than That of Outbred $Col1a1^{oim}$ Heterozygotes or Their Wild-Type Littermates" was presented at the 2004 ASBMR annual meeting.

"Assessment of Bone Quality at the Sub-micron Scale in Chain Deficiency Osteogenesis Imperfecta" was presented as a poster at the 2005 ASBMR/NIAMS Bone Quality Meeting. Dr. Lopez received a young investigator award for this presentation.

Patents and Licenses
None

Degrees Granted
Gloria E. Lopez Franco is expected to receive an MS in Bacteriology in May, 2004. Her thesis described the oral flora in HcB/13 and HcB/14 mice.

Cell Lines and other Biological Reagents
None

Informatics Resources and Models
We have developed a MS-Access/VBA utility to facilitate mouse colony management. This system automatically assigns unique names to mice, keeps a calendar of when husbandry tasks must be accomplished, and facilitates organization of specimens and genotypes.

Other Funding
A new application, entitled "Genetics of Bone Tissue Material Properties in Mice" was submitted to the Department of Veterans' Affairs Merit Review program in December, 2001. The application was approved for funding and the project will run from 10/1/02-9/30/06 and will

allow a second intercross, between HcB/8 and HcB/23 to be undertaken. The application was modeled on the USAMRAA project.

Two grant applications are pending. One, based on the $Col1a2^{oim}$ work supported in this application, proposes an intercross of C57BL/6 $Col1a1^{Mov-13/+}$ X FVB/N is assigned to NIAMS.

A second, proposing construction of congenic strains harboring QTLs identified in this work is under review at USAMRMC.

Two undergraduate students working in my laboratory have received competitive awards based in part on their work with me. Tyriina K. O'Neil received a Morris Udall Scholarship for the 2004-2005 academic year and again for the 2005-2006 academic year. Jonathan L. Vu received a University of Wisconsin McNair Scholarship for the 2005-2006 academic year.

Employment and other Research Opportunities
Work on this project has resulted in the formation of an interdisciplinary bone research group at the University of Wisconsin. The group includes physicists, engineers, and biologists and meets approximately monthly. In addition to 9 independent investigators based in Madison, the group also includes Dr. N.P. Camacho of the Hospital for Special Surgery, New York, NY. The group's goal is to determine the role that spatial organization of bone tissue plays in biomechanical performance. Several new grant proposals, including two currently being reviewed, are planned.
We recently completed experiments performed in collaboration with Drs. Mohammed Akhter, Diane Cullen, and Robert Recker at Creighton University, investigating tissue level biomechanics in mice harboring an $LRP5^{HBM}$ transgene and their nontransgenic littermates. We found that modulus is greater in the transgenic animals. An abstract reporting these findings has been submitted for the 2005 ASBMR meeting.

17

CONCLUSIONS

Data generated in this project to date suggest that all elements of the statement of work will ultimately be realized. The data acquisition has essentially been completed for statement of work items 1 and 2. Statement of work item 3 has been deferred because of the impossibility of undertaking it without fuller analysis of the item 1 data.

The HcB/13 X HcB/14 intercross, representing item 1, will ultimately provide the ability to seek epistatic interactions between pairs of genes, as originally planned. The heritability and phenotypic effects observed in the cross correspond quite well with predictions made at the outset. An important pattern of findings in the phenotypic analysis of the cross is that the 13 X 14 and 14 X 13 arms of the cross differ from each other. Differences between cross arms are apparent for multiple traits, including body mass and biomechanical performance. These observations suggest that there may be important loci mediating these traits on the X chromosome. In addition, this aspect of the work led us to consider application of DXA methodology to mice in some detail. Lastly, we have observed disparities between left and right long bones of individual animals. This observation may represent the skeletal manifestation of behaviorally documented lateralization in the mouse.

Mapping modifiers of $Col1a2^{oim}$ has provided independent evidence supporting the presence of important skeletal genes on chromosomes 4 and 6, where others had found QTLs for BMD and femoral cross-sectional area in crosses of wild type mice. It remains an open question whether additional modifiers, with significance limited to the disease state, also exist. Our investigation of this murine OI model has also led to 2 significant developments outside this project's plan of work. First, we have characterized a dental phenotype in mice harboring the $Col1a2^{oim}$ mutation. Second, our work has led to the formation of an accomplished interdisciplinary group to study the relationship between bone tissue's structural organization and bone strength. A subset of the interdisciplinary group's objectives are being pursued in a VA Merit award arising from work supported by the USAMRMC award. Third, we have developed nanoindentation testing as an additional capability in our laboratory.

Work on this project has been behind schedule for 2 reasons. First, some time was lost as a consequence of my move from the Hospital for Special Surgery to the University of Wisconsin. Second, reconstruction and analysis of micro-CT data has proven far more labor-intensive and time consuming than anticipated.

REFERENCES

1. Robling, A.G., J. Li, K.L. Shultz, W.G. Beamer, and C.H. Turner, *Evidence for a skeletal mechanosensitivity gene on mouse chromosome 4.* Faseb J, 2003. **17**(2): p. 324-6.

2. Rosen, C.J., G.A. Churchill, L.R. Donahue, K.L. Shultz, J.K. Burgess, D.R. Powell, C. Ackert, and W.G. Beamer, *Mapping quantitative trait loci for serum insulin-like growth factor-1 levels in mice.* Bone, 2000. **27**(4): p. 521-8.

3. Beamer, W.G., K.L. Shultz, L.R. Donahue, G.A. Churchill, S. Sen, J.R. Wergedal, D.J. Baylink, and C.J. Rosen, *Quantitative Trait Loci for Femoral and Lumbar Vertebral Bone Mineral Density in C57BL/6J and C3H/HeJ Inbred Strains of Mice.* J Bone Miner Res, 2001. **16**(7): p. 1195-1206.

4. Klein, R.F., R.J. Turner, L.D. Skinner, K.A. Vartanian, M. Serang, A.S. Carlos, M. Shea, J.K. Belknap, and E.S. Orwoll, *Mapping quantitative trait loci that influence femoral cross-sectional area in mice.* J Bone Miner Res, 2002. **17**(10): p. 1752-60.

5. Yershov, Y., T.H. Baldini, S. Villagomez, T. Young, M.L. Martin, R.S. Bockman, M.G. Peterson, and R.D. Blank, *Bone strength and related traits in HcB/Dem recombinant congenic mice.* J Bone Miner Res, 2001. **16**(6): p. 992-1003.

6. Blank, R.D., *Breaking down bone strength: a perspective on the future of skeletal genetics.* J Bone Miner Res, 2001. **16**(7): p. 1207-11.

7. Boskey, A.L., R.D. Blank, and S.B. Doty, *Vitamin C-sulfate inhibits mineralization in chondrocyte cultures: a caveat.* Matrix Biol, 2001. **20**(2): p. 99-106.

8. Wurzburger, R.J., R. Gupta, A.P. Parnassa, S. Jain, J.A. Wexler, J.L. Chu, K.B. Elkon, and R.D. BLank, *Utility of GC Clamps in Mutation Detection by Denaturing High Performance Liquid Chromatography.* Clin Med Res, 2003. **1**(2): p. 111-118.

9. Blank, R.D., T.H. Baldini, M. Kaufman, S. Bailey, R. Gupta, Y. Yershov, A.L. Boskey, S.N. Coppersmith, P. Demant, and E.P. Paschalis, *Spectroscopically determined collagen Pyr/deH-DHLNL cross-link ratio and crystallinity indices differ markedly in recombinant congenic mice with divergent calculated bone tissue strength.* Connect Tissue Res, 2003. **44**(3-4): p. 134-42.

10. Lopez Franco, G.E., T.K. O'Neil, S.J. Litscher, M. Urban-Piette, and R.D. Blank, *Accuracy and precision of PIXImus densitometry for ex vivo mouse long bones: comparison of technique and software version.* J Clin Densitom, 2004. **7**(3): p. 326-33.

11. Blank, R.D., *A Thematic Overview of Some Recent Advances in Skeletal Genetics.* IBMS BoneKEy, 2004. **110.1138/ibmske;1/7/4.**

12. Lopez Franco, G.E., S.J. Litscher, T.K. O'Neil, M. Piette, P. Demant, and R.D. Blank, *Dual Energy X Ray Absorptiometry of ex vivo HcB/Dem Mouse Long Bones: Left Are Denser Than Right.* Calcif Tissue Int, 2005. **76**(1): p. 26-31.

13. Hansen, K.E., N. Binkley, R. Christian, N. Vallarta-Ast, D. Krueger, M.K. Drezner, and R.D. Blank, *The Inter-Observer Reproducibility of Criteria for Vertebral Body Exclusion.* J Bone Miner Res, 2005. **20**(3): p. 501-508.

14. Lopez Franco, G.E., A. Huang, N.P. Camacho, and R.D. Blank, *Dental Phenotype of the Col1a2^{oim} Mutation: DI Is Present in Both Homozygotes and Heterozygotes.* Bone, in press.

Vitamin C-sulfate inhibits mineralization in chondrocyte cultures: a caveat

Adele L. Boskey*, Robert D. Blank, Stephen B. Doty

Mineralized Tissues Research Section, Research Division, The Hospital for Special Surgery and Weill Medical College of Cornell University, 535 East 70th Street, New York, NY 10021, USA

Abstract

Differentiating chick limb-bud mesenchymal cell micro-mass cultures routinely mineralize in the presence of 10% fetal calf serum, antibiotics, 4 mM inorganic phosphate (or 2.5 mM β-glycerophosphate), 0.3 mg/ml glutamine and either 25 μg/ml vitamin C or 5–12 μg/ml vitamin C-sulfate. The failure of these cultures to produce a mineralized matrix (assessed by electron microscopy, ^{45}Ca uptake and Fourier transform infrared microscopy) led to the evaluation of each of these additives. We report here that the 'stable' vitamin C-sulfate (ascorbic acid-2-sulfate) causes increased sulfate incorporation into the cartilage matrix. Furthermore, the release of sulfate from the vitamin C derivative appears to be responsible for the inhibition of mineral deposition, as demonstrated in cultures with equimolar amounts of vitamin C and sodium sulfate. © 2001 Elsevier Science B.V./International Society of Matrix Biology. All rights reserved.

Keywords: Ascorbic acid; Ascorbic-acid-2 sulfate; Vitamin C; Mineralization; Cell culture

1. Introduction

Ascorbic acid (vitamin C) is an obligatory requirement in cultures of differentiated osteoblasts (Dean et al., 1994; Franceschi et al., 1995; Siggelkow et al., 1999; Torii et al., 1996; Tullberg-Reinert and Jundt, 1999) and chondrocytes (Boskey et al., 1991b; Hall, 1981; Leboy et al., 1989; Shapiro et al., 1991; Sullivan et al., 1994; Venezian et al., 1998) where it is a co-factor for collagen hydroxylases (Tschank et al., 1994), an activator of alkaline phosphatase gene expression (Leboy et al., 1989; Venezian et al., 1998) and a stimulator of chondrocyte maturation (Leboy et al., 1997). Because vitamin C is rapidly oxidized to form toxic ascorbyl radicals (Makino et al., 1999) it must be prepared fresh before each charge of cell

culture medium. Vitamin C persists in cultured tissues for approximately 24 h, although it is detectable in tissue culture medium for only 2 h (Roach et al., 1985). Addition of fresh vitamin C is not possible for cell culture experiments carried out in bioreactors on board the space shuttle or in biosatellites. To circumvent this problem, following preliminary evaluation, vitamin C-sulfate, a reportedly stable derivative of vitamin C (Machlin et al., 1976; Tolbert et al., 1975), was used in chondrocyte cultures flown on the several NASA shuttle missions (Doty et al., 1999). Recently, to save technician time, we replaced the addition of fresh vitamin C with vitamin C-sulfate for ground-based laboratory experiments. We report here that vitamin C-sulfate inhibits matrix mineralization of differentiating mesenchymal cell micro-mass cultures supplemented with inorganic phosphate or β-glycerophosphate, without having effects on cell viability, overall matrix synthesis, or alkaline phosphatase activity.

*Corresponding author. Tel.: +1-212-606-1453; fax: +1-212-472-5331.

E-mail address: boskeya@hss.edu (A.L. Boskey).

2. Materials and methods

2.1. Cell culture methodology

Chick limb-bud mesenchymal cells were isolated from stage 21–24 (Hamburger and Hamilton, 1951) fertilized White Leghorn eggs (Truslow Farms, Chestertown, MD) as described in detail elsewhere (Boskey et al., 1992b). The eggs were maintained in a humidified incubator at 37°C for 4.5 days. The embryos were then sterilely withdrawn from the eggs and their limb buds removed into 0.9% USP grade saline (Abbott Laboratories, N Chicago, IL). Cells, released from the limb buds by digestion with 5 ml 0.25 wt.% trypsin-0.53 mM EDTA (GIBCO, Grand Island, NY), were separated from debris by passage through two layers of 20-μm Nitex membrane (Tetko Inc., Ardsley, NY). Cells were counted with a hemocytometer, checked for viability by trypan blue dye exclusion and pelleted in the cold at 2300 rev/min. In all cases, viability was greater than or equal to 97%. Cells were resuspended in medium containing 1.3 mM Ca and plated using the micro-mass technique (Ahrens et al., 1977), at a density of 0.75 million cells per 20 μl drop in 35 × 10 mm Falcon dishes and allowed to attach for 2 h in a humidified atmosphere of 5% CO_2 at 37°C. After 2 h, Dulbecco's modified essential medium (DMEM, GIBCO Formula 80-0303A, Grand Island, NY) which initially contained 1 mM inorganic phosphate and 0.3 mM calcium, was adjusted to have final concentrations of 1.3 mM calcium chloride, 1000 mg/l glucose and 50 units/ml penicillin and 25 μg/ml streptomycin, 10% fetal calf serum (GIBCO, Grand Island, NY) and 0.3 mg/ml glutamine. Mineralizing cultures were further supplemented with 3 mM inorganic phosphate from day 2 onward, making the total inorganic phosphate content 4 mM. In preparation for a NASA space flight, the cultures were maintained in a CellMax Quad artificial capillary cell culture system (Cellco, Inc., Germantown, MD), consisting of a chamber to contain cells flushed with medium at controlled temperatures and pressure. Medium containing 2.5 mM β-glycerophosphate was recycled through the chambers at a rate of 6 ml/min. Half of the chambers received 25 μg/ml vitamin C, prepared fresh with each medium change, with the medium bottles changed every 2 days. The other half received 5 μg/ml vitamin C-sulfate prepared once and recycled for the length of the experiment. Based on the results of that study (Fig. 1), vitamin C-sulfate was used for NASA experiments. For the purpose of the study reported here, the vitamin C supplements (described below) were added with every medium change from day 2. Non-mineralizing cultures received no phosphate supplements but did receive the ascorbate supplements. Medium was changed every 48 h. Cul-
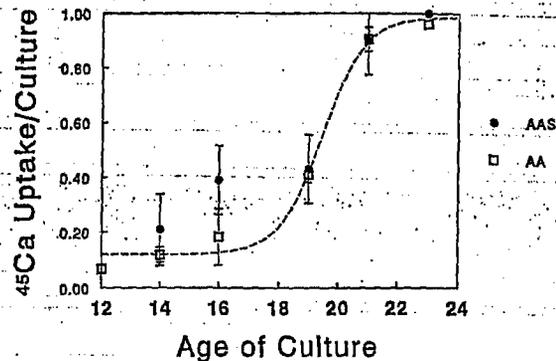
Fig. 1. ^{45}Ca uptake in differentiating chick-limb bud mesenchymal cell cultures, maintained in Cell-Max cartridges for 15 days, in the presence of recirculating medium with (open squares) 25 μg/ml (0.28 μM) vitamin C (AA) changed every 2 days, or (closed circles) 5 μg/ml vitamin C-sulfate (AAS, 0.05 μM). The dotted line is fitted to both sets of data. No significance differences were detected at any time point.

tures were maintained for 21 days with day 0 referring to the day of plating.

2.2. Vitamin C additives

Vitamin C [sodium ascorbate (Sigma Chemicals, St Louis, MO)], vitamin C-sulfate [sodium ascorbate-2-sulfate (Sigma Chemicals, St Louis, MO)] stored at −20°C as per manufacturers directions) or vitamin C plus an equal molar concentration of sodium sulfate (Fisher Chemicals, Springfield, NJ) were added to cultures in concentrations of 25, 12.5 or 5 μg/ml. Vitamin C was also added at a concentration of 50 μg/ml. To determine whether the Vitamin C-sulfate degraded 'on the shelf', in some experiments the reagent which was acquired in 1995 (old) and was still valid according to the manufacturer, was used, while in others the vitamin C-sulfate was used within 1 week of receipt from the manufacturer and prepared fresh with each change of medium (fresh). Another batch of cultures received this same vitamin C-sulfate prepared at the start of the experiment, but not remade for each change of medium (new). In another set of experiments, the 'new' reagent was heated at 60°C for 4 h to accelerate any breakdown. Cultures prepared from the same cell preparation but maintained with the different vitamin C sources were collected for analyses on days 5, 12, 16, 19 and 21. Cell viability and the ability to form chondrocyte nodules was determined on day 5, based on propidium iodide and alcian blue staining, respectively.

2.3. Matrix and cell parameters

Cell and matrix morphology and mineral localization were analyzed by transmission electron micro-

scopy (TEM). Samples were washed first with 0.05 M cacodylate buffer and then fixed in the culture dish for 12–18 h at 4°C in EM fixative (0.5% glutaraldehyde, 2% paraformaldehyde, 0.05 M pH 7.2 cacodylate buffer). After removal of the fixative, samples were stored at 4°C in 0.05 M cacodylate buffer containing 7% sucrose. Fixed cultures were removed from the dish, post-fixed with 2% aqueous osmium, dehydrated in a graded series of alcohols and embedded in Spurr's resin. Thin sections were collected on water containing bromthymol blue as an indicator for pH above 8.0 to prevent mineral dissolution. Sections stained with lead citrate and alcoholic uranyl acetate were examined on a Philips CM12 electron microscope and representative micrographs photographed for presentation.

Matrix properties in cultures treated with different supplements were measured on day 16. Specifically, total proteoglycan content was determined using a modification of the dimethylene blue staining method (Farndale et al., 1982), with relative values reported as absorbance at 595 nm. To determine the extent of proteoglycan sulfation, parallel dishes labeled at day 15 with $^{35}SO4$ (1 uCi/ml) for 16 h were subjected to the dimethylene blue staining procedure and the radiolabelled dimethylene blue-proteoglycan complex extracted into 4 M guanidine hydrochloride and an aliquot of the extract subjected to scintillation counting. Data was expressed as $^{35}SO_4$/proteoglycan absorbance. Collagen hydroxyproline was measured in 0.1-mg aliquots of lyophilized mineralizing day 16 cultures. Cultures were hydrolyzed in 6 N HCl in vacuo, after flushing with nitrogen, at 110°C for 24 h. An aliquot of each hydrolysate was then analyzed for hydroxyproline on a Varian HPLC 9012/9050 configured as an amino acid analyzer (AA911 column, Interaction) with ninhydrin color development at 135°C monitored at 440 nm (Uzawa et al., 1998). Data
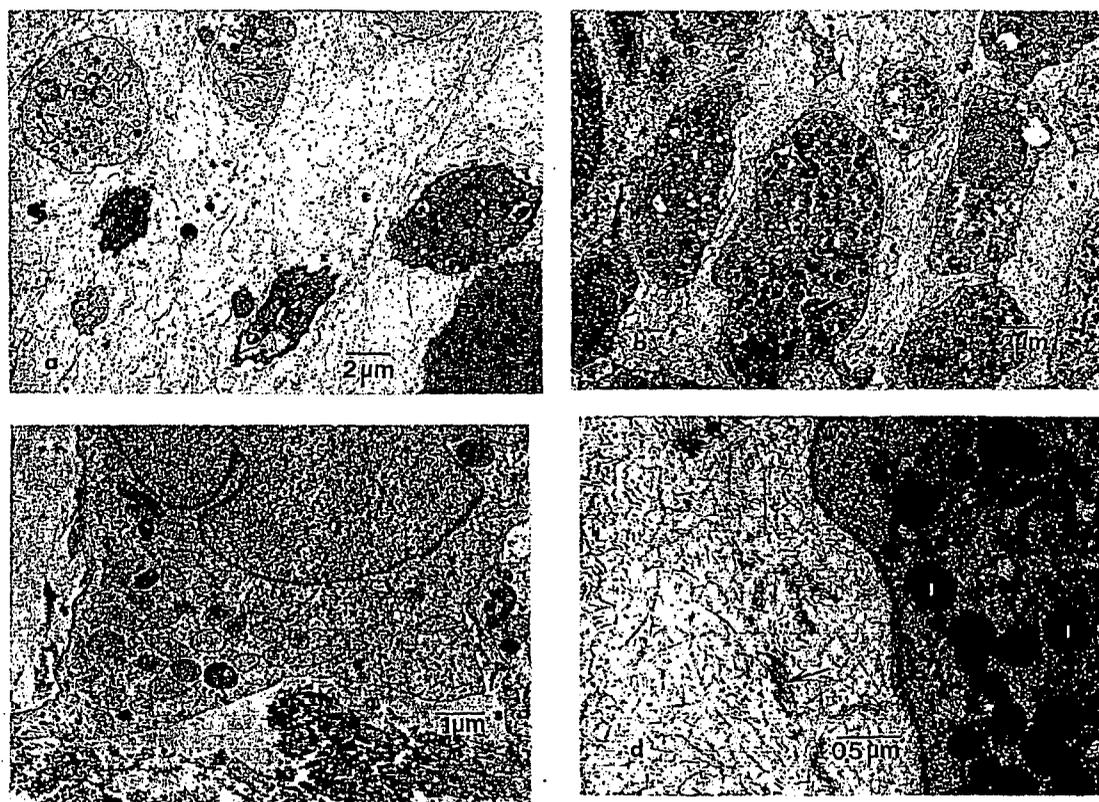
Fig. 2. Morphological differences between in vitro cartilage growth in the presence of 25 µg/ml vitamin C (Fig. 2a,c) and 12.5 µg/ml vitamin C-sulfate (Fig. 2b,d). Fig. 2a,b are control, non-mineralizing cultures and figures c and d are mineralizing cultures. (a) The typical appearance with vitamin C shows chondrocytes with normal cytology (i.e. endoplasmic reticulum (ER), golgi, mitochondria, etc.) and significant space between each cell which is filled with collagen fibers and proteoglycans. (b) These chondrocytes, grown in the presence of 12.5 µg/ml vitamin C-sulfate show membrane bound cytoplasmic inclusions (arrows) scattered among the normal cytoplasmic organelles. In addition, the cells are closely positioned to each other because of reduced matrix volume compared to the standard vitamin C treated cells shown in Fig. 2a. (c) Typical day 21 mineralizing culture with vitamin C. The mineral has completely covered the underlying collagen matrix. A calcific deposit has formed in the cartilage matrix adjacent to a chondrocyte with normal looking cytoplasmic content. (d) Mineralizing culture treated with vitamin C-sulfate. This, day 21, culture shows a small amount of electron dense material (arrows) deposited along some of the collagen fibers. Well-formed calcific deposits were not found. At this magnification, membrane bound cytoplasmic inclusions (I) within the chondrocytes are noted.

were expressed as nmoles hydroxyproline per mg dry culture weight.

Alkaline phosphatase activity (Sigma Test Kit 104-LL, Sigma Diagnostics, St Louis, MO) was monitored on day 12. The cultures were washed twice with 0.9% sodium chloride and digested at room temperature for 30 min in a buffer containing 0.15 M pH 9.0 Tris, 0.1 mM magnesium chloride, 0.1 mM zinc chloride and 1% Triton. The cultures were broken apart with a cell scraper and the incubation repeated and the activity of the total extract measured using p-nitro-phenyl-phosphate as the substrate.

2.4. Mineral analyses

The accumulation of mineral in the cultures was assayed, as detailed elsewhere (Boskey et al., 1992b, 1996, 1997b) based on ^{45}Ca uptake (expressed per total culture). In brief, ^{45}Ca uptake was determined for each micromass culture spot, following hydrolysis of the spot in 2 N HCl (2 h, 60°C) and scintillation counting. Uptake was expressed as percentage of min-eralizing control cultures at day 21. The presence of mineral was also validated by Fourier transform in-frared microspectroscopy, FT-IR (Boskey et al., 1992a). FTIR imaging and microscopy studies were done on fresh cultures, placed and air dryed, on barium fluoride IR windows. Spectra were recorded at 20-μm resolution using a BioRad Infrared Spec-trometer (Cambridge, MA) with an MCT detector.

2.5. Statistical evaluation

Each experiment was performed at least in tripli-cate, with three–four dishes of each condition for each time point for each individual experiments. In each independent experiment, the average for each condition at each time point was calculated and these average values used to calculate means for all experi-ments. Significant differences between experimental and control conditions were evaluated based on ANOVA and the appropriate statistical test. A $P \leq$ 0.05 was taken as significant.

3. Results

Fig. 1 presents the ^{45}Ca uptake in the Cell-Max cartridges, comparing a typical culture with 5 μg/ml vitamin C-sulfate (made once) and 25 μg/ml vitamin C (prepared fresh every other day). As can be seen, there was no detectable difference.

Fig. 2 presents typical micrographs which indicate that the appearance of the cellular morphology and mineral deposition in cultures treated with 12.5 μg/ml vitamin C-sulfate differs from those treated with 25

μg/ml vitamin C. Although the appearance of the matrix seems normal in both non-mineralizing (Fig. 2a,b) and mineralizing cultures (Fig. 2c,d), in all mi-crographs examined, there was less matrix between chondrocytes following vitamin C-sulfate treatment (Fig. 2b,d) compared to vitamin C alone (Fig. 2a,c). Also, many of the chondrocytes showed inclusion bodies (Fig. 2d) suggesting that cell function is not completely normal after exposure to vitamin C-sulfate. The appearance of the collagen and proteoglycans, however, was not noticeably different.

The various vitamin C preparations also did not have a significant effect on nodule size (not shown), or on total proteoglycan content (Fig. 3a), however, ^{35}SO$_4$ incorporation into the proteoglycans present was significantly increased in all cultures treated with vitamin C-sulfate (Fig. 3b). Furthermore, the extent of the increase was greater with the higher doses of vitamin C-sulfate. ^{35}SO$_4$ uptake could not be mea-sured in cultures treated with vitamin C and sodium sulfate, because of the relative concentrations of cold and radiolabelled sulfate. Alkaline phosphatase activ-ity (Fig. 3c) was not altered by the various vitamin C treatments at day 12.

The hydroxyproline content of the matrix of the mineralizing cultures was slightly but not significantly reduced in cultures treated with vitamin C-sulfate as contrasted with cultures given vitamin C. The three concentrations of vitamin C used (12.5, 25 and 50 μg/ml) yielded the same hydroxyproline content and there was not a dose-dependent effect of vitamin C-sulfate (Fig. 4) on hydroxyproline content. The min-eralizing matrices of the cultures treated with vitamin C-sulfate or vitamin C and sodium sulfate had a lower mass at day 16 (3.05 ± 0.38 mg) as contrasted to 5.08 ± 1.1 mg for the cultures treated with ascorbate ($P < 0.003$, Welch non-parametric t-test).

The failure to mineralize in the cultures given the sulfated form of vitamin C or vitamin C + Na$_2$SO$_4$ was evidenced by the decreased ^{45}Ca uptake (Fig. 5) as well as the absence of mineral in FT-IR spectra (not shown). The data in Fig. 5 show an average of the data for each of the concentrations tested, as the uptake in cultures with 5 or 12.5 μg/ml vitamin C-sulfate did not differ by more than 5% and the uptake in cultures with 12.5, 25 and 50 μg/ml vitamin C agreed to within 2%. Cultures given 'fresh' vitamin C-sulfate, from a new bottle and prepared with each medium change, were most similar to control cul-tures, but ^{45}Ca uptake was highly variable. Cultures which received the same ('new') vitamin-C sulfate solution, prepared only at the start of the experiment, showed a decrease in calcium accumulation. Cultures given the old vitamin C-sulfate, heated vitamin C-sulfate, or fresh vitamin C plus sodium sulfate showed no mineral accretion. Furthermore, ^{45}Ca uptake in

Total Proteoglycan Content
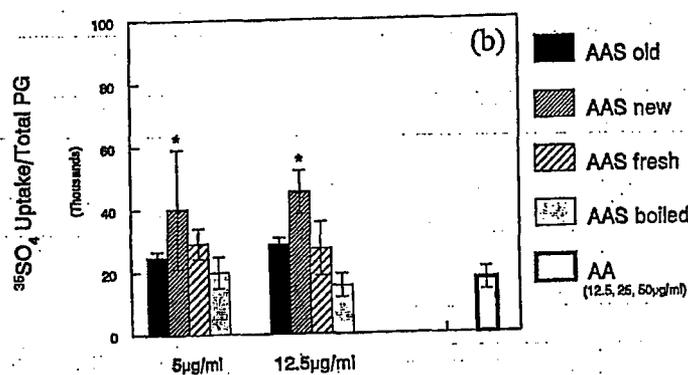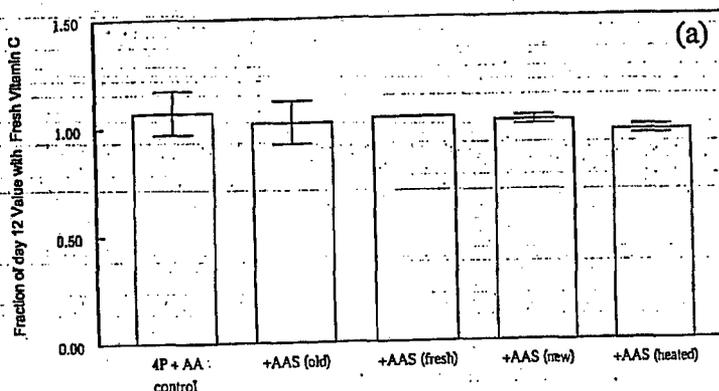
Alkaline Phosphatase Activity
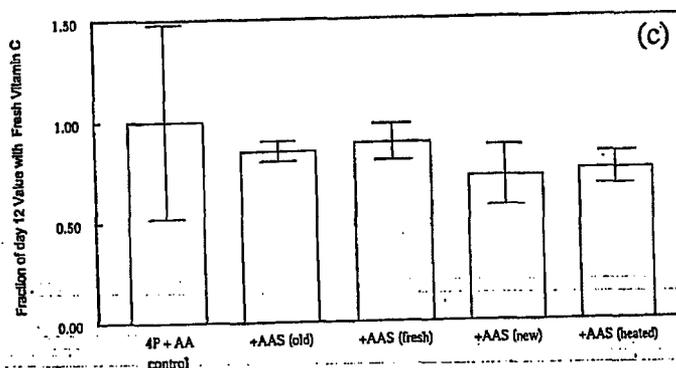
Fig. 3. Effect of vitamin C additives on (a) total proteoglycan content, (b) $^{35}SO_4$ incorporation into proteoglycans and (c) alkaline phosphatase activity, measured on day 12. Values are mean ± S.D. for $n = 3$ experiments. AA = vitamin C, AAS = vitamin C-sulfate.

the non-mineralizing vitamin C supplemented cultures was relatively constant, whereas, in the vitamin C-sulfate supplemented cultures, ^{45}Ca uptake increased 100% within 10 days and the rate of calcium uptake was 3 × that in the vitamin C treated cultures (data not shown).

4. Discussion

This study was not undertaken to investigate the mechanism of action of vitamin C as compared to vitamin C-sulfate, which has been described in detail elsewhere (Tolbert et al., 1975), but rather to de-
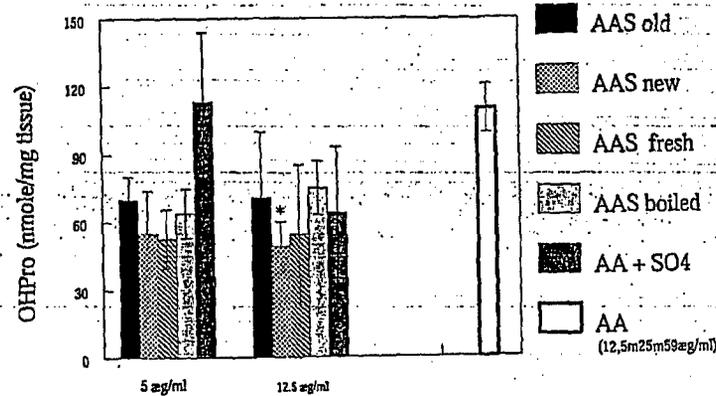
Fig. 4. Effect of vitamin C additives on hydroxyproline content of the culture matrix. Hydroxyproline content was measured on day 16 in mineralizing cultures supplemented with 5 or 12.5 µg/ml vitamin C-sulfate (AAS) from an old bottle (old), vitamin C-sulfate prepared with each medium change (fresh), vitamin C-sulfate from a new bottle, but not prepared fresh for each medium change (new), vitamin C-sulfate that was heated to promote breakdown (heated) and vitamin C with equimolar amounts of sodium sulfate (AA + SO₄). Freshly prepared vitamin C (AA) was used in concentrations of 12.5, 25 and 50 µg/ml and results are shown as mean for all concentrations ($n = 9$).

termine why cultures which had a reproducible pattern of mineral deposition for many years (e.g. Boskey et al., 1991b, 1992a,b, 1996, 1997b) stopped mineralizing when for the purpose of efficiency, our laboratory switched from using vitamin C to vitamin C-sulfate.

Our initial studies had shown vitamin C-sulfate at concentrations less than 12.5 µg/ml were not toxic in these cultures and that was confirmed here. Vitamin C-sulfate, which was not prepared fresh with each

change of medium, however, or was not newly acquired from the manufacturer, inhibited mineralization. Since there is no advantage to using the sulfated form if it has to be prepared with each medium change, there appears to be no rationale for the use of this 'stable' form in this type of culture. A vitamin C-2-phosphate that does not form ascorbyl radicals is also available (Makino et al., 1999) and this stable vitamin C derivative has been used in several os-
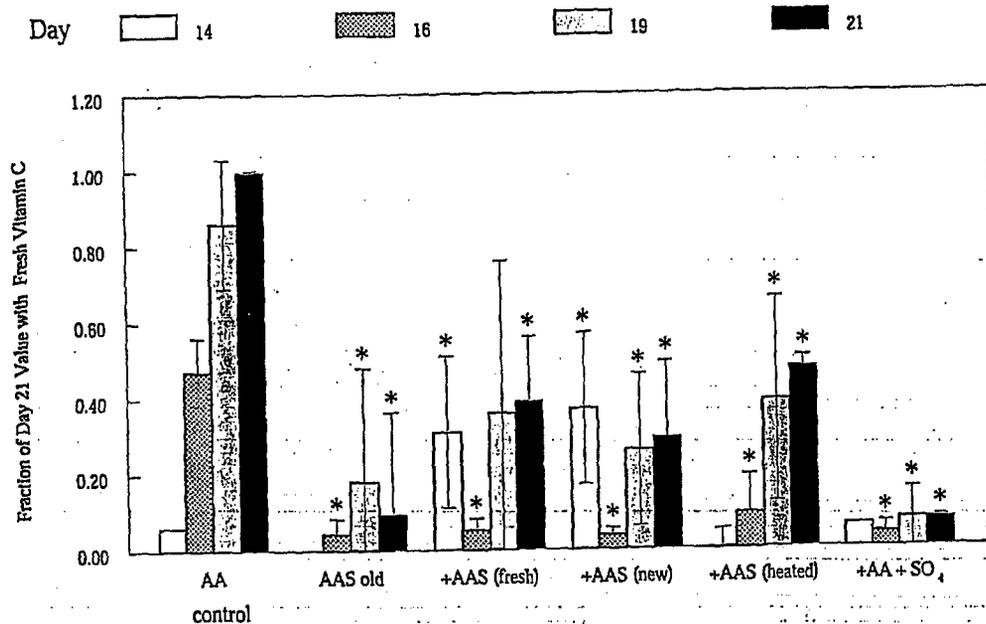
Fig. 5. Effect of vitamin C supplements on mineral accumulation in differentiating mesenchymal cell cultures supplemented with freshly prepared vitamin C (AA) in concentrations of 12.5, 25 and 50 µ/ml, or 5 or 12.5 µg/ml vitamin C-sulfate (AAS) from an old bottle (old), vitamin C-sulfate prepared with each medium change (fresh), vitamin C-sulfate from a new bottle, but not prepared fresh with each medium change (new), vitamin C-sulfate that was heated to promote breakdown (heated) and vitamin C with equimolar amounts of sodium sulfate (AA + SO₄). Absolute ^{45}Ca uptake has been normalized to uptake at 21 days in mineralizing cultures (4P + AA), values are mean ± S.D. for three–six cultures per time point. *Significantly different from same time point in mineralizing cultures with 25 µg/ml AA cultures, $P < 0.05$.

teoblast (Gronthos et al., 1994; Hitomi et al., 1992; Jaiswal et al., 1997; Tullberg-Reinert and Jundt, 1999; Torii et al., 1994) and other connective tissue and muscle (Fermor et al., 1998; Mitsumoto et al., 1994) culture systems. Although this phosphorylated-derivative might have been preferable in the mineralizing culture, it would have slightly increased local phosphate concentrations in the non-mineralizing controls which are very sensitive to changes in phosphate content (Boskey et al., 1992b) and thus we did not investigate its use.

There are several possible explanations for the observed effects of vitamin C-sulfate on development of a mineralized matrix. Vitamin C (ascorbic acid) is oxidized generating toxic ascorbyl radicals and peroxides (Wilgus and Roskoski, 1988) and we have previously shown in this system that high vitamin C doses cause demonstrable cell death (Boskey et al., 1991b). The vitamin C-sulfate concentrations used in our culture system, however, are far below this value. With the lower concentrations of vitamin C-sulfate used in these cultures, there was no EM evidence of cell death and the vitamin-C concentrations were 1/8 that previously shown to cause cell necrosis in this system. Thus, while viable cells are required for cartilage calcification (Boskey et al., 1996), the failure to mineralize does not appear to be due to cell death. The use of vitamin C-sulfate did slightly (but not significantly) decrease the extent of prolylhydroxylation, suggesting that collagen production was not extensively altered. The lack of significance may be related to the decreased weight of cultures treated with sulfated vitamin C, however, the ~40% difference in weight is most likely attributable to the presence of mineral in the vitamin C treated cultures and not to different amounts of collagen being present.

Vitamin C-sulfate is a substrate for sulfatases (Fluharty et al., 1976; Hatanaka and Egami, 1976; Roy, 1979) that are abundant in cartilage (Schwartz and Adamy, 1976) and most likely in this culture system. In cartilage, the proteins sulfated are most likely the proteoglycans, which are known inhibitors of calcification both in solution (Boskey, 1989; Boskey et al., 1997a), in animal models (Boskey et al., 1991a) and in this culture system (Boskey et al., 1997b). Total proteoglycan content was not decreased in the presence of vitamin C-sulfate, however, sulfate incorporation into total proteoglycans was significantly increased, suggesting that increased Ca-chelation by the over-sulfated proteoglycans is the major factor causing decreased mineralization.

Shapiro and Poon (1975) noted that the sulfate transfer from vitamin C-sulfate to chondroitin sulfate proteoglycans in chondrocyte cultures did not occur by direct transfer, but was accounted for by decomposition during storage at −20°C for several days. It is,

therefore, likely that in the present study, the decomposition of the vitamin C-sulfate results in increased sulfation of proteoglycans (Brand et al., 1989; Silbert and DeLuca, 1969; van der Kraan et al., 1988), hence, the high ^{45}Ca uptake in the non-mineralizing controls, reflecting Ca chelation by the matrix. Calcium chelation by the more highly sulfated proteoglycans could contribute to the failure of those cultures to support mineralization. Because it is tempting to use a stable as contrasted with an unstable essential additive, it is important to consider the consequences of a seemingly innocuous medium supplement such as vitamin C-sulfate on culture behavior.

Acknowledgements

References

Ahrens, P.B.A., Solursh, M., Reiter, R.S., 1977. Stage related capacity for limb chondrogenesis in cell culture. Dev. Biol. 60, 69–82.

Boskey, A.L., 1989. Hydroxyapatite formation in a dynamic gel system: Effects of type I collagen, lipids, and proteoglycans. J. Phys. Chem. 93, 1628–1633.

Boskey, A.L., Doty, S.B., Stiner, D., Binderman, I., 1996. Viable cells are a requirement for in vitro cartilage calcification. Calcif. Tissue Int. 58, 177–185.

Boskey, A.L., Maresca, M., Hjerpe, A., 1991a. Hydroxyapatite formation in the presence of proteoglycans of reduced sulfate content: studies in the brachymorphic mouse. Calcif. Tissue Int. 49, 389–393.

Boskey, A.L., Stiner, D., Doty, S., Binderman, I., 1991b. Requirement of vitamin C for cartilage calcification in a differentiating chick limb-bud mesenchymal cell culture. Bone. 12, 277–282.

Boskey, A.L., Pleshko, N., Mendelsohn, R., Doty, S.B., Binderman, I., 1992a. FT-IR microscopic mappings of early mineralization in chick limb bud mesenchymal cell cultures. Calcif. Tissue Int. 51, 443–448.

Boskey, A.L., Spevak, M., Doty, S., Rosenberg, L., 1997a. Effects of bone proteoglycans, decorin and biglycan on hydroxyapatite formation in a gelatin gel. Calcif. Tissue Int. 61, 298–305.

Boskey, A.L., Stiner, D., Binderman, I., Doty, S.B., 1997b. Effects of proteoglycan modification on mineral formation in a differentiating chick limb-bud mesenchymal cell culture system. J Cell Biochem. 64, 632–643.

Boskey, A.L., Stiner, D., Leboy, P., Doty, S., Binderman, I., 1992b. Optimal conditions for cartilage calcification in differentiating chick limb-bud mesenchymal cells. Bone Mineral 16, 11–37.

Brand, H.S., van Kampen, G.P., van de Stadt, R.J., Kuijer, R., van der Korst, J.K., 1989. Effect of sulfate concentration on gly-

cosaminoglycan synthesis in explant cultures of bovine articular cartilage. Cell. Biol. Int. Rep. 13, 153–162.

Dean, D.D., Schwartz, Z., Bonewald, L. et al., 1994. Matrix vesicles produced by osteoblast-like cells in culture become significantly enriched in proteoglycan-degrading metalloproteinases after addition of beta-glycerophosphate and ascorbic acid. Calcif. Tissue Int. 54, 399–408.

Doty, S.B., Stiner, D., Telford, W., 1999. The effect of spaceflight on cartilage cell cycle and differentiation. J. Gravit. Physiol. 6, 89–90.

Farndale, R.W., Sayers, C.A., Barrett, A.J., 1982. A direct spectrophotometric microassay for sulfated glycosaminoglycans in cartilage cultures. Connect. Tissue Res. 9, 247–248.

Fermor, B., Urban, J., Murray, D., Pocock, A., Lim, E., Francis, M., Gage, J., 1998. Proliferation and collagen synthesis of human anterior cruciate ligament cells in vitro: effects of ascorbate-2-phosphate, dexamethasone and oxygen tension. Cell Biol. Int. 22, 635–640.

Fluharty, A.L., Stevens, R.L., Miller, R.T., Shapiro, S.S., Kihara, H., 1976. Ascorbic acid-2-sulfate sulfhohydrolase activity of human arylsulfatase A. Biochim. Biophys. Acta 429, 508–516.

Franceschi, R.T., Wilson, J.X., Dixon, S.J., 1995. Requirement for Na(+)-dependent ascorbic acid transport in osteoblast function. Am. J. Physiol. 268, C1430–A1439.

Gronthos, S., Graves, S.E., Ohta, S., Simmons, P.J., 1994. The STRO-1+ fraction of adult human bone marrow contains the osteogenic precursors. Blood. 84, 4164–4173.

Hall, B.K., 1981. Modulation of chondrocyte activity in vitro in response to ascorbic acid. Acta Anat. (Basel) 109, 51–63.

Hamburger, V., Hamilton, H.L., 1951. A series of normal stages in the development of the chick embryo. J. Morphol. 88, 49–92.

Hatanaka, H., Egami, F., 1976. Sulfate incorporation from ascorbate 2-sulfate into chondroitin sulfate by embryonic chick cartilage epiphysis. J. Biochem. 80, 1215–1221.

Hitomi, K., Torii, Y., Tsukagoshi, N., 1992. Increase in the activity of alkaline phosphatase by L-ascorbic acid 2-phosphate in a human osteoblast cell line, HuO-3N1. J. Nutr. Sci. Vitaminol. 38, 535–544 (Tokyo).

Jaiswal, N., Haynesworth, S.E., Caplan, A.I., Bruder, S.P., 1997. Osteogenic differentiation of purified, culture-expanded human mesenchymal stem cells in vitro. J Cell Biochem. 64, 295–312.

Leboy, P.S., Sullivan, T.A., Noorayayazdun, M., Venezian, R.A., 1997. Rapid chondrocyte maturation by serum-free culture with BMP-2 and ascorbic acid. J Cell Biochem. 66, 394–403.

Leboy, P.S., Vaias, L., Uschmann, B., Golub, E., Adams, S.L., Pacifici, M., 1989. Ascorbic acid induces alkaline phosphatase, type X collagen and calcium deposition in cultured chick chondrocytes. J. Biol. Chem. 264, 17281–17586.

Machlin, L.J., Garcia, F., Kuenzig, W., Richter, C.B., Spiegel, H.E., Brin, M., 1976. Lack of antiscorbutic activity of ascorbate 2-sulfate in the rhesus monkey. Am. J. Clin. Nutr. 29, 825–831.

Makino, Y., Sakagani, H., Takeda, M., 1999. Induction of cell death by ascorbic acid derivatives in human renal carcinoma and glioblastoma cell lines. Anticancer Res. 19, 3125–3132.

Mitsumoto, Y., Liu, Z., Klip, A., 1994. A long-lasting vitamin C derivative, ascorbic acid 2-phosphate, increases myogenin gene expression and promotes differentiation in L6 muscle cells. Biochem. Biophys. Res. Commun. 199, 394–402.

Roach, H.I., Hillier, K., Shearer, J.R., 1985. Stability of ascorbic acid and uptake of the vitamin by embryonic chick femurs during long-term culture. Biochim. Biophys. Acta 842, 133–138.

Roy, A.B., 1979. The hydrolysis of ascorbate 2-sulfate by sulfatase A. Methods Enzymol. 62, 42–47.

Schwartz, E.R., Adamy, L., 1976. Effect of ascorbic acid on arylsulfatase A and B activities in human chondrocyte cultures. Connect. Tissue Res. 4, 211–218.

Shapiro, I.M., Leboy, P.S., Tokuoka, T., Forbes, E., DeBolt, K., Adams, S.L., Pacifici, M., 1991. Ascorbic acid regulates multiple metabolic activities of cartilage cells. Am. J. Clin. Nutr. 54, 1209S–1213S.

Shapiro, S.S., Poon, J.P., 1975. Apparent sulfation of glycosaminoglycans by ascorbic acid 2-[3 5-S] sulfate: an explanation. Biochim. Biophys. Acta 385, 22–29.

Siggelkow, H., Rebenstorff, K., Kurre, W., Niedhart, C., Engel, I., Schulz, H., Atkinson, M.J., Hufner, M., 1999. Development of the osteoblast phenotype in primary human osteoblasts in culture: comparison with rat calvarial cells in osteoblast differentiation. J. Cell Biochem. 75, 22–35.

Silbert, J.E., DeLuca, S., 1969. Biosynthesis of chondroitin sulfate. (3) Formation of a sulfated glycosaminoglycan with a microsomal preparation from chick embryo cartilage. J. Biol. Chem. 244, 876–881.

Sullivan, T.A., Uschmann, B., Hough, R., Leboy, P.S., 1994. Ascorbate modulation of chondrocyte gene expression is independent of its role in collagen secretion. J. Biol. Chem. 269, 22500–22506.

Tolbert, B.M., Downing, M., Carlson, R.W., Knight, M.K., Baker, E.M., 1975. Chemistry and metabolism of ascorbic acid and ascorbate sulfate. Ann. N.Y. Acad. Sci. 258, 48–69.

Torii, Y., Hitomi, K., Tsukagoshi, N., 1996. Synergistic effect of BMP-2 and ascorbate on the phenotypic expression of osteoblastic MC3T3-E1 cells. Mol. Cell. Biochem. 165, 25–29.

Torii, Y., Hitomi, K., Tsukagoshi, N., 1994. L-ascorbic acid 2-phosphate promotes osteoblastic differentiation of MC3T3-E1 mediated by accumulation of type I collagen. J. Nutr. Sci. Vitaminol. 40, 229–238 (Tokyo).

Tschank, G., Sanders, J., Baringhaus, K.H., Dallacker, F., Kivirikko, K.V., Gunzler, V., 1994. Structural requirements for the utilization of ascorbate analogues in the prolyl 4-hydroxylase reaction. Biochem. J. 300, 75–79.

Tullberg-Reinert, H., Jundt, G., 1999. In situ measurement of collagen synthesis by human bone cells with a sirius red-based colorimetric microassay: effects of transforming growth factor beta2 and ascorbic acid 2-phosphate. Histochem. Cell Biol. 112, 271–276.

Uzawa, K., Marshall, M.K., Katz, E.P., Tanzawa, H., Yeowell, H.N., Yamauchi, M., 1998. Altered post-translational modifications of collagen in keloid. Biochem. Biophys. Res. Commun. 249, 652–655.

van der Kraan, P.M., Vitters, E.L., de Vries, B.J., van den Berg, W.B., van de Putte, L.B., 1988. Synthesis of aberrant glycosaminoglycans during cartilage culture in 'sulfate free' medium. J. Biochem. Biophys. Methods. 15, 273–277.

Venezian, R., Shenker, B.J., Datar, S., Leboy, P.S., 1998. Modulation of chondrocyte proliferation by ascorbic acid and BMP-2. J. Cell. Physiol. 174, 331–341.

Wilgus, H., Roskoski Jr., R., 1988. Inactivation of tyrosine hydroxylase activity by ascorbate in vitro and in rat PC12 cells. J. Neurochem. 51, 1232–1239.

Bone Strength and Related Traits in HcB/Dem Recombinant Congenic Mice

YEVGENIY YERSHOV,[1-3] TODD H. BALDINI,[1,2] SEAGRAM VILLAGOMEZ,[1,2,4] TODD YOUNG,[1,2,5]
MELISSA L. MARTIN,[2,6] RICHARD S. BOCKMAN,[2,6] MARGARET G.E. PETERSON,[2]
and ROBERT D. BLANK[2,6,7]

ABSTRACT

Fracture susceptibility depends jointly on bone mineral content (BMC), gross bone anatomy, and bone microarchitecture and quality. Overall, it has been estimated that 50–70% of bone strength is determined genetically. Because of the difficulty of performing studies of the genetics of bone strength in humans, we have used the HcB/Dem series of recombinant congenic (RC) mice to investigate this phenotype. We performed a comprehensive phenotypic analysis of the HcB/Dem strains including morphological analysis of long bones, measurement of ash percentage, and biomechanical testing. Body mass, ash percentage, and moment of inertia each correlated moderately but imperfectly with biomechanical performance. Several chromosome regions, on chromosomes 1, 2, 8, 10, 11, and 12, show sufficient evidence of linkage to warrant closer examination in further crosses. These studies support the view that mineral content, diaphyseal diameter, and additional nonmineral material properties contributing to overall bone strength are controlled by distinct sets of genes. Moreover, the mapping data are consistent with the existence of pleiotropic loci for bone strength–related phenotypes. These findings show the importance of factors other than mineral content in determining skeletal performance and that these factors can be dissected genetically. (J Bone Miner Res 2001;16:992–1003)

Key words: skeleton, fractures, biomechanics, linkage genetics, quantitative trait

INTRODUCTION

FRACTURES OCCURRING as a consequence of skeletal fragility are an important health problem.[(1,2)] Yet, relatively little is known regarding the determination of bone strength. Most investigations have focused on bone mineral density (BMD), because this is a phenotype that is easily and reproducibly measured[(1)] and for which pharmacologic interventions are available.[(2)] However, although BMD possesses some predictive value with regard to human fracture risk, other risk factors have been identified, including past fracture history, maternal fracture history, visual acuity, height, level of physical activity, general health status, and use of steroids or anticonvulsants.[(3)] From epidemiological surveys, some of these additional risk factors appear to be comparable in importance with BMD but have not been studied in nearly as great detail.

Although the morbidity and mortality arising from skeletal fragility are suffered predominantly by the elderly, many aspects of bone strength are determined early in

[1]These authors contributed equally to this work.
[2]Mineralized Tissue Section, The Hospital for Special Surgery, New York, New York, USA.
[3]Present Address: State University of New York at Stony Brook Medical School, Stony Brook, New York, USA.
[4]Present Address: New York University School of Medicine, New York, New York, USA.
[5]Present Address: New York Medical College, Valhalla, New York, USA.
[6]Weill Medical College of Cornell University, New York, New York, USA.
[7]Current address: University of Wisconsin Medical School, Madison, Wisconsin, USA.

life.[4] Bone mass peaks at approximately age 30 years, with bone mineral loss occurring over the remainder of the life cycle. Both peak bone mass achieved and rate at which bone loss occurs are complex traits, determined by interactions between genetic constitution and environmental factors. Overall, it has been estimated that 50–70% of bone strength is determined genetically.[5,6–15]

Because of the difficulty in performing studies of the genetics of bone strength in humans, we have used the HcB/Dem series of recombinant congenic (RC) mice to investigate this phenotype. The RC mice used in this report are inbred lines descended from third generation backcross brother-sister pairs in which strain C3H/DiSnA (C3H) was the background progenitor and C57BL/ScSnA (B10) was the donor progenitor.[16–18] Each of the 27 HcB/Dem strains carries an average of 12.5% B10 genome, but each has a different combination of donor and recipient strain alleles. The chromosome regions derived from each progenitor can be determined by genotyping for markers distributed throughout the genome. Because they are inbred, the results of mapping apply to all members of the strain and are cumulative. Phenotyping RC strains allows one to include multiple individuals as replicates, allowing generation of sample sizes that are sufficiently large to establish the presence of small differences between individual strains, just as is true of any inbred strain.

The experiments reported here were performed to achieve three objectives. First, we sought to describe the long bone properties of C3H, B10, and 24 of the HcB/Dem strains. Failure load, structural stiffness, failure stress, and modulus were determined through three-point bend tests of the animals' left humeri. Middiaphyseal inner diameter (ID) and outer diameter (OD) cross-sectional area (CSA), and moment of inertia (I) were determined through image analysis of radiographs. Ash percentage of femora from the same animals was determined gravimetrically. Body mass and body mass index (BMI) were determined by weighing and measuring animals at death. Second, these phenotypic data and the published HcB/Dem genotypic data[19,20] were used to perform quantitative trait locus (QTL) linkage mapping of the genes that contribute to the measured phenotypes. Third, we investigated the interrelationships among the various bone properties by developing multivariate regression models of failure load and by examining patterns of pleiotropy among the QTLs discovered by linkage analysis. The ability to define components of biomechanical performance and map them individually contributes to a deeper understanding of how genetic factors determine bone strength than would the study of any single parameter. This comprehensive approach allows simultaneous estimation of the degree to which individual parameters share common genetic determinants and the contribution of each identified genomic region to biomechanical performance.

MATERIALS AND METHODS

Mice

The HcB/Dem strains were established and are maintained at the Netherlands Cancer Institute. Briefly, the HcB/Dem mice are inbred strains derived from arbitrary pairs of N3 backcross animals.[16–18] The HcB/Dem strains have been genotyped at 130 marker loci distributed over each of the autosomes.[19,20] Because they are inbred, individuals from a single strain have the same genetic composition, except for new mutations and residual unfixed chromosome segments.[21,22] Less than 5% of the genome was unfixed at the time of genotyping; residual heterozygosity is expected to be reduced by half in each generation of inbreeding. The mice described in this report were provided by Dr. Peter Demant and maintained at the Hospital for Special Surgery until 6–7 months of age under 12 h light-dark cycling and fed irradiated PICO 5058 rodent chow (Purina, St. Louis, MO, USA) and autoclaved tap water ad lib. Beamer and colleagues have reported that although mice continue to grow over the lifespan, peak bone mass is achieved at 4 months of age.[23] We examined strains HcB/1 through HcB/9, HcB11 through HcB/15, HcB/17, HcB/18, HcB/20 through HcB/23, HcB/25, HcB/26, HcB/28, and HcB/29. HcB/16 is extinct and HcB/27 is an unassigned number; so HcB/10, HcB/19, and HcB/24 were unexamined because these strains were unavailable at the time the experiments described here were performed. Between 4 and 10 animals of each strain were studied, yielding 179 HcB/Dem mice. Animals were allowed ad lib activity and were housed 1–5 animals/cage. Only females were studied, because inclusion of males would have introduced sex-dependent variability in the traits in addition to the strain-specific and environmental variability already encountered. At death, body mass and rostroanal length were measured. This work satisfied The Hospital for Special Surgery's requirements for the ethical use of laboratory research animals.

Ash percentage

Bone mineral fraction was calculated by comparison of dry, defatted bone weight to ash weight of homogenized tissue.[24,25] We chose to use entire bones rather than bones from which the epiphyses and marrow have been removed because the former technique is more reproducible in our hands. No ash data were obtained from the HcB/6 strain because of a laboratory accident.

Radiographic analysis

Image analysis of fine focus contact radiographs of dissected humeri was performed as described and used to calculate CSA and I.[25] Humeral length was defined as the distance along the diaphysis from the trochlea to the humeral head's most distant point. ODs and IDs were measured in orthogonal projections just distal to the deltoid tuberosity, perpendicular to the diaphyseal axis. CSA was calculated according to the elliptical approximation.[25]

$$CSA = \pi(ML\ OR * AP\ OR - ML\ IR * AP\ IR),$$

where OR is the outer radius and IR is the inner radius in either the mediolateral (ML) or anteroposterior (AP) projection. I also was calculated according to the elliptical approximation[26]

$$I = \pi/4[(ML\ OR)^3(AP\ OR - (ML\ IR)^3(AP\ IR)].$$

Image analysis was performed with SigmaScan (Jandel Scientific) image analysis software. All radiographs included stepped aluminum densitometric phantoms. Radiographic images were digitized with a digital camera (Kodak, Rochester, NY, USA), with the photographic field including a length scale.

Biomechanical testing

Quasi-static three-point bend testing was performed on left humeri using posts designed and machined in-house with the MTS apparatus (MTS Systems Corp., Eden Prairie, MN, USA) and Instron (Canton, MA, USA) electronics as described.[27,28] Humeri were oriented with the deltoid tuberosity downward and the specimens were oriented with the central post adjacent to the distal end of the deltoid tuberosity. This orientation corresponds to the ML axis being parallel to the applied force. Posts were separated by 3.75 mm except for the B10 specimens, which were tested at a post separation of 3.0 mm.

Biomechanical data were analyzed following several important assumptions. First, we assumed that bone strength is determined entirely by the cortical bone in the middiaphysis. Second, we assumed that the humeral diaphysis is an ellipse with its major axis lying in the ML plane and its minor axis lying in the AP axis. Calculated biomechanical parameters were obtained according to the following standard formulas for three-point bending of ellipses[26]: stress (σ; MPa) = $FLc/4I$, where F is force, L, is length, and c is ML OR; strain (ϵ; mm/mm) = $12cd/\text{liter}^2$, where c is ML OR, d is displacement, and L is length; and Young's Modulus (E; MPa) = $(F/\text{day})(L^3/48I)$.

Linkage analysis

Linkage mapping was carried out using the QTL cartographer software suite,[29,30] using sib-recombinant inbred as the cross type. The breeding scheme of RC mice is equivalent to that for recombinant inbred mice except for the fact that full-sib matings are started after the third backcross rather than the second filial generation. This breeding scheme results in multiple opportunities for recombination to occur before fixation of the genotype. Consequently, linkage relationships are weakened according to the relationship $R = 4r/(1 + 6r)$, where R is the observed fraction of recombinant genotypes and r is the single generation recombination fraction between a pair of loci.[21,22] Briefly, data were first analyzed for normality and those traits for which Fisher's cumulant test for normality[31] was significant at the 5% level were log-transformed (failure stress, modulus, body mass, and BMI) before further analysis. Transformed data were distributed normally by this criterion. Interval mapping was carried out to generate the final model.[32,33] A permutation test using 1000 simulated data sets was performed to estimate empirically significance levels.[34,35] Linkage maps were plotted with Gnuplot.[36] Linkage maps were generated for strain-averaged data.

Other statistical analysis

All values are shown as the mean ± SD. Continuous variables were analyzed by analysis of variance (ANOVA)
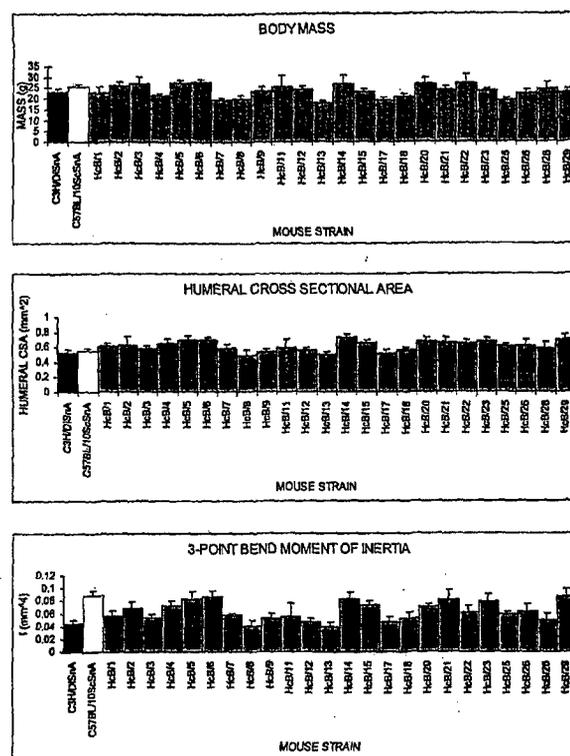
FIG. 1. Body masses, humeral CSAs, and humeral *I*'s for the HcB/Dem strains. Each bar graph shows the average ±1 SD for C3H/DiSnA, C57BL/10ScSnA, and each of the HcB strains tested. Sample sizes range between 4 and 10 animals/strain.

f test. Phenotypes that were not distributed normally were log-transformed before analysis. In the specific case of BMI, the transform was log(1 + BMI). In general, the α-level was 0.05 with adjustment for multiple comparisons. We used linear regression with stepwise addition and backward elimination to generate the multivariate model for failure load as a function of the other parameters, using an initial inclusion criterion of $p < 0.047$ for adding parameters and a criterion of $p < 0.05$ for their retention.

RESULTS

Size and skeletal morphology

The body masses, humeral CSAs, and *I*s are shown in Fig. 1. The parental strains do not differ with respect to body mass or CSA, with C3H mice having a body mass of 23.2 ± 1.5 g and a CSA of 0.53 ± 0.03 mm² and B10 mice having a body mass of 25.4 ± 1.4 g and a CSA of 0.55 ± 0.04 mm². However, they differ markedly with respect to *I* (0.044 ± 0.005 mm⁴ for C3H and 0.089 ± 0.007 mm⁴ for B10). Although only *I* differs between the parental strains, each of these parameters varies markedly among the HcB/Dem strains. Minimum and maximum values for the various parameters and the corresponding strains are shown in Table 1. Also included in Table 1 are summary data for the diaphyseal diameters used to calculate CSA and *I*. The

TABLE 1. PARENTAL PHENOTYPES AND PHENOTYPIC RANGES

	Parentals		All strains	
Trait	C3H/DiSnA (C3H)	C57BL/ 10ScSnA (B10)	Minimum value and strain	Maximum value and strain
Body mass (g)	23.2 ± 1.5	25.4 ± 1.4	18.2 ± 0.5 HcB/13	27.9 ± 1.3 HcB/6
BMI (g/cm^2)	0.270 ± 0.014	0.295 ± 0.017	0.232 ± 0.010 HcB/25	0.311 ± 0.009 HcB/3
Humeral ML OD (mm)	1.06 ± 0.03	1.33 ± 0.04	1.02 ± 0.06 HcB/13	1.33 ± 0.04 B10
Humeral AP OD (mm)	0.83 ± 0.04	0.96 ± 0.04	0.81 ± 0.05 HcB/8	0.98 ± 0.02 HcB/14
Humeral ML ID (mm)	0.53 ± 0.05	0.89 ± 0.09	0.46 ± 0.06 HcB/22	0.89 ± 0.09 B10
Humeral AP ID (mm)	0.39 ± 0.03	0.65 ± 0.04	0.31 ± 0.04 HcB/3	0.65 ± 0.04 B10
Humeral CSA (mm^2)	0.53 ± 0.03	0.55 ± 0.04	0.49 ± 0.06 HcB/8	0.72 ± 0.05 HcB/14
Humeral I (mm^4)	$0.044 \pm .005$	$0.089 \pm .007$	$0.040 \pm .007$ HcB/13	$0.089 \pm .007$ B10
Femoral ash percentage	69.1 ± 1.1	64.2 ± 1.9	64.2 ± 1.9 B10	70.2 ± 1.5 HcB/23
Failure load (N)	7.4 ± 0.3	7.7 ± 1.4	6.1 ± 1.0 HcB/13	10.4 ± 1.2 HcB/14
Structural stiffness (N/mm)	17.9 ± 3.7	21.2 ± 12.9	17.2 ± 5.2 HcB/18	40.8 ± 8.5 HcB/14
Failure stress (MPa)	173 ± 14	87 ± 11	87 ± 11 B10	192 ± 36 HcB/8
Young's modulus (MPa)	3570 ± 1160	1130 ± 700	1130 ± 700 B10	5340 ± 880 HcB/26
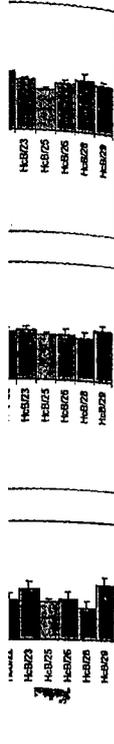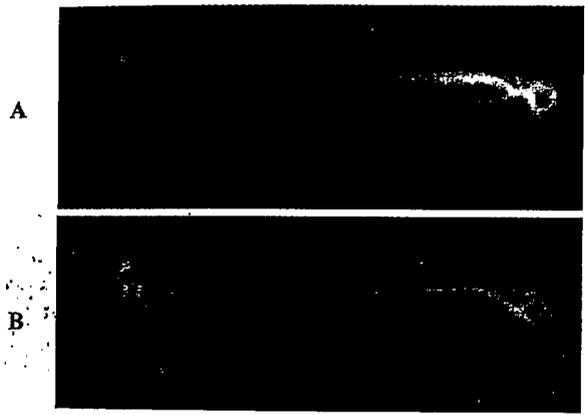
FIG. 2. Humeri of the parental strains. ML contact radiographs of (A) C3H/DiSnA and (B) C57BL/10ScSnA are shown.

distribution of values among the HcB/Dem strains is consistent with segregation between the parental strains contributing to each of these phenotypes. Body masses of the HcB/Dem strains ranged between 18.2 ± 0.5 g (HcB/13) and 27.9 ± 1.3 g (HcB/6). Most HcB/Dem strains had larger CSAs than the parental strains, ranging from a minimum of 0.49 ± 0.06 mm^2 (HcB/8) to a maximum of 0.72 ± 0.05 mm^2 (HcB/14).

The magnitude of the differences in CSA and I is shown in Fig. 2. Although CSA is equal between the parental strains, the source of their marked difference in I is apparent from this figure, which shows the striking dissimilarity of their diaphyseal diameters. Thus, although C3H mice have a thick diaphyseal cortex and a small diaphyseal diameter, B10 mice have the converse phenotype. This is reflected in I, which is proportional to the product of CSA and the square of the distance of that CSA from the bending axis for the three-point bending test. The divergence of CSA among the HcB/Dem strains arises as a result of dissociation of

diaphyseal diameter from cortical bone thickness. HcB/14 has both a thick diaphyseal cortex and a large overall diameter, while HcB/8 is characterized by a thin cortex and a small overall diameter.

Biomechanical performance and ash analysis

We performed quasi-static three-point bending tests of the left humeri for each animal. In this test, the fracture is initiated in the plane of contact between the specimen and the central post of the apparatus. This protocol allows the central post to be placed at a recognizable anatomical site and measurements of the bone can be made at the same site. Results of these studies are summarized in Table 1 and Fig. 3. Failure load is one of the most basic measures of structural strength—the force needed to fracture the bone. The parental strains do not differ in this parameter, with C3H mice having a failure load of 7.4 ± 0.3 N and B10 mice having a failure load of 7.7 ± 1.4 N. Nevertheless, a wide range of failure loads was observed over the HcB/Dem strains, from HcB/13's value of 6.1 ± 1.0 N to HcB/14's value of 10.4 ± 1.2 N. A similar pattern is seen for structural stiffness as well, with C3H having a value of 17.9 ± 3.7 N/mm and B10 having a value of 21.2 ± 12.9 N/mm. The most divergent strains are HcB/18 (17.2 ± 5.2 N/mm) and HcB/14 (40.8 ± 8.5 N/mm).

It is useful to distinguish between structural and material properties in considering biomechanical testing data. Structural properties characterize the specimen as a whole, encompassing both its anatomy and its material. The structural properties are measured directly during the performance of the test. Material properties, in contrast, are calculated from the measured structural properties and the measured anatomical parameters. Failure stress is the material analogue to failure load and corrects for a specimen's CSA and diameter at the break point. In contrast to the data for failure load, the parental strains have widely divergent failure stresses, 173 ± 14 MPa for C3H and 87 ± 11 MPa for B10. B10's
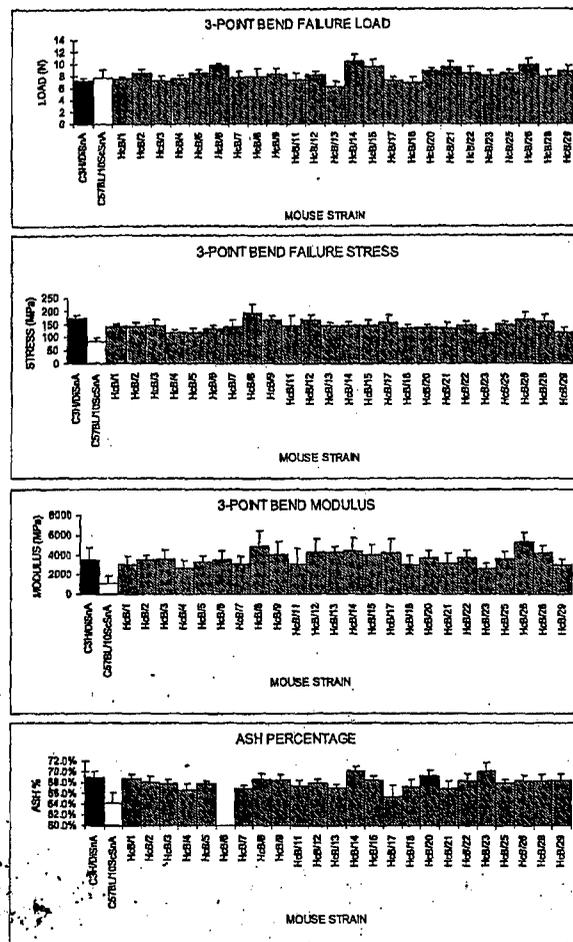
FIG. 3. Biomechanical performance of the HcB/Dem strains. Each bar graph shows the average ±1 SD for C3H/DiSnA, C57BL/10ScSnA, and each of the HcB strains tested. Sample sizes range between 4 and 10 animals/strain.

failure stress is the minimum for the strains studied and HcB/8's value of 192 ± 36 MPa is the maximum. Young's modulus is the material measure of stiffness; the parental strains' difference in failure stress is reflected by their moduli as well, with C3H having a modulus of 3570 ± 1160 MPa and B10 having a modulus of 1130 ± 700 MPa. B10 has the least stiff bone tissue observed in this study, whereas HcB/26, with a modulus of 5340 ± 880 MPa, has the stiffest bone tissue observed. These data show that both structural and material strength and stiffness vary widely among the HcB/Dem strains.

As a first step in characterizing the contribution of material properties to overall biomechanical performance, we performed ash analysis of femora from the same animals used for biomechanical testing. Ash percentage reflects the mineral content of the bone tissue and is the parameter most closely related to clinical measurements of BMD or bone mineral content (BMC). The results are summarized in Table 1 and Fig. 3 and show that C3H, with a value of 69.1 ± 1.1%, and B10, with a value of 64.2 ± 1.9%, differ markedly for this parameter. B10 has the minimum ash

percentage of the strains studied and HcB/23, with a value of 70.2 ± 1.5%, has the maximum ash percentage. Thus, substantial variations exist in the mineral content of bones from the HcB/Dem strains.

Contributions of the measured parameters to bone strength

Data presented in the previous section show that marked variations in animal size, anatomy as reflected by diaphyseal diameter and I, and BMC exist among the HcB/Dem strains and each of these are expected to contribute to differences in biomechanical performance among them. As an initial step in understanding the contribution of each of these parameters to biomechanical performance, we performed a simple correlation analysis of each of the parameters in a pairwise fashion, after log-transforming data for parameters with skewed distributions. Results of this analysis are summarized in Table 2.

We used these data to guide successive addition/elimination and elimination only stepwise regression analyses of failure load as a linear function of the other traits (Table 3). Such models express a single variable, in this case failure load, as a linear function of a subset of the other measured variables and an intercept given by the constant term of the equation. These other variables are included in the model only if they add to the model's explanatory power, as reflected by an increase in R^2. A perfect model has an $R^2 = 1.0$ and the R^2 value gives the fraction of the variation in failure load that is attributable to variation in the other traits.

In the first model, we used all other measured parameters as possible independent variables. This model found that over 90% of the failure load could be accounted for as a function of log(failure stress), CSA, and I. The model's $R^2 = 0.906$ and its equation is

$$failure\ load\ =\ -39.83\ +\ 18.63\ log(failure\ stress)$$
$$+\ 5.93\ CSA\ +\ 67.77\ I.$$

This model, although accounting for over 90% of the failure stress, is limited by the fact that failure stress is a function of load and I.

In the second model, we allowed only variables that were measured directly rather than calculated from measured quantities. This model had poorer predictive ability, accounting for nearly 57% of failure load. Its $R^2 = 0.568$ and its equation is given by

$$failure\ load\ =\ -13.48\ +\ 5.51\ log(structural\ stiffness)$$
$$+\ 0.11\ ash\%\ +\ 4.19\ log(body\ mass)\ +\ 1.97\ AP\ ID.$$

The majority of the explanatory power of this model came from the structural stiffness, which by itself explained 50% of the failure load. In both models, the same results were obtained by stepwise addition/elimination and elimination-only analyses.

Mapping of loci contributing to the phenotypes

Previously published genotypic data were used with the phenotypic analysis described previously to map loci con-

TABLE 2. CORRELATIONS AMONG BONE PARAMETERS

Parameters	Structure stiffness	Stress	Modulus	Ash %	I	CSA	ML OD	ML ID	AP OD	AP ID	Body mass	BMI
Load	0.714	0.236	0.272	0.505	0.707	0.726	0.655	0.275	0.442	0.294	0.454	0.236
	<0.001	0.002	<0.001	0.014	<0.001	<0.001	<0.001	<0.001	<0.001	<0.001	<0.001	0.002
Structural stiffness	—	NS	0.581	0.168	0.461	0.484	0.456	0.227	0.437	0.293	0.363	0.171
			<0.001	0.03	<0.001	<0.001	<0.001	0.003	<0.001	<0.001	<0.001	0.023
Stress		—	0.685	NS	−0.674	−0.641	−0.636	−0.331	−0.523	−0.303	−0.153	NS
			<0.001		<0.001	<0.001	<0.001	<0.001	<0.001	<0.001	0.046	
Modulus			—	NS	−0.388	−0.328	−0.412	−0.272	−0.211	NS	NS	NS
					<0.001	<0.001	<0.001	<0.001	0.006			
Ash %				—	NS	−0.449	NS	NS	0.157	NS	0.269	NS
						0.032			0.044		0.001	
I					—	0.893	0.959	0.566	0.716	0.462	0.461	0.192
						<0.001	<0.001	<0.001	<0.001	<0.001	<0.001	0.012
CSA						—	0.787	0.228	0.798	0.277	0.507	0.234
							<0.001	<0.001	<0.001	<0.001	<0.001	0.002
ML OD							—	0.649	0.533	0.372	0.454	0.222
								<0.001	<0.001	<0.001	<0.001	0.003
ML ID								—	0.289	0.267	NS	NS
									<0.001	<0.001		
AP OD									—	0.666	0.308	NS
										<0.001	<0.001	
AP ID										—	NS	NS
Body mass											—	0.786
												<0.001

Parameters were log-transformed before analysis. Significant correlation coefficients are shown on the top line and their associated p values are shown on the second line of each cell.

TABLE 3. STEPWISE REGRESSION MODELS OF FAILURE LOAD

Step	Parameter	p	Coefficient[a]	ΔR^2
	Model 1. All parameters included as potential independent variables			
1	Log(structural stiffness)	<0.001		0.432
2	ML OD	<0.001		0.0519
3	Log(stress)	<0.001	18.626	0.302
4	CSA	<0.001	5.927	0.113
5	I	<0.001	67.774	0.011
6	Remove log(structural stiffness)	0.126		−0.001
7	Remove ML OD	0.059		−0.002
	Model 2. Only directly measured parameters included as potential independent variables			
1	Log(structural stiffness)	<0.001	5.514	0.503
2	Log(body mass)	<0.001	4.192	0.040
3	Ash%	0.025	0.111	0.013
4	AP ID	0.035	1.973	0.012

[a] The coefficient is included only for those parameters retained in the final model.

tributing to each of the studied traits. The mapping data for selected chromosomes are summarized in Fig. 4. Mapping data for other traits (data not shown) reveal that LOD score graphs for all the diaphyseal diameters closely parallel each other. This also is true of CSA, I, failure stress, and modulus, which are calculated using the diaphyseal diameters. Because these parameters are codependent, only I is included in Fig. 4 along with the independently measured traits of failure load, structural stiffness, ash percentage, and body mass.

We performed a 1000-iteration permutation test to estimate experiment-wide significance levels for each trait as summarized in Table 4. As shown in Fig. 4, none of the strain-averaged QTL peaks achieved experiment-wide statistical significance,[37,38] regions on multiple chromosomes had LOD scores in excess of 1.7. An LOD ≥ 1 threshold is commonly used for exploratory genome scans of complex traits in a staged searching strategy.[37] However, given that we performed linkage mapping for five independently measured traits, it is appropriate to raise the exploratory threshold to the Bonferroni-corrected value of LOD ≥ 1.7.

On several chromosomes, LOD peaks for different traits map to the same genomic locations. Overlapping mapping assignments are consistent with the existence of pleiotropic
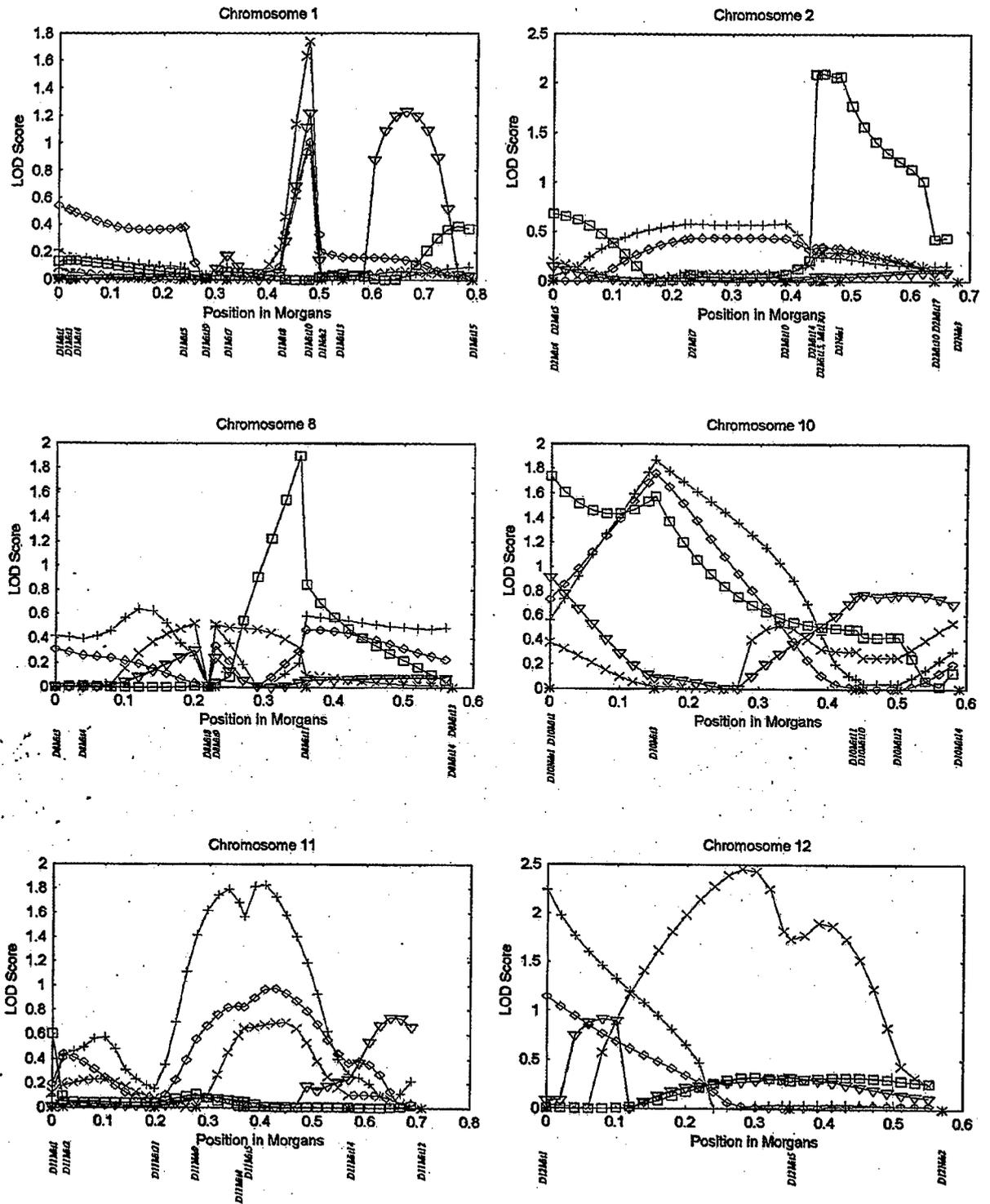
FIG. 4. Linkage maps for five traits. Linkage maps for failure load (red diamonds), structural stiffness (green + signs), ash percentage (blue squares), I (magenta X's), and body mass (navy triangles) are shown for each autosome in which the maximum LOD for any trait exceeded 1.0. The X dimension measures position in morgans (1 M = 100 cM) from the most centromeric marker. No "tails" flanking the outermost markers are included in the maps. The Y dimension measures LOD score. Marker positions are indicated below the x axis.

TABLE 4. EXPERIMENTAL-WIDE SIGNIFICANCE LEVELS

Significance level	Load	Structural stiffness	Ash%	I	Mass
0.01	3.45	3.22	2.96	3.47	3.52
0.025	3.01	3.03	2.77	3.22	3.17
0.05	2.71	2.79	2.55	2.92	2.88
0.10	2.45	2.44	2.41	2.62	2.59

(affecting multiple traits) QTLs at these locations. The degree of overlap among the mapping assignments is variable. Failure load and structural stiffness linkage maps are nearly parallel throughout the genome. A lesser degree of overlap is seen between failure load and I, and even less is observed between failure load and ash percentage. The linkage data suggest that there are distinct but overlapping sets of QTLs that contribute to each of the bone strength-related traits shown in the HcB/Dem system. This is well illustrated in comparing the maps of chromosomes 1 and 10 (Fig. 4). On chromosome 1, a peak centered at $D1Mit10$ includes failure load, structural stiffness, I, and body mass, but not ash percentage. Conversely, the peak on chromosome 10 centered on $D10Mit3$ includes failure load, structural stiffness, and ash percentage but not I or body mass.

DISCUSSION

This report presents bone phenotypes for 24 of the 27 HcB/Dem RC strains. These strains span nearly a 2-fold range of failure loads and vary widely for multiple related traits. Many phenotype pairs, even excluding those that are trivially related, display significant correlations. A multivariate linear regression model including only traits that were measured directly accounts for more than half the difference in failure load among the strains. The phenotypic data were used to generate the QTL maps for five independently measured traits in the HcB/Dem strains shown in Fig. 4.

The linkage maps reveal that potential QTLs for distinct traits sometimes colocalize to a single position in the genome, which we interpret as the presence of a single gene with pleiotropic effects (affecting multiple traits) at each multitrait LOD peak. An alternative explanation for colocalization is that distinct but closely linked QTLs are responsible for each of the phenotypes. Although the pleiotropy and multiple linked gene models cannot be distinguished by our data, the pleiotropy model is both more economical and consistent with present understanding of bone strength. Our data reveal coincident LOD peaks for distinct subsets of the traits at several positions in the genome. There is prior evidence relating these traits to failure load.[26,28,39-44] The existence of pleiotropic QTLs would provide a biological basis for the observed clinical correlations between body mass and bone strength. The biological importance of these putative pleiotropic loci is reinforced by the fact that they are based on very different, independently measured phenotypes. Mechanistically, pleiotropy most likely reflects the many developmental and biochemical steps separating the products of the putative pleiotropic loci and the measured phenotypes. If one accepts

the pleiotropy interpretation, it also is worth noting that colocalization of LOD peaks for multiple independent traits mitigates lack of statistical significance for linkage assignments. Permutation tests determine the frequency with which peaks of a given LOD threshold will occur anywhere in the genome by chance alone. Because there are many genomic locations where artifactual LOD peaks may occur, coincidence of peaks for multiple, independently measured traits can be interpreted more plausibly as representing biology rather than statistical accident. On this basis, we would predict that further experiments in this system are more likely to find significant QTLs on chromosomes 1, 10, and 11 than on chromosomes 2, 8, and 12.

In the linkage analysis, LOD scores may be increased because of epistasis between specific locus pairs. In previous work, Demant and colleagues showed large epistatic interactions between tumor susceptibility loci.[45,46] The small number of genotypes studied here will tend to magnify the contributions of individual loci, because main effects cannot be distinguished from interactions. These limitations of the data presented here can best be addressed by performing additional crosses; these are in progress.

Genetic differences are believed to account for a substantial portion of the variability in the bone strength of both mice and humans. In mice, Beamer and colleagues have measured volumetric BMD and cortical thickness by quantitative computed tomography (CT) scanning in a panel of 11 inbred mouse strains, noting that C57BL/6J and C3H/HeJ are the most extreme strains in their sample for these parameters.[23] These strains are related closely to the progenitors of the HcB/Dem RC strains. These investigators have begun to map volumetric BMD in crosses between C57BL/6J and CAST/EiJ[47] and between C57BL/6J and C3H/HeJ.[48] In these crosses, a highly significant QTL centered at $D1Mit15$ falls in a region that may overlap with our LOD peak centered at $D1Mit10$. Two groups have studied the genetic basis of peak bone mass in the SAM/P6 senescence-accelerated, osteoporotic mouse. Shimizu and colleagues[49] used a midfemoral cortical thickness index as a measure of bone mass in a cross between SAMP6 and SAMP2, reporting a highly significant QTL on chromosome 11 between $D11Mit90$ and $D11Mit59$ that may overlap our peak on that chromosome. Benes et al. have performed linkage mapping of areal BMD in crosses of SAMP6 with SAMR1 and AKR/J.[50] These workers also found a significant QTL in the corresponding chromosome 11 region. Klein and colleagues analyzed areal (i.e., projected) BMD in the B × D recombinant inbred strains as measured by dual-energy X-ray absorptiometry.[51] This study, like ours, was exploratory in nature because of the limited number of
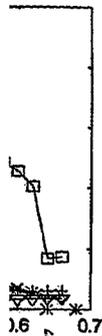
genotypes examined. These related investigations have identified genomic regions that overlap partially with our results, providing independent evidence that LOD score peaks noted in the HcB/Dem system reflect true QTLs.

It is important to note two important differences between our experiments and the work performed by the other groups. First, although the phenotypes investigated are related, they are not the same and therefore may be under somewhat different genetic control. Second, the progenitors in each investigation are different. Consequently, in each system, a different set of loci and alleles segregates. These caveats are particularly important in relating the data presented here with other mapping studies. Colocalization of putative QTLs from different experiments, although providing evidence that a relevant gene is present, still requires caution if the phenotypic measures differ, as is true for chromosomes 1 and 11. Conversely, it is not surprising that some distinct loci contribute to bone strength in each experiment, given the diversity of traits and strains studied.

A human locus controlling bone mass (HBM) has been mapped to chromosome 11 q12–13[52] and there is evidence that this locus may account for variation in bone mass in a broader-based population as well.[53] The murine homologue to the human HBM locus is predicted to map to near the centromere of chromosome 19.

Thus far, mapping studies of bone properties have been heavily weighted toward radiographically determined mineral content as the phenotype. There are good reasons for this, most notably the existence of several well-characterized precise methods for measuring this parameter. However, as illustrated by the data presented here and consistent with clinical experience in humans, mineral content is only one among several factors contributing to overall bone strength and fracture risk.[3,40,43,54] Our observations also suggest that material properties of bone that were not investigated contribute to differences of failure stress and Young's modulus as well as failure load. These might include crystal size and morphology, degree of crystal perfection, degree of substitution of carbonate in the mineral, degree or pattern of collagen cross-linking, and differences in noncollagenous proteins. In this study, we have exploited the genetic homogeneity of inbred mice to allow biomechanical data to be used as a phenotype in a preliminary mapping study. The HcB/Dem RC strains each contain a distinct complement of B10 alleles on a background of the C3H genome. Both progenitors are "wild type," lacking mutations affecting skeletal structure, function, or development in an obvious fashion. Yet, the cumulative effects of allelic differences between these strains lead to quite dramatic differences in the cortical bone properties of adult mice.

Recently, increased attention has been focused on how anatomy affects bone strength in humans. Myers and colleagues[55] related load to fracture for cadaveric human forearms to BMD, BMC, CSA, and I. They found that both CSA and I were more predictive of biomechanical performance than either BMD or BMC measured by dual-energy X-ray absorptiometry, consistent with our phenotypic data. Several groups have suggested that a longer hip axis length (HAL) increases the risk of femoral neck fractures.[56–66] Bell and colleagues have reported cross-sectional data suggesting that loss of cortical bone mass in the anteroinferior-posterosuperior axis of the femoral neck increases the risk

of hip fracture.[67] They hypothesize that formation of "giant" Haversian canals in the femoral neck contributes to the specific loss of cortical bone mass.[68] Duan and colleagues assessed the contributions of reduced bone size and reduced volumetric BMD to vertebral fracture risk.[69] These investigators found in a cross-sectional sample that both contributed to fracture risk and that reduced vertebral body size accounted for 16% of the areal BMD deficit of fracture patients relative to controls. This bone size effect accounts for the apparent discrepancy between the work of Beamer and colleagues, who find C57BL/6J to be a low BMD strain, and that of Klein and colleagues, who find C57BL/6J to be the high BMD progenitor in the B × D recombinant inbred system. The Beamer group follows volumetric BMD whereas the Klein group follows areal BMD. Like C57BL/10ScSnA, the progenitor of the HcB/Dem RC series, C57BL/6J is characterized by a large diaphyseal diameter,[70] resulting in a bone volume–dependent increase in areal BMD. As in different strains of mice, humans display ethnic differences in bone volume[10,11,61,71–74] and bone size is a highly heritable trait.[5,6–9,12–15,75] Areal BMD's better performance in predicting fracture risk compared with volumetric BMD thus is seen to be the result of its inherently compound nature—it includes a measure of bone mineralization and superimposes an anatomic factor that reflects I.[73,76–81] Mapping QTLs that allow resolution of the anatomic and material aspects of bone strength therefore is a notable step toward unraveling the complexities of fracture risk.

Work to date has made it apparent that family relationships among genes have been conserved over evolution. One practical result of these findings is that genes' functions are similar in humans to their functions in model organisms. Moreover, we have learned that the organization of chromosome structure in these two species is highly conserved, with the preservation of so-called syntenies, or groups of physically linked genes that have remained together over the course of evolution. Only about 200 major chromosome rearrangements are thought to have occurred since the human and murine lineages diverged.[82–85] Therefore, a second practical consequence of the genome project's progress is that genetic mapping data from the mouse can be used to predict the locations of corresponding human genes. The existence of conserved synteny relationships will allow testing of the roles of genetic loci identified in the mouse in human populations.

The data presented previously are limited in several important ways. First, sample sizes are relatively small and are limited to 6-month-old female mice. Beamer and colleagues have shown that bone mass in mice does not remain constant throughout adulthood and that change in BMC follows different time courses in different strains.[23] Loss of bone mass during aging also has been established by the SAMP6 mouse, which develops osteoporosis as it ages.[86] Our data do not address any aspect of bone turnover over an individual's lifetime.

Second, there are important differences in bone metabolism between mice and humans. The mouse skeleton undergoes virtually no osteonal remodeling,[87] whereas such remodeling is a central feature of human bone. Although mice grow primarily during the first 4 months of life, their epiphyses remain open throughout their lives. The murine

estrous cycle is quite dissimilar to human menses and mice do not undergo menopause in midlife. Each of these differences limits the applicability of the findings reported here to human bone properties.

Third, important limitations accompany the choice of the HcB/Dem system. Only 24 strains were examined, limiting the power of the linkage study to an exploratory level. Mapping was performed with strain-averaged data, obscuring intrastrain variability and weighting the individuals from the strains with the smallest sample sizes most heavily. Genotypic data for the HcB/Dem strains only include approximately 130 markers and their genotypes include some relatively large untyped segments.[19,20] The RC breeding scheme aggravates the impact of gaps in the HcB/Dem strain distribution pattern. There are multiple opportunities for crossing over to occur during the inbreeding process, so that the extent of the genome spanned by each marker in RC lines is only approximately one-fourth that spanned by markers in a single-generation experiment.[21,22,88] There are likely to be additional small, unidentified differential segments between the two parental strains. Moreover, there may be segregating QTLs that contribute to the phenotypes examined that this experiment was unable to detect. Incorporation of additional markers to the HcB/Dem strain distribution pattern will allow this issue to be addressed.

Fourth, although biomechanical tests are more closely related to fracture risk than is BMC, the fractures generated in these tests are still artifactual with regard to fracture site and fracture mechanism. Three-point bending of the mouse humerus assesses cortical bone strength, because the site is virtually devoid of trabecular bone. The stresses that lead to human fragility fractures and hip fractures in particular probably differ from the fractures generated in our biomechanical tests in important ways.

Fifth, not all the phenotypes studied are of equivalent status. Failure load, structural stiffness, body mass, BMI, ash percentage, and the various diameters are measured directly. Failure stress, modulus, CSA, and I, in contrast, are calculated from the directly measured phenotypes. Although all measurements are subject to potential errors, only the calculated parameters are subject to compounded errors.

Sixth, the LOD scores of potential QTLs are systematically overestimated as discussed previously, primarily as a consequence of the small number of independent genotypes examined. This means that QTL mapping assignments based on either recombinant inbred or RC strain data must be confirmed in an independent breeding experiment. This limitation applies equally to the data presented here and those presented by Klein and coworkers.[51]

These limitations notwithstanding, the experiments reported here are a comprehensive analysis of the biomechanical properties of humeri and of their structural, material underpinnings and a preliminary investigation of their genetic basis in the HcB/Dem RC system. The virtue of combining QTL mapping with comprehensive phenotypic analysis is that insight is gained not only regarding the chromosomal locations of the genes contributing to bone strength, but also regarding the mechanisms by which strength is achieved.

REFERENCES

1. Kleerekoper M, Nelson DA 1997 Which bone density measurement? J Bone Miner Res 12:712–714.
2. Eastell R 1998 Treatment of postmenopausal osteoporosis. N Engl J Med 338:736–746.
3. Cummings SR, Nevitt MC, Browner WS, Stone K, Fox KM, Ensrud KE, Cauley J, Black D, Vogt TM 1995 Risk factors for hip fracture in white women. Study of Osteoporotic Fractures Research Group. N Engl J Med 332:767–773.
4. Newton-John HF, Morgan DB 1968 Osteoporosis: Disease or senescence. Lancet 1:232–233.
5. Lutz J 1986 Bone mineral, serum calcium, and dietary intakes of mother/daughter pairs. Am J Clin Nutr 44:99–106.
6. Smith DM, Nance WE, Kang KW, Christian JC, Johnston CC Jr 1973 Genetic factors in determining bone mass. J Clin Invest 52:2800–2808.
7. Sowers MR, Burns TL, Wallace RB 1986 Familial resemblance of bone mass in adult women. Genet Epidemiol 3:85–93.
8. Pokock NA, Eisman JA, Hopper JL, Yeates MG, Sambrook PN, Ebert S 1987 Genetic determinants of bone mass in adults. J Clin Invest 80:706–710.
9. Dequeker J, Nijs J, Verstraeten A, Geusens P, Gevers G 1987 Genetic determinants of bone mineral content at the spine and radius: A twin study. Bone 8:207–209.
10. Liel Y, Edwards J, Spicer KM, Gordon L, Bell NH 1988 The effects of race and body habitus on bone mineral density of the radius, hip, and spine in premenopausal women. J Clin Endocrinol Metab 66:1247–1250.
11. Pollitzer WS, Anderson JJB 1989 Ethnic and genetic differences in bone mass: A review with a hereditary vs. environmental perspective. Am J Clin Nutr 50:1244–1259.
12. Christian JC, Yu P-L, Slemenda CW, Johnston CC Jr 1989 Heritability of bone mass: A longitudinal study in aging male twins. Am J Hum Genet 44:429–433.
13. Seeman E, Hopper JL, Bach LA, Cooper ME, Parkinson E, McKay J, Jerums G 1989 Reduced bone mass in daughters of women with osteoporosis. N Engl J Med 320:554–558.
14. Lutz J, Tesar R 1990 Mother-daughter pairs: Spinal and femoral bone densities and dietary intakes. Am J Clin Nutr 52:872–877.
15. Seeman E, Tsalamandris C, Formica C, Hopper JL, McKay J 1994 Reduced femoral neck bone density in the daughters of women with hip fractures: The role of low peak bone density in the pathogenesis of osteoporosis. J Bone Miner Res 9:739–743.

16. Demant P, Hart AA 1986 Recombinant congenic strains—a new tool for analyzing genetic traits determined by more than one gene. Immunogenetics 24:416–422.

17. Moen CJ, van der Valk MA, Snoek M, van Zutphen BF, von Deimling O, Hart AA, Demant P 1991 The recombinant congenic strains—a novel genetic tool applied to the study of colon tumor development in the mouse. Mamm Genome 1:217–227.

18. van Zutphen LF, Den Bieman M, Lankhorst A, Demant P 1991 Segregation of genes from donor strain during the production of recombinant congenic strains. Lab Anim 25:193–197.

19. Groot PC, Moen CJ, Dietrich W, Stoye JP, Lander ES, Demant P 1992 The recombinant congenic strains for analysis of multigenic traits: Genetic composition. FASEB J 6:2826–2835.

20. Stassen AP, Groot PC, Eppig JT, Demant P 1996 Genetic composition of the recombinant congenic strains. Mamm Genome 7:55–58.

21. Taylor BA 1978 Recombinant inbred strains: Use in gene mapping. In: Morse HC (ed.) Origins of Inbred Mice. Academic Press, New York, NY, USA, pp. 423–438.

22. Bailey DW 1981 Recombinant inbred strains and bilineal congenic strains. In: Foster HL, Small JD, Fox JG (eds.) The Mouse in Biomedical Research. Academic Press, New York, NY USA, pp. 223–239.

23. Beamer W, Donahue L, Rosen C, Baylink D 1996 Genetic variability in adult bone density among inbred strains of mice. Bone 18:397–403.

24. Donnelly R, Bockman R, Di Carlo E, Betts F, Boskey A 1993 The effect of gallium nitrate on healing of vitamin D- and phosphate-deficient rickets in the immature rat. Calcif Tissue Int 53:400–410.

25. Camacho NP, Rimnac CM, Meyer RAJ, Doty S, Boskey AL 1995 Effect of abnormal mineralization on the mechanical behavior of X-linked hypophosphatemic mice femora. Bone 17:271–278.

26. Turner CH, Burr DB 1993 Basic biomechanical measurements of bone: A tutorial. Bone 14:595–608.

27. Simske SJ, Luttges MW, Wachtel H 1990 Age Dependent Development of Osteopenia in the Long Bones of Tail-Suspended Mice ISA, vol. 90–014, pp. 87–94.

28. Ferretti JL, Spiaggi EP, Capozza R, Cointry G, Zanchetta JR 1992 Interrelationships between geometric and mechanical properties of long bones from three rodent species with very different biomass: Phylogenetic implications. J Bone Miner Res 7:S433–S435.

29. Basten CJ, Weir BS, Zeng Z-B 1994 Zmap—a QTL cartographer. In: Smith C, Gavora JS, Benkel B, Chesnais J, Fairfull W, Gibson JP, Kennedy BW, Burnside EB (eds.) Fifth World Conference on Genetics Applied to Livestock Production: Computing Strategies and Software, vol. 22, Guelph, Ontario, Canada, pp. 65–66.

30. Basten CJ, Weir BS, Zeng Z-B 1999 QTL cartographer, 1.13 ed. North Carolina State University, Raleigh, NC.

31. Kanji GK 1993 100 Statistical Tests. SAGE Publications, London, UK, pp. 42–44.

32. Lander ES, Green P, Abrahamson J, Barlow A, Daly MJ, Lincoln SE, Newburg L 1987 MAPMAKER: An interactive computer package for constructing primary genetic linkage maps of experimental and natural populations. Genomics 1:174–181.

33. Lander ES, Botstein D 1989 Mapping Mendelian factors underlying quantitative traits using RFLP linkage maps. Genetics 121:185–199.

34. Churchill GA, Doerge RW 1994 Empirical threshold values for quantitative trait mapping. Genetics 138:963–971.

35. Doerge RW, Churchill GA 1996 Permutation tests for multiple loci affecting a quantitative character. Genetics 142:285–294.

36. Williams T, Kelley C, Lang J, Kotz D, Campbell J, Elber G 1986–1993 Gnuplot, 3.0 ed.

37. Lander E, Schork N 1994 Genetic dissection of complex traits. Science 265:2038–2048.

38. Lander E, Kruglyak L 1995 Genetic dissection of complex traits: Guidelines for interpreting and reporting linkage results. Nat Genet 11:241–247.

39. Hayes W 1986 Basic biomechanics of the skeleton. In: Ulthoff HK, Jaworski ZFG (eds.) Current Concepts of Bone Fragility. Springer-Verlag, Heidelberg, Germany, pp. 3–18.

40. Cummings SR 1996 Treatable and untreatable risk factors for hip fracture. Bone 18:165S–167S.

41. Nguyen TV, Eisman JA, Kelly PJ, Sambrook PN 1996 Risk factors for osteoporotic fractures in elderly men. Am J Epidemiol 144:255–263.

42. Ross PD, Davis JW, Epstein RS, Wasnich RD 1991 Pre-existing fractures and bone mass predict vertebral fracture incidence in women. Ann Intern Med 114:919–923.

43. Ross PD, Davis JW, Wasnich RD 1993 Bone mass and beyond: Risk factors for fractures. Calcif Tissue Int 53(Suppl 1):S134–S138.

44. Wasnich R 1993 Bone mass measurement: Prediction of risk. Am J Med 95:6S–10S.

45. Fijneman RJ, de Vries SS, Jansen RC, Demant P 1996 Complex interactions of new quantitative trait loci, Sluc1, Sluc2, Sluc3, and Sluc4, that influence the susceptibility to lung cancer in the mouse. Nat Genet 14:465–467.

46. van Wezel T, Stassen AP, Moen CJ, Hart AA, van der Valk MA, Demant P 1996 Gene interaction and single gene effects in colon tumour susceptibility in mice. Nat Genet 14:468–470.

47. Beamer WG, Shultz KL, Churchill GA, Frankel WN, Baylink DJ, Rosen CJ, Donahue LR 1999 Quantitative trait loci for bone density in C57BL/6J and CAST/EiJ inbred mice. Mamm Genome 10:1043–1049.

48. Beamer WG, Rosen CJ, Donahue LR, Frankel WN, Churchill GA, Shultz KL, Baylink DJ, Pettis JL 1998 Location of genes regulating volumetric bone mineral density in C57BL/6J (low) and C3H/HeJ (high) inbred strains of mice. ASBMR-IBMS Second Joint Meeting, Bone, vol. 23, San Francisco, CA, USA, p. S162.

49. Shimizu M, Higuchi K, Bennett B, Xia C, Tsuboyama T, Kasai S, Chiba T, Fujisawa H, Kogishi K, Kitado H, Kimoto M, Takeda N, Matsushita M, Okumura H, Serikawa T, Nakamura T, Johnson TE, Hosokawa M 1999 Identification of peak bone mass QTL in a spontaneously osteoporotic mouse strain. Mamm Genome 10:81–87.

50. Benes H, Weinstein RS, Zheng W, Thaden JJ, Jilka RL, Manolagas SC, Shmookler Reis RJ 2000 Chromosomal mapping of osteopenia-associated quantitative trait loci using closely related mouse strains. J Bone Miner Res 15:626–633.

51. Klein RF, Mitchell SR, Phillips TJ, Belknap JK, Orwoll ES 1998 Quantitative trait loci affecting peak bone mineral density in mice. J Bone Miner Res 13:1648–1656.

52. Johnson ML, Gong G, Kimberling W, Recker SM, Kimmel DB, Recker RB 1997 Linkage of a gene causing high bone mass to human chromosome 11 (11q12–13). Am J Hum Genet 60:1326–1332.

53. Koller DL, Rodriguez LA, Christian JC, Slemenda CW, Econs MJ, Hui SL, Morin P, Conneally PM, Joslyn G, Curran ME, Peacock M, Johnston CC, Foroud T 1998 Linkage of a QTL contributing to normal variation in bone mineral density to chromosome 11q12–13. J Bone Miner Res 13:1903–1908.

54. Wasnich RD, Davis JW, Ross PD 1994 Spine fracture risk is predicted by non-spine fractures. Osteoporos Int 4:1–5.

55. Myers ER, Hecker AT, Rooks DS, Hipp JA, Hayes WC 1993 Geometric variables from DXA of the radius predict forearm fracture load in vitro. Calcif Tissue Int 52:199–204.

56. Boonen S, Koutri R, Dequeker J, Aerssens J, Lowet G, Nijs J, Verbeke G, Lesaffre E, Geusens P 1995 Measurement of femoral geometry in type I and type II osteoporosis: Differences in hip axis length consistent with heterogeneity in the

pathogenesis of osteoporotic fractures. J Bone Miner Res 10:1908–1912.

57. Faulkner KG, Cummings SR, Black D, Palermo L, Gluer CC, Genant HK 1993 Simple measurement of femoral geometry predicts hip fracture: The study of osteoporotic fractures. J Bone Miner Res 8:1211–1217.

58. Faulkner KG, McClung M, Cummings SR 1994 Automated evaluation of hip axis length for predicting hip fracture. J Bone Miner Res 9:1065–1070.

59. Flicker L, Faulkner KG, Hopper JL, Green RM, Kaymacki B, Nowson CA, Young D, Wark JD 1996 Determinants of hip axis length in women aged 10–89 years: A twin study. Bone 18:41–45.

60. Gluer CC, Cummings SR, Pressman A, Li J, Gluer K, Faulkner KG, Grampp S, Genant HK 1994 Prediction of hip fractures from pelvic radiographs: The study of osteoporotic fractures. The Study of Osteoporotic Fractures Research Group. J Bone Miner Res 9:671–677.

61. Mikhail MB, Vaswani AN, Aloia JF 1996 Racial differences in femoral dimensions and their relation to hip fracture. Osteoporos Int 6:22–24.

62. Nakamura T, Turner CH, Yoshikawa T, Slemenda CW, Peacock M, Burr DB, Mizuno Y, Orimo H, Ouchi Y, Johnston CJ 1994 Do variations in hip geometry explain differences in hip fracture risk between Japanese and white Americans? J Bone Miner Res 9:1071–1076.

63. O'Neill TW, Grazio S, Spector TD, Silman AJ 1996 Geometric measurements of the proximal femur in UK women: Secular increase between the late 1950s and early 1990s. Osteoporos Int 6:136–140.

64. Reid IR, Chin K, Evans MC, Jones JG 1994 Relation between increase in length of hip axis in older women between 1950s and 1990s and increase in age specific rates of hip fracture. BMJ 309:508–509.

65. Reid IR, Chin K, Evans MC, Cundy T 1996 Longer femoral necks in the young: A predictor of further increases in hip fracture incidence? N Z Med J 109:234–235.

66. van der Meulen MC, Ashford MW Jr, Kiratli BJ, Bachrach LK, Carter DR 1996 Determinants of femoral geometry and structure during adolescent growth. J Orthop Res 14:22–29.

67. Bell KL, Loveridge N, Power J, Garrahan N, Stanton M, Lunt M, Meggitt BF, Reeve J 1999 Structure of the femoral neck in hip fracture: Cortical bone loss in the inferoanterior to superoposterior axis. J Bone Miner Res 14:111–1119.

68. Bell KL, Loveridge N, Power J, Garrahan N, Meggitt BF, Reeve J 1999 Regional differences in cortical porosity in the fractured femoral neck. Bone 24:57–64.

69. Duan Y, Parfitt A, Seeman E 1999 Vertebral bone mass, size, and volumetric density in women with spinal fractures. J Bone Miner Res 14:1796–1802.

70. Akhter MP, Cullen DM, Pedersen EA, Kimmel DB, Recker RR 1998 Bone response to in vivo mechanical loading in two breeds of mice. Calcif Tissue Int 63:442–449.

71. Bhudhikanok GS, Wang MC, Eckert K, Matkin C, Marcus R, Bachrach LK 1996 Differences in bone mineral in young Asian and Caucasian Americans may reflect differences in bone size. J Bone Miner Res 11:1545–1556.

72. Cummings SR, Cauley JA, Palermo L, Ross PD, Wasnich RD, Black D, Faulkner KG 1994 Racial differences in hip axis lengths might explain racial differences in rates of hip fracture.

Study of Osteoporotic Fractures Research Group. Osteoporos Int 4:226–229.

73. Seeman E 1998 Growth in bone mass and size—are racial and gender differences in bone mineral density more apparent than real? J Clin Endocrinol Metab 83:1414–1419.

74. Seeman E 1999 The structural basis of bone fragility in men. Bone 25:143–147.

75. Niu T, Chen C, Cordell H, Yang J, Wang B, Wang Z, Fang Z, Schork NJ, Rosen CJ, Xu X 1999 A genome-wide scan for loci linked to forearm bone mineral density. Hum Genet 104:226–233.

76. Katzman DK, Bachrach LK, Carter DR, Marcus R 1991 Clinical and anthropometric correlates of bone mineral acquisition in healthy adolescent girls. J Clin Endocrinol Metab 73:1332–1339.

77. Bonjour JP, Theintz G, Law F, Slosman D, Rizzoli R 1994 Peak bone mass. Osteoporos Int 4(Suppl 1):7–13.

78. Bass S, Delmas PD, Pearce G, Hendrich E, Tabensky A, Seeman E 1999 The differing tempo of growth in bone size, mass, and density in girls is region-specific. J Clin Invest 104:795–804.

79. Zamberlan N, Radetti G, Paganini C, Gatti D, Rossini M, Braga V, Adami S 1996 Evaluation of cortical thickness and bone density by roentgen microdensitometry in growing males and females. Eur J Pediatr 155:377–382.

80. Gilsanz V, Boechat MI, Gilsanz R, Loro ML, Roe TF, Goodman WG 1994 Gender differences in vertebral sizes in adults: Biomechanical implications. Radiology 190:678–682.

81. Gilsanz V, Loro ML, Roe TF, Sayre J, Gilsanz R, Schulz EE 1995 Vertebral size in elderly women with osteoporosis. Mechanical implications and relationship to fractures. J Clin Invest 95:2332–2337.

82. Nadeau JH 1989 Maps of linkage and synteny homologies between mouse and man. Trends Genet 5:82–86.

83. Eppig JT, Nadeau JH 1995 Comparative maps: The mammalian jigsaw puzzle. Curr Opin Genet Dev 5:709–716.

84. DeBry RW, Seldin MF 1996 Human/mouse homology relationships. Genomics 33:337–351.

85. Seldin MF 1997 Human/Mouse Homology Relationships. National Center for Biotechnology Information, Bethesda, MD, and Davis, CA, USA.

86. Takeda T, Hosokawa M, Higuchi K 1991 Senescence-accelerated mouse (SAM): A novel murine model of accelerated senescence. J Am Geriatr Soc 39:911–919.

87. Frost HM, Jee WSS 1992 On the rat model of human osteopenias and osteoporoses. Bone Miner 18:227–236.

88. Blank RD, Campbell GR, D'Eustachio P 1986 Possible derivation of the laboratory mouse genome from multiple wild Mus species. Genetics 114:1257–1269.

Address reprint requests to:
Dr. R.D. Blank
University of Wisconsin Medical School
H4/556 CSC (5148)
600 Highland Avenue
Madison, WI 53792, USA

Perspective

Breaking Down Bone Strength:
A Perspective on the Future of Skeletal Genetics

ROBERT D. BLANK

INTRODUCTION

WITH INCREASING INTENSITY over the past decade, researchers have pursued genetic approaches to understanding the basis of skeletal fragility. This month's issue of the *JBMR* includes a report by Beamer and associates[1] that identifies quantitative trait loci (QTLs) for femoral and vertebral volumetric bone mineral density (vBMD) and presents us with an opportunity to reflect on recent progress and future directions in bone genetics.

CHOICE OF PHENOTYPES

BMD is only one of several parameters related to biomechanical performance. Fracture, not BMD, is the clinically relevant outcome; ideally, scientists would perform genetic analyses with fracture as an endpoint rather than on surrogate traits that correlate imperfectly with this abnormality. Deng and colleagues[2] estimated that the narrow-sense heritability of Colles' fracture was approximately 0.25 in a cohort of white American women, thus accounting for approximately one-quarter of total Colles' fracture risk variation observed. This indicates that the magnitude of the genetic contribution to fracture warrants further study, but important caveats exist. Fractures are relatively rare and tend to occur late in life. Should the genetic basis of human fracture prove to be quantitative, then the contributions of individual loci to the total fracture risk are likely too small to allow successful mapping of individual QTLs with realistic sample sizes. These considerations impose important and possibly insurmountable obstacles to recruitment of an adequate population in which to perform mapping studies of Colles' fracture in humans. In addition, because Colles' fractures are frequent relative to hip fractures, collecting an adequate sample to perform equivalent analyses of hip fracture may prove a daunting challenge. Further, vertebral fractures, although relatively common, do not always come to clinical attention[3,4] and their diagnosis may prove uncertain,[5-9] posing potential problems in the study of vertebral fracture risk.

Investigators have adopted alternative strategies using surrogate endpoints to overcome the practical limitations of studying human fracture directly. One approach uses biomechanical performance in a contrived experimental scheme as an analog for natural fracture; this allows functional assessment of the bone, but the mechanisms in biomechanical testing differ from those of naturally occurring fractures. In addition, cadaver specimens and specimens obtained from model organisms, both used frequently in these investigations, impose additional differences from in vivo human fractures. A second approach, based on epidemiological data, focuses on predictors of fracture rather than analogs of fracture and is reflected by the vast literature on densitometric assessment of bone. The success of these methods is incontrovertible; indeed the World Health Organization (WHO) diagnostic criteria for osteoporosis rely primarily on densitometric assessment.[10] The same logic underlies investigations based on instruments that assess lifestyle factors, comorbidities, and mobility, and there is broad agreement in the community regarding the risk factors for fracture.[11,12] However, markers of fracture risk are variously defined and although related are nevertheless distinct. This is readily apparent when comparing densitometric parameters; cross-calibrating fracture risk based on T scores obtained by different techniques at different sites[13-19] poses an important patient care problem. Similarly, consid-

Department of Medicine, Endocrinology, Diabetes and Metabolism Section, University of Wisconsin Medical School, Madison, Wisconsin, USA.

erable overlap exists among the data included in assessments of clinical risk factors for fracture, but cross-calibration among instruments has not yet been achieved.

Optimizing predictive ability does not necessarily advance mechanistic understanding of fracture biology. Areal BMD (aBMD) measured by dual-energy X-ray absorptiometry (DXA) is the single best predictor of fracture risk at the studied site (using lateral view at the spine). Scientists have established that large bones have higher aBMDs than small bones having equal vBMD[20] because of projection artifact. We also know that larger bones are stronger than smaller bones having equivalent tissue strength. By combining both size and mineral density into a single measure, aBMD achieves better fracture prediction than vBMD (in which the contribution of bone size is explicitly removed from consideration). Yet, to understand the underlying bone biology, we must treat bone size and BMD as distinct properties.[21–23]

In contrast, biomechanical studies[24,25] divide performance into components that promote investigation of mechanisms. The most basic distinction is between structural and material properties. Structural properties are possessed by an entire bone and are determined jointly by its anatomy and its tissue strength. Material properties are those of the bone tissue per se, after correction for differences in anatomy. Distinct components of biomechanical performance also can be identified in interpreting the load-deformation curve obtained in testing a specimen, and each of these properties has a corresponding material parameter obtained by normalizing for anatomy. Different testing schemes yield information on other mechanical properties; for example, repetitive, low-intensity loading can be used to assess fatigue. Similarly, the anatomic component of structural strength can be divided further; the distinction between cortical and trabecular bone reflects this division, as do ongoing efforts to quantify various architectural bone properties.

Biomechanical studies naturally lead to efforts to analyze bone strength into ever more refined components, but such partition is not always achieved in practice. Bone is an anisotropic tissue, and its biomechanical performance varies according to the orientation of the tissue relative to the applied load[26,27]; this is particularly evident in trabecular bone.[28–30] Despite these limitations, a reductionistic program does advance our understanding of the biomechanical properties of bone.

The reductionist approach embodied by biomechanics does not preclude epidemiological assessment. Both epidemiological and interventional investigations have identified risk factors for fracture other than bone mass. Advancing age,[31,32] past personal atraumatic fracture history,[11,33–35] and maternal hip fracture history[12] increase fracture risk. In trials of alendronate and transdermal estrogen, the fracture benefit exceeded that predicted from the observed BMD increase.[36,37] In contrast, sodium fluoride treatment increases BMD but does not improve and may even worsen fracture outcomes.[38,39] Taken together, these data show that non-BMD factors, often referred to collectively as bone quality, contribute to the material strength of bone, thereby linking disparate research areas.

LINKAGE GENETICS OF BONE: PRESENT STATUS

Researchers use several different strategies to study skeletal genetics. Each provides a potentially valuable approach and addresses somewhat different questions.[40] The linkage studies considered here address the locations of genes (loci) in which segregation contributes to differences in the trait of interest. In human samples, this question is distinct from that of identifying which allele of that gene is responsible for different values of the trait. In contrast, the existence of inbred mouse lines allows investigation of both loci and alleles to be accomplished simultaneously.[41]

In human samples scientists have successfully mapped a locus conferring high BMD as a simple Mendelian trait.[42] Koller et al. implicate the same genomic region as a QTL contributing to less dramatic variation in BMD.[43,44] Two other human genome scans reported evidence of possible linkage for hip and spine[45] and forearm.[46] These investigations found evidence for a QTL on chromosome 2p in spite of the different sites and populations studied. Each of these studies used aBMD as the phenotypic endpoint, based on the ease, economy, safety, and acceptance of aBMD as a surrogate measure of skeletal fragility.

In mice, researchers have studied a broader range of phenotypes. Klein et al.[47] studied whole body aBMD in the B × D recombinant inbred lines. Using DXA scanning, Benes and colleagues[48] examined vertebral aBMD in a pair of crosses between SAMP6 and either SAMR2 or AKR/J. Shimizu et al.[49] studied femoral cortical thickness index, the fraction of diaphyseal cross-section occupied by cortical bone on plain radiographs, in a cross between SAMP6 and SAMP2. Beamer and colleagues have reported two related studies: a cross between C57BL/6J and Cast/EiJ in which femoral vBMD was mapped[50] and a study of insulin-like growth factor 1 (IGF-1) levels in a cross between C57BL/6J and C3H/HeJ.[51] Humeral biomechanical performance and dimensions, ash percentage, and body mass in the HcB/Dem recombinant congenic strains were assessed by Yershov et al.[52]

In this issue of the *JBMR*, Beamer et al. present the results of mapping femoral and vertebral vBMD in a cross between C57BL/6J and C3H/HeJ.[1] Their results are notable for several reasons. First, a subset of the QTLs contributes to vBMD at both sites studied, while others contribute to vBMD at only one site, providing a biological context for the clinical finding of disparate BMDs at different sites in the same individual. Second, in several cases the same QTLs have been mapped in different crosses, using different but related phenotypes. This provides compelling evidence that a bone mass gene in fact has been identified. Third, the number of animals studied in this cross enabled testing for pairwise epistatic interactions, which were not found. It is too soon to say that epistasis does not contribute significantly to vBMD variation in general, but these efforts remind us that we must investigate gene-gene and gene-environment interactions. Fourth, the authors are unequivocal in stating their ambition to help clarify our understanding of the mechanisms underlying bone phenotypes.

THE FUTURE OF SKELETAL GENETICS

Successfully mapping QTLs represents an early step in understanding the genetic basis of skeletal function. With the approximate locations of some vBMD QTLs identified, we must face the problem of determining which of the positional candidates thus defined are the relevant gene(s). Similar research efforts in other diseases, notably type I diabetes[53–55] and other autoimmune diseases,[56–58] suggest that successfully subdividing the overall phenotype into pathophysiologically relevant intermediate phenotypes is one of the major tasks that lies ahead. Subdivision of traits may lead to phenotypes, the genetics of which are Mendelian rather than quantitative, greatly simplifying their genetic analysis, as illustrated by the high bone mass locus.[42] Even if we do not succeed in reducing traits to oligogenic phenotypes, the effort undoubtedly will stimulate new ideas about how whole bone anatomy is established, how bone responds to mechanical loading, how matrix proteins and minerals interact, and how bone metabolism changes during development and aging. Successful integration of all these research areas into genetic investigations of fracture risk should enable us to choose among the myriad of potential intermediate phenotypes. In addition, new instruments and new analytical methods provide opportunities to define additional phenotypes.[59–62]

Work to date has already used a variety of different, albeit related, phenotypes. Intermediate phenotypes will add more traits into the mix and present us with the additional challenge of relating the phenotypes to each other. If we design future genetic experiments to include a variety of traits, we may discover evidence of pleiotropy, that is, a single gene controlling multiple phenotypes.[52,63,64] The data presented by Beamer and colleagues[1] contribute to this effort by distinguishing between QTLs acting at both femur and spine and QTLs acting in a site-specific manner.

Finally, progress in genomics favors investigations based on interesting and insightful biology. Recent completion of the human genome sequence[65] and the pending completion of the mouse and rat sequences will devalue some of the skills geneticists have mastered. High-density maps and microarray technologies will allow adoption of multigenerational association analyses having greater statistical power than traditional linkage methods.[66] These advances demand that the bone geneticists of the future have command of bone biology. The article by Beamer et al.[1] provides a first step in achieving this goal.

ACKNOWLEDGMENTS

REFERENCES

1. Beamer WG, Shultz KL, Donahue LR, Churchill GA, Sen S, Wergedal JR, Baylink DJ, Rosen CJ 2001 Quantitative trait loci for femoral and lumbar vertebral BMD in C57BL/6J and C3H/HeJ inbred strains of mice. J Bone Miner Res 16:1195–1206.
2. Deng HW, Chen WM, Recker S, Stegman MR, Li JL, Davies KM, Zhou Y, Deng H, Heaney R, Recker RR 2000 Genetic determination of Colles' fracture and differential bone mass in women with and without Colles' fracture. J Bone Miner Res 15:1243–1252.
3. Ettinger B, Black DM, Nevitt MC, Rundle AC, Cauley JA, Cummings SR, Genant HK 1992 Contribution of vertebral deformities to chronic back pain and disability. The Study of Osteoporotic Fractures Research Group. J Bone Miner Res 7:449–456.
4. Nevitt MC, Ettinger B, Black DM, Stone K, Jamal SA, Ensrud K, Segal M, Genant HK, Cummings SR 1998 The association of radiographically detected vertebral fractures with back pain and function: A prospective study. Ann Intern Med 128:793–800.
5. Minne HW, Leidig G, Wuster C, Siromachkostov L, Baldauf G, Bickel R, Sauer P, Lojen M, Ziegler R 1988 A newly developed spine deformity index (SDI) to quantitate vertebral crush fractures in patients with osteoporosis. Bone Miner 3:335–349.
6. Melton LJ III, Kan SH, Frye MA, Wahner HW, O'Fallon WM, Riggs BL 1989 Epidemiology of vertebral fractures in women. Am J Epidemiol 129:1000–1011.
7. Eastell R, Cedel SL, Wahner HW, Riggs BL, Melton LJ III 1991 Classification of vertebral fractures. J Bone Miner Res 6:207–215.
8. Ross PD, Yhee YK, He YF, Davis JW, Kamimoto C, Epstein RS, Wasnich RD 1993 A new method for vertebral fracture diagnosis. J Bone Miner Res 8:167–174.
9. McCloskey EV, Spector TD, Eyres KS, Fern ED, NOR, Vasikaran S, Kanis JA 1993 The assessment of vertebral deformity: A method for use in population studies and clinical trials. Osteoporos Int 3:138–147.
10. 1994 Assessment of fracture risk and its application to screening for postmenopausal osteoporosis. Report of a WHO Study Group. World Health Organ Tech Rep Ser 843:1–129.
11. Ross PD, Davis JW, Wasnich RD 1993 Bone mass and beyond: Risk factors for fractures. Calcif Tissue Int 53(Suppl 1):S134–S138.
12. Cummings SR, Nevitt MC, Browner WS, Stone K, Fox KM, Ensrud KE, Cauley J, Black D, Vogt TM 1995 Risk factors for hip fracture in white women. Study of Osteoporotic Fractures Research Group. N Engl J Med 332:767–773.
13. Martin JC, Reid DM 1996 Appendicular measurements in screening women for low axial BMD. Br J Radiol 69:234–240.
14. Takada M, Engelke K, Hagiwara S, Grampp S, Jergas M, Gluer CC, Genant HK 1997 Assessment of osteoporosis: Comparison of radiographic absorptiometry of the phalanges and dual X-ray absorptiometry of the radius and lumbar spine. Radiology 202:759–763.
15. Grampp S, Genant HK, Mathur A, Lang P, Jergas M, Takada M, Gluer CC, Lu Y, Chavez M 1997 Comparisons of noninvasive bone mineral measurements in assessing age-related loss, fracture discrimination, and diagnostic classification. J Bone Miner Res 12:697–711.
16. Yeap SS, Pearson D, Cawte SA, Hosking DJ 1998 The relationship between BMD and ultrasound in postmenopausal and osteoporotic women. Osteoporos Int 8:141–146.
17. Frost ML, Blake GM, Fogelman I 1999 Contact quantitative ultrasound: An evaluation of precision, fracture discrimina-

tion, age-related bone loss and applicability of the WHO criteria. Osteoporos Int 10:441–449.

18. Guglielmi G, Cammisa M, De Serio A, Scillitani A, Chiodini I, Carnevale V, Fusilli S 1999 Phalangeal US velocity discriminates between normal and vertebrally fractured subjects. Eur Radiol 9:1632–1637.

19. Faulkner KG, von Stetten E, Miller P 1999 Discordance in patient classification using T scores. J Clin Densitom 2:343–350.

20. Jergas M, Breitenseher M, Gluer CC, Yu W, Genant HK 1995 Estimates of volumetric bone density from projectional measurements improve the discriminatory capability of dual X-ray absorptiometry. J Bone Miner Res 10:1101–1110.

21. Bass S, Delmas PD, Pearce G, Hendrich E, Tabensky A, Seeman E 1999 The differing tempo of growth in bone size, mass, and density in girls is region-specific. J Clin Invest 104:795–804.

22. Duan Y, Parfitt A, Seeman E 1999 Vertebral bone mass, size, and volumetric density in women with spinal fractures. J Bone Miner Res 14:1796–1802.

23. Gilsanz V, Loro ML, Roe TF, Sayre J, Gilsanz R, Schulz EE 1995 Vertebral size in elderly women with osteoporosis. Mechanical implications and relationship to fractures. J Clin Invest 95:2332–2337.

24. Hayes W 1986 Basic Biomechanics of the Skeleton. In: Uhthoff HK (ed.) Current Concepts of Bone Fragility. Springer-Verlag, Heidelberg, pp. 3–18.

25. Turner CH, Burr DB 1993 Basic biomechanical measurements of bone: A tutorial. Bone 14:595–608.

26. Martin RB, Ishida J 1989 The relative effects of collagen fiber orientation, porosity, density, and mineralization on bone strength. J Biomech 22:419–426.

27. Martin RB, Boardman DL 1993 The effects of collagen fiber orientation, porosity, density, and mineralization on bovine cortical bone bending properties. J Biomech 26:1047–1054.

28. Goulet RW, Goldstein SA, Ciarelli MJ, Kuhn JL, Brown MB, Feldkamp LA 1994 The relationship between the structural and orthogonal compressive properties of trabecular bone. J Biomech 27:375–389.

29. Muller R, Hahn M, Vogel M, Delling G, Ruegsegger P 1996 Morphometric analysis of noninvasively assessed bone biopsy specimens: Comparison of high-resolution computed tomography and histological sections. Bone 18:215–220.

30. Augat P, Link T, Lang TF, Lin JC, Majumdar S, Genant HK 1998 Anisotropy of the elastic modulus of trabecular bone specimens from different anatomical locations. Med Eng Phys 20:124–131.

31. Paganini-Hill A, Chao A, Ross RK, Henderson BE 1991 Exercise and other factors in the prevention of hip fracture: The Leisure World Study. Epidemiology 2:16–25.

32. Graafmans WC, Ooms ME, Bezemer PD, Bouter LM, Lips P 1996 Different risk profiles for hip fractures and distal forearm fractures: A prospective study. Osteoporos Int 6:427–431.

33. Ross PD, Davis JW, Epstein RS, Wasnich RD 1991 Preexisting fractures and bone mass predict vertebral fracture incidence in women. Ann Intern Med 114:919–923.

34. Kotowicz MA, Melton LJ III, Cooper C, Atkinson EJ, O'Fallon WM, Riggs BL 1994 Risk of hip fracture in women with vertebral fracture. J Bone Miner Res 9:599–605.

35. Wasnich RD, Davis JW, Ross PD 1994 Spine fracture risk is predicted by nonspine fractures. Osteoporos Int 4:1–5.

36. Lufkin EG, Wahner HW, O'Fallon WM, Hodgson SF, Kotowicz MA, Lane AW, Judd HL, Caplan RH, Riggs BL 1992 Treatment of postmenopausal osteoporosis with transdermal estrogen. Ann Intern Med 117:1–9.

37. Liberman UA, Weiss SR, Broll J, Minne HW, Quan H, Bell NH, Rodriguez-Portales J, Downs RW Jr, Dequeker J, Favus M 1995 Effect of oral alendronate on BMD and the incidence of fractures in postmenopausal osteoporosis. The Alendronate

Phase III Osteoporosis Treatment Study Group. N Engl J Med 333:1437–1443.

38. Hedlund LR, Gallagher JC 1989 Increased incidence of hip fracture in osteoporotic women treated with sodium fluoride. J Bone Miner Res 4:223–225.

39. Riggs BL, Hodgson SF, WM OF, Chao EY, Wahner HW, Muhs JM, Cedel SL, Melton LJ III 1990 Effect of fluoride treatment on the fracture rate in postmenopausal women with osteoporosis. N Engl J Med 322:802–809.

40. Blank RD 1999 Linkage, association, and the genetic analysis of BMD and related phenotypes: An overview for clinicians. J Clin Densitom 2:59–70.

41. Lander E, Schork N 1994 Genetic dissection of complex traits. Science 265:2038–2048.

42. Johnson ML, Gong G, Kimberling W, Recker SM, Kimmel DB, Recker RB 1997 Linkage of a gene causing high bone mass to human chromosome 11 (11q12–13). Am J Hum Genet 60:1326–1332.

43. Koller DL, Rodriguez LA, Christian JC, Slemenda CW, Econs MJ, Hui SL, Morin P, Conneally PM, Joslyn G, Curran ME, Peacock M, Johnston CC, Foroud T 1998 Linkage of a QTL contributing to normal variation in BMD to chromosome 11q12–13. J Bone Miner Res 13:1903–1908.

44. Koller DL, Econs MJ, Morin PA, Christian JC, Hui SL, Parry P, Curran ME, Rodriguez LA, Conneally PM, Joslyn G, Peacock M, Johnston CC, Foroud T 2000 Genome screen for QTLs contributing to normal variation in BMD and osteoporosis. J Clin Endocrinol Metab 85:3116–3120.

45. Devoto M, Shimoya K, Caminis J, Ott J, Tenenhouse A, Whyte MP, Sereda L, Hall S, Considine E, Williams CJ, Tromp G, Kuivaniemi H, Ala-Kokko L, Prockop DJ, Spotila LD 1998 First-stage autosomal genome screen in extended pedigrees suggests genes predisposing to low BMD on chromosomes 1p, 2p and 4q. Eur J Hum Genet 6:151–157.

46. Niu T, Chen C, Cordell H, Yang J, Wang B, Wang Z, Fang Z, Schork NJ, Rosen CJ, Xu X 1999 A genome-wide scan for loci linked to forearm BMD. Hum Genet 104:226–233.

47. Klein RF, Mitchell SR, Phillips TJ, Belknap JK, Orwoll ES 1998 Quantitative trait loci affecting peak BMD in mice. J Bone Miner Res 13:1648–1656.

48. Benes H, Weinstein RS, Zheng W, Thaden JJ, Jilka RL, Manolagas SC, Shmookler Reis RJ 2000 Chromosomal mapping of osteopenia-associated quantitative trait loci using closely related mouse strains. J Bone Miner Res 15:626–633.

49. Shimizu M, Higuchi K, Bennett B, Xia C, Tsuboyama T, Kasai S, Chiba T, Fujisawa H, Kogishi K, Kitado H, Kimoto M, Takeda N, Matsushita M, Okumura H, Serikawa T, Nakamura T, Johnson TE, Hosokawa M 1999 Identification of peak bone mass QTL in a spontaneously osteoporotic mouse strain. Mamm Genome 10:81–87.

50. Beamer WG, Shultz KL, Churchill GA, Frankel WN, Baylink DJ, Rosen CJ, Donahue LR 1999 Quantitative trait loci for bone density in C57BL/6J and CAST/EiJ inbred mice. Mamm Genome 10:1043–1049.

51. Rosen CJ, Churchill GA, Donahue LR, Shultz KL, Burgess JK, Powell DR, Beamer WG 2000 Mapping quantitative trait loci for serum insulin-like growth factor-1 levels in mice. Bone 27:521–528.

52. Yershov Y, Baldini TH, Villagomez S, Young T, Martin ML, Bockman RS, Peterson MGE, Blank RD 2001 Bone Strength and Related Traits in HcB/Dem Recombinant Congenic Mice. J Bone Miner Res 16:992–1003.

53. Todd JA 1999 From genome to etiology in a multifactorial disease, type 1 diabetes. Bioessays 21:164–174.

54. Paterson AD, Petronis A 2000 Age of diagnosis-based linkage analysis in type 1 diabetes. Eur J Hum Genet 8:145–148.

55. Becker KG 1999 Comparative genetics of type 1 diabetes and autoimmune disease: Common loci, common pathways? Diabetes 48:1353–1358.

56. Postma DS, Bleecker ER, Amelung PJ, Holroyd KJ, Xu J, Panhuysen CI, Meyers DA, Levitt RC 1995 Genetic susceptibility to asthma—bronchial hyperresponsiveness coinherited with a major gene for atopy. N Engl J Med 333:894–900.

57. Daniels SE, Bhattacharyya S, James A, Leaves NI, Young A, Hill MR, Faux JA, Ryan GF, le Souef PN, Lathrop GM, Musk AW, Cookson WO 1996 A genome-wide search for quantitative trait loci underlying asthma. Nature 383:247–250.

58. Morel L, Wakeland EK 2000 Lessons from the NZM2410 model and related strains. Int Rev Immunol 19:423–446.

59. Marcott C, Reeder RC, Paschalis EP, Tatakis DN, Boskey AL, Mendelsohn R 1998 Infrared microspectroscopic imaging of biomineralized tissues using a mercury-cadmium-telluride focal-plane array detector. Cell Mol Biol (Noisy-le-grand) 44:109–115.

60. Majumdar S, Link TM, Millard J, Lin JC, Augat P, Newitt D, Lane N, Genant HK 2000 In vivo assessment of trabecular bone structure using fractal analysis of distal radius radiographs. Med Phys 27:2594–2599.

61. Laib A, Hildebrand T, Hauselmann HJ, Ruegsegger P 1997 Ridge number density: A new parameter for in vivo bone structure analysis. Bone 21:541–546.

62. Smit TH, Schneider E, Odgaard A 1998 Star length distribution: A volume-based concept for the characterization of structural anisotropy. J Microsc 191(Pt 3):249–257.

63. Comuzzie AG, Mahaney MC, Almasy L, Dyer TD, Blangero J 1997 Exploiting pleiotropy to map genes for oligogenic phenotypes using extended pedigree data. Genet Epidemiol 14:975–980.

64. Rogers J, Mahaney MC, Beamer WG, Donahue LR, Rosen CJ 1997 Beyond one gene-one disease: Alternative strategies for deciphering genetic determinants of osteoporosis. Calcif Tissue Int 60:225–228.

65. Venter JC, Adams MD, Myers EW, Li PW, Mural RJ, Sutton GG, Smith HO, Yandell M, Evans CA, Holt RA, Gocayne JD, Amanatides P, Ballew RM, Huson DH, Wortman JR, Zhang Q, Kodira CD, Zheng XH, Chen L, Skupski M, Subramanian G, Thomas PD, Zhang J, Gabor Miklos GL, Nelson C, Broder S, Clark AG, Nadeau J, McKusick VA, Zinder N, Levine AJ, Roberts RJ, Simon M, Slayman C, Hunkapiller M, Bolanos R, Delcher A, Dew I, Fasulo D, Flanigan M, Florea L, Halpern A, Hannenhalli S, Kravitz S, Levy S, Mobarry C, Reinert K, Remington K, Abu-Threideh J, Beasley E, Biddick K, Bonazzi V, Brandon R, Cargill M, Chandramouliswaran I, Charlab R, Chaturvedi K, Deng Z, Di Francesco V, Dunn P, Eilbeck K, Evangelista C, Gabrielian AE, Gan W, Ge W, Gong F, Gu Z, Guan P, Heiman TJ, Higgins ME, Ji RR, Ke Z, Ketchum KA, Lai Z, Lei Y, Li Z, Li J, Liang Y, Lin X, Lu F, Merkulov GV, Milshina N, Moore HM, Naik AK, Narayan VA, Neelam B, Nusskern D, Rusch DB, Salzberg S, Shao W, Shue B, Sun J, Wang Z, Wang A, Wang X, Wang J, Wei M, Wides R, Xiao C, Yan C 2001 The sequence of the human genome. Science 291:1304–1351.

66. Risch N, Merikangas K 1996 The future of genetic studies of complex human diseases. Science 273:1516–1517.

Address reprint requests to:
Robert D. Blank
Department of Medicine
Endocrinology, Diabetes, and Metabolism Section
University of Wisconsin Medical School
H4/556 CSC (5148)
600 Highland Avenue
Madison, WI 53792, USA

Original Research

Use of GC Clamps in DHPLC Mutation Scanning

Robert J. Wurzburger, MS, *Research Division, Hospital for Special Surgery, New York, New York*
*Rajarsi Gupta, BA, *Laboratory for Fluorescence Dynamics, Physics Department, University of Illinois, Urbana-Champaign, Urbana, Illinois*
*Andrew P. Parnassa, BA, *Department of Microbiology and Immunology, Weill Medical College, Cornell University, New York, New York*
*Sargam Jain, BA, *State University of New York at Stony Brook, School of Medicine, Stony Brook, New York*
*Jason A. Wexler, MD, *Division of Endocrinology, Clinical Nutrition and Vascular Medicine, University of California, Davis Medical Center, Sacramento, California*
*Jia Li Chu, MD, *Division of Rheumatology, University of Washington, Seattle, Washington*
*Keith B. Elkon, MD, *Division of Rheumatology, University of Washington, Seattle, Washington*
*Robert D. Blank, MD, PhD, *Section of Endocrinology, Department of Medicine, University of Wisconsin-Madison, Madison, Wisconsin and Geriatrics Research, Education and Clinical Center, William S. Middleton Veterans Hospital, Madison, Wisconsin*

Author affiliated with Research Division, Hospital for Special Surgery, New York, New York

ABSTRACT

OBJECTIVE

Development of a systematic mutation detection assay strategy for denaturing high performance liquid chromatography (DHPLC).

DESIGN

Adaptation of Guanine and Cytosine (GC)-clamping from denaturing gradient gel electrophoresis (DGGE) to DHPLC.

METHODS

Three target sequences harboring known allelic variants were studied to develop a general DHPLC assay design strategy. These were exon 10 of the human *RET* (REarranged during Transfection) gene, exon 52 of the mouse *Colla2* gene, and exon 9 of the human *FAS* (APO-1, CD-95) gene. Available software was used to analyze melting curves and determine assay conditions. GC clamps of 20 bp or 36 bp were added to polymerase chain reaction (PCR) primers to introduce a high melting temperature (T_m) domain to each of the target molecules. DHPLC was performed under partially denaturing conditions.

RESULTS

DHPLC assays of PCR-amplified sequences can be developed using a personal computer. The following three steps allowed for mutation detection in all three targets.
1) The target sequence should have a uniform T_m
2) GC clamps of length sufficient to introduce a second melting domain with a $T_m \geq 8°$ above that of the target sequence should be appended to one of the primers.
3) The DHPLC assay should be performed at the highest temperature at which the target sequence is predicted to be $\geq 90\%$ double stranded

CONCLUSION

Addition of GC-clamps to primers facilitates mutation detection by DHPLC.
The theoretical basis for this observation is identical to that underlying the utility of GC-clamps in DGGE.

REPRINT REQUESTS:
Robert D. Blank, MD, PhD
Section of Endocrinology
Department of Medicine
University of Wisconsin-Madison
H4/556 CSC (5148)
600 Highland Avenue
Madison, Wisconsin 53792
Telephone: 608-263-7780
Fax: 608-263-9983
Email: rdb@medicine.wisc.edu

INTRODUCTION

Efficient, robust mutation detection methods can potentially have a major impact on the diagnosis of genetic disorders and the identification of genetic contributions to multifactorial disorders. Many investigations depend on relating genotypic variations to specific phenotypes. Such assays should ideally possess several widely recognized performance characteristics.[1,2]

This report describes a simplified strategy for designing mutation detection assays by denaturing high performance liquid chromatography (DHPLC), based on DHPLC's ability to separate partially denatured double stranded DNA molecules. Particular attention is devoted to the use of GC clamps with this system, allowing assay design to be carried out in a nearly algorithmic fashion. This approach allows investigators to shift their efforts from mutation detection assay design to interpretation of the biological consequences of detected sequence variation.

MATERIALS AND METHODS

DNA preparation
Mouse and human DNA were prepared from tail and peripheral blood mononuclear cells using the Invitrogen (Carlsbad, CA) and Puregene (Minneapolis, MN) DNA extraction kits, respectively. Human subjects provided written informed consent under protocols approved by the Memorial Sloan-Kettering Cancer Center's IRB[3,4] or the Hospital for Special Surgery's IRB.[5-7]

PCR
All amplifications were performed in 50 μL reactions including 1 U of Red Taq DNA Polymerase (Sigma, St. Louis, MO), 0.2 mM dNTP mix (Amersham Pharmacia, Piscataway, NJ), and 10 mM Tris-HCl (pH 8.3) containing 50 mM KCl, 1.5 mM $MgCl_2$, 0.1% gelatin, and 20 to 50 ng of genomic DNA. Primers were designed using Primer 0.5 software.[8] Reactions were performed in a PE Biosystems (Norwalk, CT) 2400 thermal cycler. Amplifications were carried out by an initial denaturation of 3 minutes at 95°C, followed by 35 cycles of 94°C x 30 seconds, $T_{annealing}$ x 30 seconds, and 72°C x 30 seconds, and concluded by a final denaturation at 95°C x 5 minutes followed by slow cooling to room temperature. Primer sequences and annealing temperatures are as follows:
clamp 20 = GCGGCCCGCCGCCCCCGCCG
clamp 36 = CGCCCGCCGCGCCCCGCGCCCGTCCCGC-CGCCCCCG[9], FOIM = GAAATGGCTTTCCTAGACC-CCG, ROIM = AATGATTGTCTTGCCCCATTCA with $T_{annealing}$ = 60°C, primers HFAS47 and HFAS49[5] and primers FRET10 and RRET10[10] and their annealing temperatures were previously published.

DHPLC conditions
Loading, elution and washing of the DHPLC column was carried out with varying combinations of three buffers injected at a flow rate of 0.9 ml/min: Buffer A contains 100 mM triethylamine acetate (TEAA), pH 7.0 and 0.025%

acetonitrile, Buffer B contains 25% acetonitrile, 100 mM TEAA, pH 7.0, and 0.1 mM EDTA, and Buffer D contains 75% acetonitrile. Loading and elution buffers are combinations of buffers A and B, whose relative proportions form a gradient over a specified time interval. Buffer D is used to wash the column. DHPLC elution buffer gradients were generated by WAVEMAKER version 3.3.3 software (Transgenomic, Omaha, NE) and are reported as % buffer B at specified times. Assays were performed using the WAVE DNA fragment analysis system (Transgenomic, Omaha, NE). Oven temperature was determined from inspection of the melting profile, choosing the highest temperature at which the target sequence was predicted to be >90% duplex. Following the gradient elution, all remaining bound material was washed from the column for 36 seconds with buffer D and the column was re-equilibrated with the loading buffer for 156 seconds. Sample elution was monitored by absorbance at 260 nm.

DNA Sequencing
PCR products were purified by passage through Microcon microconcentrating centrifugal filter columns (Millipore, Bedford, MA) prior to sequencing. Sequencing reactions were performed using the Applied Biosystems Dye-Terminator Kit and analyzed on a ABI Prism 377 DNA sequencer (Applied Biosystems, Foster City, CA).

RESULTS

First, an established denaturing gradient gel electrophoresis (DGGE) assay to DHPLC was adapted, since both DGGE and DHPLC-based mutation detection operate on the principle of detecting differences in melting behavior among individual species in a mixed population of DNA molecules. Previously a GC-clamped DGGE assay was developed to detect pathogenic mutations in exon 10 of the RET pro-tooncogene,[3,4] this was used as the starting point in adapting GC-clamping to DHPLC. Without a GC clamp, the target sequence has a single, uniform melting domain, with a predicted T_m between 66°C (>90% double stranded) and 67°C (>80% single stranded). Addition of a 36 bp GC clamp introduces a second higher T_m melting domain (figures 1A and 1B). The target sequence therefore denatures under conditions in which the GC clamp remains double-stranded. The WAVEMAKER-generated elution profile was loading in 44% buffer B, 49% buffer B at 30 seconds, and 58% buffer B at 300 seconds. The software recommended 67°C for assay performance. RET exon 10 was amplified from subjects harboring the C620F and C620R mutations, suffering from familial medullary carcinoma of the thyroid and MEN 2A, respectively, and from unaffected family members.[4] Mutations were detected at 66°C (figure 1C) and 67°C (not shown), but not at 65°C or 68°C (not shown) when the GC clamp was included. At 65°C a single sharp peak was seen, regardless of genotype, while at 68° all genotypes eluted as a broad, low intensity peak. Resolution of heteroduplex peaks was clearer at 66°C than at 67°C. These mutations were resolved at 60°C using a 20% to 60% gradient by DGGE.[3] Mutations were not detected either by DHPLC or
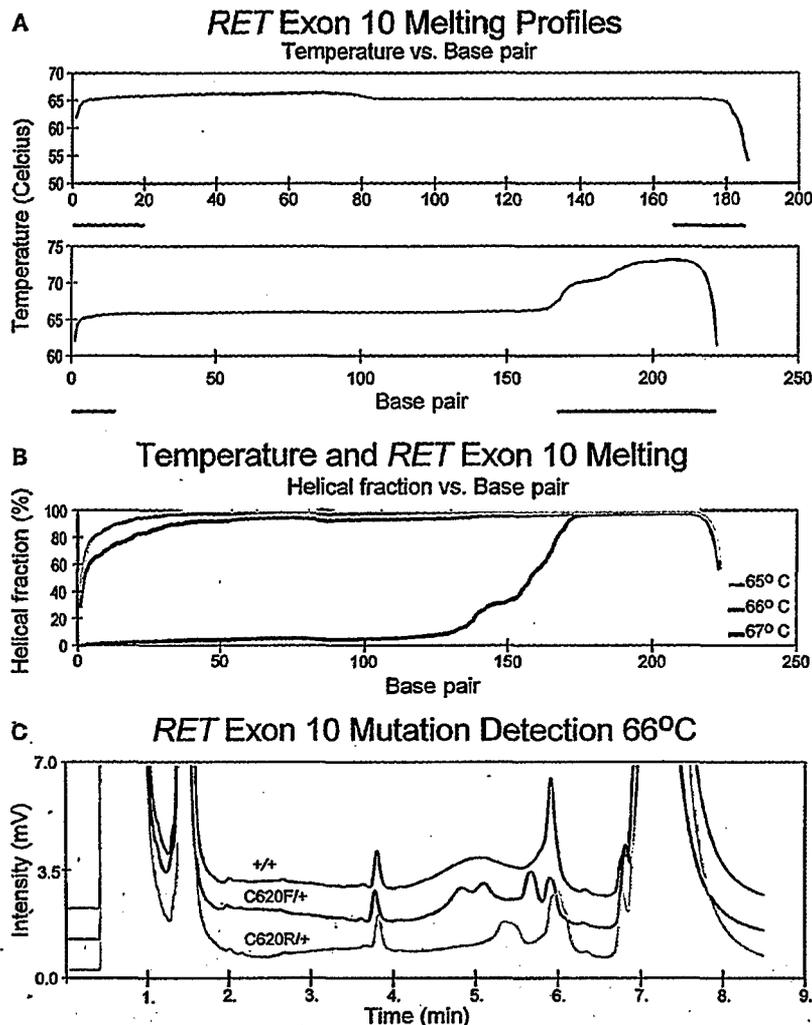
Figure 1.
A. Wavemaker-generated melting profiles for *RET* exon 10 without (top) and with (bottom) inclusion of a 36 base GC clamp on the 3′ amplification primer. The bold lines under the base pair axis indicate the extent of the primer sequences.
B. Predicted melting behavior of GC clamped *RET10* amplicons at 65°C, 66°C, and 67°C. The GC clamp remains double stranded at all 3 temperatures. The target sequence is ≥ 90% double stranded at 65°C and 66°C, but not at 67°C.
C. CDHPLC elution profiles for 3 *RET* genotypes at 66°. Heterozygotes harboring the C620F and C620R mutations are readily distinguished from normals and from each other.

DGGE when the GC clamp was not used (not shown). At 65°C and 66°C, unclamped samples elute as a single sharp peak regardless of genotype, while at 67°C and 68°C they elute as a broad, low-amplitude peak regardless of genotype.

Next we designed a mutation detection assay for the mouse *Col1a2oim* mutation; a one-base pair deletion of a G residue in exon 52, encoding the c-terminal propeptide of the α2 chain of type 1 procollagen.[11,12] The melting profile was determined to be uniform in the target region (figure 2A). The target sequence is >90% double stranded at 58°C but not at 59°C, so assays were conducted at 58°C (figure 2B). Gradient conditions were injection in 43% buffer B, 48% buffer B at 30 seconds, and 57% buffer B at 300 seconds. Heterozygotes were readily distinguished from either wild-

type or mutant homozygotes when a 36 bp GC clamp was included (figure 2C), but not when it was omitted (not shown). As in the case of *RET* exon 10, the unclamped products all elute as single sharp peaks at 58°C, a temperature at which the molecule is predicted to be double stranded. We did not attempt to resolve this target at other temperatures. A 50:50 mix of wild-type and mutant homozygous samples eluted as a single sharp peak when unheated, but eluted as a pair of peaks when heated to 95°C and cooled slowly (figure 2D). This demonstrates that assay conditions are robust for detecting heterozygosity, but are not adequate for determining the allele present in homozygous samples. Moreover, the behavior of the unheated mixture reveals that there is no difference in the elution times of the wild-type and mutant products, as the peak is not broadened relative to the peak

A. Col1a2 Melting Profile
Temperature vs. Base pair

B. Temperature and Col1a2 Melting
Helical fraction vs. Base pair

C. Col1a2 Mutation Detection 58°C

D. oim/oim and +/+ Co-Elute
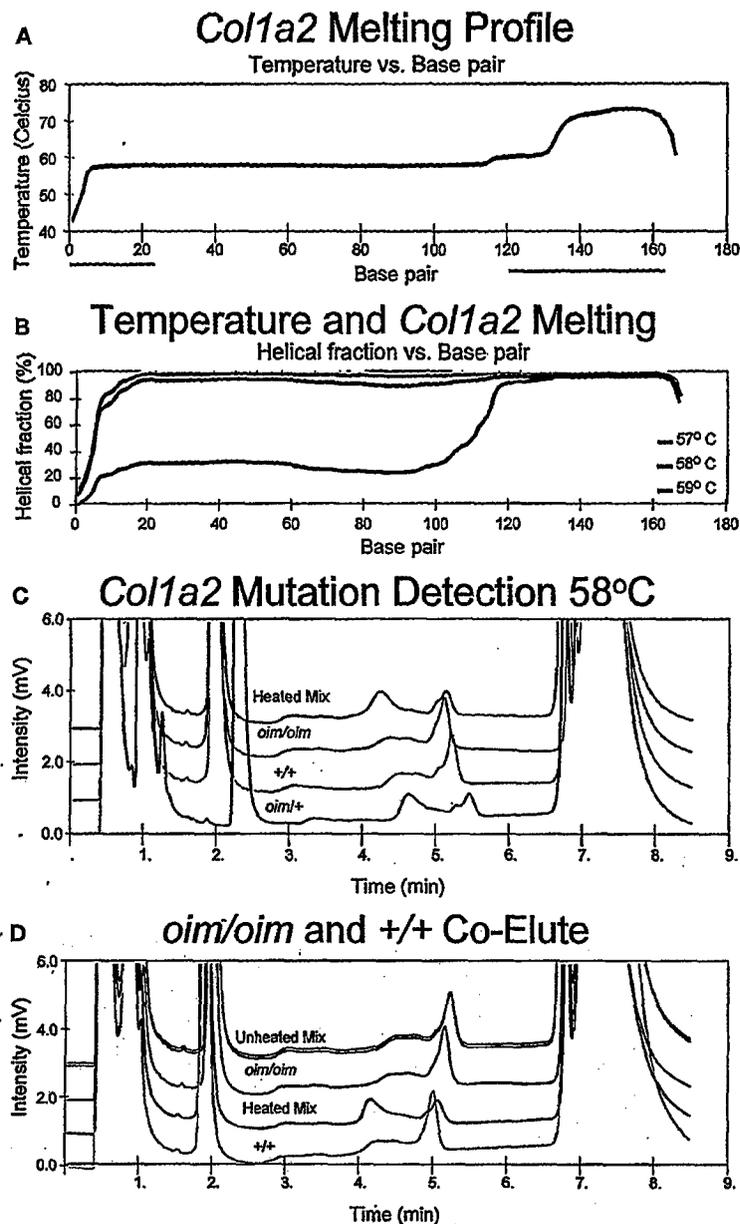
Figure 2.
A. Wavemaker-generated *Col1a2* GC clamped melting profile. The bold lines under the base pair axis indicate the extent of the primer sequences.
B. The predicted melting behavior of *Col1a2* amplicons at 57°C, 58°C, and 59°C.
C. Resolution of *Col1a2* heterozygotes from homozygotes. A *Col1a2*$^{oim/+}$ heterozygote is separated from either wild type or *oim/oim* homozygotes. A denatured and slowly reannealed mixture of the wild type and *oim/oim* PCR products produces an elution profile identical to that of the *oim/+* heterozygote.
D. Inability to resolve +/+ homozygotes from *oim/oim* homozygotes. Both homozygotes and an unheated mixture of *oim/oim* and +/+ PCR products result in single elution peaks. However, heating the mixture to denature the DNA and allowing it to reanneal slowly allows heteroduplex formation and results in the appearance of a second elution peak, as for *oim/+* heterozygotes.

generated by homozygous samples. This finding indicates that decreased T_m at the site of mismatch is a critical element of mutation detection by DHPLC.

Homozygous samples can be genotyped in a two-step assay.
1) The assay is performed on a pure sample
2) Samples found to be homozygous are mixed with a reference wild-type sample, denatured, reannealed and reanalyzed

Mutant homozygotes will yield a heterozygous pattern on mixing, while wild-type homozygotes will retain a homozygous pattern on mixing.

The same strategy was applied for the detection of the D244G and R234P missense mutations in exon 9 of the human *FAS (APO-1, CD95)* gene, which cause the Canale-Smith Syndrome[5,7]. The melting profile predicts that 59°C is the highest temperature at which the target sequence is >90% double stranded (figures 3A and 3B). DHPLC analysis at 59°C with injection at 45% buffer B and elution with a gradient profile of 50% buffer B at 30 seconds, and 59% at 300 seconds is shown in figure 3C. The mutations were readily detected with a 20 bp GC clamp, while omission of the GC clamp did not allow us to detect the mutations under these conditions, with all genotypes eluting as a single sharp peak (not shown).

DISCUSSION

Sheffield and colleagues demonstrated the utility of GC clamps in designing DGGE assays,[9] showing that the inclusion of a clamp allowed detection of mutations in the murine β^{major} globin gene that were undetectable without clamping. The additional sensitivity arose from detection of mutations in the highest T_m domain of the target sequence. Subsequent sensitivity analyses of DGGE have consistently found that analyses performed with GC clamps have sensitivities of ~95% and specificities approaching unity.[13-16] The theoretical basis for this increase in sensitivity is that resolution of the various molecular species occurs primarily when individual molecules are partially denatured. Inclusion of a GC clamp provides an artificial, high T_m domain in the molecules being analyzed, allowing the target sequence to occur in the context of a low T_m domain. The data suggest
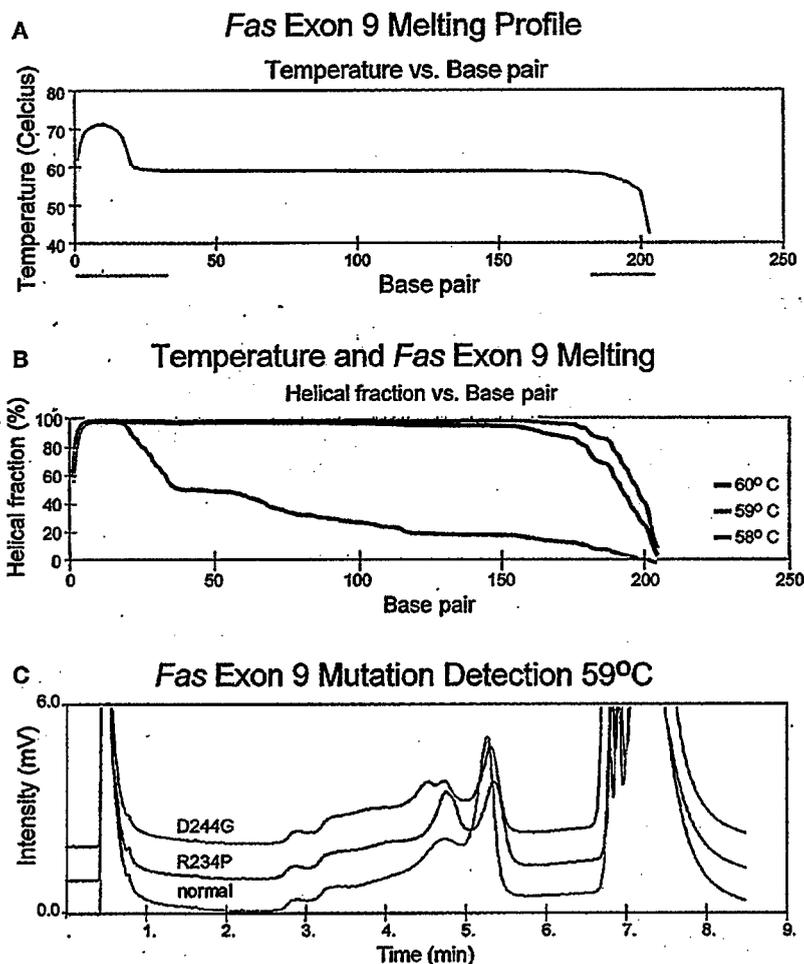
Figure 3.
A. Wavemaker-generated *FAS* exon 9 GC clamped melting profile.
B. Temperature and *FAS* Exon 9 Melting. The predicted melting behavior of *FAS* amplicons at 58°C, 59°C and 60°C.
C. Resolution of R234P and D244G heterozygotes from a normal homozygote.

that resolution of the various molecular species by DHPLC also occurs primarily when these have partially denatured, so that the principles guiding design of DGGE assays can be applied to DHPLC mutation detection.

Heteroduplexes include mismatches of one or more base pairs, resulting in early melting of the mismatched region. DHPLC allows resolution of heteroduplex from homoduplex DNA molecules based on differences in their retention time in the column under partially denaturing conditions, with heteroduplex molecules eluting earlier. This behavior mirrors heteroduplexes' lower T_m's and is similar to retardation of electrophoretic transport at different points along a denaturing gradient gel. In DGGE, mutations in the highest T_m domain are resolved poorly, if at all. It was determined that while the analytical technology differs in DHPLC, the principle of heteroduplex detection should be the same as in DGGE and that inclusion of GC clamps would facilitate mutation detection. The inability to detect sequence variants in the highest T_m domain may explain the anecdotally poor ability of DHPLC to detect mutations in short amplicons (K. Hecker, personal communication), which often include only a single melting domain.

A basic and general approach to designing new mutation screening assays by DHPLC was established. First, the target region's sequence is evaluated for uniformity of T_m. If this condition is not satisfied, alternative primers are chosen in order to generate a target sequence with a uniform T_m. Second, a GC clamp of sufficient length to create a high-T_m domain is appended to one of the primers. Once again, the predicted melting curve is inspected, to ensure that the clamp produces the desired high T_m domain, as illustrated in the "A" panels of the figures. Melting curves of the PCR product are calculated and the highest temperature at which the target sequence is >90% duplex is chosen for assay performance, as illustrated in the "B" panels of the figures. WAVEMAKER software, native to our DHPLC instrument, allowed both the calculation of melting profiles and generation of elution profiles. When using this software, inspection of the melting profiles is necessary. WAVEMAKER sometimes suggests an assay temperature that is too high for optimal resolution of sequence variation. Freely accessible programs perform equivalent calculations and give equivalent results.[17-20]

The trio of assays described here demonstrate that inclusion of a GC clamp allows detection of mutations by DHPLC under conditions that can be fully established prior to assay performance, using predicted melting curves. The experiments presented above do not exclude the development of assays without GC clamps, but rather show that the conditions identified *in silico* work well without further optimization when GC clamps are included. Unclamped primers for *RET* exon 10 were tested at four temperatures. The other two assays were tested at a single temperature. We did not attempt to optimize gradient conditions. It was expected that such optimization would likely have allowed mutation detection, even with unclamped molecules.

In the assays described here, the GC clamp had a melting point 8°C to 13°C higher than the target sequence, while the target sequence varied in T_m by no more than 3°C. Therefore, investigators should include GC clamp sequences sufficiently long to provide an 8°C increment in T_m relative to the target. The required length will vary according to the T_m of the target sequence, but it is straightforward to determine the minimum necessary length with melting profile software prior to ordering modified primers.

Theoretically, psoralen clamping provides an alternative to GC clamping by generating a covalent interstrand bond rather than by raising the T_m of a region of the target molecule.[21] The covalent bond introduced by psoralenation and subsequent UV light exposure effectively clamps one end of the molecule regardless of temperature. The advantage of psoralen compared to GC clamping is that the clamp need not be changed from assay to assay; the disadvantage is that an additional UV crosslinking step must be added prior to analysis. However, experiments with psoralen clamps were not conducted, as a result it is not known if this approach would perform as well in practice as in theory.

Electrophoretic mutation detection assays are difficult to perform on a large scale, since casting and loading gels are tasks that are difficult to automate. Because DGGE and Single Strand Conformation Polymorphism (SSCP) suffer from these limitations, the DHPLC-based assay is more readily adaptable to even a medium-throughput setting. The WAVE system can load samples automatically from a 96-sample block. Each sample is processed in approximately 6 to 9 minutes. The automation provided by the WAVE system vs. the gel-based methods, allows investigators to perform mutation screens at higher throughput and with less hands-on time. Further improvements in throughput might be achieved by pooling samples prior to DHPLC analysis, as has been done for gel-based methods.[22] These scale issues are most relevant to research laboratories engaged in mutation screening and genotype-phenotype correlation, and may become applicable to diagnostic clinical laboratories as well.

The assays we describe here scan relatively short target sequences and therefore cannot estimate the maximum length over which DHPLC based methods might work. High sensitivity and specificity have been reported for DHPLC in a growing body of analyses for sequences up to 400 bp in length.[23-32] Our approach to primer design has a shorter practical limit of about 250 bp, imposed by our criterion that target sequences have a uniform T_m.

Other approaches may lead to further improvements in mutation scanning methodology. For example, two groups have recently described a purely optical assay strategy that obviates the need for physical separation of homoduplex and heteroduplex molecules.[33,34] This approach may prove applicable to large-scale genotyping applications, but has yet to be widely validated.

The mutation detection strategy presented in this article leads to higher primer costs than other approaches, because of the need for either GC-clamped or psoralen-clamped primers, and shorter target sequences. At an estimated incremental cost of $0.70/base x 30 bases for "ordinary" scale primer synthesis, the extra primer costs for a typical length GC clamp is about $21. Psoralen clamps are more expensive than GC-clamps, requiring both an arbitrary primer adaptor arm and the psoralenation, thus adding about $40 to the cost of each clamped primer. Theoretically, psoralen primers could be reserved for the most GC-rich targets, in which GC clamps of practical length would not impact T_m. Costs arising from extra primer pairs needed as a result of studying shorter target sequences are less easily quantified and depend in part on the scope of the length of DNA to be scanned for mutations and the nature of its sequence. At an average cost of $50/GC clamped primer pair, addition of 10 additional primer pairs leads to a relatively small incremental cost. These are trivial costs compared with the time of technical personnel, whose salaries will typically exceed $10/hour. Therefore, even modest reductions in assay development time lead to net cost savings.

The greatest limitation on mutation scanning throughput, however, remains the time necessary to design mutation detection assays. Several previous reports addressed DHPLC assay design optimization.[18,30,31,35,36] These authors all recommend performing assays at various temperatures to maximize sensitivity and some narrow the buffer gradient ranges, requiring a still greater number of temperatures. Another report[37] suggests that a gradual decrease in T_m from the clamp to the free end of a molecule is the optimal configuration for mutation detection by heteroduplex-based methods. We have demonstrated that inclusion of GC clamps obviates the need for tedious assay optimization. GC clamps of sufficient length to create a domain with T_m 8°C greater than that of the target sequence allows an experimenter to develop a working assay in less than one hour. As genomic analysis moves from determination of additional sequence data to understanding the biological consequences of sequence variation, the ability to perform mutation screening efficiently will become ever more valuable. The algorithm for establishing DHPLC conditions described here will facilitate this.

CONCLUSION

Assay design principles adapted from those previously established for DGGE facilitate development of DHPLC mutation scanning strategies, as both methods resolve sequence variants by virtue of differences in the melting behavior of partially denatured DNA molecules. Use of GC clamps in DHPLC obviates the need for empirical optimization of new assays. The use of clamps is preferable to evaluation of a greater number of assay conditions for two reasons. First, unlike the situation with model assays such as those we have used for illustration, investigators performing mutation screens will not have positive controls available to test conditions. Second, the alternative strategy of varying

conditions to increase sensitivity depends primarily on varying assay temperature. Heating and cooling the instrument oven is slow, and the time needed for temperature equilibration eliminates much of the time advantage arising from DHPLC.

REFERENCES

1. Grompe M. The rapid detection of unknown mutations in nucleic acids. Nat Genet 1993;5:111-117.
2. Cotton RG. Slowly but surely towards better scanning for mutations. Trends Genet 1997;13:43-46.
3. Blank RD, Sklar CA, Martin ML. Denaturing gradient gel electrophoresis to diagnose multiple endocrine neoplasia type 2. Clin Chem 1996;42:598-603.
4. Blank RD, Sklar CA, Dimich AB, LaQuaglia MP, Brennan MF. Clinical presentations and RET protooncogene mutations in seven multiple endocrine neoplasia type 2 kindreds. Cancer 1996;78:1996-2003.
5. Drappa J, Vaishnaw AK, Sullivan KE, Chu JL, Elkon KB. Fas gene mutations in the Canale-Smith syndrome, an inherited lymphoproliferative disorder associated with autoimmunity. N Engl J Med 1996;335:1643-1649.
6. Vaishnaw AK, Toubi E, Ohsako S, Drappa J, Buys S, Estrada J, Sitarz A, Zemel L, Chu JL, Elkon KB. The spectrum of apoptotic defects and clinical manifestations, including systemic lupus erythematosus, in humans with CD95 (Fas/APO-1) mutations. Arthritis Rheum 1999;42:1833-1842.
7. Vaishnaw AK, Orlinick JR, Chu JL, Krammer PH, Chao MV, Elkon KB. The molecular basis for apoptotic defects in patients with CD95 (Fas/Apo-1) mutations. J Clin Invest 1999;103:355-363.
8. Lincoln SE, Daly MJ, Lander ES. Primer: a computer program for automatically selecting PCR primers. Whitehead Institute for Biomedical Research; Cambridge, MA, 1991.
9. Sheffield VC, Cox DR, Lerman LS, Myers RM. Attachment of a 40-base-pair G + C-rich sequence (GC-clamp) to genomic DNA fragments by the polymerase chain reaction results in improved detection of single-base changes. Proc Natl Acad Sci U S A 1989;86:232-236.
10. Donis-Keller H, Dou S, Chi D, Carlson KM, Toshima K, Lairmore TC, Howe JR, Moley JF, Goodfellow P, Wells SA Jr. Mutations in the RET proto-oncogene are associated with MEN 2A and FMTC. Hum Mol Genet 1993;2:851-856.
11. Chipman SD, Sweet HO, McBride DJ Jr, Davisson MT, Marks SC Jr, Shuldiner AR, Wenstrup RJ, Rowe DW, Shapiro JR. Defective pro alpha 2(I) collagen synthesis in a recessive mutation in mice: a model of human osteogenesis imperfecta. Proc Natl Acad Sci U S A 1993;90:1701-1705.
12. McBride DJ Jr, Shapiro JR. Confirmation of a G nucleotide deletion in the Cola-2 gene of mice with the osteogenesis imperfecta mutation. Genomics 1994;20:135-137.
13. Guldberg P, Henriksen KF, Guttler F. Molecular analysis of phenylketonuria in Denmark: 99% of the mutations detected by denaturing gradient gel electrophoresis. Genomics 1993;17:141-146.

14. Nissen H, Petersen NE, Mustajoki S, Hansen TS, Mustajoki P, Kauppinen R, Horder M. Diagnostic strategy, genetic diagnosis and identification of new mutations in intermittent porphyria by denaturing gradient gel electrophoresis. Hum Mutat 1997;9:122-130.

15. Macek M Jr, Mercier B, Mackova A, Miller PW, Hamosh A, Ferec C, Cutting GR. Sensitivity of the denaturing gradient gel electrophoresis technique in detection of known mutations and novel Asian mutations in the CFTR gene. Hum Mutat 1997;9:136-147.

16. Gejman PV, Cao Q, Guedj F, Sommer S. The sensitivity of denaturing gradient gel electrophoresis: a blinded analysis. Mutat Res 1998;382:109-114.

17. Oefner PJ, Underhill PA. DNA mutation detection using denaturing high-performance liquid chromatography (DHPLC). In: Current Protocols in Human Genetics. New York: Wiley & Sons;1998. p. 7.10.1-7.10.12.

18. Jones AC, Austin J, Hansen N, Hoogendoorn B, Oefner PJ, Cheadle JP, O'Donovan MC. Optimal temperature selection for mutation detection by denaturing HPLC and comparison to single-stranded conformation polymorphism and heteroduplex analysis. Clin Chem 1999;45:1133-1140.

19. Hansen NF, Oefner PJ. DHPLC Melt. 2002, Stanford Genome Technology Center.

20. Lerman LS, Silverstein K, Fripp W, Sauer P, Dresselhaus C. Melt94. 1994, MIT: Cambridge, MA.

21. Costes B, Girodon E, Ghanem N, Chassignol M, Thuong NT, Dupret D, Goossens M. Psoralen-modified oligonucleotide primers improve detection of mutations by denaturing gradient gel electrophoresis and provide an alternative to GC-clamping. Hum Mol Genet 1993;2:393-397.

22. Zarbl H, Aragaki C, Zhao LP. An efficient protocol for rare mutation genotyping in a large population. Genet Test 1998;2:315-321.

23. Liu WO, Oefner PJ, Qian C, Odom RS, Francke U. Denaturing HPLC-identified novel FBN1 mutations, polymorphisms, and sequence variants in Marfan syndrome and related connective tissue disorders. Genet Test 1997-98;1:237-242.

24. Liu W, Smith DI, Rechtzigel KJ, Thibodeau SN, James CD. Denaturing high performance liquid chromatography (DHPLC) used in the detection of germline and somatic mutations. Nucleic Acids Res 1998;26:1396-1400.

25. O'Donovan MC, Oefner PJ, Roberts SC, Austin J, Hoogendoorn B, Guy C, Speight G, Upadhyaya M, Sommer SS, McGuffin P. Blind analysis of denaturing high-performance liquid chromatography as a tool for mutation detection. Genomics 1998;52:44-49.

26. Choy YS, Dabora SL, Hall F, Ramesh V, Niida Y, Franz D, Kasprzyk-Obara J, Reeve MP, Kwiatkowski DJ. Superiority of denaturing high performance liquid chromatography over single-stranded conformation and conformation-sensitive gel electrophoresis for mutation detection in TSC2. Ann Hum Genet 1999;63:383-391.

27. Gross E, Arnold N, Goette J, Schwarz-Boeger U, Kiechle M. A comparison of BRCA1 mutation analysis by direct sequencing, SSCP and DHPLC. Hum Genet 1999;105(1-2):72-78.

28. Wagner T, Stoppa-Lyonnet D, Fleischmann E, Muhr D, Pages S, Sandberg T, Caux V, Moeslinger R, Langbauer G, Borg A, Oefner P. Denaturing high-performance liquid chromatography detects reliably BRCA1 and BRCA2 mutations. Genomics 1999;62:369-376.

29. Dobson-Stone C, Cox RD, Lonie L, Southam L, Fraser M, Wise C, Bernier F, Hodgson S, Porter DE, Simpson AH, Monaco AP. Comparison of fluorescent single-strand conformation polymorphism analysis and denaturing high-performance liquid chromatography for detection of EXT1 and EXT2 mutations in hereditary multiple exostoses. Eur J Hum Genet 2000;8:24-32.

30. Buyse IM, Fang P, Hoon KT, Amir RE, Zoghbi HY, Roa BB. Diagnostic testing for Rett syndrome by DHPLC and direct sequencing analysis of the MECP2 gene: identification of several novel mutations and polymorphisms. Am J Hum Genet 2000;67:1428-1436.

31. Takashima H, Boerkoel CF, Lupski JR. Screening for mutations in a genetically heterogeneous disorder: DHPLC versus DNA sequence for mutation detection in multiple genes causing Charcot-Marie-Tooth neuropathy. Genet Med 2001;3:335-342.

32. Genet Med 2001 Sep-Oct;3(5):335-42 Denaturing high-performance liquid chromatography (DHPLC) is a highly sensitive, semi-automated method for identifying mutations in the TSC1 gene. J Biochem Biophys Methods 2001;47:33-37.

33. Lipsky RH, Mazzanti CM, Rudolph JG, Xu K, Vyas G, Bozak D, Radel MQ, Goldman D. DNA melting analysis for detection of single nucleotide polymorphisms. Clin Chem 2001;47:635-644.

34. Akey JM, Sosnoski D, Parra E, Dios S, Hiester K, Su B, Bonilla C, Jin L, Shriver MD. Melting curve analysis of SNPs (McSNP): a gel-free and inexpensive approach for SNP genotyping. Biotechniques 2001;30:358-362, 364, 366-367.

35. Erlandson A, Stibler H, Kristiansson B, Wahlstrom J, Martinsson T. Denaturing high-performance liquid chromatography is a suitable method for PMM2 mutation screening in carbohydrate-deficient glycoprotein syndrome type IA patients. Genet Test 2000;4:293-297.

36. Antonarakis ES, Sampson JR, Cheadle JP. Temperature modulation of DHPLC analysis for detection of coexisting constitutional and mosaic sequence variants in TSC2. J Biochem Biophys Methods 2002;51:161-164.

37. Gille C, Gille A. TGGE-STAR: primer design for melting analysis using PCR gradient gel electrophoresis. Biotechniques 2002;32:264, 266, 268.

Taylor & Francis
healthsciences

Spectroscopically Determined Collagen Pyr/deH-DHLNL Cross-Link Ratio and Crystallinity Indices Differ Markedly in Recombinant Congenic Mice with Divergent Calculated Bone Tissue Strength

Robert D. Blank,[1,2,3] Todd H. Baldini,[3] Michael Kaufman,[4] Stephanie Bailey,[5] Rajarsi Gupta,[3] Yevgeniy Yershov,[3] Adele L. Boskey,[3] Susan N. Coppersmith,[4] Peter Demant,[6] and Eleftherios P. Paschalis[3]

[1]Endocrinology Section, Department of Medicine, University of Wisconsin Medical School, Madison, Wisconsin, USA
[2]Geriatrics Research, Education, and Clinical Center, William S. Middleton Veterans' Hospital, Madison, Wisconsin, USA
[3]Research Division, The Hospital for Special Surgery, New York, New York, USA
[4]Department of Physics, University of Wisconsin, Madison, Wisconsin, USA
[5]Department of Physics, University of Virginia, Charlottesville, Virginia, USA
[6]Department of Molecular Genetics, Netherlands Cancer Institute, Amsterdam, The Netherlands

Whole bone strength can be partitioned into structural and material components. In three-point bending tests of 6-month-old female humeri from the HcB/Dem recombinant congenic series, strains HcB/8 and HcB/23 differed markedly in calculated failure stress but not ash percentage. Fourier transform infrared spectroscopic imaging was used to determine whether differences in the ratio of pyridinoline (pyr; nonreducible) to dehydrodihydroxynorleucine (de-DHLNL; reducible) collagen cross-links (XLR), mineral crystallinity, or spatial ordering could account for the strains' differing biomechanical performance. HcB/8 had significantly higher XLR and significantly higher crystallinity than HcB/23. XLR and crystallinity were highly and similarly correlated in both strains. There were no significant differences between the strains' one-dimensional spatial correlation functions, suggesting no difference in short-range order between them. The strong correlation between XLR and crystallinity reflects the interdependence of the protein and mineral elements of bone. The data illustrate the importance of material properties in addition to mineral quantity to bone tissue strength.

INTRODUCTION

Fracture is the most significant clinical measure of bone's biomechanical performance. Epidemiologically, several types of fracture are recognized as "osteoporotic," occurring in the setting of minimal trauma. However, bone mineral density (BMD), while a useful clinical predictor of fracture risk, does not fully account for individual differences in fracture risk [1–6].

Biomechanical testing of bones harvested from experimental organisms is one approach by which the various contributors to bone strength can be studied [7, 8]. By loading bones according to contrived but reproducible protocols, such tests are capable of distinguishing strain-specific differences in mechanical performance. Moreover, it is well established that the structural strength of a whole bone can be partitioned into architectural and material components. The bone's architecture takes into account the bone's size and shape, while the bone's material reflects the underlying strength of the tissue.

Recently, interest has been growing in understanding the factors contributing to whole bone strength, which is determined by the inherent material strength of the tissue, its size and geometry, and its architecture. Geometrical and architectural investigations have included human studies of hip axis length [9–15], femoral neck bone distribution [16, 17], crumpling ratio [18], sexual dimorphism of bone modeling [19–22], and trabecular connectivity [23–26]. In addition, in animal models there has

been explicit use of anatomical measurements in the interpretation of biomechanical studies [27–30]. Investigation of bone material strength historically has relied upon biochemical and biophysical methods and has included quantitation of various protein and mineral components of bone tissue through a variety of technical approaches. Recently, by coupling a Fourier transform infrared (FTIR) spectrometer with a microscope and an array detector, spectral analysis has been carried out on thin histologic preparations of bone, allowing the material properties of bone to be investigated on scales of 6–7 μm [31, 32]. These methods allow investigation of the role, if any, the microscopic organization of bone tissue plays in determining its material strength.

In this article, we extend previous observations of biomechanical performance in HcB/Dem recombinant congenic mice [30]. Those experiments demonstrated that the calculated tissue strength of bone in strains HcB/8 and HcB/23 differ greatly, in spite of similar mineral content (ash percentage). Here, characterization of these strains is extended to include FTIR imaging data from cortical bone samples, since three-point bending is a cortical bone test. We found that the strains differed markedly in the ratio of nonreducible pyridinoline (pyr) to reducible dehydrodihydroxynorleucine (de-DHLNL) collagen cross-links (XLR) and bone mineral (apatite) crystal size and perfection (crystallinity). We also found that these two indices were highly correlated. No statistically significant differences were noted in the one-dimensional spatial correlation of either XLR or crystallinity parallel to the bone surface. These data are considered with regard to the mechanistic basis of bone tissue strength.

MATERIALS AND METHODS

Mice

The HcB/Dem strains were established and are maintained at the Netherlands Cancer Institute. Briefly, the HcB/Dem mice are inbred strains derived from arbitrary pairs of N3 backcross animals [33–35]. Each HcB/Dem strain contains a random 12.5% of the C57BL/10ScSnA genome and 87.5% of the C3H/DiSnA genome. HcB/8 and HcB/23 received different, slightly overlapping portions of the C57BL/10ScSnA genome; hence they differ in approximately 25% of the genome. The HcB/Dem strains have been genotyped at 130 marker loci distributed over each of the autosomes [36, 37]. Because they are inbred, individuals from a single strain have the same genetic composition, save for new mutations and residual unfixed chromosome segments [38, 39].

Less than 5% of the genome was unfixed at the time of genotyping; residual heterozygosity is expected to be reduced by half in each subsequent generation of inbreeding. The mice described in this report were maintained at the Hospital for Special Surgery until 6 to 7 months of age under 12-hr light-dark cycling and fed irradiated PICO 5058 rodent chow and autoclaved tap water ad lib. Only females were studied, because inclusion of males would have introduced sex-dependent variability in the traits in addition to the strain-specific and environmental variability already encountered. At sacrifice, body mass and rostroanal length were measured. This work satisfied The Hospital for Special Surgery's requirements for the ethical use of laboratory research animals.

Ash Percentage

Bone mineral fraction was calculated by comparison of dry, defatted bone weight to ash weight of homogenized tissue [40, 41]. We used entire bones rather than bones from which the epiphyses and marrow have been removed because the former technique is more reproducible in our hands.

Radiographic Analysis

Image analysis of fine focus contact radiographs of dissected humeri was performed as described [41] and used to calculate cross-sectional area (CSA) and cross-sectional moment of inertia (I). Humeral length was defined as the distance along the diaphysis from the trochlea to the humeral head's most distant point. Outer and inner diameters were measured in orthogonal projections just distal to the deltoid tuberosity, perpendicular to the diaphyseal axis. CSA was calculated according to the elliptical approximation:

$$\text{CSA} = \pi(\text{ML OR} * \text{AP OR} - \text{MR IR} * \text{AP IR}) \qquad (1)$$

where OR is the outer and IR the inner radius in either the mediolateral (ML) or anteroposterior (AP) projection. I also was calculated according to the elliptical approximation [8]:

$$I = \pi/4[(\text{ML OR})^3(\text{AP OR}) - (\text{ML IR})^3(\text{AP IR})] \qquad (2)$$

Image analysis was performed with SigmaScan (Jandel Scientific) image analysis software. All radiographs included stepped aluminum densitometric phantoms. Radiographic images were digitized with a Kodak digital camera, with the photographic field including a length scale.

Biomechanical Testing

Quasistatic three point bend testing was performed on left humeri using posts designed and machined in-house with the MTS apparatus and Instron electronics as described [42, 43]. Humeri were oriented with the deltoid tuberosity downward and the specimens oriented with the central post adjacent to the distal end of the deltoid tuberosity. This orientation corresponds to the ML axis being parallel to the applied force. Posts were separated by 3.75 mm.

Biomechanical data were analyzed following several important assumptions. First, we assumed that bone strength is determined entirely by the cortical bone in the mid-diaphysis. Second, we assumed that the humeral diaphysis is an ellipse with its major axis lying in the ML plane and its minor axis lying in the AP axis. Calculated biomechanical parameters were obtained according to the following standard formulas for three-point bending of ellipses [8]:

Stress (σ), (MPa) $=$ FLc/4I, with F $=$ force, L $=$ length, c $=$ ML OR

Strain (ε), (mm/mm) $= 12cd/L^2$, with c $=$ ML OR, d $=$ displacement, L $=$ length

Young's Modulus (E), (MPa) $= (F/d)(L^3/48I)$

FTIR Imaging

The left tibia from one mouse of each strain was fixed in buffered formalin, dehydrated in ethanol, and embedded in PMMA, from which 3 μm midsagittal sections were obtained for FTIR imaging. FTIR imaging was performed using a Bio-Rad Stingray FTIR imaging system equipped with a 64 × 64 mercury-cadmium-telluride detector, under continuous nitrogen purge. In this configuration, each field of analysis corresponds to a 400 × 400 μm, and each pixel to ~6.3 × 6.3 μm area. Water vapor and PMMA spectral contributions were accounted for, and mineral crystallinity and XLR calcualted as described elsewhere [31, 32, 44, 45]. Consequently, in each analyzed field, pixels in which either the 1660:1690 cm^{-1} ratio fell outside of the 0–2.5 range or the 1030:1020 cm^{-1} ratio fell outside the 0–2.0 range were censored as bad data.

Statistical Analysis

Most statistical analyses were performed using SigmaStat 2.03 (Jandel Scientific) and the remainder was performed with Origin version 5.0 (Microcal). Student's t-test compared HcB/8 and HcB/23 mice for anatomic features and biomechanical performance, with values for failure stress log-transformed prior to analysis to satisfy the test assumption of normality. Significance levels were Bonferroni-corrected to account for multiple comparisons. Interstrain comparisons of XLR and crystallinity indices were done by χ^2 contingency table, taking the weighted average number of pixels in each 0.25 unit interval of the distribution for each strain. The Kolmogorov-Smirnov test was used to assess normality of the FTIR imaging data. We used all bone spectra to assess the correlation of the XLR and crystallinity using the Spearman rank order method. One-dimensional spatial correlation functions (1DCs) $g(\vec{r})$ were calculated for vectors $\vec{r}$ parallel to the bone surface according to the formula

$$g(\vec{r}) = \frac{\sum_i (x_i - \bar{x})(x_{i+\vec{r}} - \bar{x})}{\sqrt{\sum_i (x_i - \bar{x})}\sqrt{\sum_i (x_{i+\vec{r}} - \bar{x})}}$$

where x_i is the index at a given pixel i; $x_{i+\vec{r}}$ is the index at a pixel located at a pixel r pixels from i; and $\bar{x}$ is the average value of the index over valid pixels in the entire field. The sum in the numerator includes overall values of i for which both x_i and $x_{i+\vec{r}}$ are valid pixels [46]. This correlation function, which quantifies the degree to which the values at pixels separated by r are correlated, is commonly used in statistical mechanics. The correlation function $g(r)$ is unity at $r = 0$; in our samples it is found to decay linearly with r for small r, and we define the correlation length as the inverse of this slope. We hypothesized that strain and index tested (XLR or crystallinity) would each influence the correlation length. To test the hypothesis, a straight-line fit was made over the linear, small r region of $g(r)$. The slopes were analyzed by two-factor ANOVA.

RESULTS

Calculated Tissue Strength Differs Between HcB/8 and HcB/23

We examined ten 6-month-old female HcB/8 and nine 6-month-old female HcB/23 mice. The anatomic and biomechanical properties of the animals are summarized in Table 1. These data show that while humeral failure load and structural stiffness is similar in the two strains, HcB/23 achieves this strength through more favorable bone architecture and less favorable bone tissue strength, whereas HcB/8 does so through less favorable bone architecture and more favorable bone tissue strength. The inferiority of HcB/23 bone tissue strength is not due to lesser mineralization, as this strain has a greater ash percentage than HcB/8. These observations prompted us to use FTIR imaging to explore the possible basis for the marked difference in bone tissue strength between the strains, examining four 400-μm^2 sections of bone from each strain.

XLR Differs Between HcB/8 and HcB/23

The amide I and II absorption bands, which in bone are representative principally of collagen, are broad and consist of underlying peaks, each corresponding to vibrations in a specific chemical environment. Of these underlying bands, we have shown previously that the ratio of absorbances at 1660 cm^{-1} and 1690 cm^{-1} is representative of the ratio of pyridinoline to deH-DHLNL, two of the major cross-links present in bone collagen

TABLE 1

Anatomic and biomechanical properties of HcB/8 and HcB/23 mice.

Trait	HcB/8 ($n = 10$)	HcB/23 ($n = 9$)	p value
Body mass (g)	19.9 ± 1.5	23.5 ± 1.1	$<10^{-4}$
BMI (g/cm^2)	0.27 ± 0.01	0.25 ± 0.01	0.001
Humeral length (mm)	11.1 ± 0.3	11.3 ± 0.2	NS
ML OD (mm)	1.07 ± 0.07	1.23 ± 0.04	$<10^{-5}$
ML ID (mm)	0.59 ± 0.07	0.59 ± 0.05	NS
AP OD (mm)	0.81 ± 0.05	0.93 ± 0.07	<0.001
AP ID (mm)	0.35 ± 0.04	0.48 ± 0.08	<0.001
CSA (mm^2)	0.49 ± 0.06	0.67 ± 0.05	$<10^{-5}$
I (mm^4)	0.041 ± 0.009	0.079 ± 0.011	$<10^{-6}$
Ash percentage	68.6 ± 1.0	70.2 ± 1.5	NS
Failure load (N)	7.9 ± 1.4	8.1 ± 0.9	NS
Structural stiffness (N/mm)	22 ± 7	23 ± 5	NS
Failure stress (MPa)	192 ± 36	118 ± 13	$<10^{-4}$
Young's modulus (MPa)	4800 ± 1570	2610 ± 490	0.002

BMI $=$ body mass, ML $=$ mediolateral, OD $=$ outer diameter, ID $=$ inner diameter, AP $=$ anteroposterior, I $=$ cross-sectional moment of inertia, N $=$ newtons, MPa $=$ megapascals. The Bonferroni-corrected significance level is 0.004.
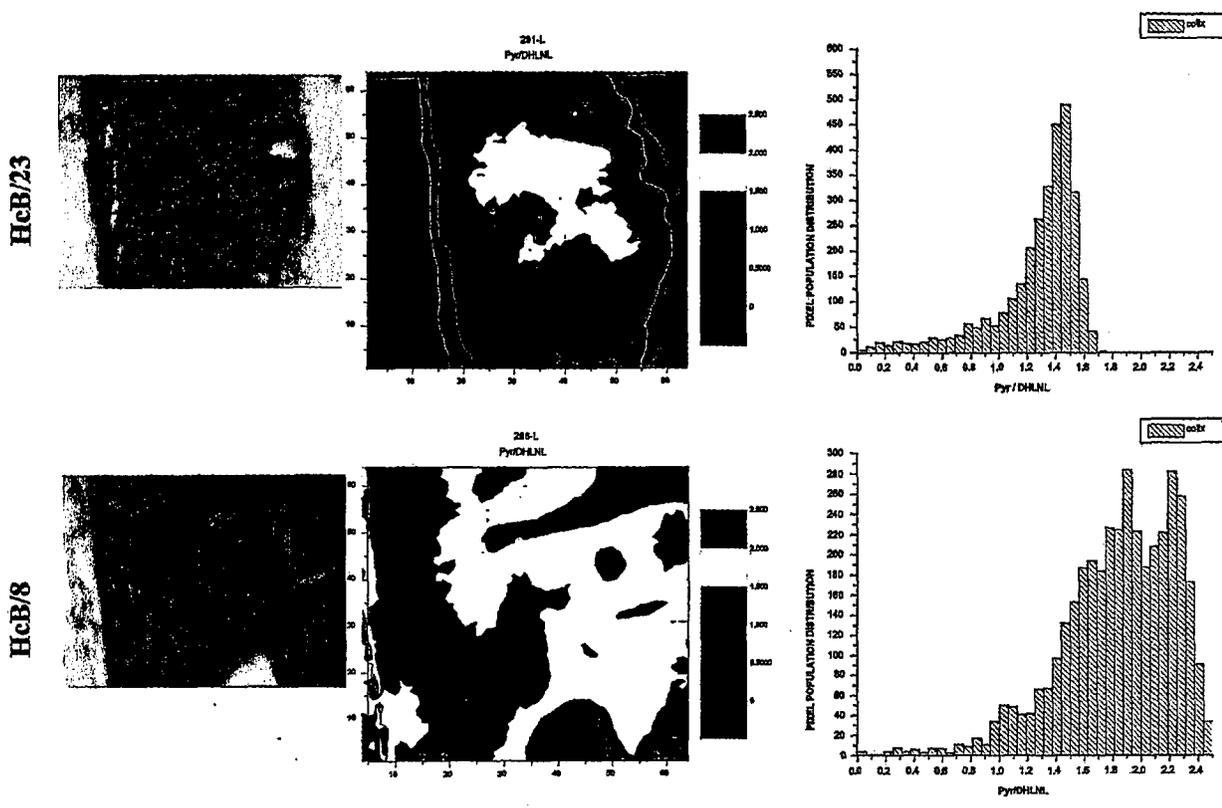
Figure 1. XLR by FTIR imaging of HcB/23 (top) and HcB/8 (bottom). Left panels show light micrographs of the specimens. Periosteal surface is to the left. The section contains the entire HcB/23 cortical thickness, but not the entire HcB/8 cortical thickness. Center panels show pseudocolor maps of XLR. Right panels show histograms of XLR for all the valid pixels.
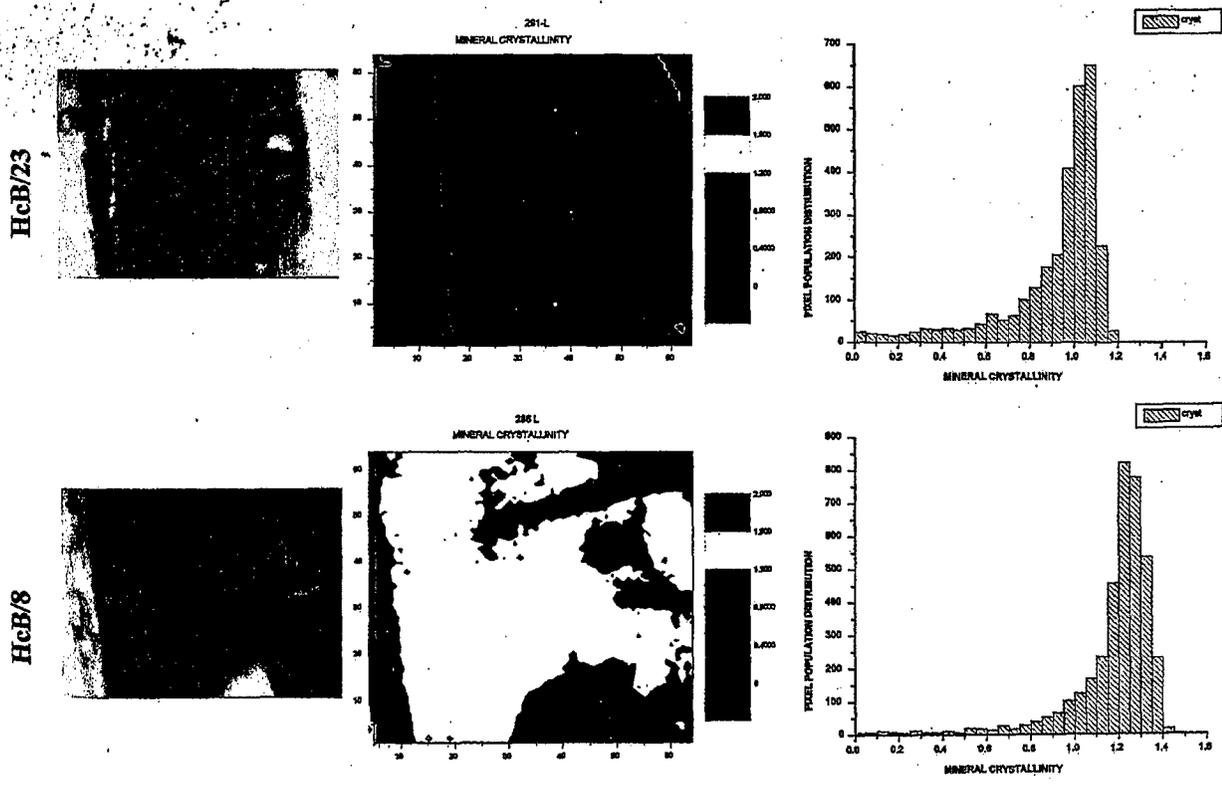
Figure 2. Crystallinity by FTIR imaging of HcB/23 (top) and HcB/8 (bottom). Left panels show light micrograhs of the specimens, taken from the same samples as Figure 1. Periosteal surface is to the left. The section contains the entire HcB/23 cortical thickness, but not the entire HcB/8 cortical thickness. Center panels show pseudocolor maps of crystallinity. Right panels show histograms of crystallinity for all the valid pixels.

[44]. Representative sections from each strain are shown in Figure 1. Overall, the difference in XLR is highly significant ($\chi^2 = 1968$, 9 degrees of freedom, $p < 10^{-15}$). The mean and median HcB/23 XLR indices are 1.27 and 1.37, respectively. For HcB/8, the mean XLR index is 1.65 and the median is 1.64. Neither of the distributions is normal, with $p < 10^{-15}$ for the Kolmogorov-Smirnov test of normality in both cases. The HcB/23 distribution is more negatively skewed than the HcB/8 distribution, with values of -1.727 and -0.185, respectively. The HcB/23 distribution has a kurtosis of 3.012 and the HcB/8 distribution has a kurtosis of 1.198. Thus, in addition to having different XLRs, the distributions are shaped differently.

Crystallinity Differs Between HcB/8 and HcB/23

The ratio of absorbances at 1030 cm^{-1} and 1020 cm^{-1} is a composite index of the mineral (apatite) crystal size and perfection, with higher ratios indicating greater mineral crystallinity. The crystallinity maps of the two strains are compared in Figure 2. As for XLR, the difference between the strains is highly significant $\chi^2 = 400$, 6 degrees of freedom, $p < 10^{-15}$). Also as for XLR, the crystallinity distributions deviate markedly from normality ($p < 10^{-15}$ in both cases). The mean and median of the crystallinity index in HcB/23 are 0.84 and 0.91, respectively. For HcB/8, the corresponding values are 0.95 and 0.97. As for the XLR distributions, the HcB/23 crystallinity distribution is more negatively skewed ($-1,408$ and -0.913) and more kurtotic (1.855 and 0.882) than the HcB/8 distribution. However, the crystallinity distributions are less dissimilar than the XLR distributions.

XLR and Crystallinity Highly Correlated

Because of the well-established relationship between the collagen and mineral components of bone's extracellular matrix, we examined the pixel-by-pixel correlation of the XLR and the crystallinity index. These properties were highly and similarly correlated in both strains, with correlation coefficients of 0.751 for HcB/8 and 0.758 for HcB/23. In both strains, the results are highly significant ($p < 10^{-16}$).

XLR and Crystallinity Correlation Lengths Similar for HcB/23 and HcB/8

The FTIR imaging data summarized above consider pixels collectively, without regard for their spatial arrangement within the cortical bone. To explore whether the similarity of closely spaced pixels differs between strains, we investigated one-dimensional spatial correlations in each of the FTIR samples. Figure 3 shows the relationship between distance parallel to the bone surface in pixels and $g(r)$, the correlation of the XLR at 2 points separated by distance r. Inspection of the figure shows that for pixel separations up to approximately 10 pixels, corresponding to a distance of 70 μm, the decay of $g(r)$ is linear. For larger r, $g(r)$ varies erratically; this is not surprising because the number of pixels summed over becomes small at large r, leading to large statistical uncertainties. Fitting $g(r)$ to the form

TABLE 2
Estimates of A, decay of correlation over distance.

	HcB/8	HcB/23
XLR	-0.027 ± 0.010	-0.029 ± 0.018
Crystallinity	-0.029 ± 0.017	-0.032 ± 0.018

XLR = 1660:1690 absorbance ratio; crystallinity = 1030:1020 absorbance ratio.

$g(r) = 1 - Ar$ for $r < 10$ yielded estimates of A as summarized in Table 2. Two-factor ANOVA showed no evidence that strain, index, or their interaction affected A.

DISCUSSION

In our initial survey of bone properties of the HcB/Dem recombinant congenic strains, we noted that HcB/8 and HcB/23 are similar with respect to failure load and ash percentage, but that HcB/23 has much inferior calculated tissue strength relative to HcB/8. While this difference is not as great as that between the parental strains C3H/DiSnA and C57BL/10ScSnA, the parental strains differ significantly in ash percentage as well [30]. These observations led us to explore the possibility that material properties amenable to investigation by FTIR imaging might provide insight into the dramatic difference in failure stress between the strains.

XLR is one such property. Following collagen synthesis and secretion, individual collagen monomers are enzymatically and nonenzymatically cross-linked in the extracellular space. In bone, the predominant covalent cross-links between type I collagen molecules are formed by condensation of hydroxylysine and, to a lesser extent, lysine residues. Initial cross-links are divalent and reducible, and then mature into the trivalent nonreducible pyridinoline, deoxy-pyridinoliene, and/or pyrrole depending on the extent of hydroxylation of the lysine residues involved [see 47 for review]. We previously showed that the 1660 cm^{-1}:1690 cm^{-1} absorbance ratio reflects the relative amounts of two of the major collagen cross-links present in bone, pyridinoline (sodium borohydrate nonreducible, trivalent) and deH-DHLNL (sodium borohydrate reducible, divalent) [44]. Since thin tissue sections were employed, ratios rather than absolute amounts were reported to minimize potential artifacts due to variations in section thickness. Cross-links are tissue- rather than collagen type-specific and confer tensile strength and viscoelasticity on bone matrix, properties that improve fracture resistance in bending [47, 48].

Apatite crystallinity is a second such property. The mineral in bone is a poorly crystalline analogue of the natural occurring geologic mineral, hydroxyapatite. In bone, the apatite is hydroxide-deficient, nonstoichiometric, and carbonate-enriched [49, 50]. Apatite crystallinity, as reflected by the 1030 cm^{-1}:1020 cm^{-1} absorbance ratio, reflects the size and perfection of the crystals [51]. The mineral component of bone matrix is poorly crystalline and highly substituted, a property that facilitates exchange of
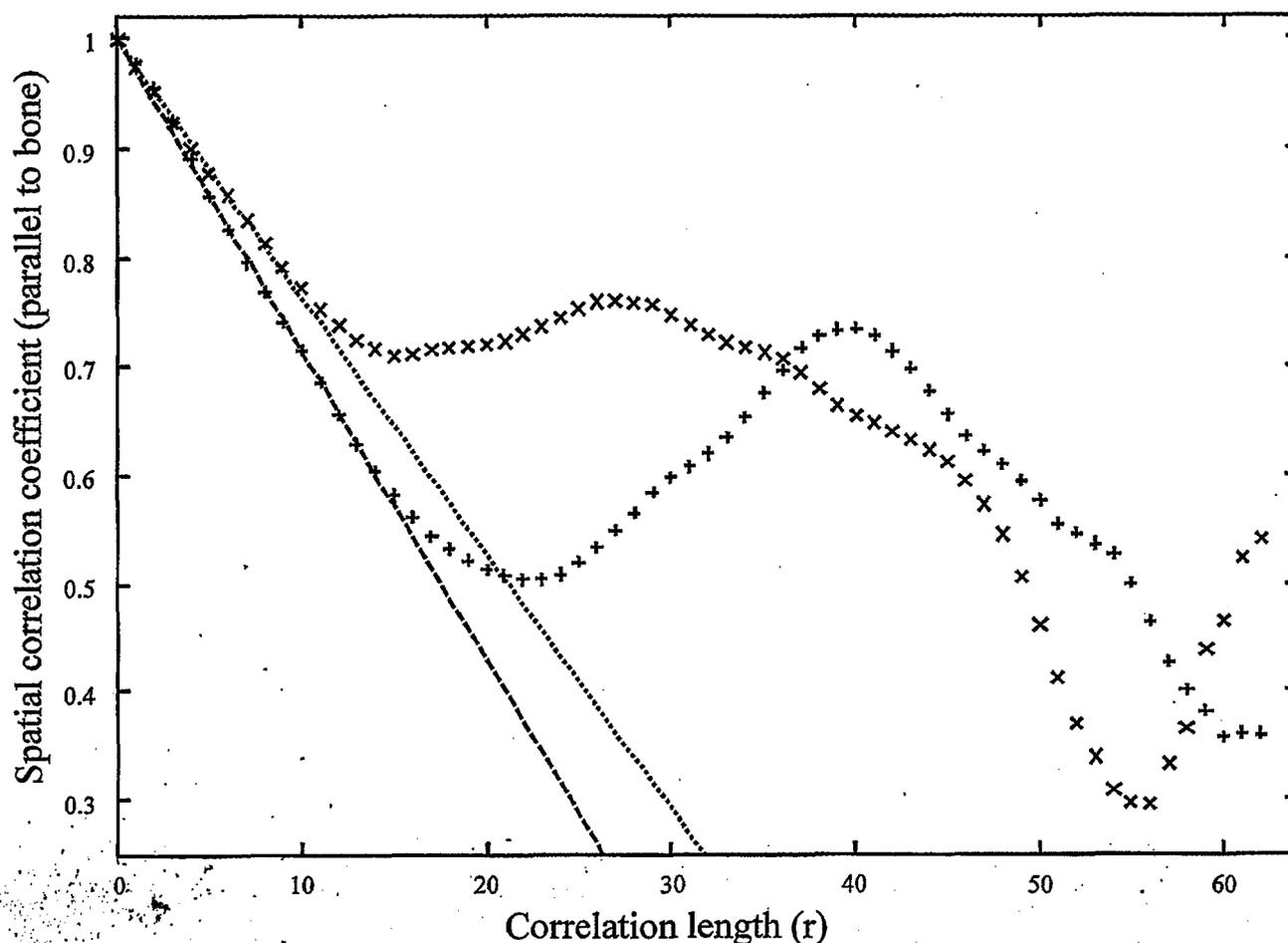
Figure 3. Two-point correlation function $g(r)$ versus separation r (in pixels) for r directed parallel to the bone surface. The graph shows one of five samples analyzed for the each strain; these results are typical. HcB/8 = + and HcB/23 = ×. The dotted lines are linear fits ($g(r) = 1-Ar$) to the initial, linear portions of the correlation functions ($r < 10$).

bone and blood calcium and phosphate levels and thus contributes to bone's metabolic function as a reservoir for calcium. Our data suggest that increased crystallinity improves mechanical performance. That distinct crystallinity optima for mechanical performance and mineral homeostasis exist is a hypothesis that warrants further study.

We report a high point-by-point correlation between XLR and crystallinity indices. It is well established that bone mineralization depends on and follows organic matrix synthesis temporally. In osteogenesis imperfecta, for example, defective type I collagen is the underlying problem, but bone mineral content generally is low as well. Studies examining degree of mineralization by either backscattered electron microscopy [52, 53] or microradiography [54, 55] demonstrate that mineralization occurs in two phases: an initial, relatively rapid initial phase followed by a subsequent slower continued mineral accretion. These earlier studies relate degree of mineralization to matrix maturation, whereas the data presented here suggest that crystallinity also is related to matrix maturation. It is tempting to speculate that these

.observations are in fact illustrations of a more general, possibly mechanistic, relationship between XLR and crystallinity.

There are important limitations to the work presented here. First, the mechanical test performed, three-point bending, measures whole bone strength, not tissue strength. Tissue modulus can be measured with comparable spatial resolution by nanoindentation. Tissue strength is calculated from the structural strength, bone dimensions measured from orthogonal plain radiographs, and a relatively crude simplifying assumption regarding the shape of the murine humeral diaphysis. These assumptions lead to important uncertainties regarding the failure stress and modulus estimates reported here. These technical limitations apply equally to the mechanical testing of both strains and should therefore not affect the magnitude of the difference between the calculated failure stress and modulus between them. Moreover, three-point bend testing is a contrived experimental fracture model and may differ mechanistically from clinical fracture. Of the whole bone tests, three-point bending offers several advantages over either four-point bending or torsion testing.

Most important is that in three-point bending the fracture occurs at a predetermined position in the bone, rather than at the bone's weakest point, wherever that may lie along the bone's length. Since bone diameters vary markedly along the bone's long axis, this eliminates an important potential source of error in calculating tissue strength. While nanoindentation theoretically allows direct measurement of tissue strength, it is difficult to perform properly, especially when working with bones as small as those used in these experiments.

The second limitation is that the FTIR imaging was restricted to single animals of each strain. While the number of individual spectra analyzed is large, interpretation must be cautious as the animals tested might not be representative of their respective strains. Third, we used tibiae for FTIR imaging, but humeri for mechanical testing. The degree to which this difference in sites affects the validity of our findings is an open question. Both the failure stress and the FTIR results reflect the cortical bone tissue, and it is generally unknown how much intersite variability exists in mammalian cortical bone. The known differences in humeral and tibial whole bone strength can be attributed to differences in their dimensions. However, more subtle differences in the tissue-level properties may exist and this study provides no insight regarding these. Fourth, we examined formalin-fixed specimens, whereas subsequent work has demonstrated that this treatment tends to increase XLR and decrease the crystallinity index relative to unfixed specimens [56]. As for the technical limitations of the mechanical testing, this constraint should not affect the difference between the strains.

These limitations notwithstanding, the data presented here provide evidence that differences in XLR and crystallinity reflect differences in biomechanical performance not only in the presence of significant pathology [57–60], but also among strains of wild-type mice. Turner and colleagues [29] also found evidence suggesting marked differences in tissue strength among the BXH recombinant inbred strains but have not yet provided a mechanistic hypothesis regarding the origin of these differences. A fuller understanding of the role of these and other non bone mineral content components of bone tissue strength will no doubt help explain the apparent disparities between fracture reduction and changes in bone mineral content in human clinical trials as well.

ACKNOWLEDGMENTS

REFERENCES

[1] Paganini-Hill, A., Chao, A., Ross, R.K., and Henderson, B.E. (1991). Exercise and other factors in the prevention of hip fracture: The Leisure World study. *Epidemiology* 2(1):16–25.

[2] Graafmans, W.C., Ooms, M.E., Bezemer, P.D., Bouter, L.M., and Lips, P. (1996). Different risk profiles for hip fractures and distal forearm fractures: A prospective study. *Osteoporos. Int.* 6(6):427–431.

[3] Ross, P.D., Davis, J.W., Epstein, R.S., and Wasnich, R.D. (1991). Preexisting fractures and bone mass predict vertebral fracture incidence in women. *Ann. Intern. Med.* 114(11):919–923.

[4] Kotowicz, M.A., Melton, L.J., 3rd, Cooper, C., Atkinson, E.J., WM, O.F., and Riggs, B.L. (1994). Risk of hip fracture in women with vertebral fracture. *J. Bone Miner. Res.* 9(5):599–605.

[5] Wasnich, R.D., Davis, J.W., and Ross, P.D. (1994). Spine fracture risk is predicted by non-spine fractures. *Osteo. Int.* 4(1):1–5.

[6] Cummings, S.R., Nevitt, M.C., Browner, W.S., Stone, K., Fox, K.M., Ensrud, K.E., Cauley, J., Black, D., and Vogt, T.M. (1995). Risk factors for hip fracture in white women. Study of Osteoporotic Fractures Research Group. *N. Engl. J. Med.* 332(12):767–773.

[7] Hayes, W. (1986). *Basic Biomechanics of the Skeleton: Current Concepts of Bone Fragility.* Heidelberg: Springer-Verlag, pp. 3–18.

[8] Turner, C.H., and Burr, D.B. (1993). Basic biomechanical measurements of bone: A tutorial. *Bone* 14(4):595–608.

[9] Faulkner, K.G., Cummings, S.R., Black, D., Palermo, L., Gluer, C.C., and Genant, H.K. (1993). Simple measurement of femoral geometry predicts hip fracture: The study of osteoporotic fractures. *J. Bone Miner. Res.* 8(10):1211–1217.

[10] Cummings, S.R., Cauley, J.A., Palermo, L., Ross, P.D., Wasnich, R.D., Black, D., and Faulkner, K.G. (1994). Racial differences in hip axis lengths might explain racial differences in rates of hip fracture. Study of Osteoporotic Fractures Research Group. *Osteoporos. Int.* 4(4):226–229.

[11] Gluer, C.C., Cummings, S.R., Pressman, A., Li, J., Gluer, K., Faulkner, K.G., Grampp, S., and Genant, H.K. (1994). Prediction of hip fractures from pelvic radiographs: The study of osteoporotic fractures. Study of Osteoporotic Fractures Research Group. *J. Bone Miner. Res.* 9(5):671–677.

[12] Nakamura, T., Turner, C.H., Yoshikawa, T., Slemenda, C.W., Peacock, M., Burr, D.B., Mizuno, Y., Orimo, H., Ouchi, Y., and Johnston, C.J. (1994). Do variations in hip geometry explain differences in hip fracture risk between Japanese and white Americans? *J. Bone Miner. Res.* 9(7):1071–1076.

[13] Boonen, S., Koutri, R., Dequeker, J., Aerssens, J., Lowet, G., Nijs, J., Verbeke, G., Lesaffre, E., and Geusens, P. (1995). Measurement of femoral geometry in type I and type II osteoporosis: Differences in hip axis length consistent with heterogeneity in the pathogenesis of osteoporotic fractures. *J. Bone Miner. Res.* 10(12):1908–1912.

[14] Mikhail, M.B., Vaswani, A.N., and Aloia, J.F. (1996). Racial differences in femoral dimensions and their relation to hip fracture. *Osteoporos. Int.* 6(1):22–24.

[15] Karlsson, K.M., Sembo, I., Obrant, K.J., Redlund-Johnell, I., and Johnell, O. (1996). Femoral neck geometry and radiographic signs of osteoporosis as predictors of hip fracture. *Bone* 18(4):327–330.

[16] Bell, K.L., Loveridge, N., Power, J., Garrahan, N., Stanton, M., Lunt, M., Meggitt, B.F., and Reeve, J. (1999). Structure of the femoral neck in hip fracture: Cortical bone loss in the inferoanterior to superoposterior axis. *J. Bone Miner. Res.* 14(1):111–119.

[17] Bell, K.L., Loveridge, N., Power, J., Garrahan, N., Meggitt, B.F., and Reeve, J. (1999). Regional differences in cortical porosity in the fractured femoral neck. *Bone* 24(1):57–64.

[18] Beck, T.J., Oreskovic, T.L., Stone, K.L., Ruff, C.B., Ensrud, K., Nevitt, M.C., Genant, H.K., and Cummings, S.R. (2001). Structural adaptation to changing skeletal load in the progression toward hip fragility: The study of osteoporotic fractures. *J. Bone Miner. Res.* 16(6):1108–1119.

[19] Beck, T.J., Ruff, C.B., Scott, W.W., Jr., Plato, C.C., Tobin, J.D., and Quan, C.A. (1992). Sex differences in geometry of the femoral neck with aging: A structural analysis of bone mineral data. *Calcif. Tissue Int.* 50(1):24–29.

[20] Beck, T.J., Ruff, C.B., and Bissessur, K. (1993). Age-related changes in female femoral neck geometry: Implications for bone strength. *Calcif. Tissue Int.* 53(suppl 1):S41–S46.

[21] Bass, S., Delmas, P.D., Pearce, G., Hendrich, E., Tabensky, A., and Seeman, E. (1999). The differing tempo of growth in bone size, mass, and density in girls is region-specific. *J. Clin. Invest.* 104(6):795–804.

[22] Duan, Y., Turner, C.H., Kim, B.T., and Seeman, E. (2001). Sexual dimorphism in vertebral fragility is more the result of gender differences in age-related bone gain than bone loss. *J. Bone Miner. Res.* 16(12):2267–2275.

[23] Majumdar, S., Kothari, M., Augat, P., Newitt, D.C., Link, T.M., Lin, J.C., Lang, T., Lu, Y., and Genant H.K. (1998). High-resolution magnetic resonance imaging: Three-dimensional trabecular bone architecture and biomechanical properties. *Bone* 22(5):445–454.

[24] Kabel, J., Odgaard, A., van Rietbergen, B., and Huiskes, R. (1999). Connectivity and the elastic properties of cancellous bone. *Bone* 24(2):115–120.

[25] Uchiyama, T., Tanizawa, T., Muramatsu, H., Endo, N., Takahashi, H.E., and Hara, T. (1999). Three-dimensional microstructural analysis of human trabecular bone in relation to its mechanical properties. *Bone* 25(4):487–491.

[26] Chappard, D., Legrand, E., Haettich, B., Chales, G., Auvinet, B., Eschard, J.P., Hamelin, J.P., Basle, M.F., and Audran, M. (2001). Fractal dimension of trabecular bone: Comparison of three histomorphometric computed techniques for measuring the architectural two-dimensional complexity. *J. Pathol.* 195(4):515–521.

[27] Akhter, M.P., Iwaniec, U.T., Covey, M.A., Cullen, D.M., Kimmel, D.B., and Recker, R.R. (2000). Genetic variations in bone density, histomorphometry, and strength in mice. *Calcif. Tissue Int.* 67(4):337–344.

[28] Jepsen, K.J., Pennington, D.E., Lee, Y.L., Warman, M., and Nadeau, J. (2001). Bone brittleness varies with genetic background in A/J and C57BL/6J inbred mice. *J. Bone Miner. Res.* 16(10):1854–1862.

[29] Turner, C.H., Hsieh, Y.F., Muller, R., Bouxsein, M.L., Rosen, C.J., McCrann, M.E., Donahue, L.R., and Beamer, W.G. (2001). Variation in bone biomechanical properties, microstructure, and density in BXH recombinant inbred mice. *J. Bone Miner. Res.* 16(2):206–213.

[30] Yershov, Y., Baldini, T.H., Villagomez, S., Young, T., Martin, M.L., Bockman, R.S., Peterson, M.G., and Blank, R.D. (2001). Bone strength and related traits in HcB/Dem recombinant congenic mice. *J. Bone Miner. Res.* 16(6):992–1003.

[31] Marcott, C., Reeder, R.C., Paschalis, E.P., Tatakis, D.N., Boskey, A.L., and Mendelsohn, R. (1998). Infrared microspectroscopic imaging of biomineralized tissues using a mercury-cadmium-telluride focal-plane array detector. *Cell Mol. Biol. (Noisy-le-grand)* 44(1):109–115.

[32] Mendelsohn, R., Paschalis, E.P., and Boskey, A.L. (1999). Infrared spectroscopy, microscopy, and microscopic imaging of mineralizing tissues. Spectra-structure correlations from human iliac crest biopsies. *Biomed. Optics* 4(1):14–21.

[33] Demant, P., and Hart, A.A. (1986). Recombinant congenic strains—a new tool for analyzing genetic traits determined by more than one gene. *Immunogenetics* 24(6):416–422.

[34] Moen, C.J., van der Valk, M.A., Snoek, M., van Zutphen, B.F., von Deimling, O., Hart, A.A., and Demant, P. (1991). The recombinant congenic strains—a novel genetic tool applied to the study of colon tumor development in the mouse. *Mamm. Genome* 1(4):217–227.

[35] Van Zutphen, L.F., Den Bieman, M., Lankhorst, A., and Demant, P. (1991). Segregation of genes from donor strain during the production of recombinant congenic strains. *Lab. Anim.* 25(3):193–197.

[36] Groot, P.C., Moen, C.J., Dietrich, W., Stoye, J.P., Lander, E.S., and Demant, P. (1992). The recombinant congenic strains for analysis of multigenic traits: Genetic composition. *FASEB. J.* 6(10):2826–2835.

[37] Stassen, A.P., Groot, P.C., Eppig, J.T., and Demant, P. (1996). Genetic composition of the recombinant congenic strains. *Mamm. Genome.* 7(1):55–58.

[38] Taylor, B.A. (1978). Recombinant inbred strains: Use in gene mapping. In Morse H.C. (ed.), *Origins of Inbred Mice.* New York: Academic Press, pp. 423–438.

[39] Bailey, D.W. (1981). Recombinant inbred strains and bilineal congenic strains. In Foster H.L., Small J.D., and Fox J.G. (eds.), *The Mouse in Biomedical Research.* New York: Academic Press, pp. 223–239.

[40] Donnelly, R., Bockman, R., Di Carlo, E., Betts, F., and Boskey, A. (1993). The effect of gallium nitrate on healing of vitamin D- and phosphate-deficient rickets in the immature rat. *Calcif. Tissue Int.* 53(6):400–410.

[41] Camacho, N.P., Rimanc, C.M., Meyer, R.A.J., Doty, S., and Boskey, A.L. (1995). Effect of abnormal minerlization on the mechanical behavior of X-linked hypophosphatemic mice femora. *Bone* 17(3):271–278.

[42] Simske, S.J., Luttges, M.W., and Wachtel, H. (1990). Age dependent development of osteopenia in the long bones of tail-suspended mice. *ISA* (90)014:87–94.

[43] Ferretti, J.L., Spiaggi, E.P., Capozza, R., Cointry, G., and Zanchetta, J.R. (1992). Interrelationships between geometric and mechanical properties of long bones from three rodent species with very different biomass: Phylognetic implications. *J. Bone Miner. Res.* 7(S2):S433–S435.

[44] Paschalis, E.P., Verdelis, K., Doty, S.B., Boskey, A.L., Mendelsohn, R., and Yamauchi, M. (2001) Spectroscopic characterization of collagen cross-links in bone. *J. Bone Miner. Res.* 16(10):1821–1828.

[45] Paschalis, E.P., DiCarlo, E., Betts, F., Sherman, P., Mendelsohn, R., and Boskey, A.L. (1996). FTIR microspectroscopic analysis of human osteonal bone. *Calcif. Tissue Int.* 59(6):480–487.

[46] Reichl, L.E. (1998). *A Modern Course in Statistical Physics,* 2nd ed. New York: John Wiley & Sons, Section 4.D.4, p. 184.

[47] Knott, L., and Bailey, A.J. (1998). Collagen cross-links in mineralizing tissues: A review of their chemistry, function, and clinical relevance. *Bone* 22(3):181–187.

[48] Knott, L., and Bailey, A.J. (1999). Collagen biochemistry of avian bone: Comparison of bone type and skeletal site. *Br. Poult. Sci.* 40(3):371–379.

[49] Rey, C., Renugopalakrishanan, V., Collins, B., and Glimcher, M.J. (1991). Fourier transform infrared spectroscopic study of the carbonate ions in bone mineral during aging. *Calcif. Tissue Int.* 49(4):251–258.

[50] Rey, C., Miquel, J.L., Facchini, L., Legrand, A.P., and Glimcher, M.J. (1995). Hydroxyl groups in bone mineral. *Bone* 16(5):583–586.

[51] Gadaleta, S.J., Paschalis, E.P., Betts, F., Mendelsohn, R., and Boskey, A.L. (1996). Fourier transform infrared spectroscopy of the solution-mediated conversion of amorphous calcium phosphate to hydroxyapatite: New correlations between X-ray diffraction and infrared data. *Calcif. Tissue Int.* 58(1):9–116.

[52] Boyde, A., Elliott, J.C., and Jones, S.J. (1993). Stereology and histogram analysis of backscattered electron images: Age changes in bone. *Bone* 14(3):205–210.

[53] Boyde, A., Jones, S.J., Aerssens, J., and Dequeker, J. (1995). Mineral density quantitation of the human cortical iliac crest by backscattered electron image analysis: Variations with age, sex, and degree of osteoarthritis. *Bone* 16(6):619–627.

[54] Meunier, P.J., and Boivin, G. (1997). Bone mineral density reflects bone mass but also the degree of mineralization of bone: Therapeutic implications. *Bone* 21(5):373–377.

[55] Boivin, G.Y., Chavassieux, P.M., Santora, A.C., Yates, J., and Meunier, P.J. (2000). Alendronate increases bone strength by increasing the mean degree

of mineralization of bone tissue in osteoporotic women. *Bone* 27(5):687–694.

[56] Aparicio, S., Doty, S.B., Camacho, N.P., Paschalis, E.P., Spevak, L., Mendelsohn, R., and Boskey, A.L. (2002). Optimal methods for processing mineralized tissues for Fourier transform infrared microspectroscopy. *Calcif. Tissue Int.* 70(5):422–429.

[57] Cassella, J.P., Pereira, R., Khillan, J.S., Prockop, D.J., Garrington, N., and Ali, S.Y. (1994). An ultrastructural, microanalytical, and spectroscopic study of bone from a transgenic mouse with a COL1.A1 pro-alpha-1 mutation. *Bone* 15(6):611–619.

[58] Landis, W.J. (1995). The strength of a calcified tissue depends in part on the molecular structure and organization of its constituent mineral crystals in their organic matrix. *Bone* 16(5):533–544.

[59] Masse, P.G., Rimnac, C.M., Yamauchi, M., Coburn, S.P., Rucker, R.B., Howell, D.S., and Boskey, A.L. (1996). Pyridoxine deficiency affects biomechanical properties of chick tibial bone. *Bone* 18(6):567–574.

[60] Camacho, N.P., Hou, L., Toledano, T.R., Ilg, W.A., Brayton, C.F., Raggio, C.L., Root, L., and Boskey, A.L. (1999). The material basis for reduced mechanical properties in oim mice bones. *J. Bone Miner. Res.* 14(2):264–272.

Journal of
Clinical
Densitometry

APPENDIX 6

ISCD
THE INTERNATIONAL SOCIETY
FOR CLINICAL DENSITOMETRY

The Official Journal of
**The International Society for
Clinical Densitometry**

Editor-in-Chief
Paul D. Miller, MD
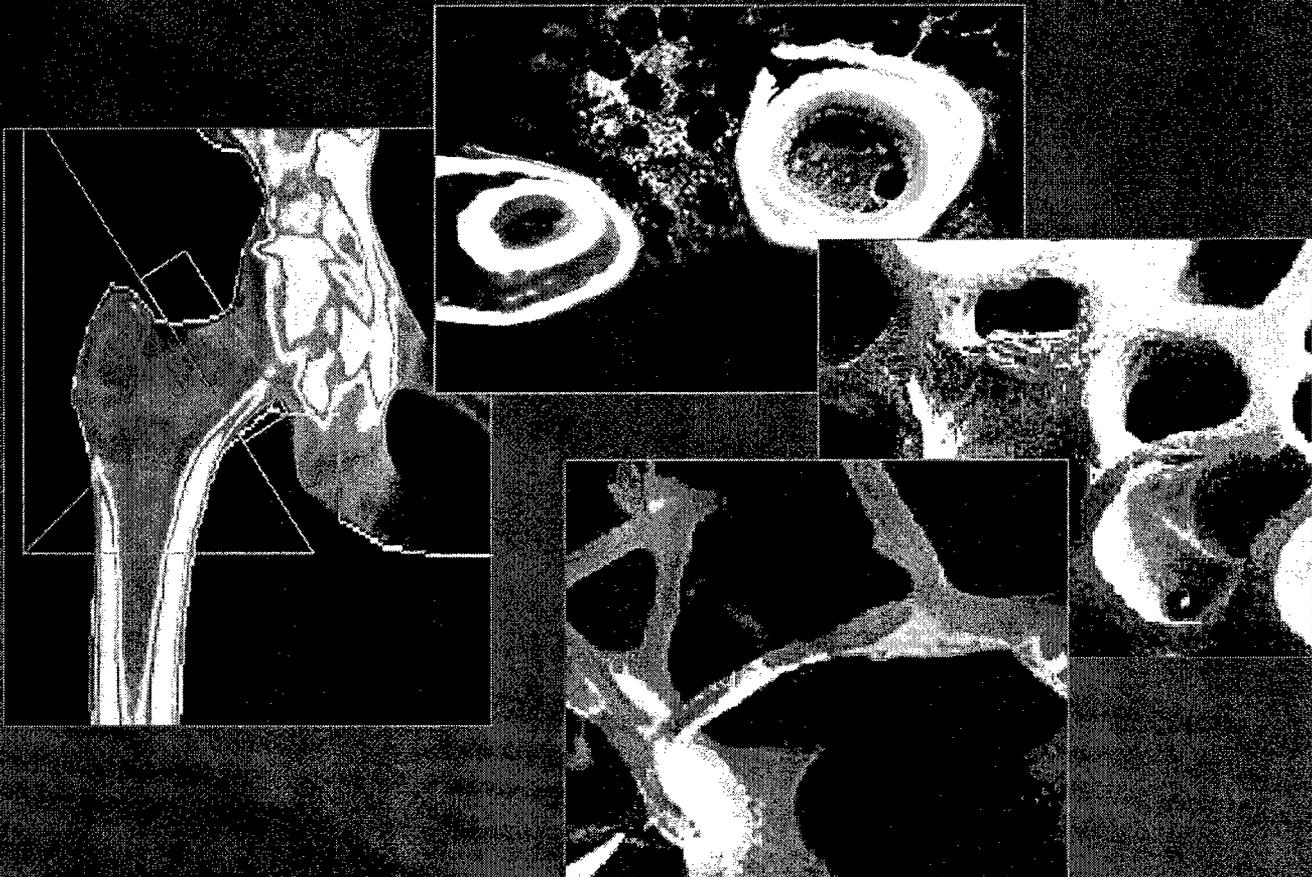
HUMANA PRESS

Original Article

Accuracy and Precision of PIXImus Densitometry for Ex Vivo Mouse Long Bones

Comparison of Technique and Software Version

Gloria E. Lopez Franco, DDS,[1] Tyriina K. O'Neil,[1] Suzanne J. Litscher, BS,[1] Michael Urban-Piette, MBA,[1] and Robert D. Blank, MD, PhD*,[1,2]

[1]*Section of Endocrinology, Department of Medicine, University of Wisconsin Medical School, Madison, WI 53792-5148 and [2]Geriatrics Research, Education, and Clinical Center, William S. Middleton Veterans' Hospital, Madison, WI 53705*

Abstract

Many densitometric studies in mice assess bone mineral density (BMD) at specified regions of interest, often using ex vivo specimens. In the present study, we sought to determine the precision and accuracy of ex vivo densitometry of mouse bones, comparing two software versions and two data acquisition techniques. The newer software allows manual adjustment of the threshold value for bone, improving the ability to analyze bone edges correctly. Root mean square standard deviations were 2–3 mg/cm^2, with coefficients of variation ranging between 3% and 5% for femora and humeri and between 6% and 7% for radii. The regression coefficients for bone mineral content as a function of ash mass were near 1 for femora and humeri, but considerably lower for radii. Coefficients of determination were inversely related to bone size, with R^2 values exceeding 0.9 at the femur, 0.8 at the humerus, and ranging between 0.3 and 0.6 at the radius. We found that our instrument has a position artifact, with BMD and bone mineral content dependent on the specimen's coordinates in the scanned field. Our findings establish the limitations of ex vivo densitometry with the PIXImus and support our recommendation that investigators seek position artifacts in their instruments.

Key Words: Bone mineral density (BMD); bone mineral content (BMC); dual energy X-ray absorptiometry (DXA); mouse; accuracy; precision.

Introduction

Dual-energy X-ray absorptiometry (DXA) is the most widely used imaging methodology to assess risk of fragility fracture. In addition to its documented ability to stratify patients for fracture risk, examination is accurate, precise, noninvasive, and entails only modest radiation exposure. Moreover, examination is feasible at the lumbar spine, hip, and wrist, corresponding to common fracture sites. These features make DXA an attractive choice for diagnosing osteoporosis, following patients to monitor effectiveness of therapy for osteoporosis, and as a surrogate end point for fracture in clinical investigation. Correspondingly, DXA has become a popular analytical technique in mice and other small animals, either as a substitute for more demanding techniques, such as biomechanical testing, histomorphometry, and gravimetry, or as an adjunct to them.

Recent progress in skeletal genetics and success in continuing efforts to develop bone pharmaceuticals have been achieved in large part through studies performed in rodents. As small-animal skeletal research continues, more detailed questions regarding differences in the behavior at specific

anatomical sites are becoming ever more prominent. Several laboratories explicitly study skeletal phenotypes at specific sites (e.g., refs. *1–5*). Interventional studies also focus on site-specific end points in small-animal models (e.g., refs. *6* and *7*). Such experiments require that site-specific data be generated and interpreted.

As in humans, site-specificity of bone mineral density (BMD) has been reported in mice *(1,3,8,9)*. One commonly used small-animal densitometer was designed primarily for determination of whole-body BMD. Although smaller regions of interest can be defined and analyzed, few normative data are available for interpreting region of interest data *(10–13)*. Moreover, the accuracy and precision of ex vivo bone densitometry has received limited attention. In order to address these gaps in our knowledge, we undertook a comparison of excised mouse femora, humeri, and radii using DXA. We compared results of femoral, humeral, and radial densitometry performed using two different scanning protocols and two versions of the analysis software, comparing densitometry to gravimetric methods.

We report that there is little difference in accuracy and precision between scans performed in air and scans performed in water. The newer software is better able to analyze the edges of radii, the smallest and least dense bones we examined. We found evidence of systematic position dependency of the densitometry data in our instrument. Our data suggest that although mouse femora and humeri can fruitfully be studied by ex vivo densitometry, data obtained from radii should be interpreted cautiously. Further, our finding of a position artifact in our instrument leads us to recommend that all investigators perform precision studies that allow such an effect to be sought.

Materials and Methods

Mice

Mice used in this study were C57BL/6J male and female retired breeders from one of several IACUC-approved protocols. Animals were housed two to five animals in a 500-cm² cage on corncob bedding, fed laboratory rodent chow 5001 (PMI Nutrition International, Richmond, IN) and tap water ad libitum, and exposed to a 12-h light/12-h dark cycle. Animals were sacrificed at various ages by CO_2 asphyxiation. Femora, humeri, and radii were dissected free of soft tissue immediately following sacrifice, wrapped in phosphate-buffered saline-saturated gauze, and stored at –70°C until analysis. One radius was broken during dissection and was not available for study.

DXA Scanning

Dissected bones were scanned by DXA using the PIXImus (GE Lunar, Madison, WI) densitometer using software version 1.45.023. Analysis was performed using either software version 1.45.023 (hereafter shortened to 1.45) or software version 2.10.013 (hereafter shortened to 2.10). We scanned a manufacturer-provided phantom daily during data collection to con-

firm the instrument's calibration. Bones were allowed to equilibrate to room temperature prior to scanning. For air scanning, bones from two mice were positioned manually in air on a Plexiglas platform provided by the instrument manufacturer to achieve similar orientations for right and left bones. For water scanning, bones from two mice were positioned manually in a 2-mm-thick polyethylene dish under 6 mm of water, and the dish was placed on top of the Plexiglas platform. Both air and water scans were repeated after rotating the platform 180°. All scans included a pair of wires placed at one corner. Acquisition time per scan was approx 5 min. We manually adjusted regions of interest to analyze each of the bones individually. Software version 1.45 did not allow adjustment of thresholds, so we excluded any bones with edges that were incorrectly identified by that software version.

Gravimetric Methods

Individual bone volumes were calculated according to Archimedes' principle following immersion in water using a Mettler Toledo AE240 balance and a Mettler Toledo 33360 density measurement kit. Bones were heated overnight at 105°C to determine dry mass. Bones were then incinerated at 600°C and ash mass determined. (Ash percentage = ash mass/dry mass and volumetric bone mineral density [vBMD] = ash mass/bone volume.)

Statistics

Precision of DXA bone mineral density (BMD) was calculated using Microsoft Excel and the International Society for Clinical Densitometry's precision calculation tool (www.iscd.org/links/calc.cfm), considering each bone as a "patient." Both root mean square standard deviation and percent coefficient of variation (%CV) are reported. Additional statistical calculations were performed using SigmaStat for Windows, version 2.03 (SPSS, Chicago, IL). The significance level was $p < 0.05$ and adjusted by Bonferroni's correction to account for multiple comparisons. Data are reported as mean ± standard deviation unless noted otherwise. We constructed Bland–Altman plots *(14)* for each bone and each densitometry technique.

Results

Software Version 2.10. Improves Ability to Analyze the Edges of Small Bones

We performed duplicate densitometry scans of ex vivo mouse bones, scanning the femora, humeri, and radii of 20 animals. Scans were performed in air and in water to compare these techniques for accuracy and precision, with the specimens rotated 180° as a group between scans. Scans were performed using software version 1.45 but were analyzed using both software versions. Version 1.45 does not allow the user to adjust the threshold value, whereas version 2.10 allows this to be altered from the default value of 1306. Using version 1.45 or the default threshold in version 2.10, 7/39 radii studied were misanalyzed on one or both scans (Fig. 1A). Adjusting the threshold to 1292 corrected analysis of the
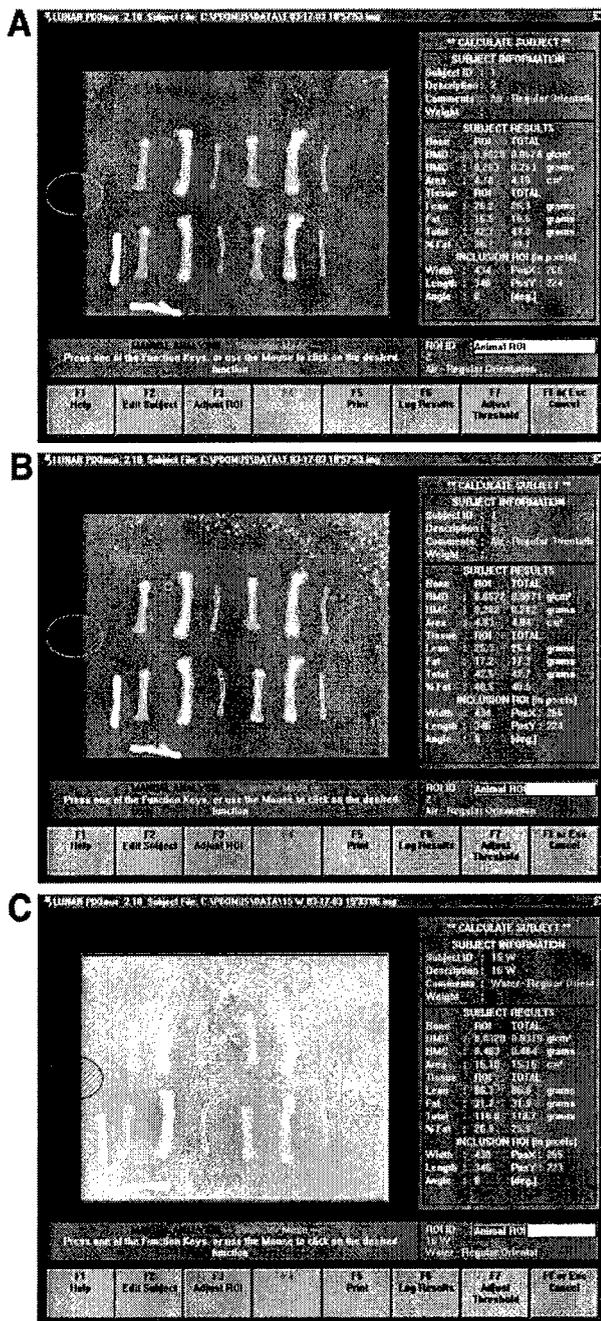
Fig. 1. Effects of threshold adjustment. **(A)** shows that edges of a radius (bottom row, middle of field) are misanalyzed at the default threshold of 1306. In **(B)**, the threshold of the same scan has been readjusted to allow the bone edges to be analyzed correctly. In **(C)**, another scan is shown, demonstrating the high background that occasionally results from threshold adjustment. The same adjusted threshold value of 1292 was used in **(B)** and **(C)**. Each scan includes a pair of wires in the lower left corner used for orienting scans. Color image available for viewing at www.humanapress. com.

Table 1
Precision by Bone, Software, and Technique

	Femur	Humerus	Radius
1.45, air			
	0.003	0.002	Undefined
	4.36%	4.13%	
1.45, water			
	0.002	0.002	Undefined
	3.54%	4.50%	
2.10, air			
	0.003	0.002	0.002
	4.30%	3.69%	6.77%
2.10, water			
	0.002	0.002	0.002
	3.39%	3.72%	6.05%

Note: Precision is shown as the root mean square standard deviation (in g/cm^2) on the first line of each cell and as %CV on the second line.

radial edges (Fig. 1B) in all but two cases, but at the cost of increasing nonspecific background (Fig. 1C). The increased background precluded analysis of one pair of water scans because suitable regions of interest could not be defined. Further analyses with software version 2.10 were performed following threshold adjustment to 1292.

Accuracy, But Not Precision, Depends on Bone Size

We performed paired scans of excised bones in air and submerged under 6 mm of distilled water. The scans were analyzed using each software version, with version 2.10 analysis following adjustment of the threshold to 1292. The results are summarized in Table 1. Because of edge analysis errors, an insufficient number of radii were analyzable with version 1.45 to allow precision to be estimated. Precision expressed as grams per square centimeter is comparable at all three sites, but the differences in bone size lead to precision expressed as %CV to be comparable at the femur and humerus, but to be larger at the radius.

To determine accuracy, we regressed the average bone mineral content (BMC) for the paired scans obtained by each technique on ash mass. These analyses are summarized in Table 2 and Fig. 2. The data demonstrate very clearly that DXA BMC is most accurate at the femur and least accurate at the radius, with coefficients of determination greater than 0.9 regardless of technique at the former site and coefficients of determination ranging from 0.32 to 0.52 at the latter site. The regression was highly significant in every case, $p < 10^{-5}$ for all of the regressions except that of radii using water scanning and software version 2.10, for which $p = 4.6 \times 10^{-4}$. In addition, although the coefficients of the regression equation are close to the ideal of unity at both the femur and humerus regardless of technique, the coefficient for the radial BMC equation is approx 0.65, suggesting that each additional milligram of ash

Table 2
Ash Mass–BMC Regressions

Site	Technique	Coefficient	Intercept	R^2
Femur	1.45, air	1.11	–0.00013	0.95
	1.45, water	0.998	0.00130	0.92
	2.10, air	1.08	0.00151	0.96
	2.10, water	1.06	0.00099	0.97
Humerus	1.45, air	1.06	–0.00054	0.83
	1.45, water	0.946	0.00700	0.80
	2.10, air	0.997	0.00069	0.89
	2.10, water	1.02	0.00013	0.91
Radius	1.45, air	0.67	0.00058	0.52
	1.45, water	0.64	0.00046	0.52
	2.10, air	0.64	0.00086	0.52
	2.10, water	0.59	0.00116	0.32

content results in only 0.65 additional milligrams of BMC as measured by the PIXImus instrument.

Bland–Altman analysis allows straightforward recognition of the pattern of differences between ash mass and BMC analyses. This graphical method plots the difference between BMC and ash mass on the y-axis and the average of BMC and ash mass on the x-axis. Significant correlation between these demonstrates a systematic relationship between mineral content and the measurement discrepancy between the two methods. Bland–Altman plots for the femora obtained by each technique are shown in Fig. 3 and data for all three sites are summarized in Table 3. Three of the four techniques yielded significant positive correlations, whereas no significant correlations were found at either the humerus or radius by any of the techniques.

Position Artifacts Have a Small But Significant Impact on Ex Vivo DXA Data

We scanned multiple bones at once, so bones were not positioned precisely at the center of the X-ray cone beam. The analysis software records the coordinates of each region of interest, allowing us to seek a relationship between specimen position and the DXA data. We did this by performing stepwise linear regression analyses in which the BMD was modeled as a function of ash mass, bone volume, specimen x coordinate, and specimen y coordinate, using data from the femora and humeri. We excluded the radii from this analysis

Fig. 2. Regression of BMC on ash mass using air scanning and software version 1.45. (A–C) show the results for femora, humeri, and radii, respectively. Note the widening of the confidence intervals as bone size decreases. *See* Table 2 for statistics related to this figure.
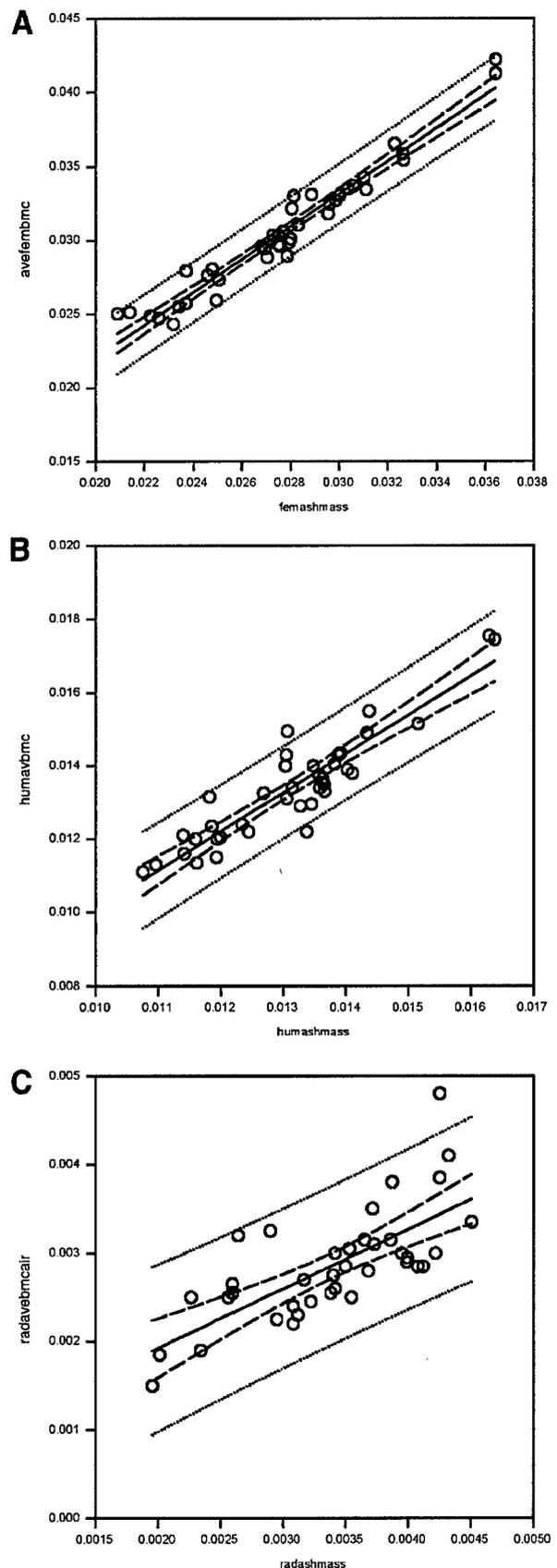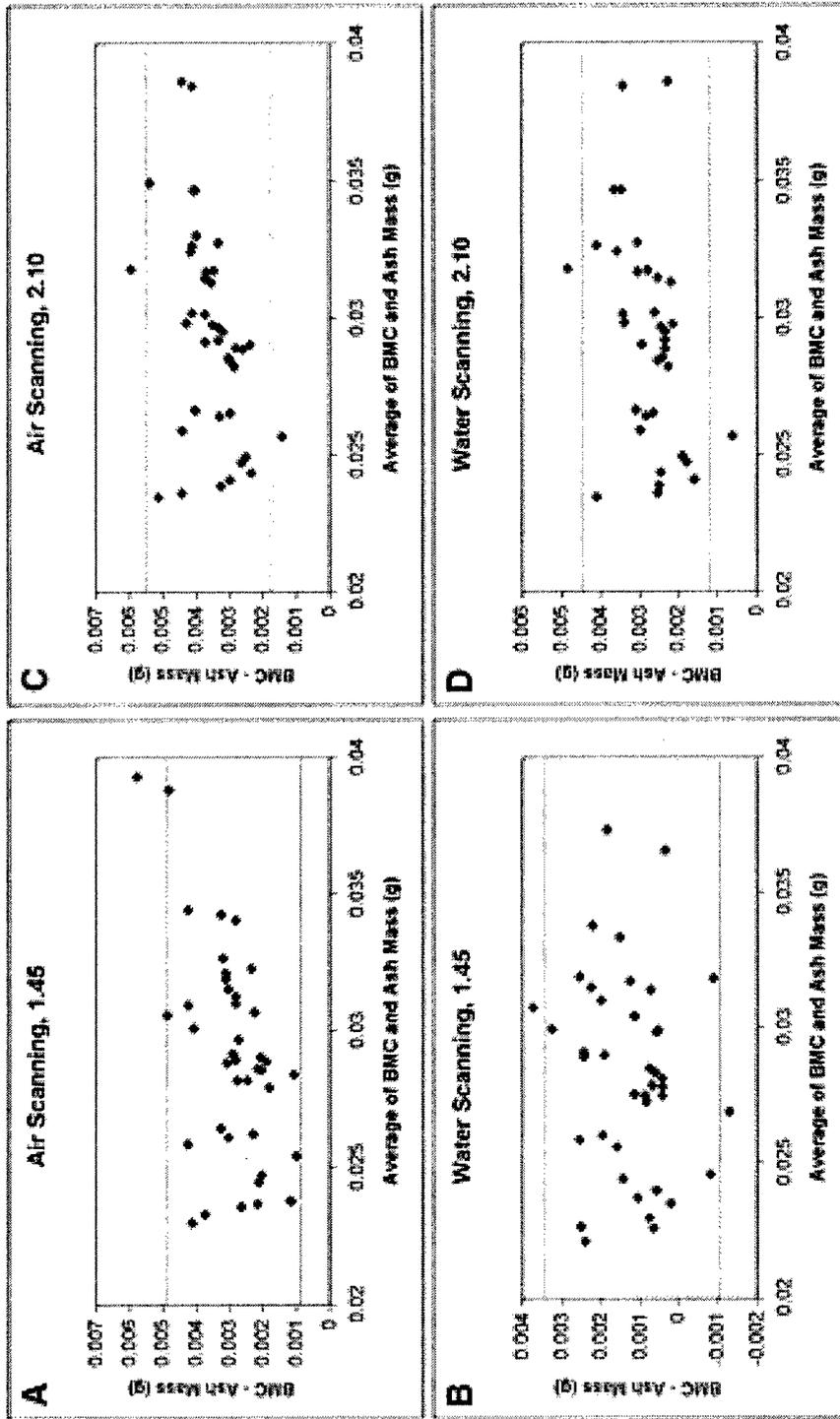
Fig. 3. Bland–Altman plots of femora. The average of ash mass and BMC is plotted on the *x*-axis and the difference between ash mass and BMC on the *y*-axis. The dotted lines show the 2-SD confidence interval of the average difference between BMC and ash mass. (A) and (B) show analysis with software version 2.10. (A) and (C) show air scanning and (B) and (D) show analysis with software version 1.45 and (C) and (D) show water scanning.

Table 3
Summary of Bland–Altman Analyses

Site	Technique	Average (BMC – Ash Mass) ± SD (mg)	R
Femur	1.45, air	2.9 ± 1.0	0.50**
	1.45, water	1.2 ± 1.1	—
	2.10, air	3.6 ± 0.9	0.42**
	2.10, water	2.8 ± 0.8	0.40*
Humerus	1.45, air	0.3 ± 0.6	—
	1.45, water	−0.6 ± 0.6	—
	2.10, air	0.7 ± 0.4	—
	2.10, water	0.4 ± 0.4	—
Radius	1.45, air	−0.5 ± 0.5	—
	1.45, water	−0.8 ± 0.5	—
	2.10, air	0.4 ± 0.5	—
	2.10, water	−0.2 ± 0.6	—

Note: $* p < 0.05$; $** p < 0.01$

Table 4
Stepwise Regression Model Parameters

Technique	a	b	c	d
1.45, air	0.0279	0.985	0.0000145	0.0000064
		0.920	0.027	0.003
1.45, water	0.0283	0.973	0.0000105	NS
		0.916	0.014	
2.10, air	0.0286	0.980	0.0000137	0.0000065
		0.926	0.025	0.003
2.10, water	0.0292	0.960	0.0000091	NS
		0.923	0.011	

Note: Coefficients are given on the top line of each cell; ΔR^2 is given on the second line. $p < 10^{-5}$ for the coefficients b and c. The d coefficient is only significant with air scanning, with $p = 6 \times 10^{-3}$ for software version 1.45 and $p = 3 \times 10^{-3}$ for software version 2.10.

because the accuracy and precision of DXA at this radius are much poorer than at the femur and humerus. Both addition and subtraction of variables included raw x and y coordinates as significant variables when scanning was performed in air, with slight differences in the regression equation depending on software version. Water scans demonstrated a significant effect of the x coordinate, but not the y coordinate, with the same models generated by addition and subtraction. The regression model parameters are summarized in Table 4 and the model equations are all of the form

$$BMD = a + b \text{ (ash mass)} + c \text{ (}x \text{ coordinate)} + d \text{ (}y \text{ coordinate)}$$

with the coordinates given in pixels. The ΔR^2 ranged between 0.011 and 0.027 for the x coordinate and between 0 and 0.003 for the y coordinate. Regression models for air scanning had slightly greater explanatory power than did those for water scanning, but the magnitude of the position artifact was slightly greater in air than in water.

Discussion

In rodent experiments, DXA scanning serves a variety of related functions. One such is to use BMD or BMC as a surrogate measurement for more technically demanding methods such as gravimetry. Another is to evaluate an explanatory factor when biomechanical testing is performed. A third is to assess longitudinal changes in a single animal. Each of these applications requires understanding of both the performance characteristics of DXA scanning and the underlying biology of the effects being sought.

We therefore performed DXA examinations of ex vivo long bones in air or water. We then used two software releases to analyze the scans. Our analyses led to the following four conclusions. First, software version 2.10 is superior to version 1.45 insofar as it allows the user to adjust the bone/soft tissue threshold. Second, there are only minimal differences in precision and accuracy between scans performed in air and scans performed in water. Third, there is an inverse relationship between bone size and DXA performance. Fourth, our instrument has a small but significant position artifact, with the BMD varying systematically according to a specimen's placement in the target area. We now comment on each of these observations.

The ability to adjust the threshold allowed us to interpret regions of interest in version 2.10 that had been misanalyzed in version 1.45. Practically, this meant that we were able to achieve a sufficient sample size to calculate precision of radial scans with the newer, but not the older, software. This adjustment entails a cost, however, as the background noise of the scan is increased with a downward adjustment of the threshold. In our experiment, the increased background intensity made two scans globally uninterpretable.

Although precision and accuracy differed slightly according to technique and software version, these variations had minimal impact. Our precision and accuracy results are comparable to those obtained by Iida-Klein and co-workers *(13)* and those obtained by Libouban and colleagues *(12)*. These differences can be attributed in part to differences in the details of the three studies. At the femur, the only common site studied by us and Iida-Klein et al., these authors reported an in vivo BMD %CV of 3.09% with a 16-h interval between scans, although the %CV was only 1.98%. Iida-Klein's study entailed more specimen handling than ours, whereas Libouban's studied rat bones rather than mouse bones. Our results support the practice of performing ex vivo scans in air rather than submerged in water or a buffer. We advocate air scanning because controlling buffer depth and composition requires additional manipulation of specimens and introduces more chances for operator error. Moreover, the comparability of our results with those of Iida-Klein suggests that there is little to be gained by fixing specimens prior to study.

With regard to scanning submerged specimens, it is worth noting that Kastl and colleagues *(10)* observed performance differences based on buffer salinity.

We observed an inverse relationship between the size of a scanned bone and the precision and accuracy of DXA measurements. This is unsurprising, as the same relationship has been established in numerous human and animal studies. Pixel size (0.18 mm^2; www.faxitron.com/PIXImus_specs.htm) is large relative to mouse long bone area (ranging between a maximum of 0.54 cm^2 for femora to a minimum of 0.06 cm^2 for radii; average data given in Table 2). It is also important to note that the performance of gravimetric determination of BMD and BMC is poorer in smaller bones. Although ashing is the historical "gold standard" for measuring BMC, it is important to recall that it is an imperfect method for very small bones, such as mouse radii. This limitation leads us to recommend that other investigators performing site-specific studies use the largest regions of interest compatible with their research questions.

Finding a position dependence of the BMD was an unexpected result of this study. To our knowledge, our's is the first study to address this issue with the PIXImus densitometer. The statistical analysis required to detect and introduce appropriate adjustment for this artifact was straightforward, relying on stepwise linear regression. By including specimen x and y coordinates as covariates in this precision study, we were able to determine coefficients for positional adjustment for our instrument. The position artifact was calculated using pooled data for all three bones, and our experiments did not provide evidence that the artifact is dependent on bone size. As for densitometry in clinical practice, investigators should perform precision studies of their instruments at regular intervals. We recommend that they also seek position artifacts, as we have done here. We expect that position artifacts will be instrument dependent, so although our approach is broadly applicable, the regression coefficients are specific to our instrument.

An important limitation of our study is that we did not compare the same bones in vivo and ex vivo. Although that comparison would be of interest to investigators, logistical limitations made it impossible for us to include it in our study. Iida-Klein and colleagues *(13)* included this comparison in their investigation and found a %CV of 9.47% between in vivo and ex vivo scans of the femur.

Our results provide guidance regarding application of DXA to ex vivo small-animal specimens, and it is important to note that the manufacturer only recommends use measurement of whole-body BMD in intact animals. Nevertheless, there are numerous studies reporting analysis of isolated specimens, so the observations reported here are relevant to current work in many laboratories.

Acknowledgments

The authors thank Dr. Neil Binkley, Dr. Ricki Colman, and Dr. Marc Drezner for helpful discussions and critical

References

1. Turner CH, Hsieh YF, Muller R, et al. 2000 Genetic regulation of cortical and trabecular bone strength and microstructure in inbred strains of mice. J Bone Miner Res 15:1126–1131.
2. Yershov Y, Baldini TH, Villagomez S, et al. 2001 Bone strength and related traits in HcB/Dem recombinant congenic mice. J Bone Miner Res 16:992–1003.
3. Beamer WG, Shultz KL, Donahue LR, et al. 2001 Quantitative trait loci for femoral and lumbar vertebral bone mineral density in C57BL/6J and C3H/HeJ inbred strains of mice. J Bone Miner Res 16:1195–1206.
4. Shimizu M, Higuchi K, Kasai S, et al. 2002 A congenic mouse and candidate gene at the chromosome 13 locus regulating bone density. Mamm Genome 13:335–340.
5. Klein RF, Turner RJ, Skinner LD, et al. 2002 Mapping quantitative trait loci that influence femoral cross-sectional area in mice. J Bone Miner Res 17:1752–1760.
6. Camacho NP, Raggio CL, Doty SB, et al. 2001 A controlled study of the effects of alendronate in a growing mouse model of osteogenesis imperfecta. Calcif Tissue Int 69:94–101.
7. Samuels A, Perry MJ, Gibson R, Tobias JH. 2001 Effects of combination therapy with PTH and 17beta-estradiol on long bones of female mice. Calcif Tissue Int 69:164–170.
8. Sheng MH, Baylink DJ, Beamer WG, Donahue LR, Lau KH, Wergedal JE. 2002 Regulation of bone volume is different in the metaphyses of the femur and vertebra of C3H/HeJ and C57BL/6J mice. Bone 30:486–491.
9. Masinde GL, Li X, Gu W, Wergedal J, Mohan S, Baylink DJ. 2002 Quantitative trait loci for bone density in mice: the genes determining total skeletal density and femur density show little overlap in f2 mice. Calcif Tissue Int 71:421–428.
10. Kastl S, Sommer T, Klein P, Hohenberger W, Engelke K. 2002 Accuracy and precision of bone mineral density and bone mineral content in excised rat humeri using fan beam dual-energy X-ray absorptiometry. Bone 30:243–246.
11. Nagy TR, Prince CW, Li J. 2001 Validation of peripheral dual-energy X-ray absorptiometry for the measurement of bone mineral in intact and excised long bones of rats. J Bone Miner Res 16:1682–1687.

12. Libouban H, Simon Y, Silve C, et al. 2002 Comparison of pencil-, fan-, and cone-beam dual X-ray absorptiometers for evaluation of bone mineral content in excised rat bone. J Clin Densitom 5:355–361.

13. Iida-Klein A, Lu SS, Yokoyama K, Dempster DW, Nieves JW, Lindsay R. 2003 Precision, accuracy, and reproducibility of dual X-ray absorptiometry measurements in mice in vivo. J Clin Densitom 6:25–33.

14. Bland JM, Altman DG. 1986 Statistical methods for assessing agreement between two methods of clinical measurement. Lancet 1:307–310.

PERSPECTIVES

A Thematic Overview of Some Recent Advances in Skeletal Genetics

Robert D. Blank

Endocrinology Section, University of Wisconsin Medical School and the Geriatrics Research, Education, and Clinical Center, William S. Middleton Veterans' Hospital, Madison, Wis.

July 2004

It has now been 10 years since Morrison *et al.* (1) reported an association between vitamin D receptor (VDR) genotype and bone mineral density (BMD), thus spurring the hope that it would be possible to identify specific alleles of a small number of "bone genes" that would account for observed population variability of fragility fracture risk. Although many scientists, myself included, doubt that the reported VDR alleles play an important role in bone biology, the authors nevertheless succeeded in raising awareness in the bone community about genetic methods and the contribution of hereditary factors in determining clinically important bone properties. Because a great deal of progress has been made in the intervening decade, providing an encyclopaedic review of work in the field is not possible. This essay reviews *some* of the most important findings in a thematic fashion, with apologies to investigators whose research is not cited.

Identification of Molecular Signaling Pathways Whose Roles in Skeletal Health Were Previously Unappreciated

Rare diseases, the genetics of which follow a simple Mendelian pattern of inheritance, offer a powerful tool for understanding some of the molecular mechanisms that operate in establishing the size and shape of bones and the properties of the matrix within bones. Sometimes, identifying the mutated gene offers limited new insight, as in the case of osteogenesis imperfecta. It surprises no one that mutations affecting the major structural protein in bone matrix result in skeletal fragility of varying severity. This is not the case for several other Mendelian disorders, in which identifying the responsible genes has revealed previously unsuspected biology.

The importance of the *WNT* signaling pathway in establishing bone mass is perhaps the best known example of an unexpected biological mechanism underlying a bone disease, but it is not the only one. Loss of function mutations of the low-density lipoprotein receptor-related protein 5 gene (*LRP5*) cause osteoporosis-pseudoglioma syndrome (2-4), whereas gain of function mutations in the gene result in the high bone mass phenotype (5-7). The *WNT* pathway was well known prior to the discovery that it contributes to bone mass regulation, dating back to early work on the *Drosophila* mutation *wingless*. Investigation of the precise roles of *LRP5* and the other genes involved in the *WNT* pathway in bone is an active research area that is informed by an understanding of *WNT* biology in a variety of other settings.

Positional cloning has also been central in establishing that a phosphate regulatory mechanism operates in conjunction with parathyroid hormone and vitamin D. Once again, uncommon hereditary diseases with simple inheritance patterns -- X-linked hypophosphatemic rickets (XLH) (8,9) and autosomal dominant hypophosphatemic

4

rickets (ADHR) -- were the starting points (10). The determination that fibroblast growth factor 23 (FGF-23) is phosphaturic, a phosphate-regulating endopeptidase on the X chromosome (PHEX) substrate, and resistant to proteolytic degradation when an ADHR mutation is present establishes a mechanistic link between the two diseases (11,12). Subsequently, high circulating levels of FGF-23 have also been found in patients with tumor-induced osteomalacia (13,14), extending the scope of the pathway's actions to acquired disorders.

The PHEX/FGF-23 story is more complex, however. Both matrix extracellular phosphoglycoprotein (15,16) and frizzled-related protein 4 (17,18) have been proposed as phosphaturic factors. Moreover, some investigators have failed to find elevations of FGF-23 in XLH or PHEX-mediated degradation of FGF-23 in vitro, whereas others have proposed that PHEX may affect phosphate regulation and bone matrix mineralization through mechanisms other than proteolysis of putative phosphaturic factors (19,20). Further complexity arises from FGF-23 and PHEX in the kidney; relationships to both renal phosphate transport and vitamin D 1-hydroxylation have been demonstrated, but not yet fully characterized (e.g., 21-23). These conflicting observations support the existence of multiple important phosphaturic factors, and ongoing research seeks to better define the roles of each in mediating phosphaturia and bone matrix mineralization. The key point in the present context -- that investigation of rare genetic diseases has spurred discovery of novel and unexpected biology -- is strengthened by current efforts to reconcile seemingly inconsistent data.

In both examples cited above, fruitful new hypotheses have emerged because the identities of disease-causing genes were surprising. None of these genes would have been considered attractive candidates in the absence of compelling linkage data, and our efforts to assimilate the implications of the linkage data have clearly advanced our understanding of bone mass and phosphate homeostasis.

Insightful Use of Animal Models

Animal models allow investigators to measure more relevant and more precisely defined phenotypes than is possible in clinical studies. Indeed, in the examples above, the focus of ongoing research has shifted from informative families to either naturally occurring mutant mice or genetically engineered mice (24-27).

Mouse and rat models are now so well integrated into bone research that there is no need to belabor the methods by which they are generated or the range of studies to which they have been applied. However, it is worth noting that several general-purpose model animals have been developed, such as those expressing reporter genes or Cre recombinase in a tissue-restricted fashion (e.g., 28,29).

Animal models remain a particularly powerful resource for identifying genes that affect bone properties, particularly in the context of identifying quantitative trait loci (QTLs). The concept underlying QTL genetics is that alternative alleles of multiple genes each contribute incrementally to a trait of interest. Furthermore, segregation of the various QTL alleles is a major source of variation in the trait among members of a population. Although human families are enormously useful in identifying genes and pathways involved in diseases with transparent inheritance patterns, human samples are poorly suited for determining the basis of differences in bone properties among members of a population. Population-level differences in bone properties are much more subtle than those encountered in disease states and are modified by environmental factors and age. Moreover, human alleles that are identical by state (i.e., according to the detection method, such as microsatellite size or restriction fragment length polymorphism) might not be identical by descent (i.e., ancestral origins may differ and therefore they may be truly different in a genetic sense). Experimental crosses in animals obviate some of the problems attending investigation of population variation. Invasive phenotypes that cannot be studied in humans can be investigated in model

5

organisms. Husbandry can be controlled and animals studied at the same age, thus limiting environmental sources of variability. Because inbred strains are available for study, one can limit the number of alleles segregating at each locus. Use of inbred strains also eliminates the problem of distinguishing identity by descent from identity by state. In experimental crosses, it is straightforward to determine both linkage (*i.e.* location of a gene) and association (*i.e.* which allele favors a high value of the trait being studied). These advantages are considerable, but entail some costs. There is no assurance that bone loci found in an experimental cross will prove important in humans. Moreover, a cross can only identify a locus if the parental strains harbor different alleles and the effect size is sufficiently large to allow detection. Finally, there is considerable work between mapping a locus and identifying the responsible gene. Limitations notwithstanding, experimental crosses have moved from being a promising strategy to a proven method for identifying genes that control bone properties.

In at least one case thus far, a QTL mapping study in mice has led to the identification of a gene -- *Alox15* -- and not just a chromosomal region (30). This study, conducted by Klein and colleagues, is the culmination of research started in the late 1990s (31,32). The recently reported findings include the validation of a chromosome 11 QTL in congenic strains; recognition of *Alox15* as a positional candidate gene, based on the strength of a microarray gene expression analysis, demonstrating an approximate 35-fold difference in *Alox15* expression between C57BL/6 (low) and DBA/2 (high); and experimental demonstration of the impact of *Alox15* on femoral BMD and biomechanical performance in three distinct and independent experimental tests. Based on the known ability of *Alox15* to metabolize arachidonic and linoleic acids to peroxisome proliferator-activated receptor gamma agonists, the investigators hypothesized that high *Alox15* activity favors differentiation of mesenchymal stem cells along the adipocyte lineage, in preference to the osteoblast lineage. As in the cases of *LRP5, FGF-23,* and *PHEX,* this work reveals a metabolic pathway that was previously not suspected of having important effects on bone. Adding further to the interest of this story is the prior detection of a human BMD QTL in the region harboring *ALOX15* (33).

The path from validated QTL (*i.e.,* the preservation of the effect in a congenic strain) to identification of the responsible gene is not always as rapid and straightforward as in the case of *Alox15*. Sometimes, on further breeding, a linkage peak proves not to be a single locus, but a group of linked genes. The bone group in the Jackson Laboratory has demonstrated precisely this phenomenon on mouse chromosome 1 (34), and the same may be true of other QTLs segregating in the C57BL/6J x C3H/HeJ cross (35). Furthermore, the number of positional candidate genes -- even if isolated within a congenic segment -- remains large, and testing these systematically is an arduous task.

Of interest, human allele association studies can be a powerful tool in the endgame of identifying which gene in a candidate interval is responsible for the phenotypic effect. The ability to undertake genetic studies involving multiple species is made possible by the existence of comparative genetic maps (*e.g.,* the mouse-human comparative map is available at http://www.ncbi.nlm.nih.gov/Homology/Davis/). This hybrid strategy is being pursued to find an X-linked gene identified as contributing to postmaturity BMD change in mice and lumbar BMD in postmenopausal women, narrowing the search to one of two genes (36). The short distances over which linkage disequilibrium persists and the complex pattern of population mixing among humans facilitate dissection of a chromosome region that is too small for crossovers to be helpful in a mouse model. Thus, some of the very features that make human populations unattractive for genome-wide scans make them ideal for fine-scale mapping of an established positional candidate.

Although identifying the responsible genes remains the primary goal of experimental crosses, congenic strains constructed to confirm linkage are valuable in a number of

6

ways that are independent of their utility in identifying the gene(s) underlying a QTL. Unlike the unique animals generated in a cross, congenics are inbred, allowing the study of multiple genetically matched individuals. In a cross, investigators often choose to sacrifice the biological depth of the traits being measured to gain either precision, ease of measurement, or both -- deferring more detailed and biologically informative phenotypic studies until congenics are available. Thus, for example, although a QTL on chromosome 4 was mapped because of its effect on femoral volumetric BMD, experiments with the resulting congenic strain have demonstrated that there is a mechanical responsiveness gene within the donor segment (37). Congenic strains are also powerful resources in studies addressing interactions among QTLs (38), between QTLs and environment (39), and between QTLs and sex (40,41). Such experiments exploit the advantages of animal models, and the study of interactions is an area in which research with experimental animals will continue to provide more insight than can be gained from clinical studies.

Human Genetic Methodology

Genome-wide screens for bone QTLs in humans, by either linkage or association methods, are potentially problematic, but recent methodological advances promise to help overcome two of the limitations inherent in human quantitative trait genetics. Genome-wide scans in humans for quantitative bone traits are generally underpowered, regardless of whether linkage or association methods are used. Underpowered genetic studies lead to two related errors: failure to identify QTLs and overestimation of the effect sizes of identified QTLs (42). Cross-sectional allele association studies are subject to false-positive results that arise from population stratification. Research addressing each of these problems is briefly noted here.

The Framingham investigators have applied principal components analysis to extract synthetic uncorrelated principal component phenotypes from a larger number of interdependent bone-related raw data measurements, including multiple dual-energy x-ray absorptiometry and quantitative heel ultrasound parameters (43). The approach is conceptually simple and can be performed with standard statistical analysis software. The multiple raw measurements are first combined into a composite measure and then broken down into a minimal set of orthogonal vectors (i.e., the principal components). All lumbar spine, femoral, and calcaneal data from the Framingham study can be represented as two principal components that accounted for 66% and 24% of the composite phenotype variability. In the case of hip data alone, a single principal component was extracted that accounted for 90% of the variability. Mapping the principal components identified several regions suggestive of linkage, but none of the regions achieved genome-wide statistical significance. It is important to note, however, that the principal component heritabilities exceeded those of the individual underlying measurements, thus demonstrating that they are more robust for mapping studies. Therefore, despite the failure to achieve significant linkage, this paper is important because of the methodological innovation.

Using data from the Indiana Sisters Study, the bone genetics group at Indiana University has measured the effects of population stratification on the rate of false-positive associations (44). If a population is stratified, association can arise artifactually -- as a consequence of coincidental differences in allele frequencies between two population groups that also differ with regard to the trait being studied, rather than as a consequence of a true biological connection between the phenotype being studied. A trivial example illustrates the point: although the HBB^S allele is associated with skin pigmentation, all recognize that this association reflects the higher prevalence of sickle cell hemoglobin in individuals of African descent, rather than an inherent causal relationship between hemoglobin genotype and skin color. The problem of population stratification is common (i.e., most populations are stratified), and the degree of stratification is often difficult or impossible to quantify. The investigators found that increasing

7

admixture increases the rate of false-positives in association studies and that one can nevertheless address admixture by including unlinked "negative control" polymorphisms to estimate the magnitude of the admixture effect. Their proposed inclusion of unlinked loci to control for admixture provides a simple, practical approach that can be used as an alternative to the more difficult alternative of performing association studies using the two-generation transmission disequilibrium test.

A Philosophical Reflection on Complex Trait Genetics

Ultimately, as a community, we face the task of achieving a philosophical advance to match the scientific advances of recent years. As scientists, we are deeply committed to seeking and understanding the causes underlying natural phenomena. Yet, our notions of causality are both inadequate and imprecise. We generally agree about acknowledging the "causality" of factors that are either *necessary* or *sufficient* for a specified outcome. Neither of these criteria of causality seems to be adequate for helping us understand complex trait genetics, because genes that contribute to bone properties may be neither necessary nor sufficient to determine biologically

important features. Similarly, simply quantifying the effect of a particular allele is also inadequate, as effect sizes can vary among populations (both human and model organisms) and according to environmental variables. One of our conceptual challenges in the future will be to develop useful ways of ascertaining and describing conditional effect sizes. Current treatments of interactions (gene x sex, gene x gene, and gene x environment) provide a starting point, but we have a long, challenging, and exciting road ahead.

Acknowledgements

References

1. Morrison NA, Qi JC, Tokita A, Kelly PJ, Crofts L, Nguyen TV, Sambrook PN, Eisman JA. Prediction of bone density from vitamin D receptor alleles. *Nature.* 1994 Jan 20;367(6460):284-7.

2. Gong Y, Vikkula M, Boon L, Liu J, Beighton P, Ramesar R, Peltonen L, Somer H, Hirose T, Dallapiccola B, De Paepe A, Swoboda W, Zabel B, Superti-Furga A, Steinmann B, Brunner HG, Jans A, Boles RG, Adkins W, van den Boogaard MJ, Olsen BR, Warman ML. Osteoporosis-pseudoglioma syndrome, a disorder affecting skeletal strength and vision, is assigned to chromosome region

11q12-13. *Am J Hum Genet.* 1996 Jul;59(1):146-51.

3. Gong Y, Slee RB, Fukai N, Rawadi G, Roman-Roman S, Reginato AM, Wang H, Cundy T, Glorieux FH, Lev D, Zacharin M, Oexle K, Marcelino J, Suwairi W, Heeger S, Sabatakos G, Apte S, Adkins WN, Allgrove J, Arslan-Kirchner M, Batch JA, Beighton P, Black GC, Boles RG, Boon LM, Borrone C, Brunner HG, Carle GF, Dallapiccola B, De Paepe A, Floege B, Halfhide ML, Hall B, Hennekam RC, Hirose T, Jans A, Juppner H, Kim CA, Keppler-Noreuil K, Kohlschuetter A, LaCombe D, Lambert M, Lemyre E, Letteboer T, Peltonen L, Ramesar RS, Romanengo M, Somer H, Steichen-

8

Gersdorf E, Steinmann B, Sullivan B, Superti-Furga A, Swoboda W, van den Boogaard MJ, Van Hul W, Vikkula M, Votruba M, Zabel B, Garcia T, Baron R, Olsen BR, Warman ML. Osteoporosis-Pseudoglioma Syndrome Collaborative Group. LDL receptor-related protein 5 (LRP5) affects bone accrual and eye development. *Cell.* 2001 Nov 16;107(4):513-23.

4. Van Wesenbeeck L, Cleiren E, Gram J, Beals RK, Benichou O, Scopelliti D, Key L, Renton T, Bartels C, Gong Y, Warman ML, De Vernejoul MC, Bollerslev J, Van Hul W. Six novel missense mutations in the LDL receptor-related protein 5 (LRP5) gene in different conditions with an increased bone density. *Am J Hum Genet.* 2003 Mar;72(3):763-71.

5. Johnson ML, Gong G, Kimberling W, Recker SM, Kimmel DB, Recker RB. Linkage of a gene causing high bone mass to human chromosome 11 (11q12-13). *Am J Hum Genet.* 1997 Jun;60(6):1326-32.

6. Little RD, Recker RR, Johnson ML. High bone density due to a mutation in LDL-receptor-related protein 5. *N Engl J Med.* 2002 Sep 19;347(12):943-4.

7. Little RD, Carulli JP, Del Mastro RG, Dupuis J, Osborne M, Folz C, Manning SP, Swain PM, Zhao SC, Eustace B, Lappe MM, Spitzer L, Zweier S, Braunschweiger K, Benchekroun Y, Hu X, Adair R, Chee L, FitzGerald MG, Tulig C, Caruso A, Tzellas N, Bawa A, Franklin B, McGuire S, Nogues X, Gong G, Allen KM, Anisowicz A, Morales AJ, Lomedico PT, Recker SM, Van Eerdewegh P, Recker RR, Johnson ML. A mutation in the LDL receptor-related protein 5 gene results in the autosomal dominant high-bone-mass trait. *Am J Hum Genet.* 2002 Jan;70(1):11-9.

8. A gene (PEX) with homologies to endopeptidases is mutated in patients with X-linked hypophosphatemic rickets. The HYP Consortium. *Nat Genet.* 1995 Oct;11(2):130-6.

9. Sabbagh Y, Jones AO, Tenenhouse HS. PHEXdb, a locus-specific database for mutations causing X-linked hypophosphatemia. *Hum Mutat.* 2000;16(1):1-6.

10. Autosomal dominant hypophosphataemic rickets is associated with mutations in FGF23. The ADHR Consortium. *Nat Genet.* 2000 Nov;26(3):345-8.

11. Bowe AE, Finnegan R, Jan de Beur SM, Cho J, Levine MA, Kumar R, Schiavi SC. FGF-23 inhibits renal tubular phosphate transport and is a PHEX substrate. *Biochem Biophys Res Commun.* 2001 Jun 22;284(4):977-81.

12. Shimada T, Muto T, Urakawa I, Yoneya T, Yamazaki Y, Okawa K, Takeuchi Y, Fujita T, Fukumoto S, Yamashita T. Mutant FGF-23 responsible for autosomal dominant hypophosphatemic rickets is resistant to proteolytic cleavage and causes hypophosphatemia in vivo. *Endocrinology.* 2002 Aug;143(8):3179-82.

13. Yamazaki Y, Okazaki R, Shibata M, Hasegawa Y, Satoh K, Tajima T, Takeuchi Y, Fujita T, Nakahara K, Yamashita T, Fukumoto S. Increased circulatory level of biologically active full-length FGF-23 in patients with hypophosphatemic rickets/osteomalacia. *J Clin Endocrinol Metab.* 2002 Nov;87(11):4957-60.

14. Jonsson KB, Zahradnik R, Larsson T, White KE, Sugimoto T, Imanishi Y, Yamamoto T, Hampson G, Koshiyama H, Ljunggren O, Oba K, Yang IM, Miyauchi A, Econs MJ, Lavigne J, Juppner H. Fibroblast

growth factor 23 in oncogenic osteomalacia and X-linked hypophosphatemia. *N Engl J Med.* 2003 Apr 24;348(17):1656-63.

15. Rowe PS, de Zoysa PA, Dong R, Wang HR, White KE, Econs MJ, Oudet CL. MEPE, a new gene expressed in bone marrow and tumors causing osteomalacia. *Genomics.* 2000 Jul 1;67(1):54-68.

16. Rowe PS, Kumagai Y, Gutierrez G, Garrett IR, Blacher R, Rosen D, Cundy J, Navvab S, Chen D, Drezner MK, Quarles LD, Mundy GR. MEPE has the properties of an osteoblastic phosphatonin and minhibin. *Bone.* 2004 Feb;34(2):303-19.

17. Kumar R. New insights into phosphate homeostasis: fibroblast growth factor 23 and frizzled-related protein-4 are phosphaturic factors derived from tumors associated with osteomalacia. *Curr Opin Nephrol Hypertens.* 2002 Sep;11(5):547-53.

18. Berndt T, Craig TA, Bowe AE, Vassiliadis J, Reczek D, Finnegan R, Jan De Beur SM, Schiavi SC, Kumar R. Secreted frizzled-related protein 4 is a potent tumor-derived phosphaturic agent. *J Clin Invest.* 2003 Sep;112(5):785-94.

19. Guo R, Rowe PS, Liu S, Simpson LG, Xiao ZS, Darryl Quarles LD. Inhibition of MEPE cleavage by Phex. *Biochem Biophys Res Commun.* 2002 Sep 13;297(1):38-45.

20. Liu S, Guo R, Simpson LG, Xiao ZS, Burnham CE, Quarles LD. Regulation of fibroblastic growth factor 23 expression but not degradation by PHEX. *J Biol Chem.* 2003 Sep 26;278(39):37419-26.

21. Beck L, Karaplis AC, Amizuka N, Hewson AS, Ozawa H, Tenenhouse HS. Targeted inactivation of Npt2 in mice leads to severe renal phosphate wasting, hypercalciuria, and skeletal abnormalities. *Proc Natl Acad Sci U S A.* 1998 Apr 28;95(9):5372-7.

22. Azam N, Zhang MY, Wang X, Tenenhouse HS, Portale AA. Disordered regulation of renal 25-hydroxyvitamin D-1alpha-hydroxylase gene expression by phosphorus in X-linked hypophosphatemic (hyp) mice. *Endocrinology.* 2003 Aug;144(8):3463-8.

23. Saito H, Kusano K, Kinosaki M, Ito H, Hirata M, Segawa H, Miyamoto K, Fukushima N. Human fibroblast growth factor-23 mutants suppress Na+-dependent phosphate co-transport activity and 1alpha,25-dihydroxyvitamin D3 production. *J Biol Chem.* 2003 Jan 24;278(4):2206-11.

24. Strom TM, Francis F, Lorenz B, Boddrich A, Econs MJ, Lehrach H, Meitinger T. Pex gene deletions in Gy and Hyp mice provide mouse models for X-linked hypophosphatemia. *Hum Mol Genet.* 1997 Feb;6(2):165-71.

25. Babij P, Zhao W, Small C, Kharode Y, Yaworsky PJ, Bouxsein ML, Reddy PS, Bodine PV, Robinson JA, Bhat B, Marzolf J, Moran RA, Bex F. High bone mass in mice expressing a mutant LRP5 gene. *J Bone Miner Res.* 2003 Jun;18(6):960-74.

26. Shimada T, Kakitani M, Yamazaki Y, Hasegawa H, Takeuchi Y, Fujita T, Fukumoto S, Tomizuka K, Yamashita T. Targeted ablation of Fgf23 demonstrates an essential physiological role of FGF23 in phosphate and vitamin D metabolism. *J Clin Invest.* 2004 Feb;113(4):561-8.

27. Shimada T, Urakawa I, Yamazaki Y, Hasegawa H, Hino R, Yoneya T, Takeuchi Y, Fujita T, Fukumoto S,

10

Yamashita T. FGF-23 transgenic mice demonstrate hypophosphatemic rickets with reduced expression of sodium phosphate cotransporter type IIa. *Biochem Biophys Res Commun.* 2004 Feb 6;314(2):409-14.

28. Dacquin R, Starbuck M, Schinke T, Karsenty G. Mouse alpha1(I)-collagen promoter is the best known promoter to drive efficient Cre recombinase expression in osteoblast. *Dev Dyn.* 2002 Jun;224(2):245-51.

29. Kalajzic Z, Liu P, Kalajzic I, Du Z, Braut A, Mina M, Canalis E, Rowe DW. Directing the expression of a green fluorescent protein transgene in differentiated osteoblasts: comparison between rat type I collagen and rat osteocalcin promoters. *Bone.* 2002 Dec;31(6):654-60.

30. Klein RF, Allard J, Avnur Z, Nikolcheva T, Rotstein D, Carlos AS, Shea M, Waters RV, Belknap JK, Peltz G, Orwoll ES. Regulation of bone mass in mice by the lipoxygenase gene Alox15. *Science.* 2004 Jan 9;303(5655):229-32.

31. Klein RF, Mitchell SR, Phillips TJ, Belknap JK, Orwoll ES. Quantitative trait loci affecting peak bone mineral density in mice. *J Bone Miner Res.* 1998 Nov;13(11):1648-56.

32. Klein RF, Shea M, Gunness ME, Pelz GB, Belknap JK, Orwoll ES. Phenotypic characterization of mice bred for high and low peak bone mass. *J Bone Miner Res.* 2001 Jan;16(1):63-71.

33. Devoto M, Shimoya K, Caminis J, Ott J, Tenenhouse A, Whyte MP, Sereda L, Hall S, Considine E, Williams CJ, Tromp G, Kuivaniemi H, Ala-Kokko L, Prockop DJ, Spotila LD. First-stage autosomal genome screen in extended pedigrees suggests genes predisposing to low bone mineral density on chromosomes 1p, 2p and 4q. *Eur J Hum Genet.* 1998 Mar-Apr;6(2):151-7.

34. Shultz KL, Donahue LR, Bouxsein ML, Baylink DJ, Rosen CJ, Beamer WG. Congenic strains of mice for verification and genetic decomposition of quantitative trait loci for femoral bone mineral density. *J Bone Miner Res.* 2003 Feb;18(2):175-85.

35. Beamer WG, Shultz KL, Donahue LR, Churchill GA, Sen S, Wergedal JR, Baylink DJ, Rosen CJ. Quantitative trait loci for femoral and lumbar vertebral bone mineral density in C57BL/6J and C3H/HeJ inbred strains of mice. *J Bone Miner Res.* 2001 Jul;16(7):1195-206.

36. Mroczkowski H, Parsons CA, Albagha OME, Reid DM, Manolagas SC, Ralston SH, Shmookler-Reis RJ. An X-Chromosome Locus Modulates Lumbar BMD in Postmenopausal Women, and Age-Dependent Decline of Spinal BMD in Mice. *J Bone Miner Res* 2003; 18 (Suppl 2):S67.

37. Robling AG, Li J, Shultz KL, Beamer WG, Turner CH. Evidence for a skeletal mechanosensitivity gene on mouse chromosome 4. *FASEB J.* 2003 Feb;17(2):324-6.

38. Rapp JP, Garrett MR, Deng AY. R Construction of a double congenic strain to prove an epistatic interaction on blood pressure between rat chromosomes 2 and 10. *J Clin Invest.* 1998 Apr 15;101(8):1591-5.

39. York B, Truett AA, Monteiro MP, Barry SJ, Warden CH, Naggert JK, Maddatu TP, West DB. Gene-environment interaction: a significant diet-dependent obesity locus demonstrated in a congenic segment on mouse chromosome 7.

11

Mamm Genome. 1999
May;10(5):457-62.

40. Orwoll ES, Belknap JK, Klein RF.
    Gender specificity in the genetic
    determinants of peak bone mass. *J
    Bone Miner Res.* 2001
    Nov;16(11):1962-71.

41. Turner CH, Sun Q, Schriefer J,
    Pitner N, Price R, Bouxsein ML,
    Rosen CJ, Donahue LR, Shultz KL,
    Beamer WG. Congenic mice reveal
    sex-specific genetic regulation of
    femoral structure and strength.
    Calcif Tissue Int. 2003
    Sep;73(3):297-303.

42. Goring HH, Terwilliger JD, Blangero
    J. Large upward bias in estimation
    of locus-specific effects from
    genomewide scans. *Am J Hum
    Genet.* 2001 Dec;69(6):1357-69.

43. Karasik D, Cupples LA, Hannan MT,
    Kiel DP. Genome screen for a
    combined bone phenotype using
    principal component analysis: the
    Framingham study. *Bone.* 2004
    Mar;34(3):547-56.

44. Koller DL, Peacock M, Lai D,
    Foroud T, Econs MJ. False Positive
    Rates in Association studies as a
    Function of Degree of Stratification.
    J Bone Miner Res. 2004; April 19
    (web-first e-publication).

12

Interobserver Reproducibility of Criteria for Vertebral Body Exclusion

Karen E Hansen,[1,2,3] Neil Binkley,[2,3,4] Rose Christian,[2,3] Nellie Vallarta-Ast,[2,5] Diane Krueger,[2] Marc K Drezner,[2,3,6] and Robert D Blank[2,3,6]

ABSTRACT: We studied reproducibility of the ISCD vertebral exclusion criteria among four interpreters. Surprisingly, agreement among interpreters was only moderate, because of differences in threshold for diagnosing focal structural defects and choice of which vertebra among a pair discordant for T-score, area, or BMC to exclude. Our results suggest that reproducibility may be improved by specifically addressing the sources of interobserver disagreement.

Introduction: Although DXA is widely used to measure vertebral BMD, its interpretation is subject to multiple confounders including osteoarthritis, aortic calcification, and scoliosis. In an attempt to standardize interpretation and minimize the impact of artifacts, the International Society for Clinical Densitometry (ISCD) established criteria for vertebral exclusion, including the presence of a focal structural defect (FSD), discrepancy of >1·SD in T-score between adjacent vertebrae, and a lack of increase in BMC or area from L_1 to L_4. Whereas the efforts of the ISCD represent an important advance in BMD interpretation, the interobserver reproducibility with application of these criteria is unknown. We hypothesized that there would be substantial agreement among four interpreters regarding application of the exclusion criteria and the final lumbar spine T-score.

Materials and Methods: Each interpreter read a set of 200 lumbar DXA scans obtained on male veterans, applying the ISCD vertebral body exclusion criteria.

Results: Surprisingly, agreement among interpreters was only moderate. Differences in interpretation resulted from differing thresholds for recognition of FSD and the choice of excluding the upper or lower vertebral body for the criteria requiring comparison between adjacent vertebrae.

Conclusions: Despite their apparent simplicity, the ISCD vertebral exclusion criteria are difficult to apply consistently. In principle, appropriate refinement of the exclusion criteria may significantly improve interobserver agreement.

J Bone Miner Res 2005;20:501–508. Published online on November 29, 2004; doi: 10.1359/JBMR.041134

Key words: aging, epidemiology, evidence/guidelines, osteoporosis, quantitation, bone densitometry

INTRODUCTION

BMD IS THE single best test to predict fragility fracture.[1-4] Although various biochemical markers of bone turnover, ultrasonic properties of bone, and quantitative CT scanning each predict fragility fracture,[5-10] BMD measured using DXA remains the gold standard for osteoporosis diagnosis and fracture risk assessment in clinical practice. However, DXA is an imperfect tool. For example, interpretation of lumbar spine bone mass is confounded by artifacts including degenerative arthritis, aortic calcification, and scoliosis.[11] To address this problem, the International Society for Clinical Densitometry (ISCD) currently recommends exclusion of individual vertebrae when interpreting lumbar spine BMD if any of four criteria are present.[12] Specifically, a vertebral body is excluded if there is a focal structural defect (FSD), unusual discrepancy in T-score between adjacent vertebrae, or a lack of increase in BMC or bone area when proceeding caudally from L_1 to L_4.[12]

While the efforts of the ISCD represent an important advance in the approach to BMD interpretation, interobserver reproducibility in the application of ISCD criteria for vertebral body exclusion is unknown. We hypothesized that interpreters could achieve good consensus in applying the ISCD exclusion criteria and determining the resultant lumbar spine T-score. To test this hypothesis, we analyzed agreement among observers in a set of 200 lumbar spine DXA scans.

[1]Rheumatology Section, Department of Medicine, University of Wisconsin and William S. Middleton Veterans Hospital, Madison, Wisconsin, USA; [2]Osteoporosis Clinical Center and Research Program, University of Wisconsin, Madison, Wisconsin, USA; [3]Endocrinology, Diabetes and Metabolism Section, Department of Medicine, University of Wisconsin, Madison, Wisconsin, USA; [4]Geriatrics Section, Department of Medicine, University of Wisconsin, Madison, Wisconsin, USA; [5]Radiology Department, William S. Middleton Memorial Veterans Hospital, Madison, Wisconsin, USA; [6]Geriatrics, Research, Education, and Clinical Center, William S. Middleton Veterans Hospital, Madison, Wisconsin, USA.
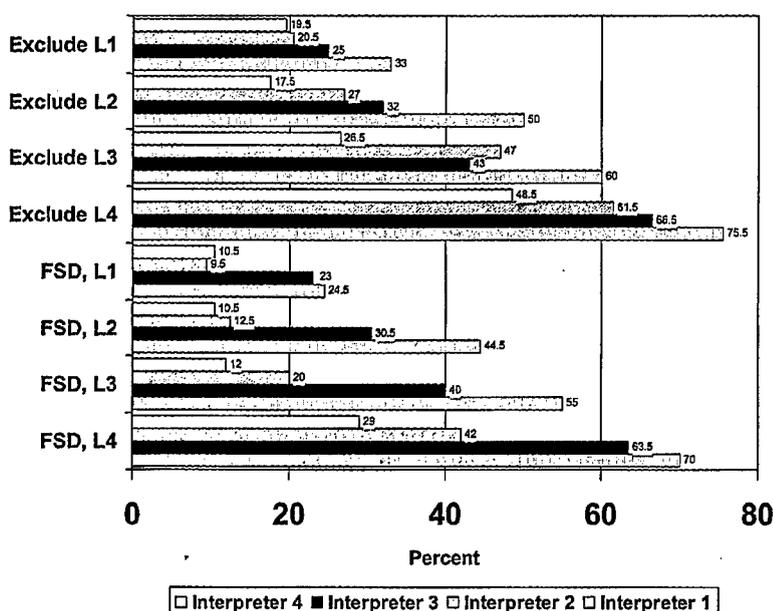
FIG. 1. Overall and FSD-related vertebral exclusion rates by observer and vertebra. For vertebral exclusion, two-way ANOVA reveals significant differences according to both interpreter and vertebra, without interaction between these factors. Posthoc analysis shows significant pairwise differences for all comparisons except L_1 vs. L_2 and observers 2 vs. 3. For FSD, two-way ANOVA reveals significant differences according to both interpreter and vertebra, without interaction between these factors. Posthoc analysis shows significant pairwise differences for all comparisons except L_1 vs. L_2, L_2 vs. L_3, and observers 1 vs. 2 and observers 3 vs. 4. Analysis by McNemar's test yielded similar results.

MATERIALS AND METHODS

Bone densitometry

De-identified lumbar spine DXA reports of 200 male veterans among 533 tested at the William S. Middleton Veterans Hospital between January 2 and October 5, 2002 were randomly chosen for evaluation. A single ISCD-trained technologist performed all examinations using a GE Medical Systems Lunar Expert-XL densitometer (Madison, WI, USA). Data were analyzed using software version 1.92 and the GE Lunar male normative database.

Subsequently, four ISCD-certified physicians reviewed the DXA images and ancillary results to estimate reproducibility of the ISCD criteria for vertebral body exclusion. The indication(s) for exclusion of vertebral bodies were noted, along with the resulting lumbar spine T-score, for each report. The GE Lunar software for these BMD reports did not permit calculation of T-score among noncontiguous vertebrae. Thus, if two adjacent and one noncontiguous vertebral body remained, interpreters were instructed to choose the mean T-score of the two adjacent vertebrae as the final lumbar spine T-score, as suggested by the ISCD position statement.[12] When two nonadjacent vertebral bodies remained after application of the exclusion criteria, interpreters were asked to choose the numerically lower T-score as the final value.

All study data were entered in duplicate into an Excel spreadsheet for statistical analysis. The University of Wisconsin Human Subjects Committee and the William S. Middleton Veterans' Hospital's Research and Development Committee reviewed the study protocol and, as all patient identifiers had been removed from the data, deemed that informed consent was not needed for this study.

Statistical analysis

To determine sample size for this study, interpreters 2 and 3 reviewed a random sample of 54 male BMD reports, applying the ISCD criteria for vertebral body exclusion. Subsequently, high agreement in lumbar spine T-score was achieved ($r = 0.98$, Pearson's correlation coefficient), with an average difference in BMD T-score of 0.08 ± 0.4 between the two interpreters. Based on these data, using a two-sided α error of 0.05, review of 200 BMD reports would provide a power of 94% to detect a difference of 0.1 in T-score between paired interpreters.

We used McNemar's and κ test statistics to assess differences in rates of, and indications for, vertebral body exclusion among interpreters. ANOVA and paired and unpaired t-tests were used to compare continuous variables, while the χ^2 test was used to compare categorical variables. We performed linear regression to compare interpreters' T-scores for each scan, obtaining the Pearson correlation coefficient, prediction equation, and SE of the estimate for each interpreter pair. Significance levels were adjusted according to Bonferroni's correction to account for multiple comparisons. Statistical analyses were performed using Analyze-It software (Leeds, UK), Sigma Stat 2.03 (SPSS), and Excel (Microsoft). Calculation of κ was based on formulas obtained from the Medical Algorithms Project.[13]

RESULTS

Clinical characteristics of the study population

Male veterans in this study had a mean age of 64 ± 12 years (range, 25–89 years). Most were white (97%), with two Hispanics and four blacks among the group. The average body mass index was 29.1 kg/m^2 (range, 17.4–45.1 kg/m^2). Current and prior alcohol use was reported among 39 (20%) and 27 (14%) men, whereas current and prior tobacco use was noted in 33 (17%) and 66 (33%) men, respectively. Among all men, 98 (49%) reported a prior fracture, including 95 (48%) with low trauma fractures.

Vertebral body exclusion

Figure 1 shows vertebral exclusion by the various observers, and two trends are apparent. First, the rate of vertebral

TABLE 1. AGREEMENT AMONG INTERPRETERS BY κ STATISTIC*

	Average κ (range)
L_1	
Exclusion	0.350 (0.256, 0.446)
FSD	0.359 (0.263, 0.434)
T-score discrepancy	0.505 (0.416, 0.668)
Bone area	0.138 (−0.039, 0.264)
BMC	0.337 (0.081, 0.615)
L_2	
Exclusion	0.350 (0.215, 0.468)
FSD	0.383 (0.211, 0.558)
T-score discrepancy	0.547 (0.291, 0.779)
Bone area	0.312 (0.167, 0.642)
BMC	0.329 (0.167, 0.517)
L_3	
Exclusion	0.430 (0.278, 0.496)
FSD	0.342 (0.145, 0.523)
T-score discrepancy	0.670 (0.552, 0.809)
Bone area	0.503 (0.377, 0.851)
BMC	0.148 (−0.005, 0.433)
L_4	
Exclusion	0.500 (0.370, 0.567)
FSD	0.407 (0.229, 0.519)
T-score discrepancy	0.687 (0.598, 0.798)
Bone area	0.652 (0.468, 0.847)
BMC	0.326 (−0.003, 0.665)

*Cut-points for κ: $\kappa \leq 0$, poor agreement; $0 < \kappa \leq 0.2$, slight agreement; $0.2 < \kappa \leq 0.4$, fair agreement; $0.4 < \kappa \leq 0.6$, moderate agreement; $0.6 < \kappa \leq 0.8$, substantial agreement $0.8 < \kappa$, excellent agreement.

FIG. 2. A DXA image showing disagreement regarding exclusion because of the presence of vertebral abnormalities. Interpreter 3 excluded L_1 only, interpreters 1 and 2 excluded L_1 and L_2, and interpreter 4 excluded all vertebral bodies, judging this scan unreadable.

body exclusion rises from L_1 to L_4. Second, each observer has a characteristic threshold for excluding vertebrae. For example, observer 1 excluded the fewest vertebrae, whereas observer 4 excluded the most vertebrae, at any given level. Both trends are significant by two-way ANOVA, with $p < 0.0001$ for vertebrae and $p = 0.0016$ for observers, without a significant interaction between vertebrae and observers. Post hoc analysis by Tukey's test reveals significant pairwise differences in vertebral body exclusion between all vertebrae except L_1 and L_2 and between all interpreters except 2 and 3.

Differences in BMD interpretation among the interpreters are also reflected by the number of scans deemed unreadable. Lumbar spine images were completely excluded from analysis in 4 cases by interpreter 1, 2 cases by interpreter 2, 16 cases by interpreter 3, and 24 cases by interpreter 4. The frequency of unreadable scans is significantly different among observers ($\chi^2 = 29.8$, $df = 3$, $p < 0.0001$). Pairwise comparisons are significant for observers 2 and 4 ($\chi^2 = 13.9$, $df = 1$, $p = 0.0002$), observers 1 and 4 ($\chi^2 = 18.1$, $df = 1$, $p = 0.00002$), and observers 1 and 3 ($\chi^2 = 9.8$, $df = 1$, $p = 0.0017$), whereas the difference is of marginal significance for observers 2 and 3 ($\chi^2 = 6.4$, $df = 1$, $p = 0.012$).

We used the κ statistic to gauge agreement among four observers regarding vertebral body exclusion and regarding application of each of the four ISCD exclusion criteria (Table 1). κ values range from −0.039, indicating no agreement, to 0.851, indicating excellent agreement. However, the majority of κ values fall between 0.2 and 0.6, indicating fair to moderate agreement between observers.

The surprisingly poor agreement among observers prompted us to seek the factors leading to different choices regarding vertebral body exclusion. Two factors account for most of the discrepancy among observers: differing thresholds for vertebral exclusion because of FSD and differing choice of which vertebra among a discordant pair to exclude.

FSDs

The four observers exhibited differing judgment regarding the presence of FSD (Fig. 1). An example of disparate exclusion based on FSD is shown in Fig. 2. In this case, interpreter 3 excluded L_1 only, interpreters 1 and 2 excluded L_1 and L_2, and interpreter 4 excluded all vertebral bodies because of FSD, resulting in an unreadable scan. We analyzed FSD by two-way ANOVA, finding significant differences in FSD frequency related to vertebra ($p = 0.00013$) and observer ($p = 0.00009$) without interaction between these factors. Posthoc analysis by Tukey's test reveals significant pairwise differences for all vertebral comparisons except L_1 versus L_2 and L_2 versus L_3 and for all observer pairs except 1 versus 2 and 3 versus 4. Overall, observer 4 had the lowest threshold for calling a FSD, followed by observers 3, 2, and 1.

In general, increasing patient age was associated with less consistent agreement regarding the presence of FSD. For example, between interpreters 1 and 2, the mean age of men for whom full agreement regarding the presence of FSD was achieved was 61.2 ± 12 years. Conversely, among men for whom disagreement regarding FSD was noted, the mean age was 68.8 ± 9.6 years ($p < 0.0001$ for comparisons

TABLE 2 AGREEMENT REGARDING FSDs AND IMPACT ON MEAN T-SCORE

	Mean T-score ± SD lower-numbered observer	Mean T-score ± SD higher-numbered observer	T-score p value*	Age p value†
Interpreters 1 and 2				
Agree, n = 111 Age 61.2 ± 12.3 years	−1.49 ± 1.37	−1.50 ± 1.34	0.78	**<0.0001**
Disagree, n = 89 Age 68.8 ± 9.6 years	−1.42 ± 1.60	−1.25 ± 1.53	**0.0001**	
Interpreters 1 and 3				
Agree, n = 64 Age 66.6 ± 10.9 years	−1.54 ± 1.42	−1.58 ± 1.36	0.0619	**0.0006**
Disagree, n = 136 Age 60.1 ± 12.5 years	−1.38 ± 1.46	−1.76 ± 1.41	**<0.0001**	
Interpreters 1 and 4				
Agree, n = 54 Age 60.2 ± 12.3 years	−1.65 ± 1.35	−1.67 ± 1.37	0.65	**0.0014**
Disagree, n = 146 Age 66.2 ± 11.2 years	−1.26 ± 1.48	−1.75 ± 1.40	**<0.0001**	
Interpreters 2 and 3				
Agree, n = 89 Age 63.0 ± 12.3 years	−1.53 ± 1.49	−1.54 ± 1.49	0.8291	0.0911
Disagree, n = 111 Age 65.8 ± 11.3 years	−1.58 ± 1.39	−1.79 ± 1.37	**0.0003**	
Interpreters 2 and 4				
Agree, n = 74 Age 63.5 ± 12.7 years	−1.68 ± 1.51	−1.69 ± 1.54	0.93	0.360
Disagree, n = 126 Age 65.13 ± 11.2 years	−1.32 ± 1.44	−1.75 ± 1.28	**0.0001**	
Interpreters 3 and 4				
Agree, n = 83 Age 62.5 ± 12.2 years	−1.70 ± 1.52	−1.75 ± 1.50	0.0875	0.0459
Disagree, n = 117 Age 66.0 ± 11.4 years	−1.93 ± 1.17	−1.83 ± 1.20	0.0929	

*Paired t-test, significant values are shown in bold.
†Unpaired t-test, significant values are shown in bold.

of age by independent t-test). Table 2 provides additional comparisons for age and agreement regarding FSD.

Exclusion criteria based on comparison of adjacent vertebrae

A T-score discrepancy of >1 SD unit among adjacent vertebrae and a lack of increase in BMC or area proceeding caudally from L_1 to L_4 are each cause for excluding a vertebral body. These exclusion criteria differ from the presence of FSD because they are applied to vertebral pairs, rather than to single vertebrae. Moreover, once a pair has been identified as warranting exclusion of one vertebral body, the interpreter must still decide which vertebral body to exclude.

The κ data in Table 1 reveal that there was greater agreement among observers for these three comparative exclusion criteria than for FSD. Moreover, good agreement was achieved between interpreters (corrected McNemar's test not significant for all but 5 comparisons among 72) when applying the three exclusion criteria. However, despite the apparent objectivity of the numeric exclusion criteria, interpreters differed in their application of these criteria. In Table 3 we show one such example, with interpreters 1 and

4 excluding L_2 and L_4, whereas interpreters 2 and 3 excluded L_1, L_3, and L_4 with application of the three comparative exclusion criteria.

Therefore, given the observer's choice regarding which of two paired vertebrae to exclude, we investigated whether scoring agreement by the vertebral pair, rather than by the single vertebra, would reveal greater concordance among observers by κ. Because exclusion of L_2 or L_3 could be due to comparison with either the vertebra above or below it, we limited this additional analysis to the L_1–L_2 and the L_3–L_4 pairs. The corrected κ for the three comparative exclusion criteria are shown in Table 4. With adjustment for arbitrarily choosing the upper or lower of two vertebral bodies, the average κ among paired interpreters increased by an average of 0.195 to a mean κ of 0.629, indicating substantial agreement. Moreover, 12 of 36 corrected comparisons yielded κ > 0.8, indicating excellent agreement among observers.

Impact of vertebral exclusion on T-score

Given that observers differ in their application of the ISCD vertebral exclusion criteria, it is important to determine the impact of interobserver differences on final T-

TABLE 3. EXAMPLE OF INTERPRETER DISAGREEMENT REGARDING VERTEBRAL EXCLUSION FOR COMPARATIVE CRITERIA

Vertebra	BMD (g/cm²)	T-score	Bone area (cm²)	BMC	Interpreters' decisions
L_1	0.815	−2.9	15.7	12.8	Interpreters 2 and 3 exclude for T-score discrepancy and lack of increase in BMC
L_2	0.722	−4.3	17.2	12.4	Interpreters 1 and 4 exclude for T-score discrepancy and lack of increase in BMC
L_3	0.954	−2.4	18.2	17.4	Interpreters 2 and 3 exclude for T-score discrepancy
L_4	0.999	−2.0	14.9	14.9	All interpreters exclude for lack of increase bone area and BMC

TABLE 4. Improvement in κ Statistic After Correction for Paired Vertebral Analysis

	Mean κ statistic* for paired vertebrae (range)	Mean improvement in κ† (range)
L_1/L_2		
T-score discrepancy	0.725 (0.559, 0.910)	0.220 (0.059, 0.318)
Bone area	0.373 (0.149, 0.865)	0.272 (0.106, 0.601)
BMC	0.603 (0.465, 0.881)	0.266 (0.136, 0.343)
L_3/L_4		
T-score discrepancy	0.832 (0.756, 0.881)	0.145 (0.087, 0.201)
Bone area	0.749 (0.609, 0.927)	0.097 (0.036, 0.182)
BMC	0.496 (0.124, 0.835)	0.170 (0.090, 0.255)

*Cut-points for κ: κ ≤ 0, poor agreement; 0 < κ ≤ 0.2, slight agreement; 0.2 < κ ≤ 0.4, fair agreement; 0.4 < κ ≤ 0.6, moderate agreement; 0.6 < κ ≤ 0.8, substantial agreement; 0.8 < κ, excellent agreement.
†Improvement relative to L_1 for L_1/L_2 pair and relative to L_4 for L_3/L_4 pair.

scores. Excluding those studies deemed not assessable by at least one interpreter ($n = 36$), the mean lumbar spine T-score was −1.55 ± 1.32 for interpreter 1, −1.70 ± 1.29 for interpreter 2, −1.82 ± 1.29 for interpreter 3, and −1.85 ± 1.29 for interpreter 4 ($p > 0.05$ by ANOVA and subsequent pairwise comparisons). For all 200 BMD reports, the mean lumbar spine T-score was −1.36 ± 1.46 for interpreter 1, −1.45 ± 1.48 for interpreter 2, −1.68 ± 1.43 for interpreter 3, and −1.73 ± 1.40 for interpreter 4 ($p > 0.05$ by ANOVA and subsequent pairwise comparisons).

Using linear regression to assess the relationship of lumbar spine T-scores between observer pairs, we determined regression equations, correlation coefficients, and SE of the estimate. Scatter plots and summarized statistics are shown in Fig. 3. All correlation coefficients exceeded 0.88. The mean difference (Δ) and SE of the estimate in lumbar spine T-score among reports and between paired observers ranged from 0.05 and 0.47 (interpreters 3 and 4) to 0.28 and 0.63 (interpreters 1 and 4), respectively. The SE of the estimate is a measure of the distance between an average data point and the regression line and provides an additional measure of agreement among observers.

Despite good correlation in T-score, review of Fig. 3 shows that, between interpreters, the final diagnostic category may differ substantially. Overall, changes in diagnostic category ranged from 18 (observers 3 and 4) to 30 patients (observers 1 and 4). For example, osteoporosis,

osteopenia, and normal bone mass were diagnosed by DXA in 50, 66, and 80 men by interpreter 1 and 54, 69, and 53 men by interpreter 4. Among 176 men with T-scores provided by both interpreters, 30 (17%) experienced a change in diagnostic category between interpreters, moving down to a lower bone mass category in all but six cases with interpreter 4 compared with interpreter 1.

We found that interobserver disparities in T-scores could be attributed largely to disagreement regarding the presence of FSD. For example, interpreters 2 and 4 agreed fully on the presence of FSD among four vertebral bodies for 76 reports, and the mean T-score was −1.68 ± 1.51 and −1.69 ± 1.54 for these reports, respectively ($p = 0.93$ by paired t-test). Conversely, for the BMD reports with less than full agreement regarding FSD ($n = 124$), interpreters 2 and 4 had significantly different mean T-scores (−1.32 ± 1.44 and −1.75 ± 1.28, respectively, $p = 0.0001$). Complete data are summarized in Table 2.

DISCUSSION

Although bone turnover markers, ultrasound, and quantitative CT scanning each predict fragility fracture,[5-10] BMD measured by DXA remains the gold standard for osteoporosis diagnosis and fracture risk assessment in clinical practice.[1-5,12] However, DXA is an imperfect tool for various reasons including artifacts such as degenerative arthritis, aortic calcification, and scoliosis.[11,12] Because DXA is widely used to diagnose and manage metabolic bone disease, methods that improve the quality of DXA interpretation will thereby improve patient care. Indeed, consistent interpretation is crucial to quality patient care and the conduct of multicenter studies using BMD endpoints. As standardization of diagnostic criteria for vertebral fracture has proven beneficial to clinical investigation and patient care,[14-19] a similar benefit may be anticipated from successful standardization of BMD interpretation.

The ISCD has taken an important first step in standardizing BMD interpretation, by developing criteria for vertebral body exclusion. However, whereas the exclusion criteria seem straightforward, we have shown that their application is problematic and variable, even among ISCD-certified physicians. Contrary to our expectation of good agreement among interpreters, we find that agreement generally falls into the moderate range and leads to disagreement in diagnostic classification. This disagreement among

A
r = 0.93 (0.90-0.94)
Δ = 0.15 + 0.55
SEE = 0.54

Interpreter 2 / Interpreter 1

B
r = 0.92 (0.89-0.94)
Δ = 0.25 ± 0.60
SEE = 0.55

Interpreter 3 / Interpreter 1

C
r = 0.88 (0.84-0.91)
Δ = 0.28 ± 0.65
SEE = 0.63

Interpreter 4 / Interpreter 1

D
r = 0.94 (0.92-0.96)
Δ = 0.10 ± 0.15
SEE = 0.48

Interpreter 3 / Interpreter 2

E
r = 0.92 (0.89-0.94)
Δ = 0.14 ± 0.56
SEE = 0.55

Interpreter 4 / Interpreter 2

F
r = 0.94 (0.92-0.95)
Δ = 0.05 ± 0.49
SEE = 0.47

Interpreter 4 / Interpreter 3
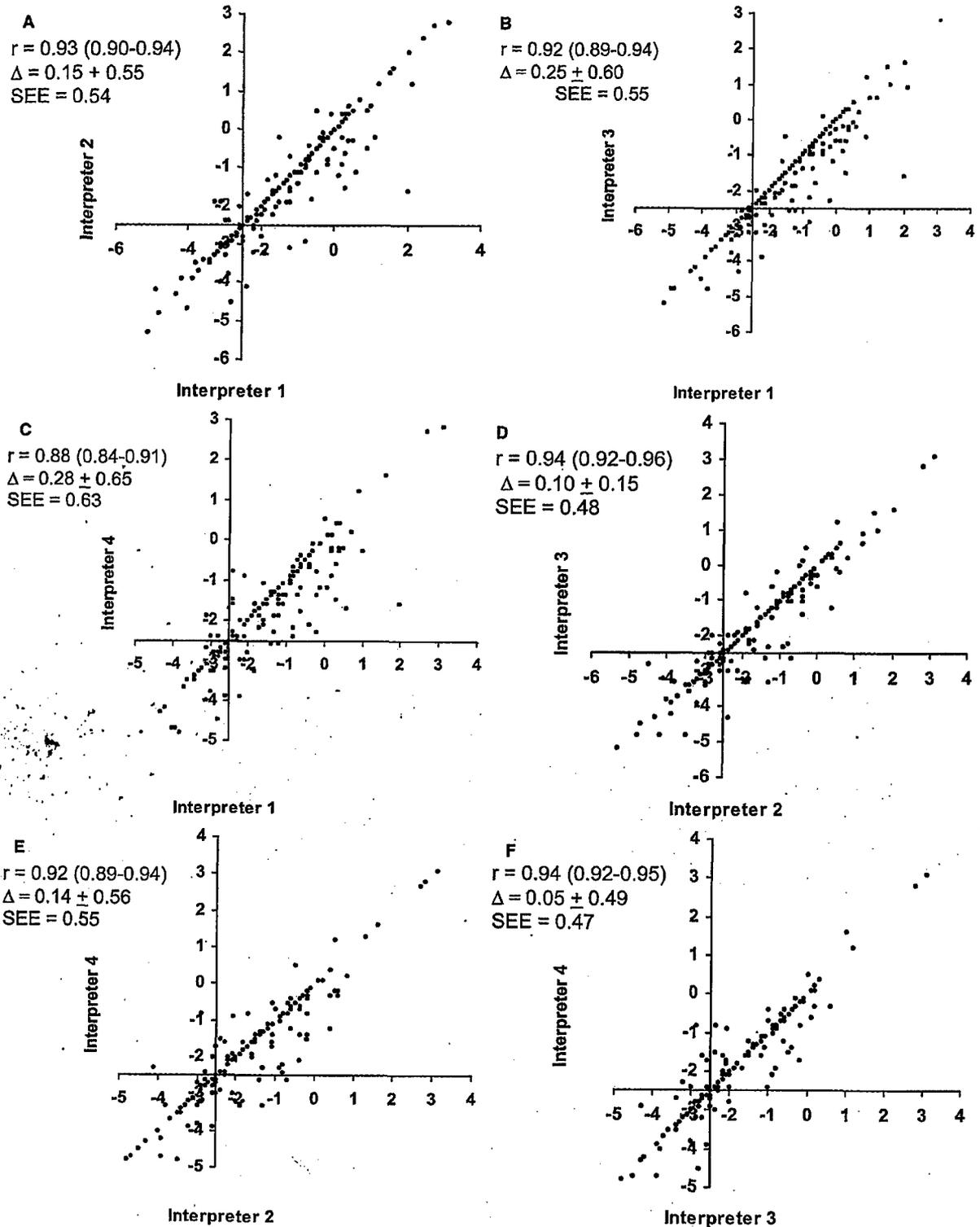
FIG. 3. Scatterplots of T-scores. Axes are set at –2.5 to highlight disagreements regarding densitometric diagnostic categories. For all regressions, $p < 0.00001$. In the equations, observer specific T-scores are denoted by T_i. (A) Observers 1 and 2, $T_2 = -0.28 + (0.90 \times T_1)$, $r = 0.93$, SEE = 0.54. (B) Observers 1 and 3, $T_3 = -0.43 + (0.89 \times T_1)$, $r = 0.92$, SEE = 0.55. (C) Observers 1 and 4, $T_4 = -0.48 + (0.87 \times T_1)$, $r = 0.88$, SEE = 0.63. (D) Observers 2 and 3, $T_3 = -0.21 + (0.94 \times T_2)$, $r = 0.94$, SEE = 0.48. (E) Observers 2 and 4, observer $4 = -0.25 + (0.93 \times T_2)$, $r = 0.92$, SEE = 0.55. (F) Observers 3 and 4, $T_4 = -0.13 + (0.94 \times T_3)$, $r = 0.94$, SEE = 0.47.

observers is secondary to differing thresholds for recognizing FSD, with a trend toward a lower final T-score among interpreters with lower thresholds for noting FSD and inconsistent exclusion of either the upper or lower vertebra from a discordant pair. Nevertheless, despite differences in vertebral exclusion, a strong linear relationship between interpreters is noted with respect to lumbar spine T-scores.

Determining when to exclude a vertebral body because of a FSD is the most subjective of the four ISCD exclusion criteria. Thus, it is not surprising that the greatest disagreement between interpreters was observed when applying this exclusion criterion. We sought, but did not find, evidence suggesting that differing thresholds for FSD are related to experience (data not shown). Moreover, when we reviewed the data reported herein, disagreements among us focused on whether FSD were of sufficient severity to warrant vertebral exclusion rather than on whether a FSD was present. Our data suggest that progress in standardizing DXA interpretation therefore will require establishment of uniform FSD definitions. Such standardization might be accomplished in any of several ways, each of which has advantages and disadvantages. One possible approach is to develop and use an atlas of FSD when training densitometrists. A second potential strategy would require that vertebral body exclusion because of FSD be accompanied by an ancillary exclusion criterion, such as an unusual discrepancy in T-score. Third, plain radiographs could be used to confirm an FSD before excluding the vertebral body. Finally, software is under development to identify differences in the digital image pixel density of each vertebra, allowing such differences to be highlighted as potential FSD in the printed report. Thus, whereas reaching consensus on FSD may be a difficult task, it is achievable in principle with adequate discussion among the bone community.

The other three ISCD exclusion criteria are based on numerical data; the only subjective decision is which of two vertebral bodies to exclude. For example, if there is a lack of increase in bone area from L_1 to L_2, the interpreter could choose to exclude L_1 or L_2. Such minimal subjectivity is likely responsible for the stronger agreement between observers when applying these three exclusion criteria. Nevertheless, we found that agreement among observers is better still if one corrects for arbitrarily excluding one or the other of a discordant vertebral body pair. Specific guidance regarding which vertebra of a pair should be excluded is therefore an important step in refining the vertebral exclusion criteria. Such guidance could be incorporated into bone density software, which could in turn highlight discordant pairs in the printed report, eliminating the possibility of arithmetic errors and allowing an interpreter to exclude vertebral bodies with more consistency.

Our study has several important limitations. Only DXA scans of predominantly white male veterans were evaluated. Reproducibility may be different among women and among subjects with more varied ethnic backgrounds. Another limitation of our study is the use of a single densitometer and technician; the performance characteristics of different technicians and instruments may affect scan performance. Most importantly, the data presented here offer no guidance regarding "best practice" in applying the ISCD

exclusion criteria. It remains an open question whether the exclusion criteria in general, and the various thresholds for recognizing FSD in particular, improve the ability of spinal BMD to predict fracture. Such guidance will ultimately require that various interpretation schemes be prospectively related to incident fractures. Other areas for future study include validation of our findings in different patient groups and a more systematic analysis of reader experience on DXA interpretation.

We conclude that, despite their apparent simplicity, the ISCD criteria for vertebral body exclusion are difficult to apply consistently. Differences in interpretation are caused by differing thresholds for FSD and choice of which vertebra of a discordant pair to exclude. Refinement of exclusion criteria can overcome both sources of disagreement.

ACKNOWLEDGMENTS

REFERENCES

1. Kanis JA, Johnell O, Oden A, Josson B, De Laet C, Dawson A 2000 Risk of hip fracture according to the World Health Organization criteria for osteopenia and osteoporosis. Bone 27:585–590.
2. Kanis JA 1994 Assessment of fracture risk and its application to screening for postmenopausal osteoporosis: Synopsis of a WHO report. Osteoporos Int 4:368–381.
3. Marshall D, Johnell O, Wedel H 1996 Meta-analysis of how well measures of bone mineral density predict occurrence of osteoporotic fractures. BMJ 312:1254–1259.
4. Schott AM, Cormier C, Hans D, Favier F, Hausherr E, Dargent-Molina P, Delmas PD, Ribot C, Sebert JL, Breart G, Meunier PJ 1998 How hip and whole-body bone mineral density predict hip fracture in elderly women. The EPIDOS prospective study. Osteoporos Int 8:247–254.
5. Garnero P, Hausherr E, Chapuy MC, Marcelli C, Grandjean H, Muller C, Cormier C, Breat G, Meunier PJ, Delmas PD 1996 Markers of bone resorption predict hip fracture in elderly women: The EPIDOS Prospective Study. J Bone Miner Res 11:1531–1538.
6. Dick IM, Devine A, Li S, Dhaliwal SS, Prince RL 2003 The T869C TGF polymorphism is associated with fracture, bone mineral density, and calcaneal quantitative ultrasound in elderly women. Bone 33:335–341.
7. Pinheiro MM, Castro CH, Frisoli A Jr, Szejnfeld VL 2003 Discriminatory ability of quantitative ultrasound measurements is

similar to dual energy X-ray absorptiometry in a Brazilian women population with osteoporotic fracture. Calcif Tissue Int 73:555–564.

8. Khaw KT, Reeve J, Luben R, Bingham S, Welch A, Wareham N, Oakes S, Day N 2004 Prediction of total and hip fracture risk in men and women by quantitative ultrasound of the calcaneus: EPID-Norfolk prospective population study. Lancet 363:197–202.

9. Rehman Q, Lang T, Modin G, Lane NE 2002 Quantitative computed tomography of the lumbar spine, not dual x-ray absorptiometry, is an independent predictor of prevalent vertebral fractures in postmenopausal women with osteopenia receiving long-term glucocorticoid and hormone-replacement therapy. Arthritis Rheum 46:1292–1297.

10. Crawford RP, Cann CE, Keaveny TM 2003 Finite element models predict in vitro vertebral body compressive strength better than quantitative computed tomography. Bone 33:744–750.

11. Genant HK, Engelke K, Fuerst T, Gluer CC, Grampp S, Harris ST, Jergas M, Lang T, Lu Y, Majumdar S, Mathur A, Takada M 1996 Noninvasive assessment of bone mineral and structure; state of the art. J Bone Miner Res 11:707–730.

12. Lenchick L, Leib ES, Hamdy RC, Binkley NC, Miller PD, Watts NB 2002 Executive Summary: International Society for Clinical Densitometry Position Development Conference. J Clin Densitom 5:S1–S3.

13. Svirbely JR Sriram MG 2004 The Medical Algorithms Project. Available online at http://www.medal.org/ch39.html. Accessed on July 1, 2004.

14. Black DM, Palermo L, Nevitt MC, Genant HK, Christensen L, Cummings SR 1999 Defining incident vertebral deformity: A prospective comparison of several approaches. The Study of Osteoporotic Fractures Research Group. J Bone Miner Res 14:90–101.

15. Grigoryan M, Guermazi A, Roemer FW, Delmas PD, Genant KH 2003 Recognizing and reporting osteoporotic vertebral fractures. Eur Spine J 12(Suppl 2):S104–S112.

16. Lunt M, Ismail AA, Felsenberg D, Cooper C, Kanis JA, Reeve J, Silman AJ, O'Neill TW 2002 Defining incident vertebral deformities in population studies: A comparison of morphometric criteria. Osteoporos Int 13:809–815.

17. McCloskey EV, Spector TD, Eyres KS, Fern ED, O'Rourke N, Vasikaran S, Kanis JA 1993 The assessment of vertebral deformity: A method for use in population studies and clinical trials. Osteoporos Int 3:138–147.

18. Nevitt MC, Ettinger B, Black DM, Stone K, Jamal SA, Ensrud K, Segal M, Genant HK, Cummings SR 1998 The association of radiographically detected vertebral fractures with back pain and function: A prospective study. Ann Intern Med 128:793–800.

19. Metthis C, Weber U, O'Neill TW, Raspe H 1998 Health impact associated with vertebral deformities: Results from the European Vertebral Osteoporosis Study (EVOS). Osteoporos Int 8:364–372.

Address reprint requests to:
Karen E Hansen, MD
Mailbox 3244, UWHC
600 Highland Avenue
Madison, WI 53792, USA
E-mail: keh@medicine.wisc.edu

Laboratory Investigations

Dual Energy X Ray Absorptiometry of *ex vivo* HcB/Dem Mouse Long Bones: Left Are Denser Than Right

Gloria E. Lopez Franco,[1] Suzanne J. Litscher,[1] Tyriina K. O'Neil,[1] Michael Piette,[1] Peter Demant,[2]
Robert D. Blank[1,3]

[1]Section of Endocrinology, Department of Medicine, University of Wisconsin Medical School, 600 Highland Ave., Madison, WI 53792, USA
[2]Department of Molecular and Cellular Biology, Roswell Park Cancer Institute, Elm and Carlton Streets, Buffalo, NY 14263, USA
[3]Geriatrics Research, Education, and Clinical Center, William S. Middleton Veterans' Hospital, 2500 Overlook Terrace, Madison, WI 53705, USA

Abstract. Dual energy X ray absorptiometry (DXA) has become a popular analytical technique in mice and other small animals. Comparative study of bone properties at different anatomical sites is an active area of study in model organisms. Such investigations require that site-specific data be generated and interpreted. There are no published data addressing the degree to which contralateral mouse bones resemble each other in the absence of an experimental intervention, nor are there data addressing the correlation of bone densitometry measurements between anatomically distant sites. To address these gaps in our knowledge, we used DXA to compare excised mouse femora and humeri. At the population level, left bones were slightly but significantly denser than right bones, with an overall adjusted bone mineral density (BMD) difference of 0.7 ± 0.3 and 0.5 ± 0.2 mg/cm^2 at the femur and humerus, respectively. At the level of bone pairs from a single animal, absolute adjusted BMD disparities between the right and left sides were 2.3 ± 1.9 mg/cm^2 at the femur and 1.7 ± 1.4 mg/cm^2 at the humerus. Correlation coefficients between left and right sides were 0.78 for adjusted BMD at both sites. The correlation coefficient between side-averaged femoral and humeral BMD was 0.81, but ranged between 0.70 and 0.75 when limited to ipsilateral or contralateral femur-humerus pairs. Our findings suggest the desirability of randomizing limbs for treatment in studies using contralateral limb controls. These observations may represent the densitometric manifestation of behavioral and neuroanatomical lateralization in laboratory mice.

Key words: Bone density technology — Bone development — Osteoporosis of animal models

Dual energy X-ray absorptiometry (DXA) has the most widely used imaging methodology to assess risk of fragility fracture. In addition to its documented ability to

Correspondence to: Gloria E. Lopez Franco; E-mail: gel@medicine.wisc.edu

stratify patients for fracture risk, examination is accurate, precise, noninvasive, and entails only modest radiation exposure. Moreover, examination is feasible at the lumbar spine, hip, and wrist, corresponding to common fracture sites. These features make DXA an attractive choice for diagnosing osteoporosis, following patients to monitor effectiveness of therapy for osteoporosis, and as a surrogate endpoint for fracture in clinical investigation. Correspondingly, DXA has become a popular analytical technique in mice and other small animals, either as a substitute for more demanding techniques, such as biomechanical testing, histomorphometry, and gravimetry, or as an adjunct to them.

Recent progress in skeletal genetics and success in continuing efforts to develop bone pharmaceuticals have been achieved in large part through studies performed in rodents. As small animal skeletal research continues, more detailed questions regarding differences in the behavior of cortical and trabecular bone and at different anatomical sites are becoming ever more prominent. For example, several laboratories have devised methods for imposing investigator-specified loading (e.g. [1–8]) and unloading (e.g. [9–13]) regimens on a single limb, using the contralateral limb as a control. Similarly, experimental investigations of fracture healing (e.g. [14–20]) in small animal models routinely use contralateral limb controls. Such experiments require that site-specific data be generated and interpreted.

As in humans, site-specificity of bone mineral density (BMD) has been reported in mice [21–24]. Regardless of species, site-specificity has been sought primarily in comparisons of skeletal sites with marked differences in the proportion of cortical to trabecular bone. Therefore, little is known regarding the extent to which anatomically distant cortical bone sites resemble each other densitometrically. Existing rodent site-specificity data are therefore insufficient to help guide interpretation of

comparative densitometry of left and right bones, as there are no published data addressing the degree to which contralateral bones are similar in the absence of an experimental intervention. In order to address these gaps in our knowledge, we undertook a comparison of excised mouse femora and humeri using DXA.

We report here that right-left correlations at each of these sites are high, as are intersite correlations using side-averaged data. These findings demonstrate the impact of region of interest analyses on measurement precision relative to whole-body analyses. Moreover, our experiments revealed that left bones have slightly but significantly greater BMD than right bones. This unexpected observation has practical implications for mouse DXA study.

Materials and Methods

Mice

The mice in this study were F1 and F2 offspring of a reciprocal intercross between recombinant congenic strains HcB/13Dem and HcB/14Dem [25, 26]. The parental strains were the most divergent of 24 recombinant congenic strains for failure load [26], and the DXA data reported here were obtained in the course of a linkage study for biomechanical performance using these strains. In our original survey of the HcB recombinant congenics, HcB/13 and HcB/14 femora had ash percentages of $67.0 \pm 0.7\%$ and $70.1 \pm 0.9\%$ (mean $\pm$ s.d.), respectively [26]. Subsequent ashing and DXA experiments confirm the initial observation (not shown). Included were 98 males and 101 females from the HcB/13 X HcB/14 arm and 103 males and 102 females from the HcB/14 X HcB/13 arm of the cross. Both F1 and F2 animals were included, and both sexes were pooled for analysis. Animals were housed at 2–5 animals/500 cm^2 cage on corncob bedding, fed laboratory rodent chow 5001 (PMI Nutrition International, Richmond, IN) and tap water *ad lib* and exposed to 12 hour light/12 hour dark cycle. Animals were sacrificed at 17 ± 1 weeks of age by CO_2 asphyxiation. Femora, humeri, and radii were dissected free of soft tissue immediately following sacrifice, wrapped in phosphate-buffered saline-saturated gauze, and stored at $-70°C$ until analysis. The animal protocol was approved by the University of Wisconsin and the William S. Middleton Veterans' Hospital IACUCs.

DXA Scanning

Dissected bones were scanned using the PIXImus (GE Lunar, Madison, WI) densitometer and software version 1.45.023. We scanned a manufacturer-provided phantom daily during data collection to confirm the instrument's calibration and precision. Bones were allowed to equilibrate to room temperature prior to scanning. All bones from a single animal were examined in the same scan. Bones were positioned manually in air on a 7 mm thick Plexiglas platform provided by the instrument manufacturer to achieve similar orientations for right and left bones. Acquisition time per scan was approximately 5 minutes. The primary analysis was performed using software version 1.45.023. We manually adjusted regions of interest to analyze each of the bones individually, excluding any bones with edges that were incorrectly identified by the software. We adjusted for bone position by multiple linear regression as described [27]. Briefly, the adjustment algorithm was developed by scanning a reference set of bones at varied positions within the PIXImus field prior to ashing. BMD was

then modeled by stepwise multiple linear regression and the final model included mineral content by ashing, X-coordinate within the scanning field, and Y-coordinate within the scanning field as significant independent variables, while distance from the center of the scanning field was not a significant independent variable. For the adjustment used here (software version 1.45 in air), the overall R^2 value is 0.95 and the ΔR^2 obtained by adjusting for X and Y coordinates are 0.027 and 0.003, respectively.

Statistics

Statistical calculations were performed using SigmaStat for Windows, version 2.03 (SPSS, Chicago, IL). Accrued data were tested for normality by the Kolmogorov-Smirnov test. Comparisons between left and right sides were made by paired Student's t test. Categorical comparisons were performed by χ^2. Comparisons between different skeletal sites were analyzed by Pearson product moment correlation or Spearman's rank order correlation. Significance level was $P < 0.05$ and adjusted by Bonferroni's correction to account for multiple comparisons. Data are reported as mean $\pm$ standard deviation unless noted otherwise.

Results

Data obtained from 403 animals were included in this study, including 401 pairs of femora, and 394 pairs of humeri. The number of pairs of bones studied at each site is less than the total number of animals because of breakage or loss. Descriptive statistics of BMD, BMC, and bone area revealed that while adjusted BMD and BMC are normally distributed at both skeletal sites, bone area is skewed at both ($P < 10^{-5}$), with a greater fraction of the distribution having larger than modal bone areas regardless of side, sex, or cross arm.

Left-sided Bones are Denser Than Right sided Bones

At both sites, BMD was significantly higher for the left than for the right side (Table 1). The side disparities did not arise as a result of anomalous data from a relatively small number of bones, but reflect a population-wide pattern. We compared the number of mice in which the left value was greater and the number of mice in which the right value was greater for each measurement and each site and found significantly more left values to be greater for BMD at both sites. Left-right disparities of BMC mirrored the BMD findings, while bone area did not differ significantly between the left and right sides at either site (not shown).

Intersite BMD Correlations

Scatterplots relating left and right BMD at the femur and humerus are shown in Figure 1. These data show equal, moderately strong correlations of 0.78 ($P < 10^{-5}$) between sides at both sites.

Our original goal in performing DXA on several long bones of the same animals was to determine how highly correlated BMD was at the various sites. These corre-

Table 1. Comparison of DXA measurements of left and right bones at 2 sites

	Femur		Humerus	
	Left	Right	Left	Right
Adjusted BMD (mg/cm^2)	57.0 ± 4.4 $P < 10^{-5}*$	56.3 ± 4.2	42.2 ± 3.4 $P = 3 \times 10^{-5}$	41.7 ± 3.3
Mean Δ (mg/cm^2)	0.7 ± 0.3		0.5 ± 0.2	
Mean Abs Δ (mg/cm^2)	2.3 ± 1.9		1.7 ± 1.4	
# greater[+]	256 $P < 10^{-5}**$	155	240 $P = 1.5 \times 10^{-5}**$	154

Mean Δ = mean (difference between left and right bones)
Mean Abs Δ = mean absolute value (difference between left and right bones)
*Paired t test
**χ^2, 1 degree of freedom
[+] Equal values for both sides counted as 0.5 for left and 0.5 for right
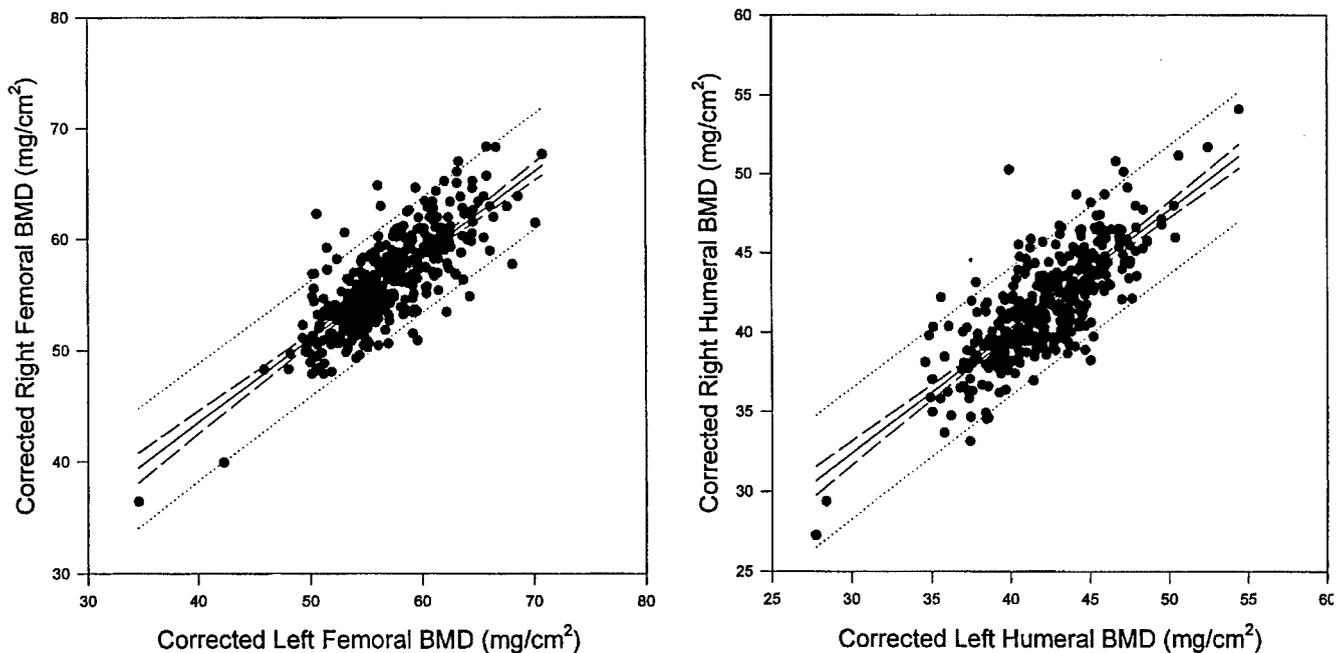
Fig. 1. Scatterplots of left and right BMD. Left, femur; right, humerus. Individual data points are adjusted BMD.

lations for individual bones and side-averaged values are summarized in Table 2 and Figure 2.

The correlations between femur and humerus are nearly as strong as those between left and right bones at a single site.

Discussion

Animal models allow investigators to address a variety of experimental questions that could not be studied, or could be studied only with great difficulty in human subjects. Many of these feature experimental intervention in one limb and use of the contralateral limb as a control. DXA scanning in these experiments serves a variety of related functions. One such is to use BMD or BMC as a surrogate measurement for more technically demanding methods such as gravimetry. Another is to

Table 2. Intersite correlation of BMD

	Femur/Humerus				
	L/L	L/R	R/L	R/R	Ave/Ave
BMD	0.75	0.70	0.71	0.71	0.80

Femoral side given first, L = left, R = right, Ave = average, $P < 10^{-5}$ for all correlations, Pearson product-moment correlation

evaluate an explanatory factor when biomechanical testing is performed. A third is to assess longitudinal changes in a single animal. Each of these applications requires understanding of both the performance characteristics of DXA scanning and the underlying biology of the effects being sought. We have addressed the for-
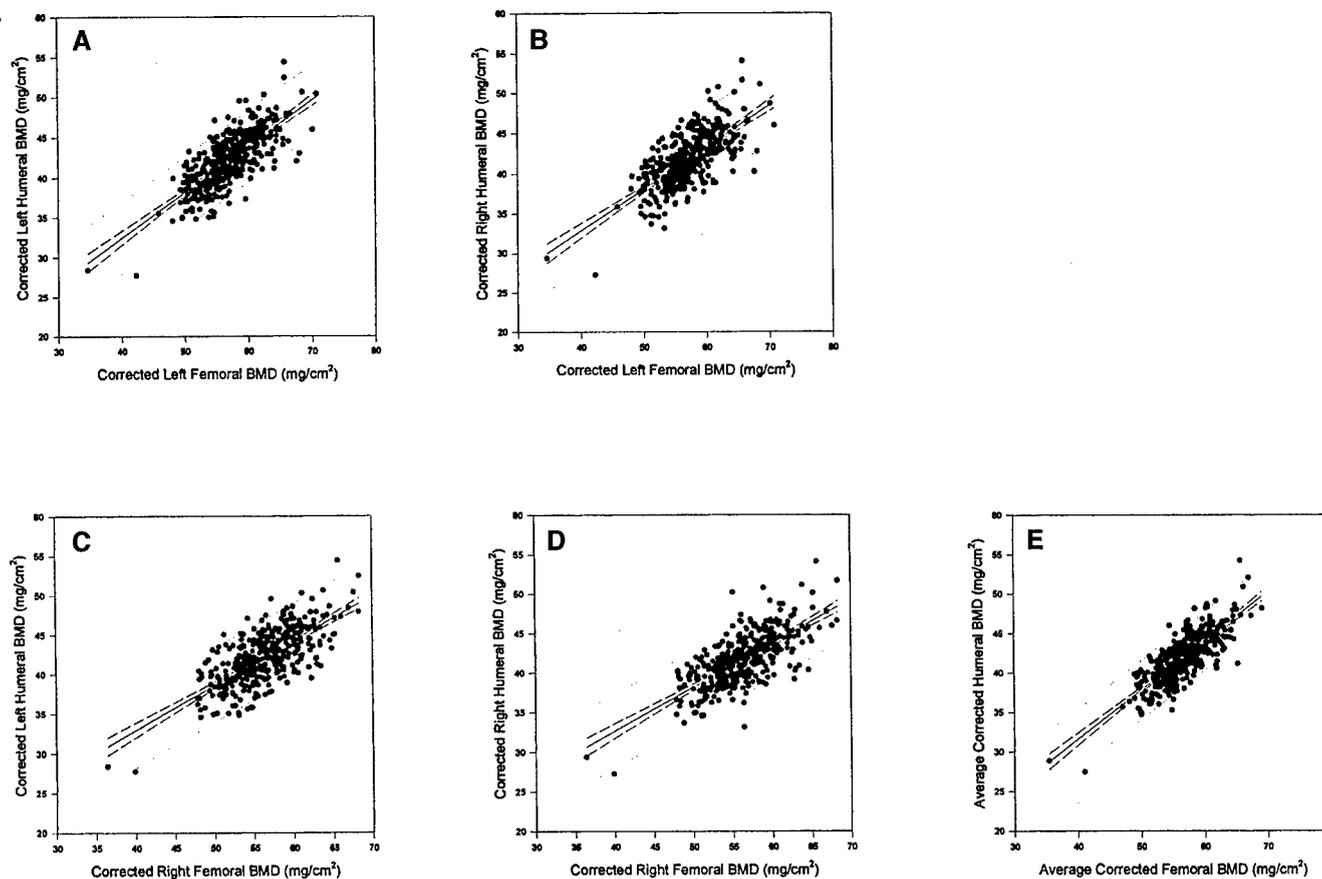
Fig. 2. Scatterplots of intersite BMD. **A** Left femur *v* left humerus; **B**. Left femur *v* right humerus, **C**. Right femur *v* left humerus, **D**. Right femur *v* right humerus, **E**. Average femur *v* average humerus. Individual data points are adjusted BMD.

mer elsewhere [27] and address the latter here. In a large experimental sample we have found small, but significant differences in BMD between the left and right sides at both the femur and the humerus. The average adjusted BMD differences between sides are approximately 2 mg/cm^2 at both sites. We report both the average difference between left and right bones and the absolute value of the difference because the absolute value of the difference is relevant in interpreting data obtained from paired limbs, as in studies in which one limb is treated while the contralateral limb serves as an untreated control. Further, we report that correlation between sides was moderately high at 0.78, and only slightly poorer between sites.

The magnitude of the absolute right/left difference is comparable with that arising from biologically important interventions [28–30]). The implication is that studies in which intervention is applied to one limb with the contralateral limb serving as a control should be randomized for whether the right or left limb is treated. This is at variance with usual practice of assigning either the left or right limb for intervention in all animals. The additional burden to investigators is small, yet protects against a potentially significant source of experimental bias. Similarly, in longitudinal studies assessing regions

of interest, care should be taken to compare the same side at each measurement in each animal. That said, it is important to note that left-right side disparities have not yet been documented in most mouse strains or in other small animal species used for limb comparison experiments. Similarly, our study was limited to data acquired by DXA; we have not rigorously proven that either micro-CT scanning or histomorphometry would reveal left-right disparities. In the absence of such data, we consider it prudent to advise randomization of limbs until data showing the absence of side disparities become available.

While our data represent, to the best of our knowledge, the first skeletal evidence of hemispheric dominance in mice, the issue of dominance has been addressed in different contexts. Others have investigated lateralization in mice using behavioral [31–38] and neuroanatomic [39, 40] assays. These earlier studies all support the interpretation that our BMD findings reflect the animals' true biology, and suggest that a majority of them are left-dominant. Taken together, these observations support the notion that mice display lateralization, but that little is known regarding either the most reliable methods of measuring it or the mechanisms underlying it.

We observed only a moderately high correlation of 0.78 between left and right BMDs at either the femur or

the humerus, much lower than the correlation observed between right and left hips in humans [41–46]. In addition, we obtained higher intersite correlations between side-averaged data than for either ipsilateral or contralateral comparisons. Lastly, we found that bone area is not normally distributed in our sample. Each of these findings reflects the relatively large pixel size (0.18 mm × 0.18 mm) relative to the bones studied, as we have discussed elsewhere in greater detail [27]. Averages obtained from 2-paired measurements are expected to be closer to the true values than either measurement taken individually. That side-averaged data are more highly correlated between anatomic sites than ipsilateral data and that the correlations of ipsilateral and contralateral intersite data are equivalent demonstrates that the magnitude of individual measurement errors is large relative to the differences between right-and left-sided data. Comparison of unilateral and bilateral femur BMD measurement in humans has led to a similar interpretation [44, 47]. Our reported intersite correlations are only slightly poorer than right/left correlations at a single anatomic site, suggesting that femoral BMD is highly predictive of humeral BMD and *vice versa*, supporting the notion that the various long bones share similar biology.

We were unable to find any prior reports of morphologic asymmetry of DXA traits in mice. In contrast, multiple human investigations have compared densitometric features of bones and related the observations to known or hypothesized differences in mechanical loading. Some investigators did not relate side comparisons to handedness [42, 44], while those who did disagree about the relationship of handedness to BMD [43, 45] and [48–50].

In addition to the caveats noted above, our study has several further limitations, which readers should bear in mind. The mice studied here derive approximately 3/4 of their genome from C3H/DiSnA and the other 1/4 of their genome from C57BL/10ScSnA.

Our results may not be generalizable to other strains of mice, let alone to other species. DXA scanning was performed *ex vivo* in air, with bones positioned on a specimen tray provided by the instrument manufacturer, and were studied individually. The PIXImus instrument and software are designed for optimal performance in scanning intact animals for total body BMD. The PIXmus instrument we used demonstrated a significant, systematic error that depended on specimen position [27].

In spite of these limitations and adjustment for them, the large number of specimens allowed us to reveal a small but significant difference in right and left long bone BMD. In this regard, the data are similar in nature to those obtained in clinical studies of blood pressure. In blood pressure studies, each individual measurement is subject to error of a magnitude that usually exceeds the treatment effect. However, the treatment effect can still be detected with a sufficient sample size. Indeed, power

calculations using our reported precision data for *ex vivo* PIXImus densitometry [27] suggest that our sample's power to detect BMD disparities of the observed magnitude approaches unity. Given the minor additional effort required to assimilate our findings into the design of future studies, we believe that our data provide a biological basis for preferring that single-limb interventions in mice be randomized prospectively.

References

1. Turner CH, Akhter MP, Raab DM, Kimmel DB, Recker RR (1991) A noninvasive, in vivo model for studying strain-adaptive bone modeling. Bone 12:73–79
2. Chambers TJ, Evans M, Gardner TN, Turner-Smith A, Chow JW (1993) Induction of bone formation in rat tail vertebrae by mechanical loading. Bone Miner 20:167–178
3. Torrance AG, Mosley JR, Suswillo RF, Lanyon LE (1994) Noninvasive loading of the rat ulna in vivo induces a strain-related modeling response uncomplicated by trauma or periostal pressure. Calcif Tissue Int 54:241–247
4. Hillam RA, Skerry TM (1995) Inhibition of bone resorption and stimulation of formation by mechanical loading of the modeling rat ulna in vivo. J Bone Miner Res 10:683–689
5. Forwood MR, Bennett MB, Blowers AR, Nadorfi RL (1998) Modification of the in vivo four-point loading model for studying mechanically induced bone adaptation. Bone 23:307–310
6. Yingling VR, Davies S, Silva MJ (2001) The effects of repetitive physiologic loading on bone turnover and mechanical properties in adult female and male rats. Calcif Tissue Int 68:235–239
7. Gross TS, Srinivasan S, Liu CC, Clemens TL, Bain SD (2002) Noninvasive loading of the murine tibia: an in vivo model for the study of mechanotransduction. J Bone Miner Res 17:493–501
8. Guo XE, Eichler MJ, Takai E, Kim CH (2002) Quantification of a rat tail vertebra model for trabecular bone adaptation studies. J Biomech 35:363–368
9. Yonezu H, Ikata T, Takata S, Shibata A (1999) Effects of sciatic neurectomy on the femur in growing rats: application of peripheral quantitative computed tomography and Fourier transform infrared spectroscopy. J Bone Miner Metab 17:259–265
10. Kodama Y, Dimai HP, Wergedal J, et al. (1999) Cortical tibial bone volume in two strains of mice: effects of sciatic neurectomy and genetic regulation of bone response to mechanical loading. Bone 25:183–190

11. Nakamura H, Morita S, Kumei Y, Aoki K, Shimokawa H, Ohya K, Shinomiya KI (2001) Effects of neurectomy and tenotomy on the bone mineral density and strength of tibiae. Acta Astronaut 49:179–190

12. Yamashita T, Sekiya I, Kawaguchi N, Kashimada K, Nifuji A, Nabeshima YI, Noda M (2001) Klotho-deficient mice are resistant to bone loss induced by unloading due to sciatic neurectomy. J Endocrinol 168:347–351

13. Ito M, Nishida A, Nakamura T, Uetani M, Hayashi K (2002) Differences of three-dimensional trabecular microstructure in osteopenic rat models caused by ovariectomy and neurectomy. Bone 30:594–598

14. Hiltunen A, Vuorio E, Aro HT (1993) A standardized experimental fracture in the mouse tibia. J Orthop Res 11:305–312

15. Olmedo ML, Weiss AP (1994) An experimental rat model allowing controlled delivery of substances to evaluate fracture healing. J Orthop Trauma 8:490–493

16. Chakkalakal DA, Strates BS, Mashoof AA, Garvin KL, Novak JR, Fritz ED, Mollner TJ, McGuire MH (1999) Repair of segmental bone defects in the rat: an experimental model of human fracture healing. Bone 25:321–332

17. Andreassen TT, Fledelius C, Ejersted C, Oxlund H (2001) Increases in callus formation and mechanical strength of healing fractures in old rats treated with parathyroid hormone. Acta Orthop Scand 72:304–307

18. Kurth AH, Wang C, Hayes WC, Shea M (2001) The evaluation of a rat model for the analysis of densitometric and biomechanical properties of tumor-induced osteolysis. J Orthop Res 19:200–205

19. Meyer RA Jr., Tsahakis PJ, Martin DF, Banks DM, Harrow ME, Kiebzak GM (2001) Age and ovariectomy impair both the normalization of mechanical properties and the accretion of mineral by the fracture callus in rats. J Orthop Res 19:428–435

20. Uusitalo H, Rantakokko J, Ahonen M, Jamsa T, Tuukkanen J, KaHari V, Vuorio E, Aro HT (2001) A metaphyseal defect model of the femur for studies of murine bone healing. Bone 28:423–429

21. Beamer WG, Shultz KL, Donahue LR, Churchill GA, Sen S, Wergedal JR, Baylink DJ, Rosen CJ (2001) Quantitative trait loci for femoral and lumbar vertebral bone mineral density in C57BL/6 J and C3H/HeJ Inbred strains of mice. J Bone Miner Res 16:1195–1206

22. Sheng MH, Baylink DJ, Beamer WG, Donahue LR, Lau KH, Wergedal JE (2002) Regulation of bone volume is different in the metaphyses of the femur and vertebra of C3H/HeJ and C57BL/6 J mice. Bone 30:486–491

23. Turner CH, Hsieh YF, Muller R, Bouxsein ML, Baylink DJ, Rosen CJ, Grynpas MD, Donahue LR, Beamer WG (2000) Genetic regulation of cortical and trabecular bone strength and microstructure in inbred strains of mice. J Bone Miner Res 15:1126–1131

24. Masinde GL, Li X, Gu W, Wergedal J, Mohan S, Baylink DJ (2002) Quantitative trait loci for bone density in mice: the genes determining total skeletal density and femur density show little overlap in F2 mice. Calcif Tissue Int 71:421–428

25. Demant P, Hart AA (1986) Recombinant congenic strains–a new tool for analyzing genetic traits determined by more than one gene. Immunogenetics 24:416–422

26. Yershov Y, Baldini TH, Villagomez S, Young T, Martin ML, Bockman RS, Peterson MGE, Blank RD (2001) Bone strength and related traits in HcB/Dem recombinant congenic mice. J Bone Miner Res 16:992–1003

27. Lopez Franco GE, O'Neil TK, Litscher SJ, Urban-Piette M, Blank RD (2004) Accuracy and precision of PIXImus densitometry for *ex vivo* mouse long bones. J Clin Densitom 7:326–333

28. Samuels A, Perry MJ, Gibson R, Tobias JH (2001) Effects of combination therapy with PTH and 17beta-estradiol on long bones of female mice. Calcif Tissue Int 69:164–170

29. Mohan S, Richman C, Guo R, Amaar Y, Donahue LR, Wergedal J, Baylink DJ (2003) Insulin-like growth factor regulates peak bone mineral density in mice by both growth hormone-dependent and independent mechanisms. Endocrinology 144:929–936

30. Kasukawa Y, Baylink DJ, Wergedal JE, Amaar Y, Srivastava AK, Guo R, Mohan S (2003) Lack of insulin-like growth factor I exaggerates the effect of calcium deficiency on bone accretion in mice. Endocrinology 144: 4682–4689

31. Collins RL (1991) Reimpressed selective breeding for lateralization of handedness in mice. Brain Res 564:194–202

32. Betancur C, Neveu PJ, Le Moal M (1991) Strain and sex differences in the degree of paw preference in mice. Behav Brain Res 45:97–101

33. Biddle FG, Coffaro CM, Ziehr JE, Eales BA (1993) Genetic variation in paw preference (handedness) in the mouse. Genome 36:935–943

34. Biddle FG, Eales BA (1996) The degree of lateralization of paw usage (handedness) in the mouse is defined by three major phenotypes. Behav Genet 26:391–406

35. Biddle FG, Eales BA (1999) Mouse genetic model for left-right hand usage: context, direction, norms of reaction, and memory. Genome 42:1150–1166

36. Signore P, Chaoui M, Nosten-Bertrand M, Perez-Diaz F, Marchaland C (1991) Handedness in mice: comparison across eleven inbred strains. Behav Genet 21:421–429

37. Signore P, Nosten-Bertrand M, Chaoui M, Roubertoux PL, Marchaland C, Perez-Diaz F (1991) An assessment of handedness in mice. Physiol Behav 49:701–704

38. Waters NS, Denenberg VH (1994) Analysis of two measures of paw preference in a large population of inbred mice. Behav Brain Res 63:195–204

39. Cassells B, Collins RL, Wahlsten D (1990) Path analysis of sex difference, forebrain commissure area and brain size in relation to degree of laterality in selectively bred mice. Brain Res 529:50–56

40. Lipp HP, Collins RL, Nauta WJ (1984) Structural asymmetries in brains of mice selected for strong lateralization. Brain Res 310:393–396

41. Faulkner KG, Genant HK, McClung M (1995) Bilateral comparison of femoral bone density and hip axis length from single and fan beam DXA scans. Calcif Tissue Int 56:26–31

42. Bonnick SL, Nichols DL, Sanborn CF, Payne SG, Moen SM, Heiss CJ (1996) Right and left proximal femur analyses: Is there a need to do both? Calcif Tissue Int 58:307–310

43. Yang R, Tsai K, Chieng P, Liu T (1997) Symmetry of bone mineral density at the proximal femur with emphasis on the effect of side dominance. Calcif Tissue Int 61:189–191

44. Mazess RB, Nord R, Hanson JA, Barden HS (2000) Bilateral measurement of femoral bone mineral density. J Clin Densitom 3:133–140

45. Rao AD, Reddy S, Rao DS (2000) Is there a difference between right and left femoral bone density? J Clin Densitom 3:57–61

46. Wong JC, McEwan L, Lee N, Griffiths MR, Pocock NA (2003) The diagnostic role of dual femur bone density measurement in low-impact fractures. Osteoporos Int 14:339–344

47. Mazess RB (2000) Measuring both femora? J Clin Densitom 3:299–301

48. Dane S, Akar S, Hacibeyoglu I, Varoglu E (2001) Differences between right- and left-femoral bone mineral densities in right- and left-handed men and women. Int J Neurosci 111:187–192

49. Akar S, Sivrikaya H, Canikli A, Varoglu E (2002) Lateralized mineral content and density in distal forearm bones in right-handed men and women: relation of structure to function. Int J Neurosci 112:301–311

50. Sadeghi H, Allard P, Prince F, Labelle H (2000) Symmetry and limb dominance in able-bodied gait: a review. Gait Posture 12:34–45

ELSEVIER

1

Dental phenotype of the *colla2*^{oim} mutation: DI is present in both homozygotes and heterozygotes

Gloria E. Lopez Franco[a,*], Alice Huang[b], Nancy P. Camacho[b], Robert D. Blank[a,c]

[a]*Endocrinology Section, Department of Medicine, H4/556 CSC (5148), 600 Highland Avenue, Madison, WI 53792, USA*
[b]*Research Division, Hospital for Special Surgery, 535 East 70th Street, New York, NY 10021, USA*
[c]*Geriatrics Research, Education, and Clinical Center, William S. Middleton Veterans' Hospital, 2500 Overlook Terrace, Madison, WI 53705, USA*

Abstract

Dentinogenesis imperfecta (DI) is a common but variable feature of osteogenesis imperfecta (OI). The *Colla2*^{oim} mutation (*oim*) is a well-studied mouse model of chain deficiency OI. Heterozygous *oim*/+ mice have subtle skeletal fragility, while homozygous *oim*/*oim* mice have marked skeletal fragility. To further define the consequences of *oim* mutation, we examined teeth by light and scanning electron microscopy (SEM). The dental phenotype in *Colla2*^{oim} (*oim*) mice is more severe in incisors than in molars and includes changes in pulp chamber size, tooth shape, and dentin ultrastructure. Teeth in *oim*/*oim* animals are clinically fragile, while *oim*/+ teeth are grossly normal. Incisor pulp chamber areas (in μm^2) are: upper +/+ = 358 ± 75, lower +/+ = 671 ± 162, upper *oim*/+ = 161 ± 54, lower *oim*/+ = 156 ± 19, upper *oim*/*oim* = 6900 ± 1040, and lower *oim*/*oim* = 66 ± 62 ($P < 10^{-5}$). Incisor non-pulp chamber cross-sectional areas (in μm^2), reflecting dentin areas, are: upper +/+ = 39,000 ± 1670, lower +/+ = 35,600 ± 1980, upper *oim*/+ = 47,500 ± 2510, lower *oim*/+ = 26,000 ± 1830, upper *oim*/*oim* = 29,800 + 315, and lower *oim*/*oim* = 36,800 ± 3450 ($P < 10^{-5}$). Ultrastructural abnormalities are more pronounced in incisors than in molars and depend on dosage of the mutant allele. These include reduction in the number and regularity of spacing of the dentinal tubules, lesser mineralization, and blurring of the boundary between peritubular and intertubular dentin. Our findings demonstrate that both *oim*/*oim* and *oim*/+ mice suffer from DI. The more severe incisor phenotype may reflect incisors' continuous growth.
© 2005 Elsevier Inc. All rights reserved.

Keywords: Osteogenesis imperfecta; Dentin; Scanning electron microscopy; Mouse; Tooth

Introduction

Osteogenesis imperfecta (OI), also known as brittle bone disease, is an inherited clinical syndrome marked by skeletal fragility and associated abnormalities (reviewed by [1–3]). Nearly all cases are caused by mutations of the genes encoding type I collagen. In the most severe cases, OI is lethal in utero, while in the mildest cases it is subclinical [4–6]. The associated abnormalities include dentinogenesis imperfecta (DI), skin fragility, hearing loss, scleral discoloration, and other manifestations of connective tissue fragility. These varied clinical manifestations reflect the abundance of type I collagen in various connective tissues, including teeth, skin, ligaments, fasciae, and tendons.

Classical features of DI include discoloration of teeth, increased tooth fragility, and obliteration of the pulp chambers. Histological and ultrastructural abnormalities reported in human DI include a decreased number of irregularly shaped dental tubules, remnants of capillary inclusions, obliterated pulps, morphological abnormalities of dental collagen fibers, and mineralization defects [7–10].

Several murine models of OI exist, including the *Colla2*^{oim} (*oim*) mutation. This mutation is a frameshift of the gene encoding the α2 chain of type I collagen, resulting in quantitatively deficient α2(I) chain protein synthesis [11]. The resulting phenotype is obvious in *oim*/*oim* homozygotes, which display impaired growth and marked skeletal fragility [11]. Phenotypic abnormalities

---

* Corresponding author.
E-mail address: gel@medicine.wisc.edu (G.E. Lopez Franco).

54 are far more subtle in *oim/+* heterozygotes, but are never-
55 theless apparent by biomechanical testing [12,13]. Bio-
56 chemical manifestations of the mutation include reduced
57 collagen cross-linking [14], reduced apatite crystallinity
58 [15], and increased proline hydroxylation [14].
59   While considerable attention has been devoted to
60 characterizing bones in *oim/oim* and *oim/+* mice, the teeth
61 remain poorly characterized in mutants. To address this gap
62 in our understanding of the consequences of *oim* mutation,
63 we examined teeth in mice of all 3 *Col1a2* genotypes by
64 light and scanning electron microscopy (SEM). We report
65 that both *oim/+* and *oim/oim* display abnormal features that
66 are similar to those described in human DI, the phenotype
67 depends on both mutant allele dosage and the specific tooth
68 examined. In particular, we report the heterozygous pheno-
69 type is more pronounced in incisors than in molars and that
70 upper and lower incisors display different abnormalities of
71 pulp chamber size and morphology.

72 **Materials and methods**

73 *Mice*

74   Mice used in this study were male and female offspring
75 of *oim/+* parents and were genotyped at *Col1a2* at weaning
76 by direct sequencing [16]. Animals were maintained in a 12-
77 h light/dark photo period, were fed powdered, irradiated
78 PICO 5058 rodent chow (Purina, St. Louis, MO) and
79 autoclaved tap water ad lib, and housed in groups of up to 5
80 mice/500 cm^2 cage between weaning and sacrifice at 11
81 weeks of age. Following sacrifice by CO_2 asphyxiation at 11
82 weeks of age, heads were stored frozen until teeth were
83 dissected free of alveolar bone for study. This work satisfied
84 the Hospital for Special Surgery's requirements for the
85 ethical use of laboratory research animals.

86 *Light microscopy*

87   Whole teeth were examined using a Leica DM-LB
88 microscope at 5× magnification. Images were stored
89 digitally as TIFF files and labeled using Photoshop 5.0 LE
90 (Adobe Systems, San Jose, CA).

91 *SEM*

92   In order to examine pulp chamber size using SEM, we
93 fractured teeth at the level of the junctional epithelium.
94 Samples were air dried, sputter coated with platinum–
95 palladium, and imaged with a Hitachi S570 SEM with
96 Gatan Digital Capture System. To analyze the surface of
97 specimens over a wide range of magnifications, we scanned
98 across the surface of the specimen using a Hitachi S570
99 SEM with Gatan Digital Capture System. For light micro-
100 scopy, images were saved in TIFF format and labeled with
101 Photoshop 5.0 LE.

102 *Image processing*

103   We used SigmaScan Pro version 5.0 (Jandel Scientific) to
104 manually select the non-pulp chamber and pulp chamber
105 regions of interest and calculate their areas.

106 *Statistics*

107   At least 3 mice of each genotype were examined at each
108 site. Pulp chamber and non-pulp areas are expressed as
109 mean ± standard deviation. We used SigmaStat version 2.03
110 (SPSS) to perform statistical analyses. Two-factor ANOVA
111 (genotype, 3 strata; and location, 2 strata) was performed
112 following square root transformation of the raw data. Post
113 hoc comparisons were performed using Tukey's test.

114 **Results**

115 *Clinical tooth phenotype in oim/oim and oim/+ mice*

116   Tooth fragility is a prominent feature of the *oim/oim*
117 phenotype. Teeth break spontaneously if animals are fed a
118 pelleted diet. In order to prevent this problem, our standard
119 husbandry practices include provision of powdered chow to
120 *oim/oim* and *oim/+* animals. In our experience, *oim/oim*
121 upper incisors uniformly display brownish discoloration
122 relative to both +/+ and *oim/+* teeth, but there is no obvious
123 abnormality of intact teeth either from other sites in 11-
124 week-old *oim/oim* animals or in any of the teeth of *oim/+*
125 animals, as shown in Fig. 1. In addition, no phenotypic
126 differences were observed between males and females for
127 any of the genotypes.

128 *Genotype and position-dependent variation of incisor*
129 *morphology*

130   While all 3 *Col1a2* genotypes have similar lower incisor
131 morphology, *oim/oim* upper incisors display a distinctive
132 triangular cross-section, as demonstrated in Fig. 2. Similarly
133 to lower incisors, there is no alteration of molar morphology
134 across *Col1a2* genotypes (data not shown).
135   In addition to overall tooth morphology, Fig. 2 also
136 reveals notable genotype and position-dependent differences
137 of pulp chamber size in incisors. Pulp chamber areas in μm^2
138 are as follows: upper +/+ = 358 ± 75, lower +/+ = 671 ± 162,
139 upper *oim/+* = 161 ± 54, lower *oim/+* = 156 ± 19, upper *oim/*
140 *oim* = 6900 ± 1040, and lower *oim/oim* = 66 ± 62. These
141 values differ significantly by 2-factor ANOVA, as summar-
142 ized in Table 1.
143   The non-pulp chamber cross-sectional area of the
144 incisors also demonstrates genotype and position-depend-
145 ent differences. Non-pulp chamber cross-sectional area
146 reflects dentin area, as all teeth exhibit only a thin outer
147 layer of enamel. Non-pulp chamber areas in are as follows:
148 upper +/+ = 39,000 ± 1670, lower +/+ = 35,600 ± 1980,
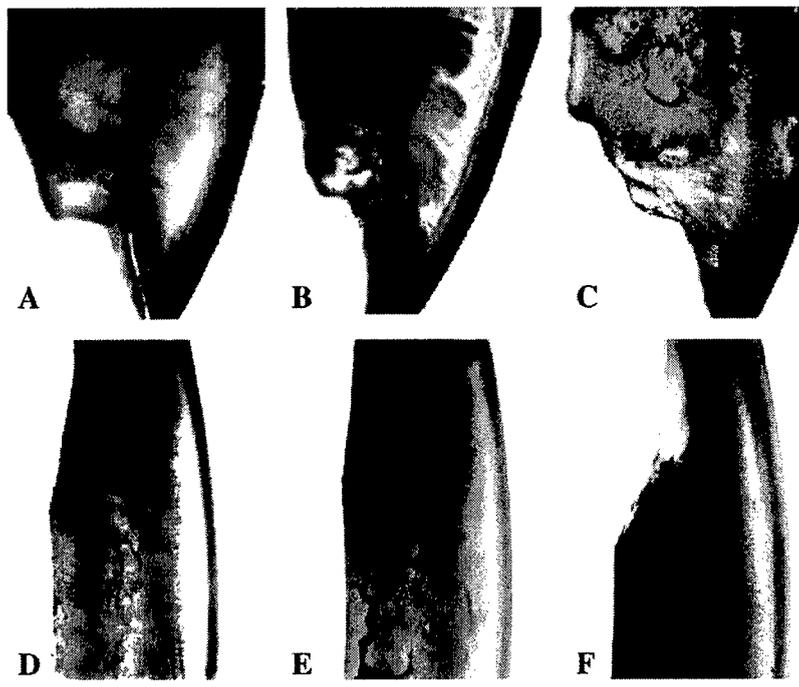
Fig. 1. Transillumination of upper and lower incisors. Images represent a medial proximal view of the light passing through the tooth. Panels A to C are from upper incisors. Panels D to F are from lower incisors. Panels A and D illustrate +/+, B and E illustrate *oim*/+, and panel C illustrates *oim/oim*. Scale bar = 500 μm.

149 upper *oim*/+ = 47,500 ± 2510, lower *oim*/+ = 26,000 ±
150 1830, upper *oim/oim* = 29,800 ± 315, and lower *oim/oim* =
151 36,800 ± 3450. These values differ significantly by 2-factor
152 ANOVA, as summarized in Table 1. In contrast to pulp
153 chamber area, where genotype has a strong impact, genotype
154 has only borderline significance for non-pulp area. However,
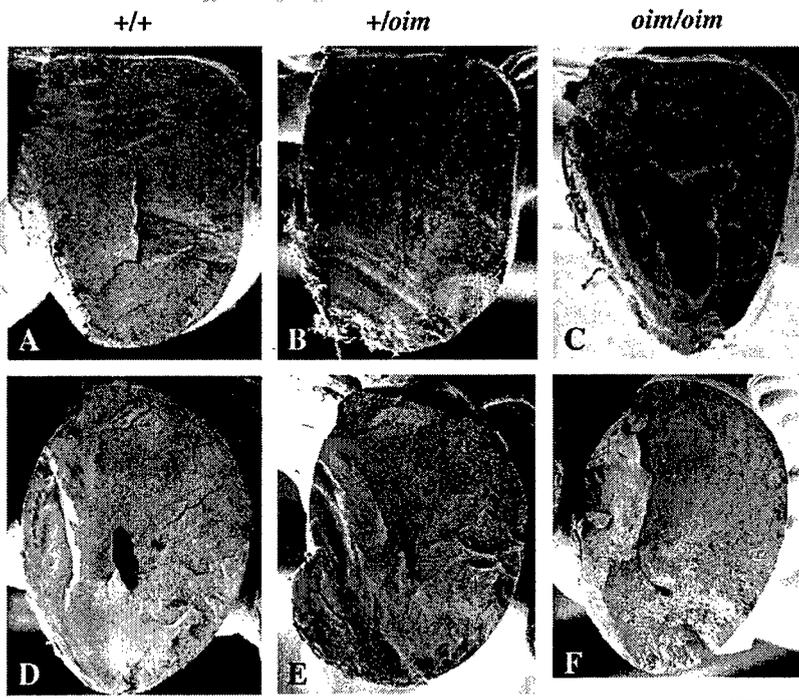
Fig. 2. SEM of tooth fracture surfaces. Images represent a cross-sectional fracture in upper and lower incisors at the level of the junctional epithelium. Panels A to C show upper incisors and panels D to F show lower incisors. Teeth are oriented with the vestibular surface at the top and the lingual surface at the bottom. Panels A and D show +/+, panels B and E show *oim*/+, and panels C and F show *oim/oim*. Scale bar = 500 μm.

t1.1	Table 1		
t1.2	Incisor cross-sectional areas		
t1.3	*Pulp chamber*		
t1.4	Overall	Genotype	$P < 10^{-5}$
t1.5		Position	$P < 10^{-5}$
t1.6		Interaction	$P < 10^{-5}$
t1.7	Within upper	+/+ vs. *oim/+*	NS
t1.8		+/+ vs. *oim/oim*	$P = 1.9 \times 10^{-4}$
t1.9		*oim/+* vs. *oim/oim*	$P = 1.9 \times 10^{-4}$
t1.10	Within lower	+/+ vs. *oim/+*	$P = 3.4 \times 10^{-4}$
t1.11		+/+ vs. *oim/oim*	0.0037
t1.12		*oim/+* vs. *oim/oim*	NS
t1.13	Within +/+	Upper vs. Lower	$P = 1.7 \times 10^{-4}$
t1.14	Within *oim/+*	Upper vs. Lower	NS
t1.15	Within *oim/oim*	Upper vs. Lower	$P = 1.7 \times 10^{-4}$
t1.16			
t1.17	*Non-pulp area*		
t1.18	Overall	Genotype	$P = 0.041$
t1.19		Position	$P = 3.1 \times 10^{-4}$
t1.20		Interaction	$P < 10^{-5}$
t1.21	Within upper	+/+ vs. *oim/+*	$P = 0.0070$
t1.22		+/+ vs. *oim/oim*	$P = 0.0018$
t1.23		*oim/+* vs. *oim/oim*	$P = 1.9 \times 10^{-4}$
t1.24	Within lower	+/+ vs. *oim/+*	$P = 8.6 \times 10^{-4}$
t1.25		+/+ vs. *oim/oim*	NS
t1.26		*oim/+* vs. *oim/oim*	$P = 4.5 \times 10^{-4}$
t1.27	Within +/+	Upper vs. Lower	NS
t1.28	Within *oim/+*	Upper vs. Lower	$P = 1.7 \times 10^{-4}$
t1.29	Within *oim/oim*	Upper vs. Lower	$P = 0.0045$

the genotype × location interaction is highly significant for both pulp and non-pulp areas.

Disturbed dentin ultrastructure in oim/oim and oim/+

As shown in Fig. 3, SEM demonstrates that compared to wild-type animals, both *oim/oim* and *oim/+* strains display a reduction in the density and regularity of dentinal tubules in the matrix adjacent to the pulp chamber. The reduction in dentinal tubule density is dependent on mutant allele dosage, with *oim/+* animals displaying a phenotype

intermediate between those of the +/+ and *oim/oim* homozygotes.

Abnormal ultrastructural features are also apparent closer to the dentino-enamel junction, as shown in Figs. 4 and 5, obtained from incisors and molars, respectively. High-power images of incisor dentin reveal that the odontoblast processes of +/+ teeth are regularly spaced and uniformly invested with accreted mineral (Fig. 4G). Moreover, fracture of the peritubular and intertubular dentin occurs in 2 discrete, well-defined planes. Teeth from *oim/+* heterozygotes (Fig. 4H) have lesser amounts of mineral adherent to the odontoblast processes, allowing visualization of protein fibrils. While the *oim/+* fracture plane is undulated, there is a less obvious distinction between the peritubular and intertubular dentin fracture planes. In *oim/oim* homozygotes (Fig. 4I), protein fibrils are abundant and it is difficult to distinguish between peritubular and intertubular regions.

The dental phenotypes described above are more pronounced in incisors (Fig. 4) than in molars (Fig. 5). In contrast, ultrastructural abnormalities are equally evident in all *oim/oim* teeth. Because of their fragility, we were unable to fracture *oim/oim* molars in a single plane, our attempts to do so resulting in a secondary fracture perpendicular to the enamel–cementum junction (Fig. 5C). That this failure is limited to the molars may simply be a consequence of the different tooth shapes. Incisors' greater ellipticity results in the sufficiency of a relatively small force to achieve fracture in the direction of the short axis. Relatively larger forces are needed to fracture the less elliptical molars, and the applied forces result in both bending and crushing.

Phenotypic variability in heterozygotes

There is also heterogeneity among *oim/+* animals studied at the same site. Fig. 6 illustrates variability of pulp chamber size in *oim/+* upper incisors. Expression of the other structural abnormalities arising from the hetero-
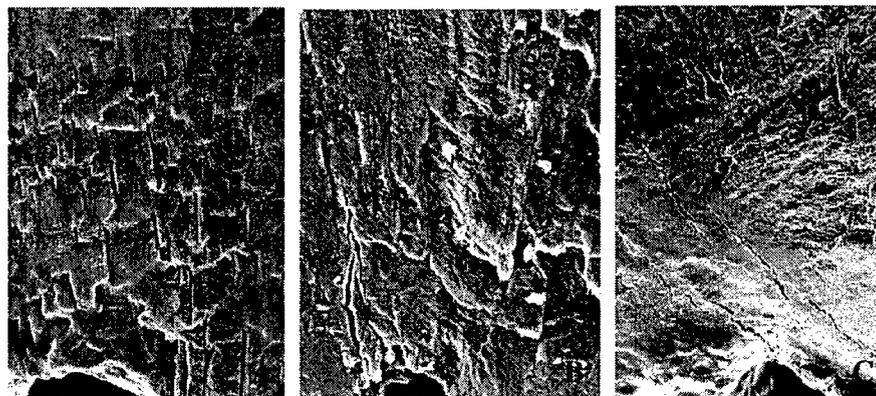
Fig. 3. SEM of dentin adjacent to the pulp chamber. Panel A shows +/+, B shows *oim/+*, and panel C shows *oim/oim*. Pulp chambers are at the lower center of each panel. Scale bar = 5 μm.
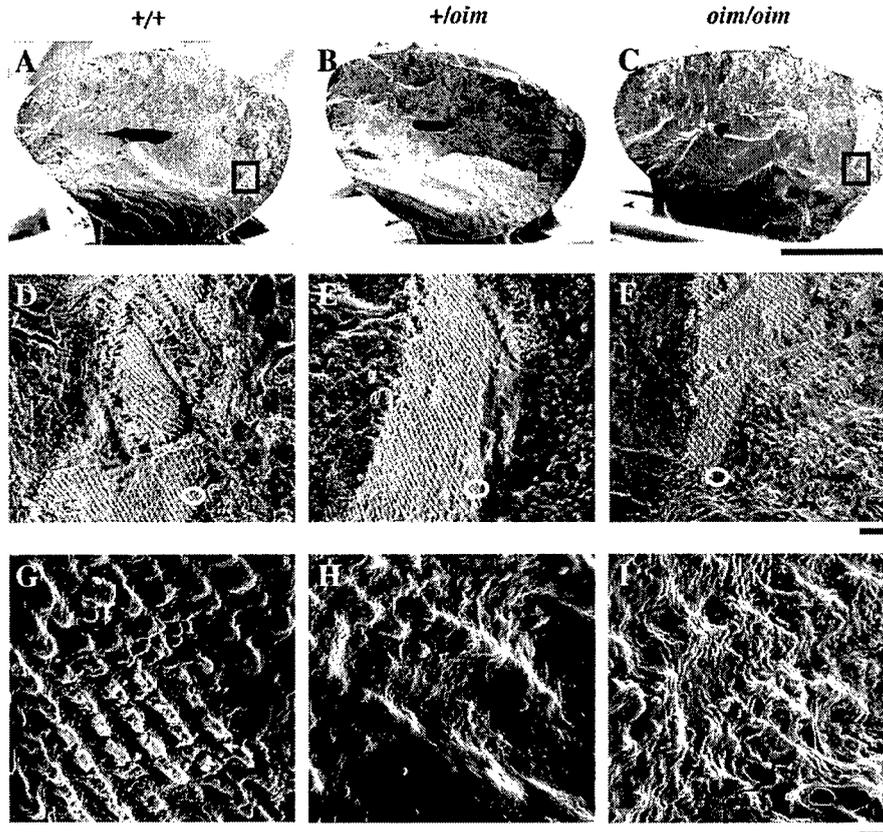
Fig. 4. SEM of lower incisors. Panels A, D, and G show +/+, panels B, E, and H show *oim*/+, and panels C, F, and I show *oim/oim*. From right to left, orientation is vestibule-lingual. Rectangles in panels A–C indicate fields shown in panels D–F and ovals in panels D–F indicate fields shown in panels G–I. Scale bars are 500 μm in panels A–C, 50 μm in panels D–F, and 5 μm in panels G–I.

zygous presence of the *oim* mutation is also variable (data not shown).

Discussion

The data shown here demonstrate that both *oim/oim* and *oim*/+ exhibit dental abnormalities. These include altered pulp chamber size, reduced numbers of dental tubules, and abnormalities of dentin mineralization, corresponding to the abnormalities encountered in human DI. These features are generally more apparent in incisors than in molars. The murine *oim* system therefore can serve as a model of type Ia1 DI, in which DI is a manifestation of primary collagen disease. The dental phenotype of *oim* resembles the skeletal phenotype insofar as its severity is dependent on the number of mutant alleles present. Abnormalities are obvious in *oim/oim* homozygotes in upper and lower incisors, and in *oim*/+ heterozygotes in upper incisors. It is worth noting that in humans with OI, ultrastructural abnormalities have been found in the teeth even in the absence of clinically apparent DI [8,9]. The presence of a microscopic DI phenotype in *oim*/+ mice is consistent with this observation in humans.

We found that the incisor non-pulp cross-sectional area is not simply related to dosage of the mutant allele, but

displays a strong genotype × position interaction. While the *oim*/+ dentin area is reduced relative to +/+ in lower incisors, it is increased in upper incisors. The *oim/oim* dentin area is reduced relative to +/+ in both upper and lower incisors, but is greater than that of *oim*/+. The pattern of dentin area is difficult to reconcile with a simple, mutant allele dose-dependent reduction of α2 chain synthesis. Any of several distinct mechanisms may contribute to the observed changes, including alteration of odontoblast numbers, alteration of synthetic activity within individual odontoblasts, and alteration of dentin matrix composition. Distinguishing among these mechanisms is an important task for future work.

The greater severity of the *oim*/+ phenotype in incisors compared to molars is another intriguing finding. One possible explanation for this observation is that in mice, incisors grow throughout life, while molars do not. It is therefore possible that in molars, slower growth is able to provide some compensation for a reduced type I collagen biosynthesis, while in incisors the developmental program of continued growth and the persistent loading demands alter such an adaptation.

In both humans and mice, DI is an inconstant OI manifestation. While DI is present in *oim*, it is absent in $Col1a1^{Mov-13}$ (*Mov-13*). This mutation is a retroviral
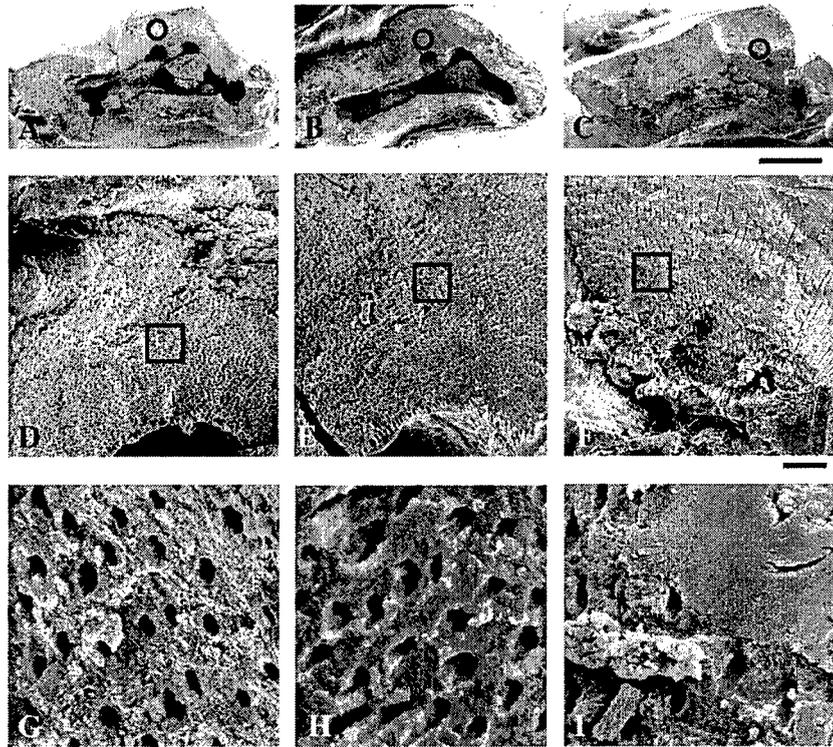
Fig. 5. Scanning electron micrographs of (upper first) molars. Panels A, D, and G show +/+, panels B, E, and H show *oim/*+, and panels C, F, and I show *oim/oim*. Rectangles in panels A–C indicate fields shown in panels D–F and ovals in panels D–F indicate fields shown in panels G–I. Scale bars are 500 μm in panels A–C, 50 μm in panels D–F, and 5 μm in panels G–I.
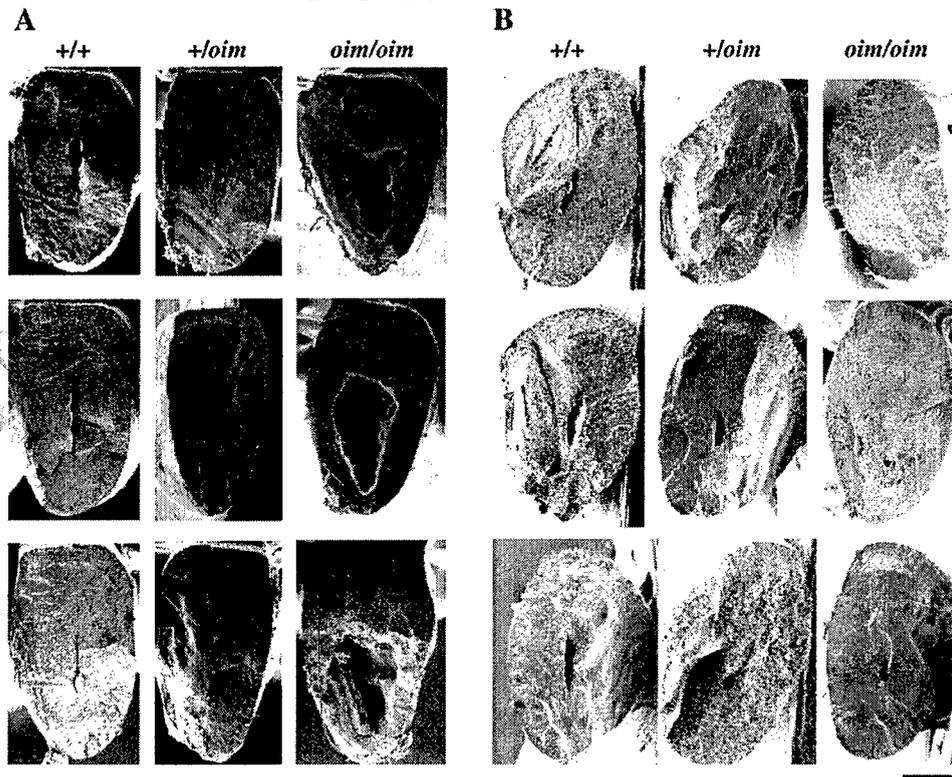
Fig. 6. Phenotypic variability in Col1a2 incisors. Panel A shows variability of pulp chamber size in upper incisors, and panel B in lower incisors. Scale bar is 500 μm.

246 insertion into the gene encoding α1(I), resulting in
247 decreased transcriptional activity [17–19]. *Mov-13/Mov-*
248 *13* homozygotes die in utero due to rupture of the great
249 vessels [20,21], while heterozygotes have skeletal fragility
250 [22–25]. However, the expression level is apparently
251 normal in teeth, so that *Mov-13/+* mice have normal teeth
252 [26]. To the best of our knowledge, dental phenotypes have
253 not been reported in other murine OI models [27–30].
254   There are important limitations to the work reported here.
255 First, we have assessed dental phenotypes in *oim/+* and *oim/*
256 *oim* mice at only a single age, 11 weeks. It is possible that
257 both additional abnormalities and additional phenotypic
258 variability would be apparent if teeth were studied over a
259 range of ages. In human OI, for example, DI is more
260 prevalent in primary teeth than in permanent teeth. In two
261 separate studies of dentin from mature, 1-year-old *oim/oim*
262 mice, molars [31] and incisors [32] were found to exhibit
263 less dramatic mineralization alterations, in contrast to the
264 findings in the current study. Second, *oim* is maintained on
265 an outbred B6C3 background, deriving its alleles ultimately
266 from either C57BL/6J or C3HeB/J. The dental phenotype
267 might differ if the mutation was to be transferred to a
268 different genetic background. Moreover, segregation of
269 parental alleles may contribute to the phenotypic variability
270 observed in *oim/+* heterozygotes. Third, our description of
271 the tooth phenotype in *oim* mice is limited to features
272 apparent by light or scanning electron microscopy. In
273 previously mentioned studies on 1-year-old teeth, the
274 mineral composition in *oim* mice was assessed by neutron
275 activation analysis [32] and by FTIR spectroscopy [31],
276 techniques that probe the chemical and molecular structure
277 of the mineral. It is possible that further investigation of the
278 teeth from growing animals with such techniques would
279 help elucidate the mechanisms by which deficiency of α2(I)
280 leads to a cascade of higher-order dentin defects.
281   In summary, we have shown that both *oim/oim* and *oim/+*
282 display dentinogenesis imperfecta. DI in homozygous
283 mutants is manifested grossly by tooth fragility. Both
284 heterozygotes and homozygous mutants have significant
285 dental abnormalities. However, both homozygotes and
286 heterozygotes demonstrate alterations of the pulp chamber
287 and decreased numbers of dental tubules. As in humans,
288 microscopy is more sensitive than clinical examination in
289 detecting DI arising in the context of OI. The *oim* model may
290 prove useful for investigating potential pharmacological
291 interventions for mild forms of DI and for better
292 understanding of collagen's role in mineralization.

293 **Acknowledgments**

References

[1] Rowe DW, Shapiro JR. Osteogenesis imperfecta. In: Avioli LV, Krane SM, editors. Metabolic bone disease. San Diego, CA: Academic Press; 1998. p. 651–95.
[2] Byers PH, Cole WG. Osteogenesis imperfecta. In: Royce PM, Steinmann B, editors. Connective tissue and its heritable disorders. New York: Wiley-Liss, Inc.; 2002. p. 385–430.
[3] Whyte MP. Osteogenesis imperfecta. In: Favus MJ, editor. Primer on the metabolic bone diseases and disorders of mineral metabolism. Washington, DC: American Society for Bone and Mineral Research; 2003. p. 470–3.
[4] Dalgleish R. The human type I collagen mutation database. Nucleic Acids Res 1997;25:181–7.
[5] Dalgleish R. The human collagen mutation database. Nucleic Acids Res 1998;26:253–5.
[6] Dalgleish, R, Database of Human Type I and Type III Collagen Mutations. 2001; 2004.
[7] Lukinmaa PL, Ranta H, Ranta K, Kaitila I. Dental findings in osteogenesis imperfecta: I. Occurrence and expression of type I dentinogenesis imperfecta. J Craniofac Genet Dev Biol 1987; 7:115–25.
[8] Lygidakis NA, Smith R, Oulis CJ. Scanning electron microscopy of teeth in osteogenesis imperfecta type I. Oral Surg Oral Med Oral Pathol Oral Radiol Endo 1996;81:567–72.
[9] Waltimo J, Ojanotko-Harri A, Lukinmaa PL. Mild forms of dentinogenesis imperfecta in association with osteogenesis imperfecta as characterized by light and transmission electron microscopy. J Oral Pathol Med 1996;25:256–64.
[10] Hall RK, Maniere MC, Palamara J, Hemmerle J. Odontoblast dysfunction in osteogenesis imperfecta: an LM, SEM, and ultrastructural study. Connect Tissue Res 2002;43:401–5.
[11] Chipman SD, Sweet HO, McBride DJ, Davisson MT, Marks SC, Shuldiner AR, et al. Defective pro alpha 2(I) collagen synthesis in a recessive mutation in mice: a model of human osteogenesis imperfecta. Proc Natl Acad Sci U S A 1993;90:1701–5.
[12] Saban J, Zussman MA, Havey R, Patwardhan AG, Schneider GB, King D. Heterozygous oim mice exhibit a mild form of osteogenesis imperfecta. Bone 1996;19:575–9.
[13] McBride DJ, Shapiro JR, Dunn MG. Bone geometry and strength measurements in aging mice with the oim mutation. Calcif Tissue Int 1998;62:172–6.
[14] Sims TJ, Miles CA, Bailey AJ, Camacho NP. Properties of collagen in OIM mouse tissues. Connect Tissue Res 2003;44(Suppl 1):202–5.
[15] Camacho NP, Hou L, Toledano TR, Ilg WA, Brayton CF, Raggio CL, et al. The material basis for reduced mechanical properties in oim mice bones. J Bone Miner Res 1999;14:264–72.
[16] Camacho NP, Dow D, Toledano TR, Buckmyer JK, Gertner JM, Brayton CF, et al. Identification of the oim mutation by dye terminator chemistry combined with automated direct DNA sequencing. J Orthop Res 1998;16:38–42.

361 [17] Jaenisch R, Harbers K, Schnieke A, Lohler J, Chumakov I, Jahner D,
362   et al. Germline integration of moloney murine leukemia virus at the
363   Mov13 locus leads to recessive lethal mutation and early embryonic
364   death. Cell 1983;32:209–16.
365 [18] Harbers K, Kuehn M, Delius H, Jaenisch R. Insertion of retrovirus
366   into the first intron of alpha 1(I) collagen gene to embryonic lethal
367   mutation in mice. Proc Natl Acad Sci U S A 1984;81:1504–8.
368 [19] Hartung S, Jaenisch R, Breindl M. Retrovirus insertion inactivates
369   mouse alpha 1(I) collagen gene by blocking initiation of transcription.
370   Nature 1986;320:365–7.
371 [20] Schnieke A, Harbers K, Jaenisch R. Embryonic lethal mutation in
372   mice induced by retrovirus insertion into the alpha 1(I) collagen gene.
373   Nature 1983;304:315–20.
374 [21] Lohler J, Timpl R, Jaenisch R. Embryonic lethal mutation in
375   mouse collagen I gene causes rupture of blood vessels and is
376   associated with erythropoietic and mesenchymal cell death. Cell
377   1984;38:597–607.
378 [22] Bonadio J, Saunders TL, Tsai E, Goldstein SA, Morris-Wiman J,
379   Brinkley L, et al. Transgenic mouse model of the mild dominant
380   form of osteogenesis imperfecta. Proc Natl Acad Sci U S A
381   1990;87:7145–9.
382 [23] Bonadio J, Jepsen KJ, Mansoura MK, Jaenisch R, Kuhn JL, Goldstein
383   SA. A murine skeletal adaptation that significantly increases cortical
384   bone mechanical properties. Implications for human skeletal fragility.
385   J Clin Invest 1993;92:1697–705.
386 [24] Jepsen KJ, Goldstein SA, Kuhn JL, Schaffler MB, Bonadio J. Type-I
387   collagen mutation compromises the post-yield behavior of Mov13
388   long bone. J Orthop Res 1996;14:493–9.
389 [25] Jepsen KJ, Schaffler MB, Kuhn JL, Goulet RW, Bonadio J, Goldstein
390   SA. Type I collagen mutation alters the strength and fatigue behavior
391   of Mov13 cortical tissue. J Biomech 1997;30:1141–7.
423

392 [26] Kratochwil K, von der Mark K, Kollar EJ, Jaenisch R, Mooslehner K,
393   Schwarz M, et al. Retrovirus-induced insertional mutation in Mov13
394   mice affects collagen I expression in a tissue-specific manner. Cell
395   1989;57:807–16.
396 [27] Pereira R, Khillan JS, Helminen HJ, Hume EL, Prockop DJ.
397   Transgenic mice expressing a partially deleted gene for type I
398   procollagen (COL1A1). A breeding line with a phenotype of
399   spontaneous fractures and decreased bone collagen and mineral. J
400   Clin Invest 1993;91:709–16.
401 [28] Pereira R, Halford K, Sokolov BP, Khillan JS, Prockop DJ.
402   Phenotypic variability and incomplete penetrance of spontaneous
403   fractures in an inbred strain of transgenic mice expressing a mutated
404   collagen gene (COL1A1). J Clin Invest 1994;93:1765–9.
405 [29] Pereira RF, Hume EL, Halford KW, Prockop DJ. Bone fragility in
406   transgenic mice expressing a mutated gene for type I procollagen
407   (COL1A1) parallels the age-dependent phenotype of human osteo-
408   genesis imperfecta. J Bone Miner Res 1995;10:1837–43.
409 [30] Forlino A, Porter FD, Lee EJ, Westphal H, Marini JC. Use of the Cre/
410   lox recombination system to develop a non-lethal knock-in murine
411   model for osteogenesis imperfecta with an alpha1(I) G349C sub-
412   stitution. Variability in phenotype in BrtlIV mice. J Biol Chem
413   1999;274:37923–31.
414 [31] Baechtold A, JT. W, Yamauchi M, Spevak M, Camacho NP, Dentin
415   Composition and Structure in the oim Mouse. In: Michel G, DDS,
416   PhD, Adele, Boskey, PhD, Colin, Robinson, PhD, editors, 6th Intl
417   Conference on the Chemistry and Biology of Mineralized Tissues,
418   1998, p. 57–61 [AAOS publication].
419 [32] Phillips CL, Bradley DA, Schlotzhauer CL, Bergfeld M, Libreros-
420   Minotta C, Gawenis LR, et al. Oim mice exhibit altered femur and
421   incisor mineral composition and decreased bone mineral density. Bone
422   2000;27:219–26.

DRAFT

Assessment of Bone Quality At The Sub-Micron Scale In Chain Deficiency Osteogenesis Imperfecta

G. E. Lopez Franco[1], D. S. Stone[2], John Jacobs[2], Alice Huang[3], Nancy Pleshko Camacho[3], Robert D. Blank[1,4]

1Medicine, University of Wisconsin-Madison, Madison, WI, USA, 2Materials Science and Engineering, University of Wisconsin-Madison, Madison, WI, USA, 3 Research Division, Hospital for Special Surgery, New York, NY, 4Geriatrics Research, Education, and Clinical Center, William S. Middleton Veterans' Hospital, Madison, WI, USA.

We will have to write an abstract. Best to do this last, when all else is done.

INTRODUCTION

Abnormalities of structural bone proteins have mechanical consequences. These have been most thoroughly characterized in animal models that allow performance of biomechanical testing under controlled conditions. However, even in the context of animal models, most mechanical investigations have been conducted at the whole bone level rather than at the tissue level.

Osteogenesis imperfecta is a family of disorders caused by mutations of the genes encoding type I collagen, the major structural protein in the bone matrix. Clinical consequences of OI vary markedly, ranging from lethal disease to subtle defects that approach the limits of detection. At the macroscopic level, many of the abnormalities resulting from OI are related to deficient bone mass and abnormal architecture, complicating determination of the specific contribution that tissue level properties make to whole bone strength. Moreover, physiological adaptation to the presence of an abnormal matrix protein during growth and development may obscure the tissue level consequences of the mutation.

Mice harboring the $Col1a2^{oim}$ mutation (*oim*) are a well-studied model of OI. This mutation is a frameshift of the gene encoding the α2 chain of type I collagen, resulting in quantitatively deficient α2(I) chain-synthesis. The resulting phenotype is obvious in *oim/oim* homozygotes, which display impaired growth and marked skeletal fragility. Phenotypic abnormalities are far subtler in *oim/+* heterozygotes, but are nevertheless apparent by biomechanical testing. Biochemical manifestations of the mutation include reduced collagen cross-linking, reduced apatite crystallinity, and increased proline hydroxylation.

In order to better characterize the tissue-level mechanical consequences of the *oim* mutation, we performed nanoindentaton of unembedded cortical bone in C57BL/6J and B6C3FeLe *a/a* with various *Col1a2* genotypes sacrificed at 11 and 17 ± 1 week of age. We report that *Col1a2* genotype, genetic background, age and possibly specimen orientation each affect tissue-level mechanical performance as assessed by nanoindentation interpreted by 2 analytical methods. Further, Atomic Force Microscopy

(AFM) revealed heterogeneous, site specific differences in topographical roughness among *Col1a2* genotypes compatible with the existence of focal areas of impaired mineralization. Moreover, examination of unembedded samples allowed us to analyze compliance, providing additional insight into bone's mechanical behavior.

MATERIAL AND METHODS

Mice: Animals were housed 2 to 5/500 cm^2 cage on corncob bedding, fed powdered, irradiated PICO 5058 or PMI 5001 laboratory rodent chow and tap water *ad lib* and exposed to 12 hour light/12 hour dark cycle. Mice used for bone analyses were sacrificed at 11 and 17 $\pm$ 1 week of age and bone specimens obtained for study. Bones were stored frozen until thawed for preparation.

Sample preparation: We prepared femoral or tibial diaphyseal specimens for study in either the longitudinal (polished approximately parallel to the bone's long axis) or cross (cut in cross-section and polished approximately perpendicular to the bone's long axis) orientation. Samples were polished sequentially with 100, 50, 20, 10, 5, and 3 μm diamond cloth, sonicated in water for 10-15 sec at 47 Hz to remove adherent debris, and mounted on stainless steel discs with superglue. Samples were prepared and studied without embedding.

Imaging: Scanning electron microscopy (SEM) images were acquired with a Hitachi S570 at 10 kV and 7 mm working distance after platinum sputter coating. AFM images were obtained with the Triboscope (Hysitron, Minneapolis, MN) nanoindentation system prior to and following indentation testing. SEM and AFM images were used to measure the area of indentation and assess material pileup. Indent dimensions were determined by using AFM and SEM images and indent area was calculated from the side lengths by Heron's formula {Press, 1978 #15}.

Nanoindentation: We performed nanoindentation using a Triboscope system. Loading, holding and unloading segments described the force profile applied to the sample by using a diamond Berkovich tip at loads between 3000 and 8000μN. We performed a minimum of 13 indents per bone. Prior to testing bone samples, a series of indents in fused quartz was performed to determine the machine compliance and calibrate the area function. Data were analyzed using the Oliver and Pharr method as implemented by the Hysitron instrument software and manually by an elasticity analysis as described previously (13). Meyer hardness was calculated as $H = L/A$, with L = maximum load and A = area of indentation. Young's Modulus was calculated from reduced Young's

Modulus (E_r) assuming a specimen Poisson ratio = 0.3 (4). Specimen compliance and tip properties were determined by using the J_0 parameter, as previously described (13). $J_0 = H/E^2_{eff}$, where E is the effective modulus, determined jointly by the Young's moduli of the sample and indenter, the Poisson ratios of the sample and indenter, and a constant determined by the geometry of the indenter tip. This treatment allows the measured unloading compliance, C, to be resolved into the sum of the machine compliance, C_m and the sample compliance, C_0. By plotting $L^{1/2}$ v $L^{1/2}C$, for indents performed at varying maximum loads, one obtains a regression line whose intercept is $J_0^{1/2}$ and whose slope is C_m. The region between 95% and 20% of the unloading portion of the curve is used to determine the slope.

Statistical analysis: Data are reported as mean + standard deviation unless otherwise noted. Comparison among ages, genotypes, and orientations was performed by ANOVA with *post hoc* application of Tukey's test.

RESULTS

ATOMIC FORCE MICROSCOPY IMAGES SUGGEST FOCAL MINERALIZATION IMPAIRMENT.

AFM images showed in figure 1 illustrate some of the qualitative topographical differences observed among *Col1a2* genotypes. In the +/+ image, no fibers are apparent. In the *oim/+* image, some fibers can be identified, while fibers are prominent in the *oim/oim* image. Other areas of *oim/+* and *oim/oim* cortical bone revealed a topography more similar to that of the wild type, but we did not encounter any fibrous regions in the +/+ bone (not shown). We interpret these observations as suggesting the presence of focal mineralization impairment in the *oim/+* and *oim/oim* tissue.

REDUCED YOUNG'S MODULUS (ER) AND HARDNESS (H) (GPA) FROM TRIBOSCOPE SOFTWARE AND FROM COMPLIANCE CORRECTION.

We analyzed the nanoindentation data in 2 ways. First, we used the Triboscope instrument software to implement analysis by the Oliver and Pharr method. Second, we performed a manual compliance analysis. Separate statistical analyses of the effects of genotype, age, and specimen orientation were performed for each analysis.

Figure 2 shows a typical indent and load-displacement curve. Table 1 summarizes the hardness data and Table 2 the Young's modulus data.

Both methods find that hardness is greater in the longitudinal than in the cross sample orientation ($P < 10^{-5}$). At 17 weeks, there is also a significant effect of genotype ($P = 0.009$), but there is no significant interaction between genotype and orientation. When comparing *oim/+* and +/+ genotypes at 11 and 17 weeks, there are significant effect of age ($P < 10^{-5}$) and genotype ($P = 0.007$) with a marginally significant interaction between them ($P = 0.02$). Limiting comparisons to the 3 *Col1a2* genotypes at 11 weeks, there is a significant difference between *oim/oim* and the other 2 genotypes by manual analysis ($P = 2 \times 10^{-5}$) and ** by software analysis (insert stats).

When comparing genotype and age, there is a statistically significant difference ($P = <0.001$) in the mean values among the different levels of Age as well as in the mean values among the different levels of Genotype ($P = 0.008$).

but the magnitude of the difference is greater according to the instrument software analysis. The instrument software finds increasing hardness as the dosage of *oim* alleles increases in 11 week old animals, while the manual analysis finds that at this age there is no difference between the +/+ and *oim/+* heterozygotes, with both having lower H than the *oim/oim* homozygotes. . There was no genotype-dependent difference in longitudinal hardness at 17 weeks in B6C3 animals, but both tested genotypes were harder than C57BL/6 by software analysis (insert stats), while only *oim/+* was harder than C57BL/6 by manual analysis (insert stats). For those genotypes studied at both 11 and 17 ages, hardness increased with age (insert stats), but once again the magnitude of the age effect was greater by the software analysis than the manual analysis.

For Young's modulus, manual analysis gave consistently higher values than those calculated by the instrument software. The instrument software finds that for the B6C3 mice, regardless of *Col1a2* genotype have a greater Young's modulus in the longitudinal orientation than in the cross orientation (insert stats), while there is no orientation-dependent difference in C57BL/6. In contrast, the manual analysis finds greater modulus in the longitudinal orientation for both the C57BL/6 and B6C3 strains (insert stats). The analyses differ most dramatically in assessing the impact of *Col1a2* genotype at 11 weeks of age. Instrument software finds that *oim/+* and *oim/oim* have lower Young's modulus than +/+ (insert statistics). Manual analysis leads to *oim/oim* mice having a significantly greater Young's modulus than either +/+ or *oim/+* animals (show stats). Both analyses show an increase in Young's modulus between 11 and 17 weeks (show stats).

COMPLIANCE IS RELATED TO CORTICAL THICKNESS IN LONGITUDINAL ORIENTATION

Figure 3 shows the J_o-based compliance analysis of bones tested in the longitudinal orientation. It reveals that in general, there is a genotype-dependent difference in system compliance, as indicated by the slope of the various regression lines. Bone from +/+ bones show essentially 0 slope, while *oim/oim* bones show a slope of approximately ***(plug in number). Heterozygous bones span the entire range

from *** to   Since machine compliance is uniform across specimens, the differences in system compliance represent differences in sample compliance. At the right of figure 3, we illustrate schematically our interpretation of the origin of the observed differences in specimen compliance. While +/+ bones have thick cortices in relation to overall bone diameter, *oim/oim* bones have a much smaller cortical thickness and *oim/+* bones have cortical thicknesses that span a wide range of values.   Unfortunately, we did not measure our specimens prior to nanoindentation testing, but figure 4 shows a SEM image of fractured +/+ and *oim/+* femora illustrating the extent of variation observed in actual specimens.

Figure 5 shows the time-depth-based creep analysis for the three *Col1a2* genotypes and reveals that +/+, *oim/+* and *oim/oim* bones behaved identically.

DISCUSSION

The experiments reported here highlight some *Col1a2* genotype-dependent features of bone tissue and illustrate the importance of nanoindentation protocol on interpretation of the data. In particular, we demonstrate the importance of embedding and specimen orientation.

AFM scanning of polished bone surfaces reveal focal areas in which mineralization appears to be reduced. This is not a uniform feature of the bone matrix, as many areas examined in the *oim/+* and *oim/oim* specimens look no different from +/+ bone. However, we did not observe any apparently undermineralized fields in any of the +/+ specimens studied.

We note substantial differences between the Young's modulus values obtained by the software and manual analyses. The manual analysis gives greater values of E, and the magnitude of the discrepancy between the 2 methods is greater in the longitudinal orientation. The compliance analysis allows us to explain these apparent discrepancies. The software analysis doesn't account for specimen compliance, while the manual analysis explicitly measures it. In the longitudinal specimen orientation, indentation occurs in a region of bone that is unsupported by an embedding substrate or by a continuous column of tissue. The specimen can therefore deform in response to

the force imparted by the indenter. The deformation is reflected in the specimen's compliance, which generally increases in relation to the specimen diameter and decreases in relation to cortical thickness. By accounting for sample deformation, the manual analysis yields an increased E. This explanation accounts for the greater impact of the analysis method in the longitudinal orientation than in the cross orientation, and in specimens with greater compliance than in specimens with lesser compliance. That specimen compliance is considered in the manual analysis leads us to consider the moduli obtained in this way as more reliable than those obtained by the instrument software.

Lesser discrepancies are observed between the hardness values obtained by the 2 methods. These reflect the areas used in calculating hardness. For the manual analysis, area was determined on the basis of imaging, while the area function was used to determine area in the software analysis. Because the manual analysis is based on a direct measurement, it should be considered more reliable.

Compliance analysis of the sort performed here is possible regardless of the methods used to prepare the specimens, but its use with unembedded bone specimens allows the application of nanoindentation methods to a novel problem. While past nanoindentation studies of bone have only sought to study hardness and Young's modulus, we show here that a bone's compliance behavior is also amenable to study. While the experiments reported here are insufficient to describe the precise relationships between bone tissue material properties, specimen geometry, and compliance, fuller elucidation of these is a topic worthy of further study.

With regard to the effects of genotype, age, and orientation on hardness and Young's modulus, we find that Young's modulus and hardness increase with age in both +/+ and *oim/+* bones tested in the longitudinal orientation. We find that these 2 genotypes do not differ significantly from each other for Young's modulus, but that hardness is marginally greater (double check for significance) in the *oim/+* bones. We find that Young's modulus is greater in *oim/oim* bone than either of the other 2 *Col1a2* genotypes in 11 week old specimens tested in the longitudinal orientation. Lastly, we find that both Young's modulus and hardness are greater in the longitudinal than the cross orientation.

These findings can be compared to past studies of biomechanical performance in the $Col1a2^{oim}$ system. (insert highlights of past work here need to include studies by Camacho, King, Landis, Fratzl. Also include your tooth data).

Our findings in the $Col1a2^{oim}$ system can also be considered in relation to other investigations of tissue-level biomechanical properties in other forms of OI. It is unsurprising that we observe increases in both hardness and Young's modulus between 11 and 17 weeks. At 11 weeks, mice are still growing, while 17 weeks is considered to be the age at which skeletal maturity is reached in wild type mice (Beamer Bone 1995 or 1996). In human OI, frequent fractures in childhood, relative sparing during young adulthood and middle age, and increased fracture frequency in the later years is a frequently observed clinical pattern (Spotila 1994 and perhaps other references within that one).

There are several limitations for the work presented here. One is that we did not obtain continuous indentation values for all groups, which precluded manual calculation of Young's Modulus and hardness for some genotypes. Another limitation is that we did not have samples for *oim/oim* at 17 weeks of age, or C57BL/6 at 11 weeks. As a consequence, we were not able to report those results. A third limitation of our study is that our nanoindentation apparatus is not housed in a controlled humidity environment. This limited our ability to ensure that the hydration status of all specimens was strictly equivalent. A fourth limitation is that nanoindentation is insensitive to anisotropy. Thus, although our data suggest the presence of anisotropic biomechanical behavior, mirroring the known anisotropy of bone's molecular components, it is likely that the impact of tissue orientation on mechanical performance has been underestimated here. Finally, it is important to recognize that analysis of unembedded specimens has magnified the differences between software and manual analysis of the data.

Regardless of the limitations, we were able to present a new approach for a deeper understanding of bone mechanics in chain deficiency

osteogenesis imperfecta. Our work can be utilized to further explore whole bone mechanical failure in other diseases such as osteoporosis. Application of nanoindentation may provide insight regarding the mechanical consequences or other mutations, drug treatments, and husbandry conditions.

BIBLIOGRAPHY

1. Camacho, N., Carroll P. ,Raggio, CL. Fourier transform infrared imaging spectroscopy (FT-IRIS) of mineralization in bisphosphonate-treated oim/oim mice. Calcified Tissue International. May. 72:604-9; 2003.

2. Camacho, N., Landis, WJ., Boskey, AL. Mineral changes in a mouse model of osteogenesis imperfecta detected by Fourier transform infrared microscopy. Connective Tissue Research 35:259-65; 1996.

3. Fan, Z., Swadener, JG., Rho, JY., Roy, ME., Pharr, GM. Anisotropic properties of human tibial cortical bone as measured by nanoindentation. Journal of Orthopedic Research 20:806-10; 2002.

4. Farah, J. W., Craig, R.G., and Meroueh, K.A Finite element analysis of three- and four-unit bridges. J. Oral Rehabil 16:1603-611; 1989.

5. Grabner, B., Landis, WJ., Roschger, P., Rinnerthaler, S., Peterlik, H., Klaushofer, K., Fratzl P. Age- and genotype-dependence of bone material properties in the osteogenesis imperfecta murine model (oim). Bone 29:453-7; 2001.

6. Kamat, S., X. Su, R. Ballarini, and A.H. Heuer, Structural basis for the fracture toughness of the shell of the conch Strombus gigas. Nature 405:1036-40; 2000.

7. Kuznetsova, N., McBride, DJ Jr., Leikin, S. Osteogenesis imperfecta murine: interaction between type I collagen homotrimers. Journal of Molecular Biology. 309:807-15; 2001.

8. Lopez Franco, G., Huang, A., Pleshko Camacho, N., Blank, RD. Dental Phenotype of the col1a2^{oim}
Mutation: DI Is Present in Both Homozygotes and Heterozygotes. Bone In press; 2005.

9. Nix., J. J. V. a. W. D. Measuring the elastic properties of
anisotropic materials by means of indentation experiments. Mechan. Phys. Solids 42:1223-1245; 1994.

10. Phillips, C., Bradley, DA., Schlotzhauer, CL., Bergfeld, M., Libreros-Minotta, C., Gawenis, LR., Morris, JS., Clarke, LL., Hillman, LS. Oim mice exhibit altered femur and incisor mineral composition and decreased bone mineral density. Bone 27:219-26; 2000.

11. Rho, J., Tsui, TY., Pharr, GM. Elastic properties of human cortical and trabecular lamellar bone measured by nanoindentation. Biomaterials 18:1325-30; 1997.

12. Sarathchandra, P., Pope, FM. ,Kayser, MV., Ali SY. A light and electron microscopic study of osteogenesis imperfecta bone samples, with reference to collagen chemistry and clinical phenotype. Journal of Pathology 192:385-95; 2000.

13. Stone, D., Yoder, KB., Sproul, WD. Hardness and Elastic Modulus of TiN Based on Continuous Indentation Technique and New Correlation. J. Vac. Sci. Technol A9:2543-47; 1991.
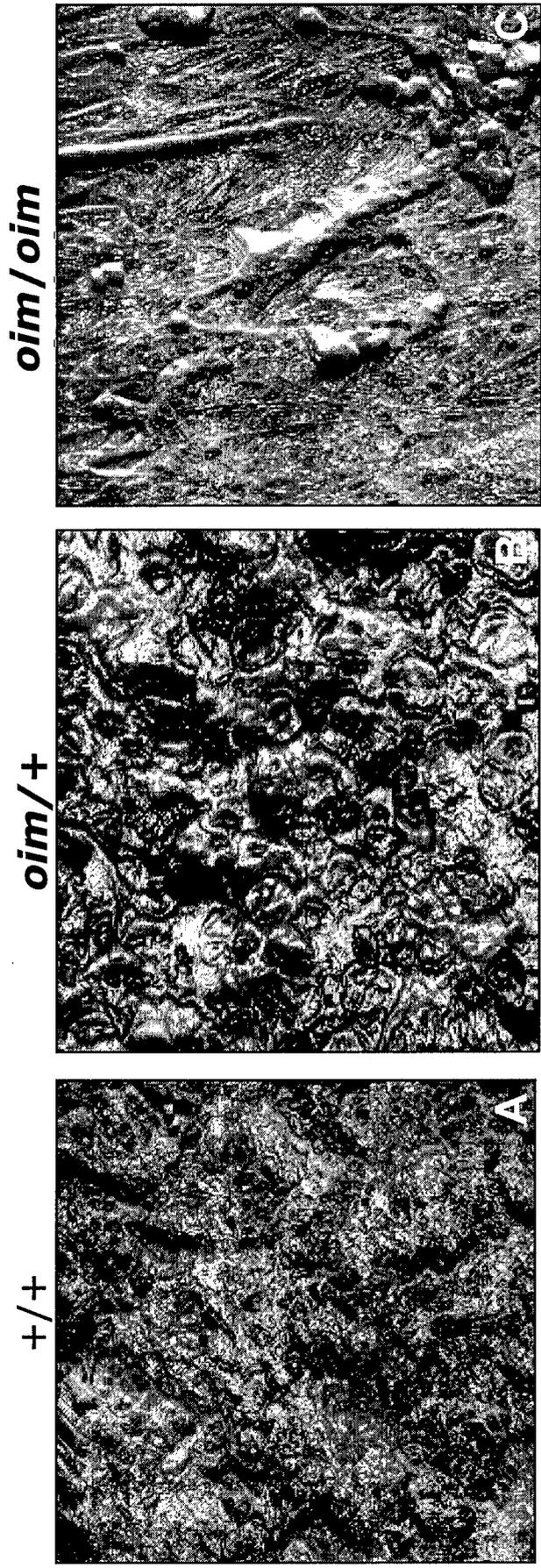
Figure 1. AFM topographical images of bone for the three *Col1a2* genotypes. +/+ is illustrated in panels A and D, *oim*/+ in panels B and E and *oim*/*oim* in panels C and F. Scale bar for A-C corresponds to 1µm. **Scale bar for D-F corresponds to 400nm.**
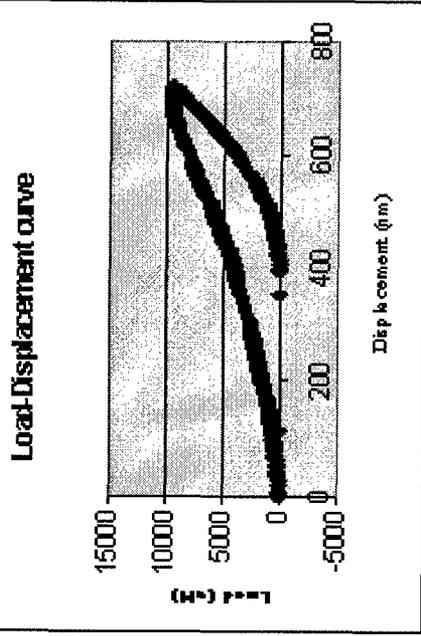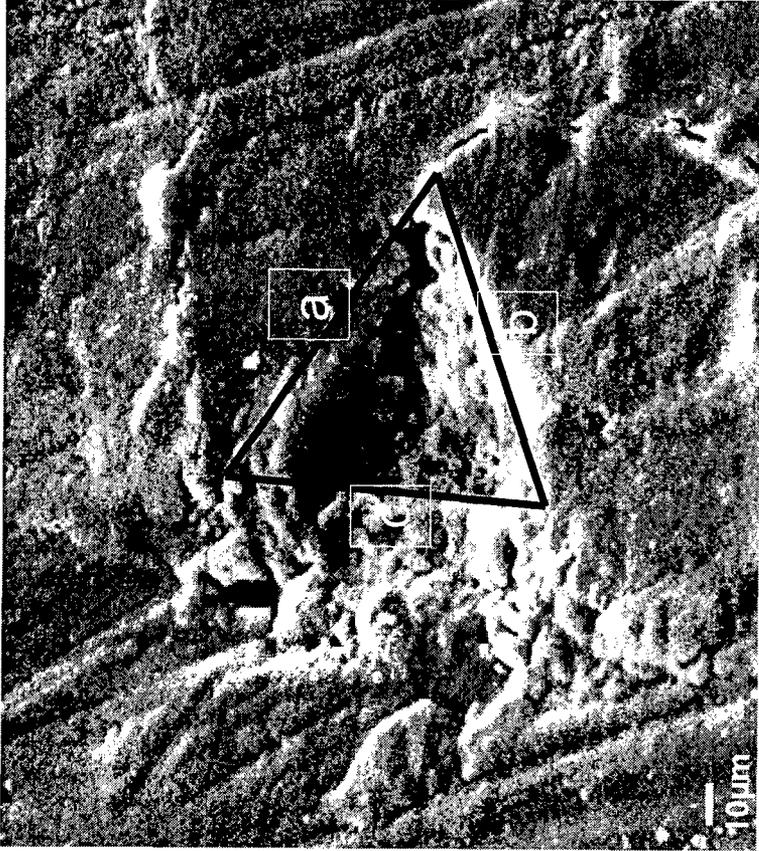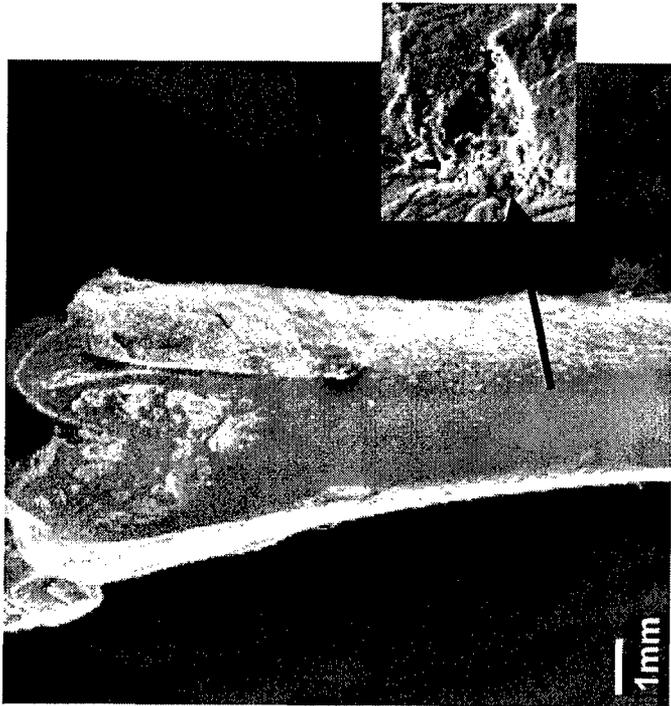
$$A = \sqrt{S(S-a)(S-b)(S-c)}$$
$$A = 17464 \ \mu m^{\wedge}2$$

Figure 2. Calculation of Hardness for Single Indent

	17 Cross		17 Long		11 Long	
	Software	Manual	Software	Manual	Software	Manual
B6	0.7 ± 0.2	0.7 ± 0.2	1.0 ± 0.1	1.1 ± 0.1	ND	ND
+/+	0.6 ± 0.1	0.7 ± 0.1	1.4 ± 0.1	1.1 ± 0.1	0.4 ± 0.1	0.5 ± 0.1
oim/+	0.5 ± 0.1	Like +/+	1.4 ± 0.1	1.2 ± 0.1	0.5 ± 0.1	0.5 ± 0.1
oim/ oim	ND	ND	ND	ND	0.6 ± 0.1	$0.6 + 0.1$

Like "+/+" corresponds to data that were obtained at one load and that fell on the same curve as data obtained at different loads

Table 1. Hardness (GPa) According to Age, Orientation, and Analysis Method

	17 Cross		17 Long		11 Long	
	Software	Manual	Software	Manual	Software	Manual
B6	18.2 ± 4	Like wt	19.7 ± 8	33.9 ± 0.8	ND	ND
+/+	16.2 ± 4	22.6 ± 4	29.3 ± 0.1	30.2 ± 4	16.20 ± 5	19.0 ± 3.8
oim/+	18.2 ± 2	Like wt	27.7 ± 4	34.6 ± 1.8	9.50 ± 4.7	18.3 ± 2.3
oim/ oim	ND	ND	ND	ND	9.50 ± 3	34.6 ± 2.4

Table 2. Young's Modulus (GPa) According to Age, Orientation, and Analysis Method
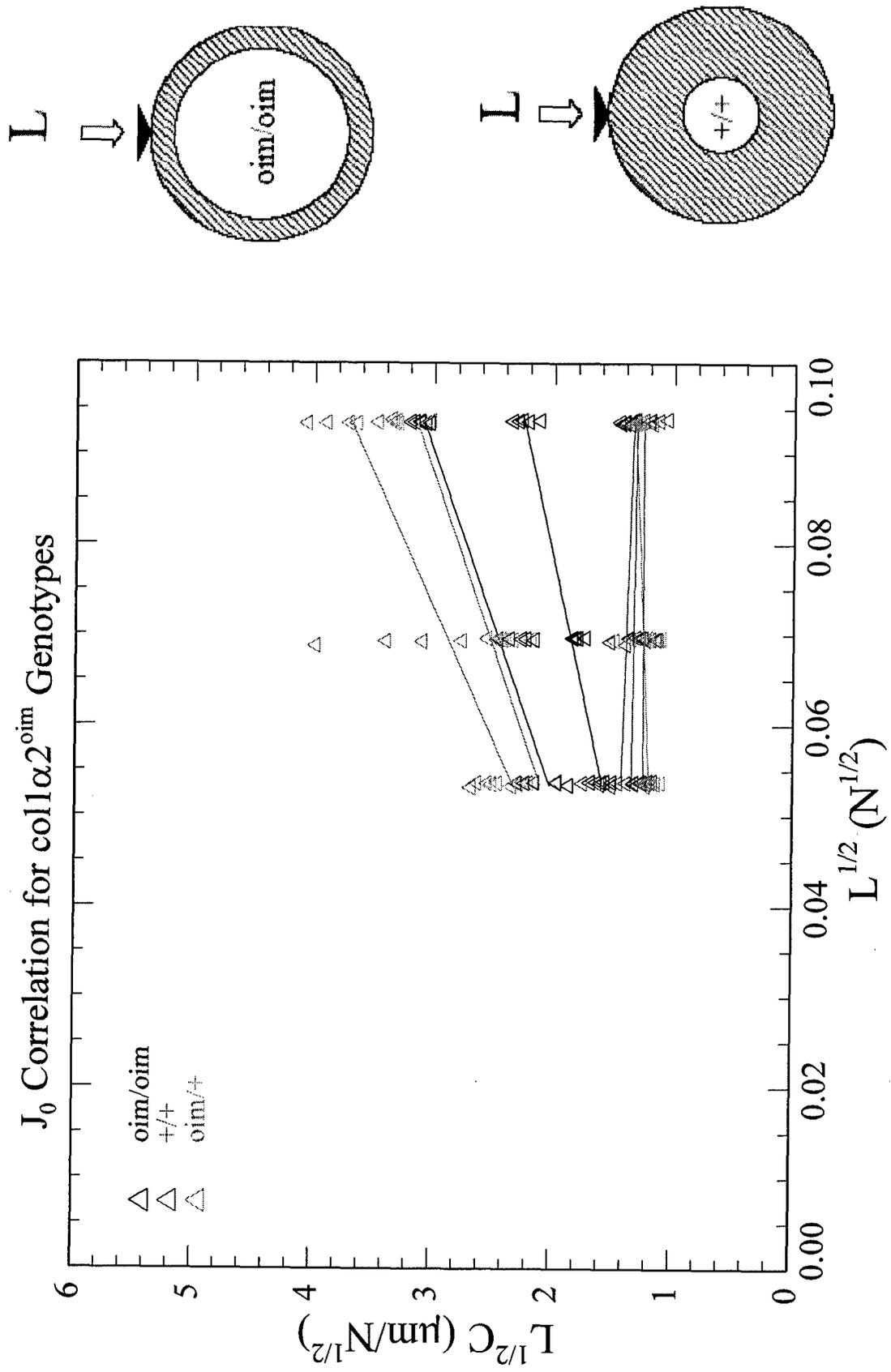
Figure 3. J0 Correlation for *col1a2oim* Genotypes. *+/+* is represented on black, *oim/+* on green and *oim/oim* is represented on black. Circles in the right illustrate scheme of compliance effects in *+/+* and *oim/oim*
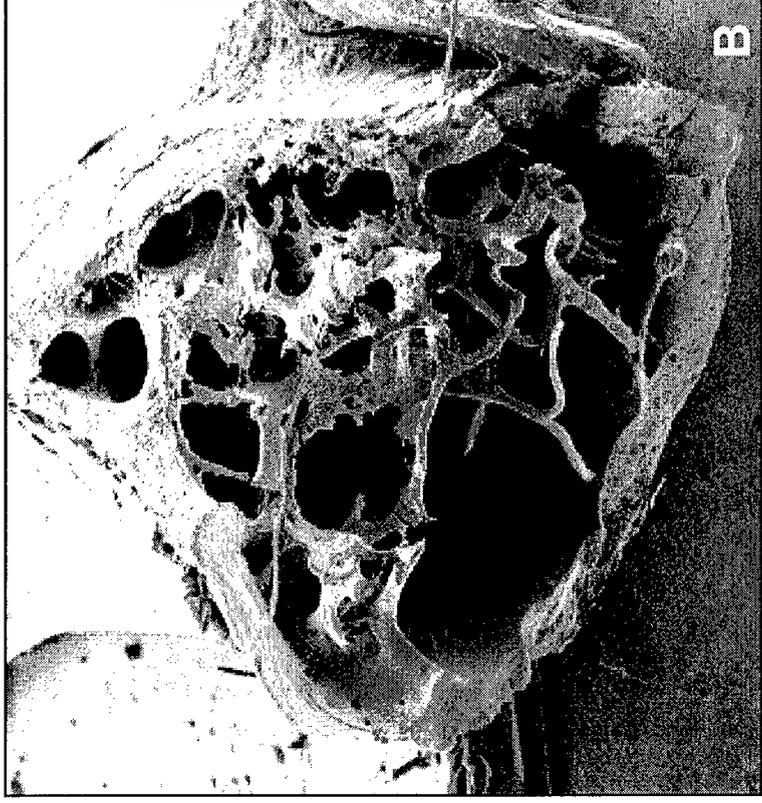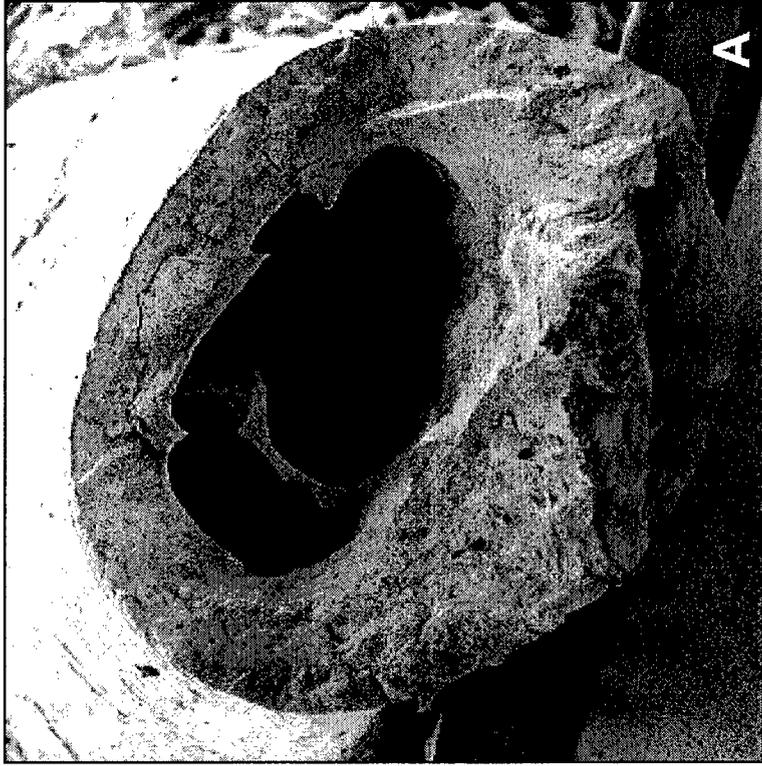
Figure 4. SEM Images of Femoral Fracture Surfaces in *+/+* (A) and *oim/+* (B)

500μm
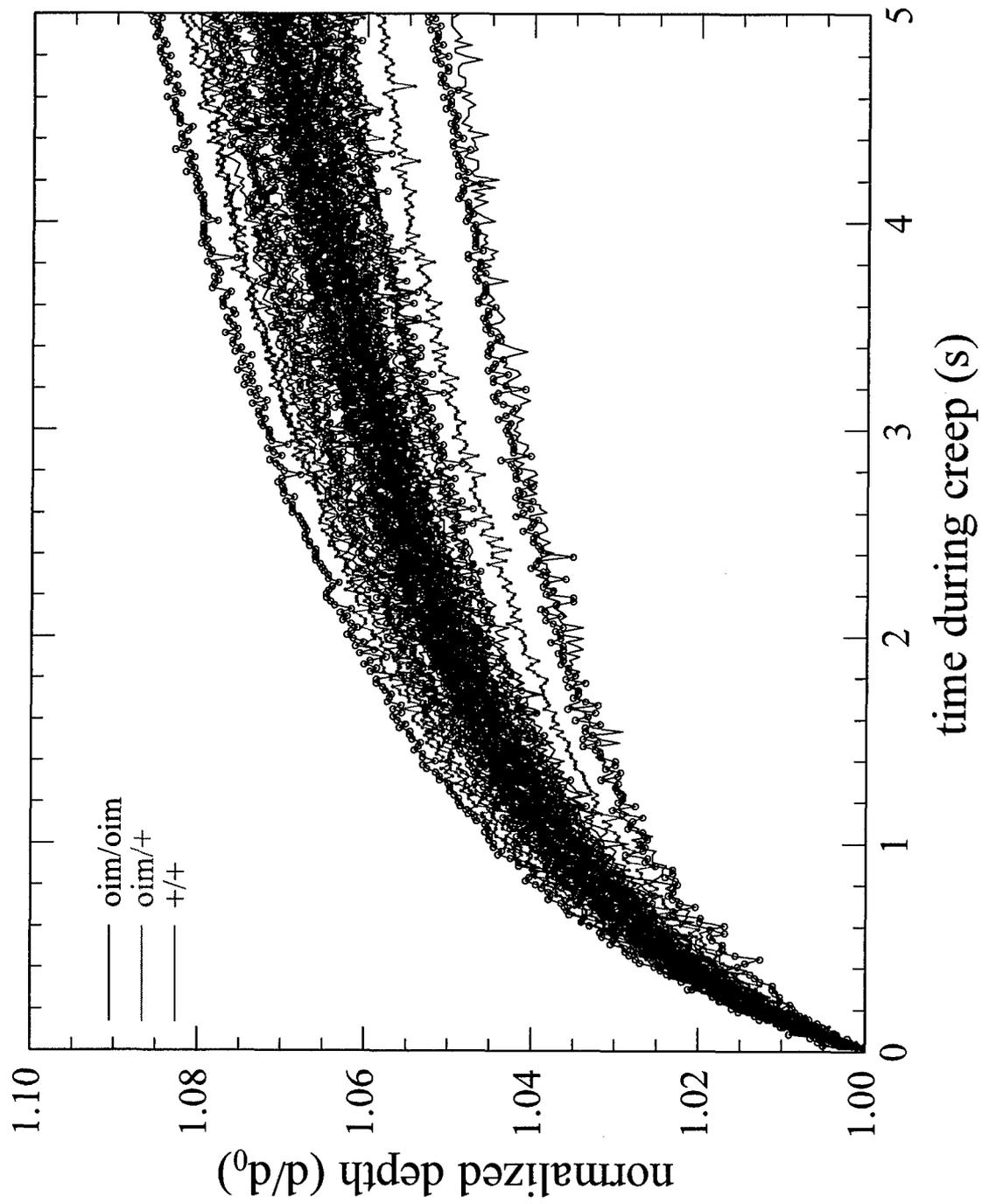
Figure 5. Representation of creep from time vs depth data for the three Col1a2 genotypes